Bridging between bioactive and biomimicking materials: cascade reactions in catalytic compartments

Inauguraldissertation

zur Erlangung der Würde

eines Doktors der Philosophie vorgelegt der

Philosophisch-Naturwissenschaftlichen Fakultät

der Universität Basel

von

Andrea Belluati

aus Italien

Basel, 2020

Genehmigt von der Philosophisch-Naturwissenschaftlichen Fakultät

auf Antrag von

Prof. Dr. Cornelia G. Palivan (Universität Basel)

und

Prof. Dr. Lucio Isa (Eidgenössische Technische Hochschule Zürich)

Basel, den 21. April 2020

Prof. Dr. Martin Spiess

Dekan

Summary

Based on the theme of this thesis, Chapter 1 introduces the concept cells as the paramount example of compartmentalization in nature and the use of polymeric assemblies encapsulating enzymes as mimics. It then proceeds to discuss the principles behind self-assembly of polymers and applications of such systems. Building on that, Chapter 2 states the aim of the thesis, delineating its background and the vision that lead to a coherent research process. For this thesis, vesicular polymeric compartments composed of the triblock copolymer PMOXA-*b*-PDMS-*b*-PMOXA were produced, harbouring various proteins in their lumen and membranes, for catalysis and membrane permeabilization.

In a first step, I contributed to the development of multicompartment cell mimics, micrometer-sized polymeric vesicles that behave like cells in their internal organization and segregation, triggered environmental responses and architectural plasticity. In Chapter 3, such assemblies are able to sense the redox potential of the exterior and, with a cascade resembling receptor-mediated pathways in cells, activate responses ranging from enzymatic activity to selective permeability and cytoskeleton reorganization.

In Chapter 4 and 5, the polymeric vesicles were "shrunk" to diameters of 200 nm and less, to work on biological settings, using sizes smaller than cells for future biomedical applications, with binary mixture of vesicles encapsulating a single type of enzyme. They lost their internal compartmentalization but gained a more intimate relationship with living matter, acting first as cell models, then as symbionts to detoxify the cell medium from uric acid (Chapter4.1) and finally as artificial organelles to study the effect of the overproduction of the signaling molecule cGMP through an already-present cascade (5.1). These two studies shed light not only on the general behavior of binary cascades at the nanoscale, but also on technological limitations of such system, that is the difficult transmembrane diffusion through the porin OmpF, and the effect of distance.

To solve the first matter, we studied melittin as a replacement for OmpF. The pore-forming peptide was studied in its interaction with PMOXA-*b*-PDMS-*b*-PMOXA membranes (Chapter 6), and we determine the parameters governing their interaction, both from the polymer (stiffness, length, chain dispersity, roughness), from the geometry of the assembly (curvature) and its stability when it interacts with the peptide. A kind of catalytically active polymeric vesicles was produced to prove melittin's functionality.

To solve the problem of substrate diffusion, we designed clusters of catalytic vesicles, tethered via complementary DNA strands, and permeabilized by melittin. Enzymes part of the same

cascade were in close proximity, below 20 nm, leading to a net gain in reaction efficiency when compared to the same unclustered conditions. Additionally, the DNA clusters adhered to the surface of lung cells, suggesting a future as targeted delivery. The conclusions of Chapter 8 summarize the results of this work and suggest the future outlook for research in this field, whereas Chapter 9 lists all the materials and methods used.

Table of contents

List of Figures

1 Introduction[1]

This chapter introduces key concepts and current scientific literature concerning this work, to provide basic knowledge for the comprehension of this work. It consists of an overview of the concept of

[1]PARTS OF THIS CHAPTER HAVE BEEN PUBLISHED AND ADAPTED WITH PERMISSION FROM:
Belluati, A.; Craciun, I.; Meyer, C. E.; Rigo, S.; Palivan, C. G., Enzymatic reactions in polymeric compartments: nanotechnology meets nature. *Curr Opin Biotechnol* **2019,** *60*, 53-62.

compartmentalization in biology, with a special focus on cells and sub-cellular structures. The concept of vesicular polymeric micro- and nanostructures as, respectively, cell and organelle mimics will be discussed, presenting several examples from recent literature, their fabrication techniques and their applications. The dissertation presents the construction of vesicular micro- and nanoreactors made of amphiphilic block copolymers and their organization to perform specialized cascade reactions, mimicking cells in shape, compartmentalization, internal structure and complexity of their environmental responses. The concept is then expanded in this thesis, showing possible applications of such systems, ranging from tools to translate cell logics into novel materials, to cell-like materials acting upon real cells.

1.1 Compartments as the basis of bottom-up synthetic biology

The field of synthetic biology field is diverse, as are the disciplines falling under this term, but can broadly be divided into two main themes: top-down approaches to design systems based on known biology to perform a specific task, and bottom-up approaches creating truly *de novo* artificial life,[1] via the emergence of life-like properties from the interactions of non-living building blocks. of nanometer building blocks, which provide spatiotemporal organization to the reactions.[2] A key concept in bottom-up synthetic biology is The resulting emergent behaviors between the derived compartments are more than the sum of the parts, since their interactions provide an additional layer of complexity. Life, in a broader sense, can be defined as an emergent phenomenon arising from smaller fundamental components.[3] Cells, the basic unit of life, are themselves compartments; moreover, they tend to specialize, which leads to the creation of consortia (unicellular organisms living in symbiosis), to the organization found in multicellular organisms, where different tissues perform specific functions. To an extent, cell biology can encroach into the territory of ecology, when considering the relationships between units.[4]

1.2 Cell membrane and compartmentalization

In both prokaryotic and eukaryotic cells, the plasma membrane (cell membrane) is the element that encapsulates the content of the cell, controls the flow of molecules in and out of the cell, involved in both passive and active transport to and from the cell, helping to maintain balance even when

conditions outside the cell change. The plasma membrane consists of two layers of phospholipids (bilayer phospholipids), where the amphiphilic molecules self-assemble into a bilayer with the hydrophilic segments oriented towards the water layer and hydrophobic tails towards the center of the sheet to minimize their free energy, delimiting an inner aqueous lumen, effectively separated from the external environment.[2]

In eukaryotic cells, the DNA is contained in the nucleus, which is wrapped in a nuclear membrane. However, within eukaryotic cells, internal subcompartments are found, called organelles, with specialized functions: for example, the nucleus, the mitochondria, the endoplasmic reticulum, the Golgi apparatus and so on (**Figure 1**).

For instance, the nucleus is the organelle that regulates the hereditary characteristics of the organism by performing processes such as protein synthesis and cell division, among others, by separating its DNA from the rest of the cell, as well as keeping the translation machinery close to it.

If the DNA was not sequestered, it would be vulnerable to damage by hazards such as enzymes, pathogens and free radicals, which would lead to defective protein production. Although part of the function of the nucleus is DNA compartmentalization, the molecules must still be able to move in and out (e.g. RNA), through the protein channels known as nuclear pores. Such organelle is an example of how membranes, within the cell, keep reactions separate, limiting and regulating flows, create specialized environments, protect them from external harmful agents and add an additional layer of complexity represented by the membrane itself.

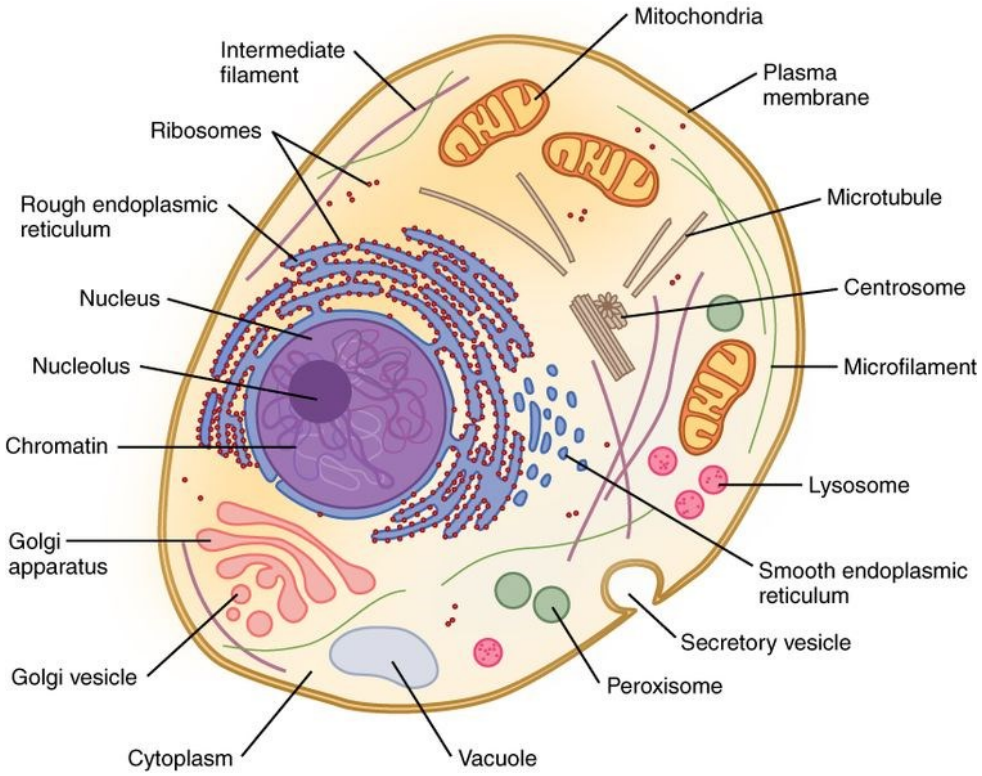

Figure 1 *Schematic representation of the internal organization of a eukaryotic (animal) cell.*

1.3 Mimicking cells with amphiphilic block copolymers

To its core, cell mimicking requires defined compartment, most often delimited by a barrier holding its catalytically active content and regulating its communication with the external environment. This basic organization can be repeated within the same cell mimic (sometimes called protocell or artificial cell), with internal subcompartments providing segregation. These cell mimics can also be defined as catalytic compartments, underlining their two basilar features. We chose to adopt this naming over the alternative micro/nanoreactor as it stresses the need of a localized catalyst –*e.g.* an enzyme– to work as intended.

In cells, compartmentalization is provided by the phospholipid membrane (although exceptions exist[5]); a plethora of cell mimics have been developed, from simple membrane-less droplets[6] to lipid-based mimics,[7] polymeric micelles and particles,[8] inorganic particles,[9] proteinosomes[10] and so on. Our focus was on polymeric structures, as polymers, natural and synthetic, are a broad and versatile class of

compounds that offers an incomparable diversity of possible chemical modifications and physical characteristics, which makes them an attractive choice for nanotechnological applications aimed at overcoming the limitations of lipids.[11] More specifically, we were particularly interested in amphiphilic block-copolymers, which can be engineered to induce self-assembly into micro/nanostructures, or assemble on a template, forming spheroidal structures with an internal lumen, very close to the basic geometry of a cell, while retaining the advantages of polymeric materials.[12]

Amphiphilic block copolymers, much like phospholipids, are formed of a hydrophobic and a hydrophilic section and can thus self-assemble in 3D structures; the most common hydrophilic blocks are PMOXA, PEG and PIAT; the hydrophobic blocks are most often PDMS, PS and PMA. In the case of layer-by-layer (LbL) capsules, layers of PDA and PLL are also frequently used.

When considering size and material, hollow spherical catalytic compartments are classified on whether they are nanometer or micrometer sized (**Figure 2**). Listed in the nanometer range are: polymersomes, polymeric vesicles and PICsomes (Polyion Complex), obtained through the interactions of oppositely charged polymers. In the micrometer-size range are GUVs (giant unilamellar vesicles), that is micrometric vesicles. The complexity of such nano- and micro-sized compartments can be further extended by self-organization into clusters with specific geometry [13] or by creating compartments-in-compartments, for example as capsosomes, polymeric capsules containing liposomal subcompartments.

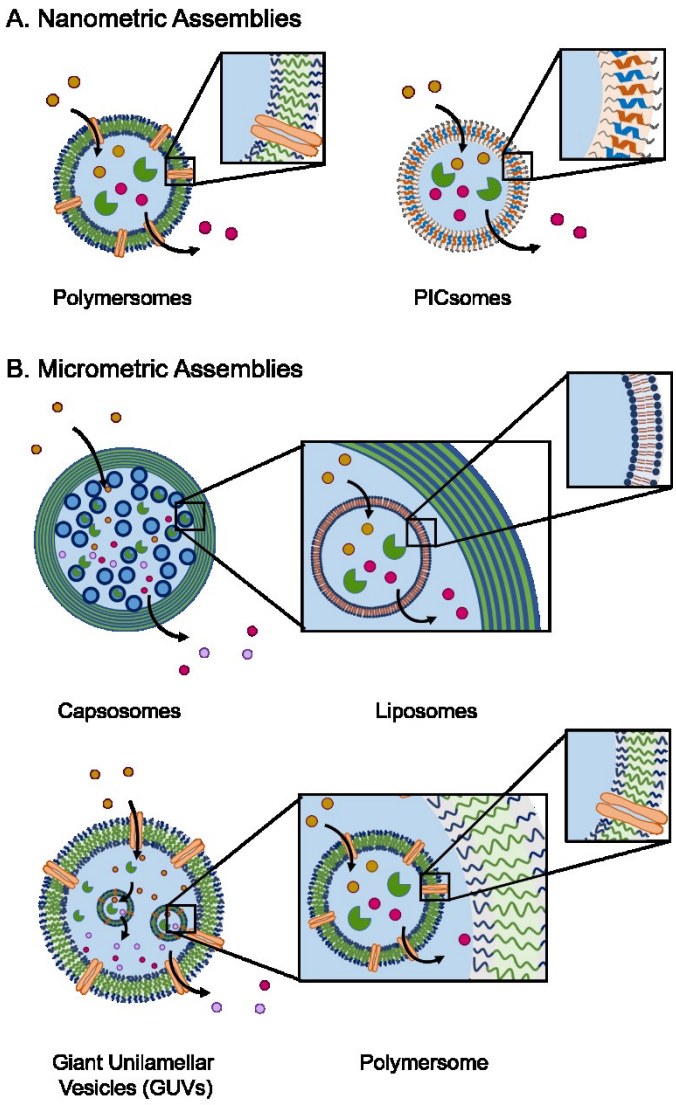

Figure 2 *Polymeric catalytic compartment architectures. (A) Catalytic reactions within polymersomes with inserted membrane proteins to allow substrate passage and PICsomes with inherently permeable membranes; (B) Catalytic reactions occurring in tandem within multicompartment structures such as capsosomes with the enzyme located within liposomes and giant unilamellar vesicles with the enzyme located within polymersomes.*

In this thesis, we will mainly treat PMOXA$_x$-*b*-PDMS$_y$- *b*-PMOXA$_x$/PMOXA$_x$- *b*-PDMS$_y$ (triblock and diblock)-based vesicles (**Figure 3**). We chose this polymer due to it biocompatibility and its impermeability which, associated to its ability to accommodate membrane proteins, peptides and ionophores results in membranes that can be made selective towards specific molecular species, using the same components that regulate cell permeability. [14]

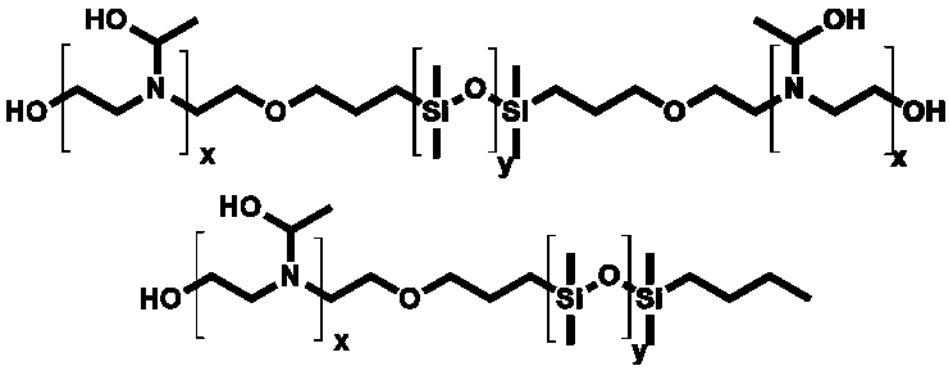

Figure 3 *Structure of a PMOXA-PDMS-PMOXA triblock copolymer and PMOXA-PDMS diblock copolymers.*

1.4 Self-assembly of amphiphilic block copolymers

1.4.1 Governing parameters

Amphiphilic block copolymers are able to self-assemble a wide range of nano- and micro-sized structures in aqueous solution, notably nanoparticles, micelles (spherical, cylindrical, and worm-like), and polymersomes, hollow vesicles. The choice of copolymers and their block ratio is very important, as the physico-chemical properties determine the behavior of the resulting assembly.[15]

The critical aggregation concentration (CAC), *i.e.* the concentration at which an amphiphilic molecule starts to form a colloidal system. For block-copolymers it is up to 10000-fold lower than for lipids,[16] increasing the assembly stability.

Different assemblies result from the inherent molecular curvature arising from the relative size difference between the hydrophilic and hydrophobic blocks. This principally defines the geometric packing of block copolymers in the resulting copolymer assemblies in aqueous solution, which is known as critical packing parameter, CPP (**Figure 4**), is defined as the ratio between the volume of the hydrophobic block and the contact area of head group (times length of hydrophobic block).[17] CPP corresponds to the ratio of the molecular volume of the hydrophobic block to the actual volume occupied in the resulting assemblies. Depending on its value, different polymer structures can assemble. For example, spherical micelles are formed when CPP ≤ 1/3, cylindrical micelles are formed with 1/3 < CPP ≤ 1/2, and vesicles are formed when 1/2 ≤ p ≤ 1 (Figure 2B).[18]

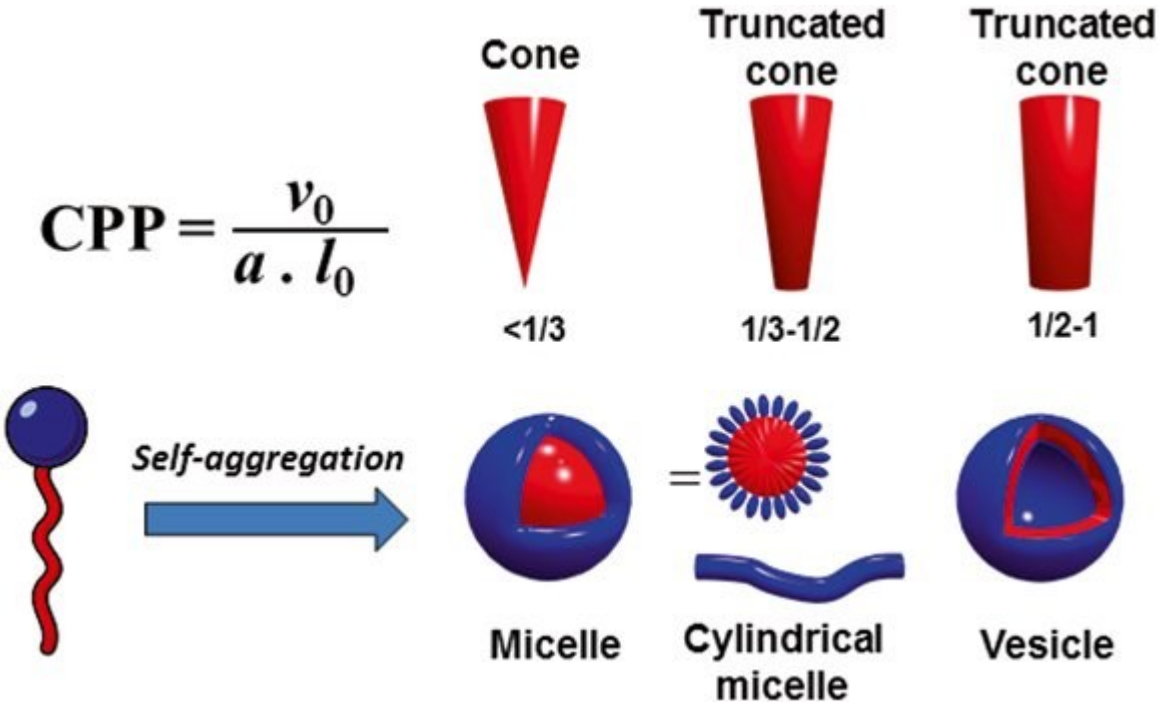

Figure 4 *Schematic illustration of CPP. V_0 is the volume of the hydrophobic chain, a is the equilibrium area per molecule at the aggregate interface and l_0 the length of the hydrophobic chain. Adapted with permission from reference [18a].*

Another important parameter is the glass-transition temperature T_g, which determines the flexibility of the membrane as a function of temperature and can go from -70 °C for rubbery materials to above 200 °C for some plastics.[19] Obviously, in case of mixed polymers, their reciprocal miscibility is fundamental as well. Finally, T_g and the block ratio are extremely important when integral membrane proteins must be incorporated, since membrane proteins have very precise hydrophobic and hydrophilic domain distribution and must insert with the least mismatch.[18a, 20]

1.4.2 Preparation techniques

To induce the assembly of block-copolymers into vesicular structures, various techniques are used. Film rehydration consists in water hydrating an anhydrous polymer film, swelling it and inducing self-assembly. Similarly, electroformation uses an oscillating electric field to assist the rehydration. In polymerization-induced self-assembly (PISA), the polymerization of hydrophilic monomers creates a hydrophobic block that induces the assembly.[21]

Solvent exchange is a family of diverse techniques involving the removal of the organic solvent dissolving the polymer, to expose it to an aqueous solution and induce aggregation. A variation of

solvent exchange is LbL, where alternating layers of oppositely charged materials are deposited on a template (usually a core particle that can be dissolved). Materials other than block-copolymers are also used and can be considered as template-assisted self-assembly. Another variant uses microfluidics, forming water/oil/water double emulsions where the organic phase hosts the polymer. The double emulsion forces polymers to orient with the polar heads toward water thus initiating the assembly.[21]
Film rehydration is the most widely used for polymersomes and GUVs; the derived electroformation is reserved for GUVs. PISA too finds use for polymersomes. "Classical" solvent exchange is versatile, used for polymersomes and PICsomes; LbL is applied to PICsomes and capsosomes. Microfluidics is used for giant vesicles.

1.4.3 Drawbacks and possible solutions

One of the drawbacks from which polymers tend to suffer is variability (dispersity, Đ) in their chain lengths, which causes in turn heterogeneity in their physical features.[12a] The dispersity of the assemblies is another issue, as most techniques produce non-uniform collections of sizes of the assemblies. Another issue with any kind of formulation is the encapsulation efficiency, which is the amount of cargo that can be loaded into a nanocompartment and can be quite low, especially when multiple enzymes are co-encapsulated. Microfluidics, albeit currently limited to micrometer-sized vesicles, is a possible way of both increasing size dispersity and encapsulation efficiency. In the future, the former problem may also be solved with the use of discrete block molecules, the latter by clustered assemblies.[13, 22]

1.5 Communication across synthetic membranes

Membranes protect catalytic compounds (enzymes, proteins, mimics) from several external agents, for example proteolytic attack,[23] allow otherwise incompatible reactions to take place[24] and, with their increased stability, biocompatibility and functionalization potential, are an attractive option for enzyme delivery and other biomedical applications. However, to obtain functional compartments able to produce *in situ* active molecules by using encapsulated catalytic compounds, the passage of substrates and products of the reaction across the membrane needs to be enabled. The permeability of a membrane can be due to inherent porosity (Table 1 and 2); the permeability can also be triggered by temperature and/or pH [25], or a chemical or enzymatic reaction. [20b, 26] A bioinspired approach is to

permeabilize the membrane by insertion of ionophores or membrane proteins; in the case of PMOXA-PDMS block-copolymers, to achieve higher selectivity, several ionophores and membrane proteins[20b, 27] can be inserted into the membrane. For catalysis purposes, channel proteins represent a convenient choice, as they allow the passage of many substrate molecules while keeping the enzymes inside. As seen in Table 1, bacterial OmpF is widely used, thanks to its high molecular weight cut-off of 600 Da (300 Da for a mutant), surpassed by α-HL, with a 4 kDa cut-off.[28] Another important feature of OmpF is the ability to retain its function when engineered to be reduction- or pH-sensitive thus expanding possible applications.[29] It must be remarked that polymeric membranes are thicker than natural lipid membranes[20b], creating a hydrophobic mismatch for all natural pores between the hydrophobic domain of the synthetic membrane and that of the protein. For this reason, the vast majority of membrane proteins were inserted only into PMOXA-PDMS or PB-PEO membranes, thanks to their high flexibility.[20b]

1.6 Michaelis-Menten enzyme kinetics

Before describing the state of the art of polymeric catalytic compartments, we must open a parenthesis on enzyme kinetics, a fundamental aspect of their characterization.

Enzymes assist in reactions by lowering the needed activation. Speeding up the rate of the reaction as it allows the product to be formed faster. Enzymes have an active site made up of a few amino acids, where the reaction occurs in the optimal conditions (*e.g.* changing local pH, proximity of nucleo/electrophilic residues, water exclusion etc.), whereas the rest of the enzyme acts as a scaffold. The active site is almost complementary to the substrate's shape and adapts slightly to fit it perfectly upon substrate binding. This forms the enzyme-substrate complex, ES. This is the induced fit model, a development of the lock and key hypothesis, postulating perfect fit before binding. Only weak bonds between the enzyme and substrate hold them in place, to allow dissociation afterwards. An enzyme has a high affinity for the transition state (the molecular species between substrate and product), higher than for its substrate, to quickly force the latter into the transition state. In enzymatic reactions, the conversion of the ES complex to the product is usually rate limiting and its rate) is directly proportional to the concentration of ES. The concentration of ES changes as the reaction progresses and, therefore, the rate of product formation also changes over time. When the reaction

reaches equilibrium (steady state) the concentration of ES (= rate) remains relatively constant. In presence of a lot of substrate, the reaction follows three different stages: pre-steady state (burst of ES complexes, speeding up as ES forms), steady state (constant concentration of ES, constant rate) and post-steady state (depletion of ES, slowing down as the substrate runs out). Since the pre-steady state is usually very fast, the steady state is the one used to measure the so-called Michaelis-Menten (MM) kinetics. [30]

The equation of the steady state is

$$v = \frac{V_{max}[S]}{K_M + [S]}$$

Equation 1

Where [S] is the substrate concentration, V_{max} is the maximum rate of reaction when all enzyme active sites are saturated with substrate and K_M (Michaelis-Menten constant) is the substrate concentration that gives half maximal velocity. K_M can be described as a measure of the affinity that enzyme has for its substrate, as a lower K_M means that less of the substrate is required to reach half of V_{max}. [30] The information obtained by the equation is how the initial reaction rate V_0, is affected by the initial substrate concentration, $[S]_0$, so only looking at the beginning of the reaction (**Figure 5**). This allows the equation to ignore the reverse reaction where substrate is formed from product, since at the start of the reaction there is no product present to go the inverse way around. Some molecules can hinder the reaction. Competitive inhibitors, competing for the active site, increase the K_M but do not alter the maximal velocity. The opposite is true for non-competitive inhibitors, binding to different locations on the enzyme, so that it is not the enzyme's affinity to be affected, but its ability to change its conformation to form the product. Many enzymes also suffer from product inhibition, where excessive concentrations impede the production of additional product. This mechanism holds true for most reactions,[31] but relies on the assumption that molecules can freely diffuse to and from the enzymes. This is not necessarily true when the enzymes are segregated and the flow is limited or channeled: this is the case of compartmentalized reactions and in cells too and must accounted for in the description of such systems, where conditions become more complex.[32]

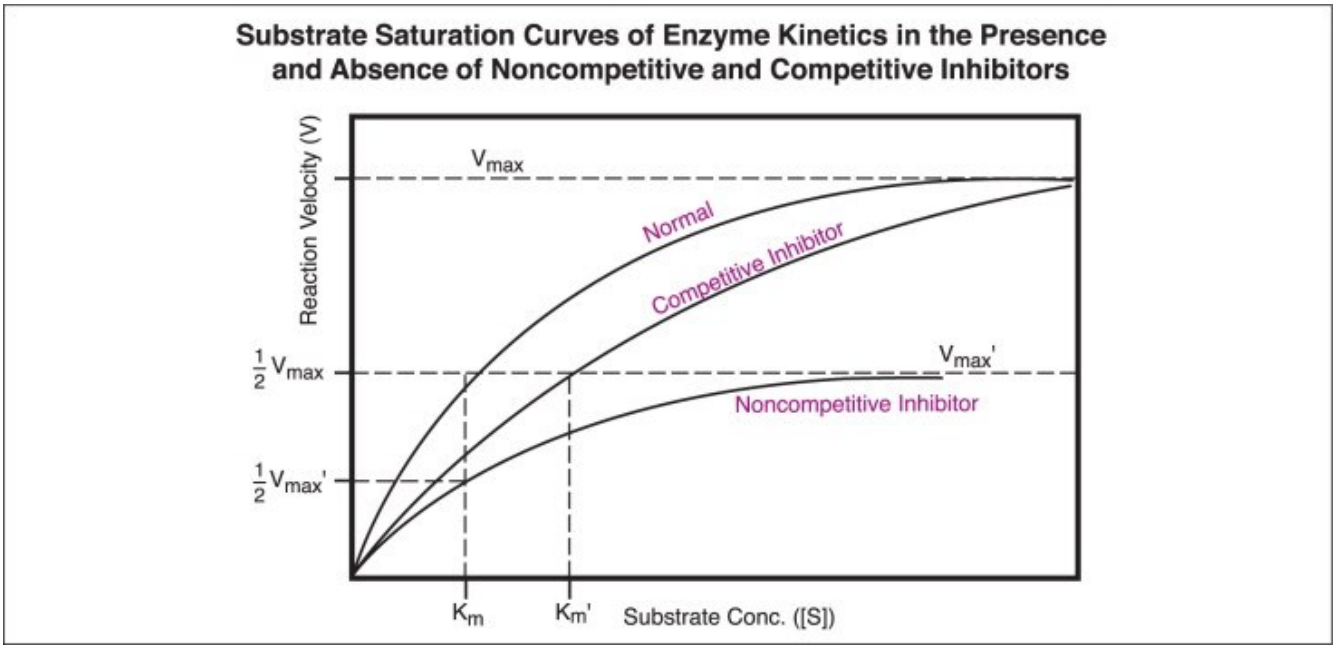

***Figure 5**. Generic MM kinetic curves, showing graphically the parameters obtained by plotting the substrate concentration vs the reaction rate, and how different kinds of inhibitors influence them. Adapted with permission from[30b].*

1.7 Cell-like polymeric catalytic compartments, state of the art

1.7.1 Encapsulation

Small molecules and proteins are encapsulated within the catalytic compartments to provide protection and stability so reactions can efficiently take place in complex biological fluids or *in vivo*.[23a, 33] With some techniques, mainly film rehydration and solvent exchange, it is possible to also encapsulate nanocompartments or even bacteria into micrometer-sized vesicles, separating catalysts or even entire life forms from the exterior.[20b, 34]

1.7.2 Compartmentalization of enzymatic cascade reactions

Cascade reactions are processes where the product of a first (upstream) reaction becomes the substrate of, or facilitates, a second (downstream) reaction, without requiring the isolation of

intermediates; the great majority of biological processes are series of enzyme-mediated cascades, acting in parallel and in specific locations.

Compartmentalization is thus a topic of tremendous interest in biocatalysis and synthetic biology; besides the already mentioned protection offered to the enzymes, segregation can influence the cascade reaction kinetics by keeping enzymes in proximity, by separating possible competing pathways and by forming locally high enzyme concentrations within the compartment, for instance lowering the Michaelis Menten constant (K_M).[35] Cascades themselves are a special case, where the interplay between substrates, cofactors and enzymes with different kinetics produces sometimes unexpected results.[35c, 36]

It is evident why any kind of nano-biotechnological approach and application must take into account and acknowledge the fact that Nature is not a one-pot reaction but rather a network of communicating processes: consequently, compartmentalization is key for facilitating catalysis, and cell mimicking must rely on it.[35a, 37] In fact, several of the examples listed in **Table 1** and **Table 2** involve multienzymatic cascades, adopting biological logics.[38]

1.7.3 Relative enzyme positions in compartments

The most common approach in compartmentalization consists of encapsulating a single enzyme in a single vesicle, polymersomes being the most widely used in this case (**Table 1 Table 2**).

To increase complexity, several enzymatic cascades have been developed with various strategies. Co-encapsulation is a possible setup.[23b, 25a, 27, 39] Partial segregation, obtained by adsorption on the outer or inner part of the membrane of one enzyme have also been used.[24, 40] Segregation in completely independent assemblies is not extensively used, as the reaction rate is decreased due to the slow diffusion between vesicles.[23a, 41]

Alternatively, enzymes can be separated from one another in different subcompartments, all part of the same micrometric multicompartment system.

1.7.4 Biomedical applications

Combining the ability to modulate membrane properties with the ability to encapsulate active molecules within the inner compartment, thus obtaining sophisticated catalytic compartments, propels

their use for multiple applications. One prominent application is in the field of enzyme replacement therapy, where non-functioning or non-native enzymes can be introduced, via encapsulation in the catalytic compartments, to perform a specific reaction or even a cascade.[23a, 28, 33, 42] The compartments work to protect the enzyme thus allowing for longer circulation times and prolonged activity. Alternatively, catalytic compartments can generate active chemotherapeutics from prodrugs at select locations, thus reducing the off-target toxicity. Recently, the potential of such a system was demonstrated *in vivo* where innately permeable compartments with encapsulated β-Gal efficiently converted the prodrug Doxgal to its active form Doxorubicin.[43] The local production of a chemotherapeutic agent can be combined with a precise initiation of the enzymatic reaction based on a stimulus for a dual activity *in vivo.* In an example of such an assembly, the block-copolymer forming the polymersome is composed of the prodrug of camptothecin, while GOX is encapsulated inside the polymersome.[25b] Under acidic conditions, glucose can permeate through the polymersome membrane initiating the enzymatic reaction to produce H_2O_2 and in turn triggering the release of camptothecin and reducing A549 tumors in mice. By co-encapsulating a photosensitizer, enzymatic activity can also be paired with photodynamic therapy (PDT).[26a] For other applications such as treatment of diabetes, the polymer can be modified to respond to disease specific triggers such as increase in glucose levels and H_2O_2. The advantage is the ability to modulate the catalytic reaction, where the reaction takes place only in presence of high blood glucose levels and is terminated once the blood glucose decreases, preventing the risk of hypoglycemia.[26c] By encapsulation of hemoglobin inside polymersomes equipped with OmpF it resulted a catalytic compartment with a dual functionality: oxygen storage and ability to detoxify harmful peroxynitrites.[44] Immobilization of the nanocompartments on a solid support is also possible and used as a tactic to obtain antimicrobial surfaces that locally produce a desired antibiotic[45].

1.7.5 Artificial cells and organelles

Another major field of interest revolves around developing catalytic compartments that mimic naturally occurring organelles or cells, the so-called artificial organelles/cells. A common application involves using these systems as a tool to understand complex cellular reactions within a simplified platform that retains many characteristics of the natural cell (Table 1 and 2). Additionally, these types of compartments can be designed to perform explicit reactions that, when incorporated into natural cells, will restore or enhance cellular functionality. For example, polymersomes with co-encapsulated SOD

and LPO were shown to effectively detoxify reactive oxygen species once incorporated into cells, acting as artificial peroxisomes.[23b] Larger multicompartment systems can be incorporated into macrophages and perform model cascade reactions, thus proving their potential future use for therapeutically relevant applications.[46] Artificial organelles that are responsive to an external stimulus, resulting in increased membrane permeability and initiation of an enzymatic reaction were developed. In one such example, a channel protein modified to include a reduction sensitive molecular cap was inserted into enzyme-loaded polymersomes.[47] Once up-taken by cells, the increased intracellular glutathione levels released the molecular cap, opening the channel protein and allowing the passage of substrate into the polymersome. The nanocompartments also maintained their structure and activity *in vivo* in Zebra fish.[47]

Table 1 *List of recent nanometric polymeric compartments: used polymer(s), encapsulated protein(s), setup, system of membrane permeabilization and envisioned application. Adapted with permission from reference[38].*

Assembly		Polymer	Encapsulated protein	Organization	Permeabilization	Application	Ref.
Nanometric	Polymersome	PMOXA-PDMS-PMOXA	GOX	Enzyme-loaded	Melittin	Glucose sensor	48
		PEG-PHMA-co-PPFMA	GOX, HRP	Enzyme-loaded	Light-triggered	Model for triggered permeabilization	49
		PMOXA-PDMS-PMOXA	UOX, HRP	Enzymes loaded separately	OmpF	Treatment of hyperuricemia, model for substrate diffusion	23a
		PMOXA-PDMS-PMOXA	HRP	Enzyme-loaded	Stimuli responsive-OmpF	Model for *in vivo* triggered permeabilization	47
		PMOXA-PDMS-PMOXA	HRP	Enzyme-loaded	Stimuli responsive-OmpF	Model for triggered permeabilization	29b
		carbohydrate-PPG	β-Gal	Enzyme-loaded	Inherent	Enzyme delivery, drug production	43
		PEG-PHPMA	GOX, HRP	Enzymes loaded separately	Inherent	Model for PISA-mediated entrapment	41
		PMOXA-PDMS-PMOXA	AGE, NAL, CSS	Enzyme-loaded + surface-immobilized	OmpF mutant	Model for reaction segregation	24
		PEG-poly(Ser-S-NI)	GOX, insulin	Enzyme-loaded	H_2O_2- and glucose-responsive	Insulin patch for diabetes	26c
		PMOXA-PDMS-PMOXA	PGM	Enzyme-loaded	α-HL	Enzyme replacement therapy	28
		PMOXA-PDMS-PMOXA	HRP	Enzyme-loaded	Ompf	Model for molecular crowding	35g
		PEG-P(CPTMA-co-PEMA)	GOX	Enzyme-loaded	pH-driven permeability	Cancer therapy	25b
		PMOXA-PDMS-PMOXA	RDH	Enzyme-loaded	GlpF	Biosensor	20b
		PEG-PS (Stomatocyte)	GOX, Cat	Co-encapsulated enzymes	Shape transformation	Model for cargo loading and release	39
		PMOXA-PDMS-PMOXA	HRP	Enzyme-loaded	Stimuli responsive-OmpF	Model for triggered permeabilization	29a
		PLGA	Cat	Enzyme-loaded	Inherent + rupture	Oxidation therapy, enhancement PDT	26a
		PMOXA-PDMS-PMOXA	PA	Enzyme-loaded	OmpF	Antimicrobial surface	45
		PNVP-PDMS-PNVP	Lac	Enzyme-loaded	Inherent	Oxidizing agents for industrial applications	50
		PDEAEM, PDMIBM	Mb, HRP, GOX	Co-encapsulated enzymes	pH-driven	Model for diffusion control	25a
		PMOXA-PDMS-PMOXA, PS-PIA	GOX, HRP	Enzyme-loaded polymersome	OmpF + inherent	Model for artificial cell	51

				within 2nd polymersome			
		PS-PIAT, PS-PEG	SOD, Cat	Enzyme-loaded co-encapsulated	Inherent	Antioxidant	[52]
		PMOXA-PDMS-PMOXA	SOD, LPO/Cat	Co-encapsulated enzymes	OmpF	Artificial peroxisome	[23b]
		PS-PAA	cytC, Ccox	Ru(II)-modified enzyme complex in membrane	Light-driven	Model for artificial chloroplast	[27]
		PMOXA-PDMS-PMOXA	Hb	Enzyme-loaded	OmpF	Antioxidant, O_2 transport	[44]
		PEG-P(S-co-TMI)	CalB	Enzyme-loaded polymersome within colloidosome	Inherent	Model for enzyme catalysis in biphasic systems	[53]
		PS-PAA	Tr	Enzyme loaded	Impermeable	Model for molecular confinement	[54]
		PS-PIAT	GOX, HRP, CalB	Encapsulated, in membrane and surface-immobilized enzymes	Inherent	Model for enzyme positioning	[40]
		PMOXA-PDMS-PMOXA	SOD	Enzyme loaded	Inherent	Antioxidant	[55]
	PICsome	PEG-P(Asp), P(Asp-AP)	L-ASNase	Enzyme-loaded	Inherent	Model for enzyme replacement therapy	[33]
		PEG-P(Asp), Homo-P(Asp-AP)	β-Gal	Enzyme-loaded	Inherent	Enzyme delivery, drug production	[42a]

Table 2 *List of recent micrometric polymeric compartments: used polymer(s), encapsulated protein(s), setup, system of membrane permeabilization and envisaged application.*

Assembly		Polymer	Encapsulated protein	Organization	Permeabilization	Application	Ref.
Micrometric	GUV	PMOXA-PDMS-PMOXA	HRP	Enzyme-loaded	OmpF	Model for artificial cell	[56]
		PEO-PB	Cat	Enzyme-loaded	Inherent + rupture	Model for cargo release	[26b]
		PLL+ PMAc + PDA	GLDH, GTR, β-Gal, GOX, Cat	Enzyme-loaded liposomes embedded within	Inherent	Model for artificial cell	[57]
	Capsosome	PAH/PMA/PNMD/PEG-P(DEAEMA-stat-BCP)	Cat, Mb, GOX	Enzyme-loaded polymersomes embedded within	Temperature- and pH-driven	Model for artificial cell	[25c]
		PLL/Liposomes/PMA/ PMAc/PNVP	GOX, HRP	Enzyme-loaded	Inherent	Model for artificial organelle	[46]
		PLL/Liposomes/PDA/PMA/ PMAc	Cat	Enzyme-loaded liposomes embedded within	Inherent	Model for tissue engineering/cell structural support	[58]
		PLL/Liposomes/PDA/ PEG/RGD	GOX	Enzyme-loaded liposomes embedded within	Inherent	Model for artificial organelle	[59]
		PLL/PMAc/Liposomes/PDA	PAL	Enzyme-loaded liposomes embedded within	Inherent	Enzyme replacement therapy	[42b]
		PLL/PMAc/Liposomes/PDA	UOX , HRP, AO	Enzyme-loaded liposomes embedded within	Inherent	Model for artificial cell	[60]
	Multicomp. GUV	PMOXA-PDMS-PMOXA	Lipase	Enzyme with co-loaded with particle-entrapped substrate	Inherent for DTT	Model for reduction-responsive subcompartments	[61]
		PS-PIAT,PB-PEO	PAMO, CalB, Alc, ADH	Enzymes-loaded polymersomes co-encapsulated in bigger enzyme-loaded vesicle	Inherent	Model for artificial cell	[62]

2 Aim of the thesis

Billions of years of evolution and natural selection lead to the emergence of systems optimized for complex sets of reactions, making cells unmatched reactors, genuine microscale computers. Any man-made material that wants to be "smart" is basically required to adopt some kind of biological logics, such as self-regulation, environmental sensitivity, or catalytic activity.

When I first approached the topic of cell mimesis, the question asked was: to what extent can we treat networks of synthetic, specialized micro- and nano-objects as quasi-living systems? Self-assembled PDMS-PMOXA catalytic compartments, imitating the shapes and functions of organelles and cells had been known for several years, having physical behaviors comparable to that of lipid membranes, but more stable, non-immunogenic and chemically versatile; however, as many biological phenomena can be said to be emergent, deriving from the combination of simpler units, these kind of reactive structures had the same potential, *i.e.* to be able to relate with one another in cascades, mimicking cells and interacting with real ones, the way an organelle or symbiont could do. In synthetic biology, such approach is called bottom-up and is aimed at constructing living (or close to living) systems from non-living matter, what we may call *abiotic life*. The task I decided to undertake was to expand the concept of catalytic compartments, using their biomimicking features to make them bioactive materials, and to develop as much as possible the potential of the technology. Far from having exhausted all possibilities, the tiny, uncharted territory that I explored showed that it is definitely possible to treat the same biological-synthetic hybrid materials (polymer vesicles + proteins) both as cell models for fundamental research and as applied tools.

Rather than starting with a pre-determined set of hypotheses to probe, this work is a non-exhaustive list of attempts at expanding the concept of bottom-up synthetic biology as a network of man-made objects operating in synergy; the story told is that of several systems, each building on the previous one and studying different aspects of this hybrid material. For the first time, polymeric catalytic compartments could be used to mimic cellular environments and serve as platform to screen cytoskeletal drugs; building on this concept, catalytic nanocompartments in cascades could be used to detoxify cells from toxic species or elicit cellular changes in homeostasis via the production of second

messengers. The concept was then optimized by studying how the permeabilization can be improved, and by controlling relative distances between compartments, improving the reaction efficiency.

The conclusion, the thesis, is emergent like the properties of the studied systems: billions of years of trial and error led to logics that can be now applied, with very little tweaking, to largely unnatural materials, in humanity's quest to simultaneously understand Nature and consciously adapt to it.

3 Mimicking cells[2]

In nature, cells respond to dynamic changes and can sense external environmental changes to maintain biological functions.[63] Mimicking cells, in this regard, means materials that are capable to sense an external change (stimulus) and modify their internal organization in response and activate specific pathways. Our aim was to adapt two fundamental features of eukaryotic cells: hierarchical spatial segregation, which is found in organelles, and responsiveness to stimuli. These two components would allow our artificial cells to have internal subcompartments that segregate small and macromolecules from the rest of the construct (and from the bulk solution), and the ability to change their internal organization based on environmental stimuli. Doing so paves the way for real cell-mimicking materials, beyond the vague concept of artificial cell / protocell.

[2] PARTS OF THIS CHAPTER HAVE BEEN PUBLISHED AND REPRINTED WITH PERMISSION FROM:

THAMBOO, S.; NAJER, A.; **BELLUATI, A**.; VON PLANTA, C.; WU, D.; CRACIUN, I.; MEIER, W.; PALIVAN, C. G., MIMICKING CELLULAR SIGNALING PATHWAYS WITHIN SYNTHETIC MULTICOMPARTMENT VESICLES WITH TRIGGERED ENZYME ACTIVITY AND INDUCED ION CHANNEL RECRUITMENT. ADVANCED FUNCTIONAL MATERIALS 2019.

BELLUATI, A *, THAMBOO, S*****, NAJER, A, MAFFEIS, V., VON PLANTA, C, CRACIUN, I.; MEIER, W.; PALIVAN, C. G., MULTICOMPARTMENT POLYMER VESICLES WITH ARTIFICIAL ORGANELLES FOR SIGNAL-TRIGGERED CASCADE REACTIONS INCLUDING CYTOSKELETON FORMATION 2020. ADVANCED FUNCTIONAL MATERIALS 2020.

ANDREA BELLUATI AND SAGANA THAMBOO HAVE CONTRIBUTED EQUALLY TO THE WORK PRESENTED IN THIS CHAPTER.

3.1 Stimuli-responsive multicompartment systems

3.1.1 Introduction

Stimuli-responsive systems are based on copolymers with a special chemical nature, inducing a change in the membrane permeability or even its disintegration upon a change in their environment, transducing a physical or chemical signal, such as light, temperature, pH, redox potential, temperature, light, magnetic fields, electric fields and mechanical force.[61, 64] We decided to use cell-sized polymeric structures as cell membrane stand-ins, harboring stimuli-sensitive and -insensitive nanostructures which could act both as "receptors" of environmental changes and artificial organelles segregating their cargos, until stimulated. A self-contained system of this sort could act, for example, as biosensor or as a platform to screen the effect of drugs on specific cell processes, which can be replicated in these structures, free from interactions happening in actual cells that can cause false readings.

3.1.2 Previous work on reduction sensitive compartments

3.1.2.1 Reduction-sensitive nanoparticles as artificial organelles

For this study, we needed to segregate molecules, keeping them "inactive" within the lumen of polymeric vesicle, and release them on demand. Stimuli-sensitive nanoparticles are an attractive choice, as they can harbor useful compounds (*e.g.* therapeutics) and release them once their surrounding environment changes as desired, and have been widely studied for drug delivery.[65] Our strategy was to use reduction-sensitive nanoparticles (NP-Graft) based on (poly(2-methyl-2-oxazoline)$_{88}$-*graft*(SS)-poly(ε-caprolactone)$_{238}$ (PMOXA$_{88}$-*g*(SS)-PCL$_{238}$) (with a grafted disulfide bridge connecting the two copolymers), capable of entrapping hydrophobic compounds and releasing them once disaggregated by a reducing agent (**Figure 6**), [54, 58] as they had been already characterized and could be confidently used as internal subcompartments.[61, 66]

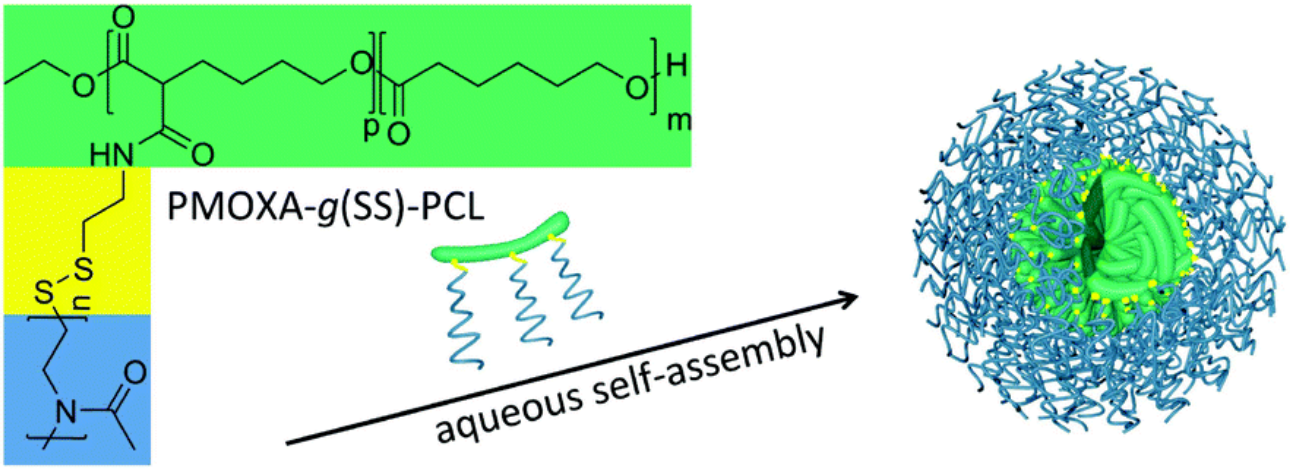

Figure 6 *Structure and self-assembly of PMOXA-g(SS)-PCL nanoparticles. Adapted with permission from reference [66b].*

Transmission electron microscopy (TEM) indicated the formation of spherical nanoparticles, and dynamic light scattering (DLS) revealed hydrodynamic diameters of circa 50 nm.[61] Once loaded in PMOXA-PDMS-PMOXA giant unilamellar vesicles (GUVs) via film rehydration in a 300 mM sucrose solution, they could only be disassembled by the reducing agent dithiothreitol (DTT), as other reducing agent could not cross the membrane encasing the NP-Grafts. [61]

When entrapping the hydrophobic dye Bodipy 630/650, and co-loaded with polymersomes encapsulating the dye Sulforhodamine B, *in situ* FCS could follow, inside the lumen of the GUVs, the selective disassembly of reduction-sensitive NP-Graft, whereas non-reduction sensitive polymersomes stayed intact (**Figure 7**). This way, the NP-Graft showed a twofold function: as artificial organelles, separating species within the lumen, and as intracellular receptors, being the responsive species to an external stimulus and enacting an internal change.[67]

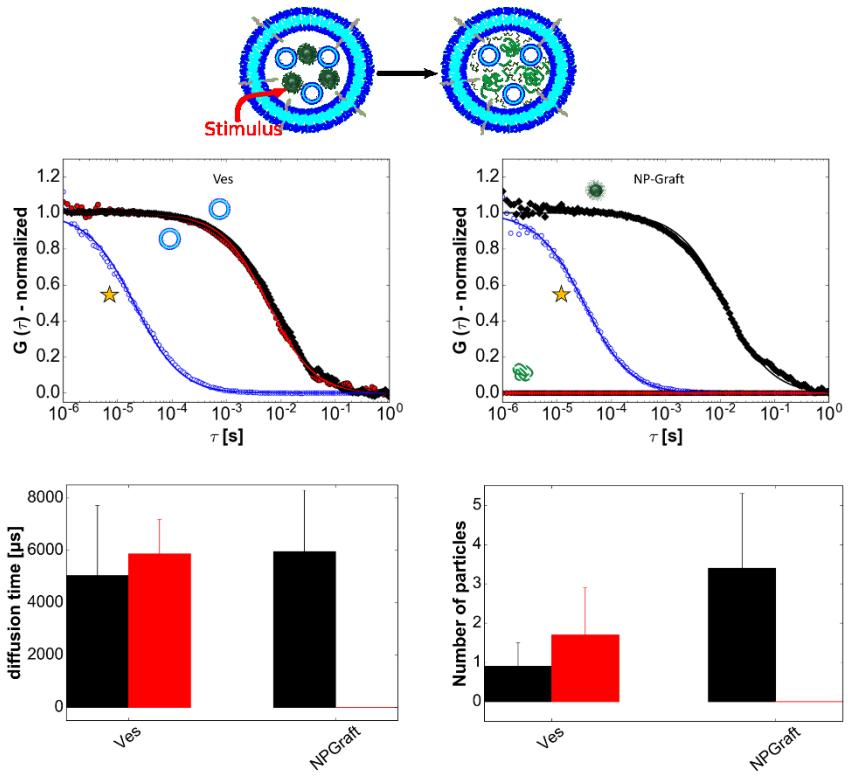

Figure 7. *Reduction sensitiveness of 2-compartment multicompartments. In presence of DTT (red) loaded NP-Graft disassembles, while non-reduction sensitive polymersome stays intact within the giant vesicle after incubation of 24 h. In absence of stimuli (DTT) (black) both types of subcompartments are stable within the GUV according to FCS measurements. Also, the diffusion times and number of particles in the GUV show that in presence of DTT (red) only the reduction sensitive NP-Graft disassembles, while both types of subcompartments are intact in absence of DTT (black) (N=3 GUVs before and after DTT and for channel). Adapted with permission from reference [61].*

3.1.2.2 DTT-triggered enzyme activity

Having shown the robustness of such system, an enzymatic reaction based on a hydrophobic and fluorogenic substrate was chosen, allowing its visualization via CLSM. The most obvious enzyme candidate was lipase, as it is specialized in hydrolyzing hydrophobic compounds. Its substrate 1,2-Di-O-lauryl-rac-glycero-3-(glutaric acid 6-methylresorufin ester) (DGGR) [68] was first incorporated in the NP-Graft to segregate it from lipase; preliminary results in sucrose showed a very limited effect on the reaction of the solution found inside the GUV lumen, after DTT had caused the disassembly of the nanoparticles (**Figure 8**).

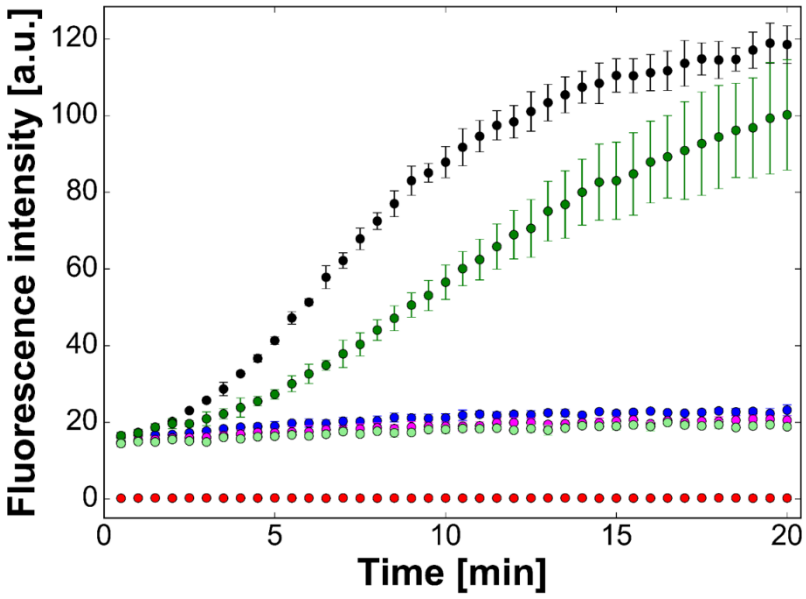

Figure 8. *Enzymatic reactions in solutions (PBS and sucrose). In PBS: Lipase mixed with DGGR loaded NP-Graft and DTT (black), Lipase and DGGR loaded NP-Graft alone (red), DGGR loaded NP-Graft and DTT alone (pink); Lipase, DGGR loaded NP-Graft, DTT and lipase inhibitor Orlistat (blue). In sucrose: Lipase mixed with DGGR loaded NP-Graft and DTT (dark green); DGGR loaded NP-Graft and DTT alone (light green). Error bars are given as mean ± standard deviation (n = 3. Ex/Em 529/600 nm. Adapted from reference [61].*

DGGR-NPs and lipase were then co-loaded inside GUVs. With DTT added to the exterior medium, it first penetrates the GUVs, it induces the disintegration of the NP-Graft and the release of DGGR, which was then accessible by lipase. Being an interface membrane, lipase tended to adsorb to the polymer membrane; this, added to the fact that the main product of the reaction is the hydrophobic methylresorufin, made the fluorescence concentrate on the inner wall of the GUV (**Figure 9**).

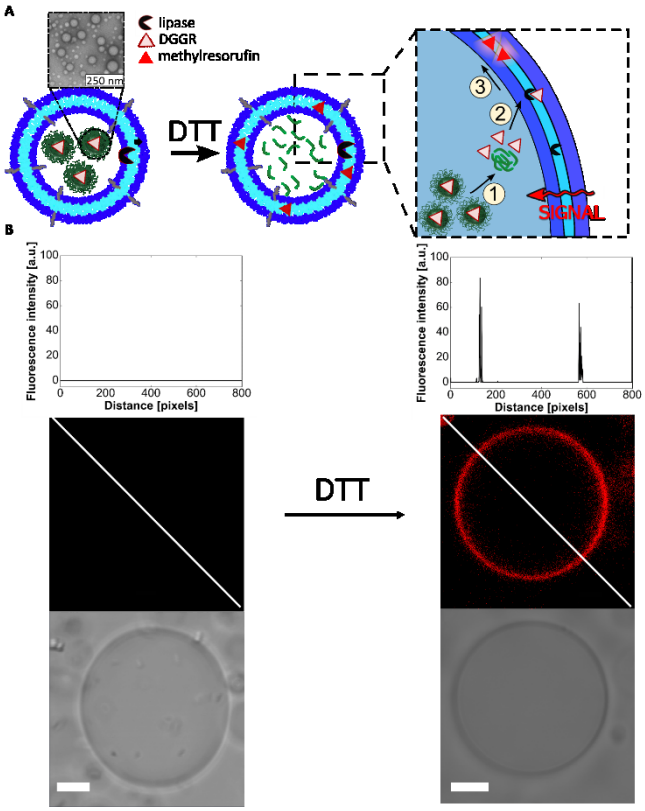

Figure 9. *Compartmentalization of enzyme reaction. (**A**) Schematic representation of signaling pathway resulting in lipase activity. The DGGR loaded NP-Graft and lipase were co-encapsulated in the giant vesicles. The substrate was released in presence of DTT and was transformed by lipase to form the fluorescent product (methylresorufin) which preferentially associated with the giant vesicle membrane. (**B**) CLSM imaging of DGGR loaded NP-Graft and lipase loaded giant vesicles in absence (left) and presence of DTT (right). Histogram along diagonal of fluorescence image (top), fluorescence image (middle) and bright field image (bottom). Scale bars, 5 μm. Adapted from reference [61].*

3.1.2.3 DTT-triggered ion channel recruitment

In parallel with DGGR-loaded NPs, the DTT-triggered release of the pore-forming peptide gramicidin A (gA) was developed, based on the same principle of encapsulating a hydrophobic compound (gA) in the NP core (gANP). In this case, its release would induce the spontaneous insertion of this pore into the GUV membrane, allowing the passage of monovalent cations. [61, 69] This system, where specific membrane permeability is induced by an external trigger, simulated the recruitment of membrane proteins from internal compartments, found for example in neurons, activated by specific stimuli. [70]

gANPs were encapsulated in the Na^+ - free GUV lumen, together with the Na^+-sensitive dye Asante Natrium Green 2 (ANG2); the GUVs were then put in a Na^+-containing buffer. Only upon addition of DTT was gA released, reconstituted into the membrane and able to let the ions go through, as confirmed by the activated fluorescence of ANG2 (**Figure 10**)

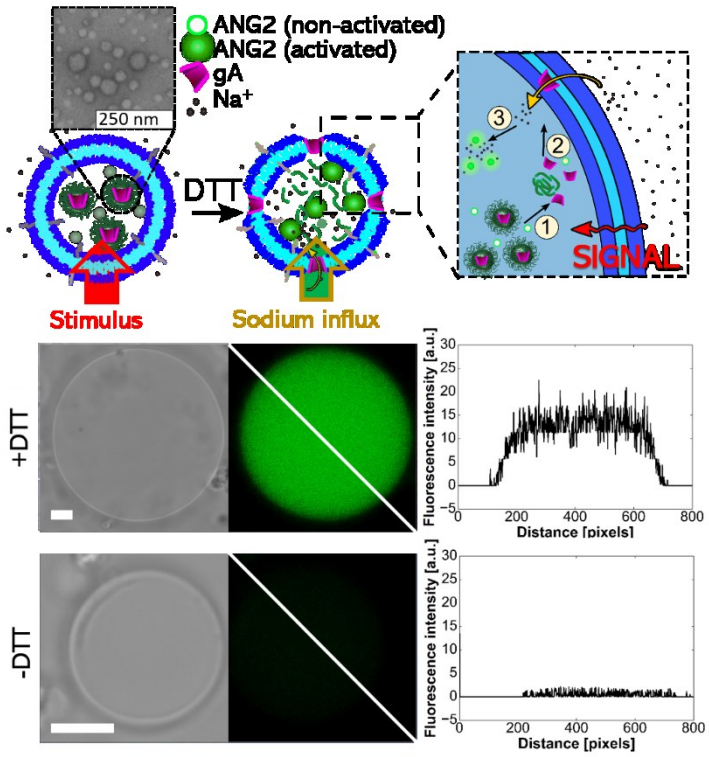

Figure 10. *Triggered gramicidin ion channel recruitment from internal subcompartments to the polymer membrane of a multicompartment using CLSM imaging. Schematic representation (top) of gA mediated import of sodium ions. Upon the addition of DTT, encapsulated gA is released from its NP-Graft and inserts into the GUV membrane boundary. This allows sodium ions from the outside to enter the GUV cavity where they activate the sodium sensitive dye ANG2. Bright field image (left), fluorescence image (middle) and histogram along the diagonal of fluorescence image (right) in presence (middle) and absence (bottom) of DTT. Adapted from*[61].

3.1.3 Two-compartment DTT-dependent lipase activation

We then decided to study how the reaction would be affected by a double subcompartmentalization, that is two different artificial organelles communicating within the same cell mimic: the partially segregated enzyme, adsorbed (thanks to its hydrophobicity) on the outer membrane leaflet of PMOXA-PDMS-PMOXA polymersomes (LipVes), and the DGGR-NPs. Vesicle-adsorbed lipase maintained its activity, again only achieved after DTT had freed DGGR from the nanoparticles. This allowed us to co-load both DGGR-NP and LipVes in the same GUVs (**Figure 12** and **Figure 11**).

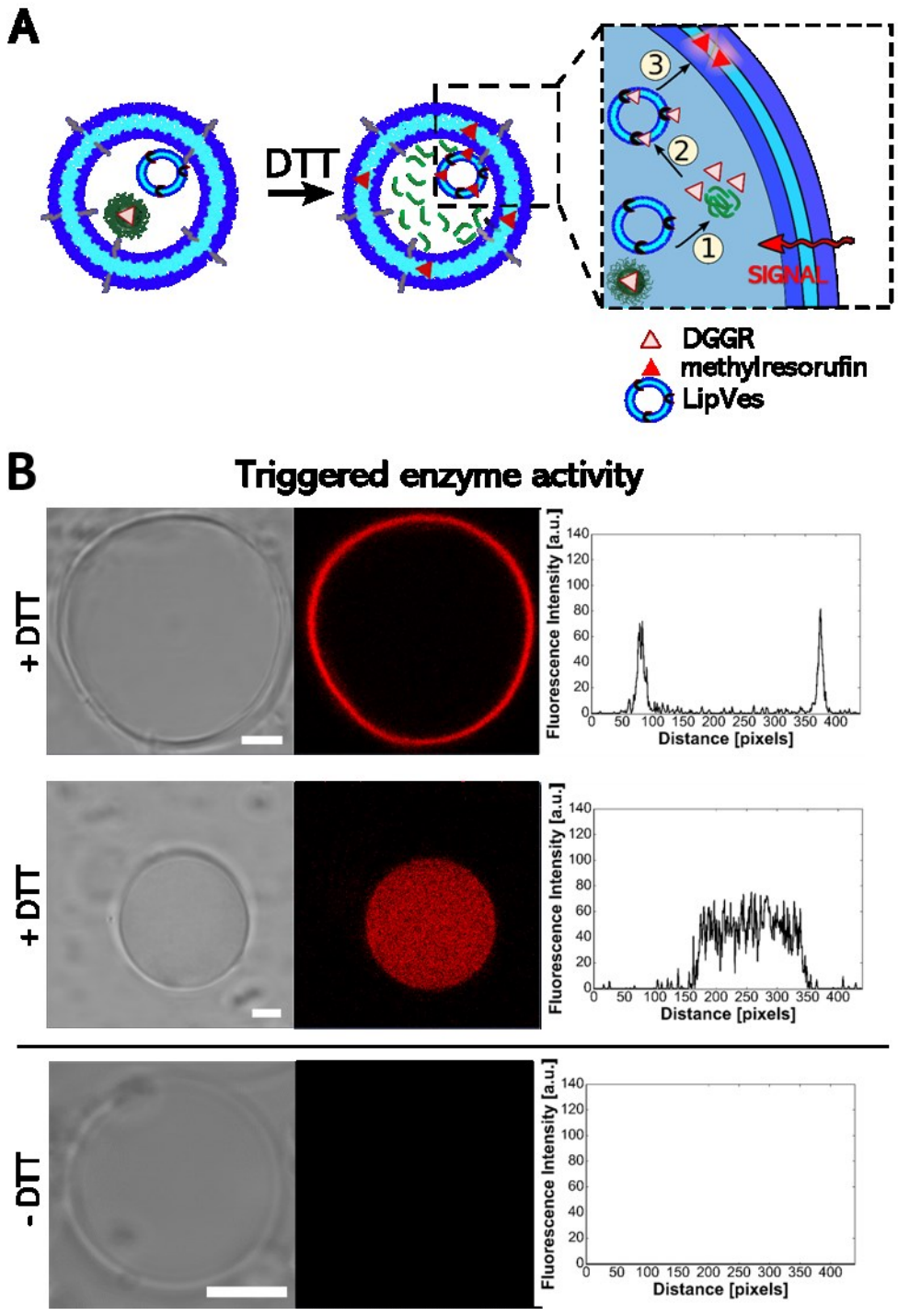

Figure 11. *(**A**) Schematic representation of enzymatic reaction using substrate (DGGR)-loaded NP-Graft and enzyme (lipase)-adsorbed polymersomes (LipVes), co-loaded into GUVs. Substrate was released from NP-Graft in presence of DTT and transformed into the fluorescent product (methylresorufin). (**B**) CLSM imaging of DGGR loaded NP-Graft and LipVes in GUVs in presence (top, middle) and absence (bottom) of DTT. Bright field image (left), fluorescence image (center) and histogram along diagonal of fluorescence image (right). Due to the hydrophobicity of methylresorufin, it either partitioned into the hydrophobic part of the GUV's membrane or also to the remaining NP-Graft debris or non-responsive LipVes membrane. Scale bars, 5 µm.*

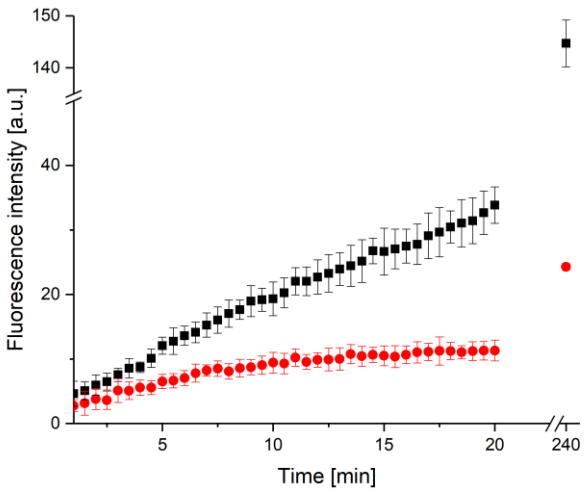

Figure 12. *Enzymatic reactions in 300 mM sucrose. Lipase adsorbed on vesicle (LipVes) and DGGR loaded NP-Graft in solution in presence (black) and in absence (red) of DTT. Error bars are given as mean ± SD (n = 3). Ex/Em 529/600 nm. Adapted from* [61].

What we remarked, compared to the previously published study, is that we did not only observe the fluorescence rings, but also a part with filled lumen(**Figure 13 A-B**), again not without DTT (**Figure 13 C**). Since the loading of nano-objects in GUVs via film rehydration is a stochastic phenomenon, only a part of the GUVs had enough vesicles for the methylresorufin to adsorb preferentially to the internal compartments, and 10% of them was not loaded enough to be detectable (**Figure 13 D**). It must be noted that the GUVs had quite a broad size distribution with sizes between 4 and 29 μm, a limitation of the film rehydration technique (**Figure 13 E**).

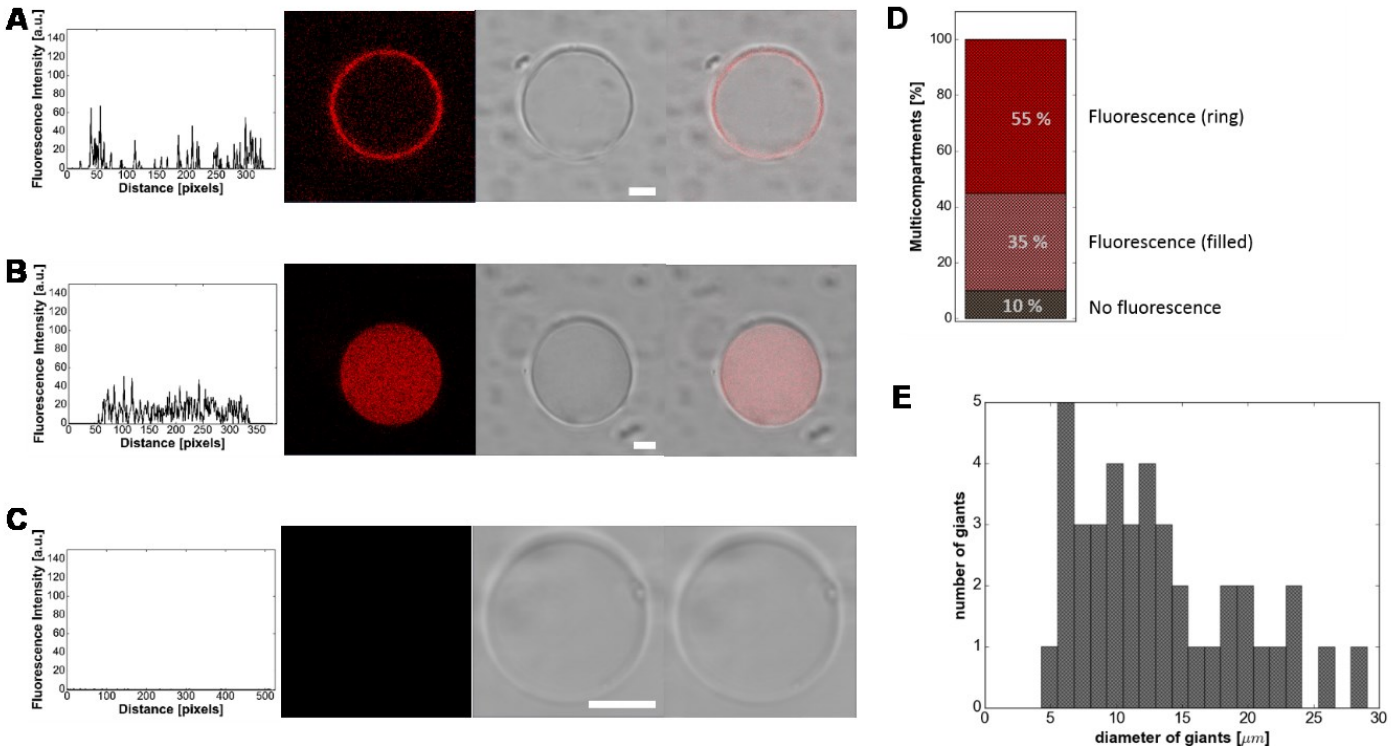

Figure 13. *Efficiency of the compartmentalization of enzyme reaction in presence of 10 mM DTT after 24 h incubation time and corresponding GUV size distribution. (**A-C**) Plot profile of the fluorescence intensity along the diagonal of the image (left), CLSM image of LipVes and DGGR-NP co-loaded in giant vesicles (middle) and corresponding bright field image and merge (right), indicating: (**A**) production of methylresorufin adsorbed to the polymer membrane (55%), (**B**) production of methylresorufin in the lumen, (**C**) absence of DTT (and fluorescence). (**D**) Percentage of GUVs showing activity, and in what form. (**E**) Sizes of GUVs, showing the broad distribution. Adapted from[71].*

3.1.4 Two-compartment DTT-dependent ionophore release

To explore the triggered release from internal stores (artificial vacuoles), in an advanced study we produced sodium-filled polymersomes (Na^+Ves), coencapsulated with gANP and ANG2, with both the lumen of the GUV and the outside buffer sodium-free. Like previously seen, GUVs in absence of DTT were completely non fluorescent; with the stimulus, sodium ions could flow outside of their small vesicles, activating the fluorescence of ANG2 (**Figure 14 A-B**).

The GUVs had a size distribution between 6 and 43 μm (N = 40 GUVs, **Figure 14 C**). 73% of multicompartments were functional and induced the dye activation via two internal types of artificial organelles within the GUVs (**Figure 14 D**). No fluorescence was detected in the remaining 27%, probably due to insufficient loading of gA in NP-Graft, sodium ion in the Na^+Ves, ANG2 into the GUVs, or a combination thereof. In addition, a fraction of gA inserted in the GUV membrane, due to being made

of the same polymer. The surface offered to gA by the encapsulated Na^+Ves is roughly 125 μm^2 for the sum of the encapsulated polymersomes (1000 per GUV), versus 452 μm^2 for the membrane of a GUV (volume 1112 μm^3) would mean comparable recruitment to the artificial organelle membrane.

organelle membrane, yet we could not observe any difference in kinetics compared to the case of insertion and ion flux across the GUV membrane due to gA insertion in GUVs membrane.

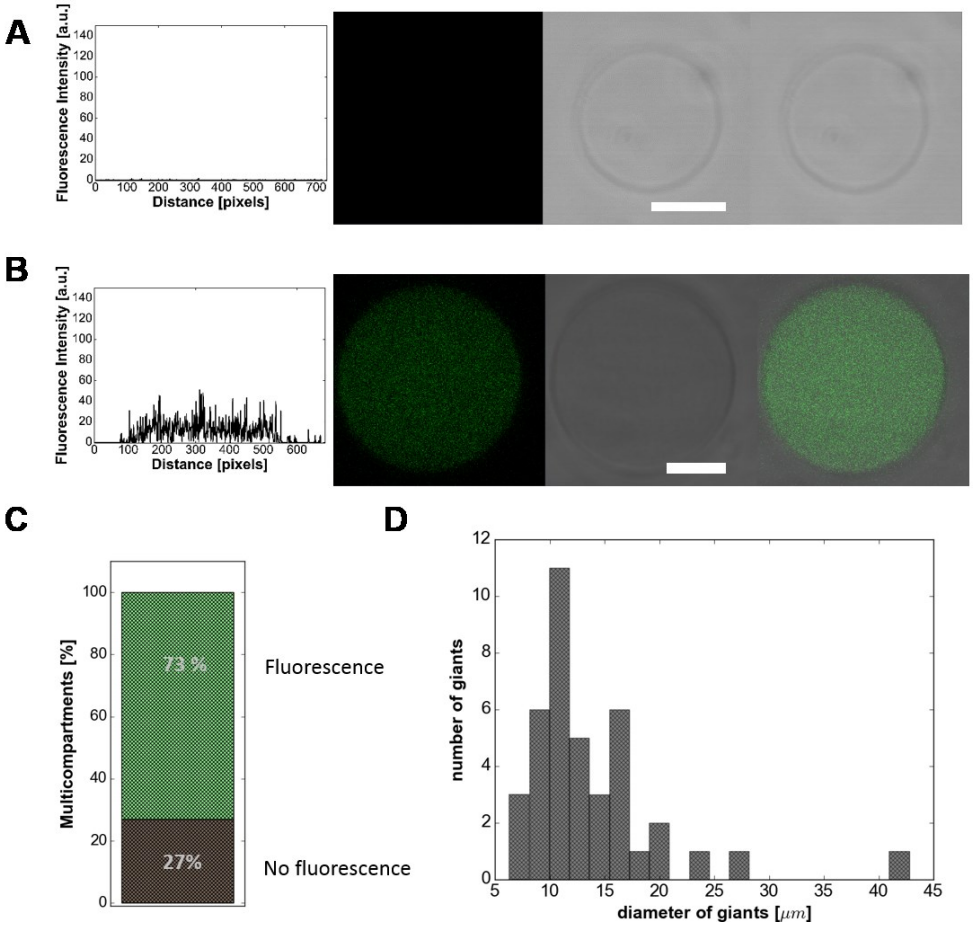

Figure 14. *Efficiency of the compartmentalized gA reconstitution into the polymer membrane to import sodium ions in presence of 10 mM DTT after 24 h incubation and corresponding size distribution. (**A-B**) Plot profile of the fluorescence intensity along the diagonal of the image (left), CLSM image of gA loaded NP-Graft and sodium loaded polymersomes (Na^+Ves) in giant vesicles (middle) and corresponding bright field image and merge (right), indicating: (**A**) remain empty (27%, no fluorescence) and (**B**) activation of ANG2 by sodium ions (73%, fluorescence). (**C**) Histogram of efficiency of gA loaded NP-Graft and ANG2 in giant vesicles in presence of DTT. (**D**) Histogram of size distribution of measured gA loaded NP-Graft, sodium loaded polymersomes (Na^+Ves) and ANG2 in GUVs in presence of DTT after 24 h incubation (N=40 GUVs). Scale bars, 5 µm. Adapted from reference [61].*

3.2 Triggered actin polymerization

We further expanded on this multistep system, taking advantage of the fact that this induced permeabilization causes a change in ion concentration within the GUV, a change in osmolarity. It is known that high salt concentrations cause the spontaneous polymerization of the cytoskeleton protein actin from its G (globular) form to the F (filamentous) form; in our GUVs this would have led to changes in the internal structure of the cell mimics in a biosimilar manner, as already demonstrated in liposomes, [72] mimicking a basic component of cells responsible for both structural stability and dynamic shape modifications. [72b, 72c, 73]

3.2.1 Subcompartment-free artificial cytoskeleton

To optimize our strategy, we investigated the formation of an actin cytoskeleton in our biomimetic system. We first confirmed fluorometrically, the concentration ranges for polymerization with monomeric pyrene-actin in solutions, showing formation of filaments in presence of various salt solutions (of KCl, $CaCl_2$ and $MgCl_2$): the higher the degree of polymerization, the higher the fluorescence of pyrene (Figure 15).

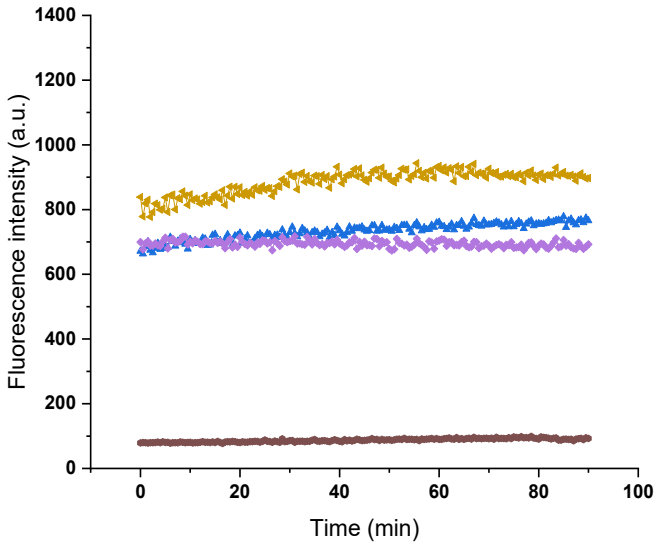

Figure 15. *Pyrene fluorescence assays of G-actin polymerization in the dependence of salts. Actin-pyrene in sucrose (300 mM, brown), in $CaCl_2$ (100 mM, purple), in KCl (100 mM, blue) and in $MgCl_2$ (100 mM, gold). The actin polymerized almost immediately, showing stable filaments for the following 90 minutes. Ex/Em 365/407 nm. Adapted from[71].*

To favor the creation of an ordered network with thick filaments (and for ease of visualization), we mechanically stabilized our actin (supplemented with ATTO488-G-actin for its visualization) cytoskeleton with the actin-binding protein filamin, a physiological mechanosensor, confirming the formation of actin-filamin bundles in ion rich solutions and only monomeric form in HEPES buffer (Figure 16).

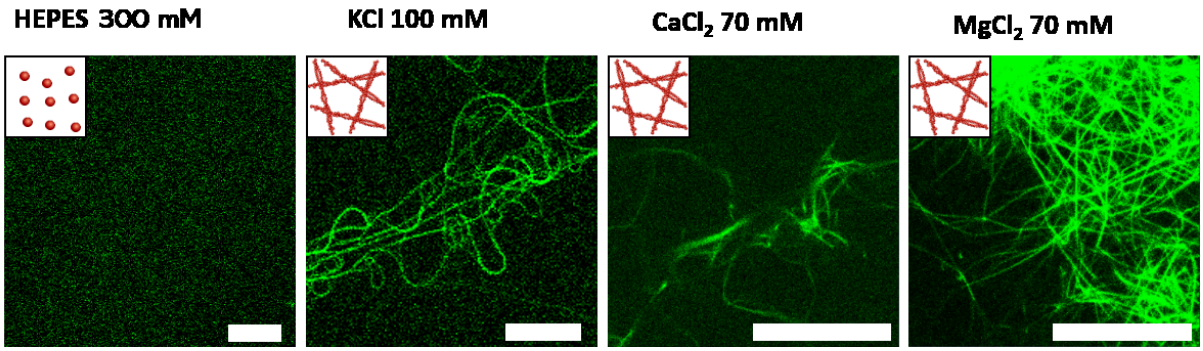

Figure 16. *Confocal images of actin networks polymerized in bulk solution in presence of different solutions. In presence of the crosslinker filamin, G-actin stays in its monomeric form in HEPES buffer (300 mM) in contrary to the solutions containing KCl, $CaCl_2$ and $MgCl_2$ induce actin polymerization and form actin-filamin networks (green). The samples were incubated for 3 h. Scale bars, 20 µm. Adapted from*[71].

We then developed a protocol for the loading of G-actin (labeled and unlabeled) and filamin. Upon addition of ions and corresponding ionophores such as ionomycin (IoNo), for the passage of Mg^{2+} and Ca^{2+} or gramicidin A (gA) for transport of K^+ ions, to the external medium, actin polymerization was induced inside the polymer compartment (Figure 17) within 24h. [73d, 74] The hydrophobic dye Bodypy630/650 was used to visualize the GUV membrane. In absence of pores and/or salts G-actin stayed in its monomeric form.

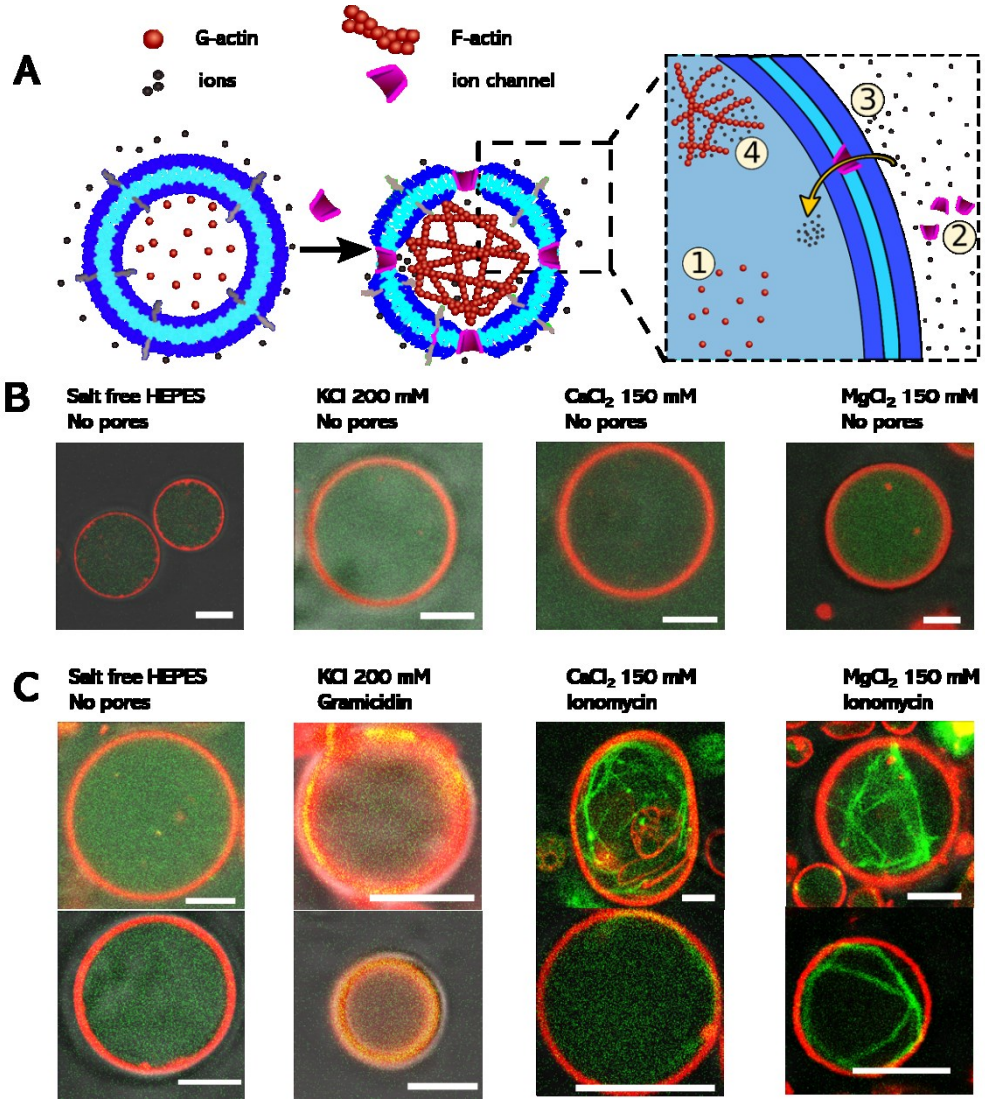

Figure 17. *Actin filament polymerization in synthetic GUVs. Actin monomers (G-actin) and the actin crosslinker filamin was loaded into giant vesicles after 24 h incubation. Pores (gA or IoNo) were introduced to the vesicle solution resulting in permeabilization of the GUV membrane towards specific ions (K^+ or Ca^{2+} and Mg^{2+}). (**A**) Schematic representation of the actin polymerization in GUVs. (**B**) In absence of pores, the monomers stayed intact, and no filaments were formed since no ions could enter the GUV cavity. (**C**) When pores where added to the surrounding solution, they reconstituted into the membrane boundary of the GUV. Then ions entered the GUV cavity, actin starts to form filaments and the bundling agent filamin crosslinks the filaments into a network. Scale bars, 5 μm. Adapted from[71].*

To visualize better the morphology of the GUV cytoskeleton, we additionally used a high resolution microscopy technique, 3D structured illumination microscopy (3D-SIM), showing that the actin network within the GUVs is composed of both thin actin filaments and actin bundles with thicker fibers (Figure 18).

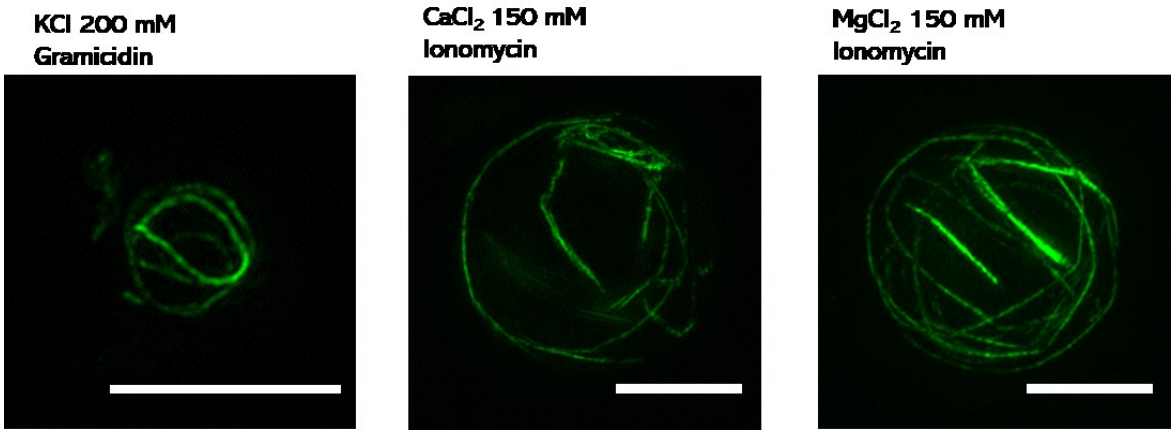

Figure 18. *Projections of actin filaments (green) polymerized within GUVs in presence of pores and ions recorded with super-resolution 3D-SIM. High resolution images (3DSIM) of Actin GUVs in salt solutions (200 mM KCl, 150 mM $CaCl_2$ and 150 mM $MgCl_2$) in presence of corresponding pore (gA, IoNo) after incubation of 48 h. Scale bars, 5 µm. Adapted from*[71].

3.2.2 Ionophore release for actin polymerization

Having confirmed the capability to induce actin polymerization by adding ionophores from the exterior, we went back to the concept of NP-Graft as stimuli-responsive units, by encapsulating either gA again (gANP), or ionomyicin (IonoNP), as they both enter spontaneously the membrane of the GUV encapsulating them, and co-loading them with actin and filamin, making multicompartment GUVs (Actin MC).

In presence of DTT, the pore-loaded NP-Graft disassembled and released their cargo (gA or IoNo). This allowed the passage of K^+, Mg^{2+} or Ca^{2+} from the exterior solution, leading to the polymerization of actin in the GUV (**Figure 19, Figure 20**).

Observations of mostly cortical rings in the case of triggered actin polymerization via responsive artificial organelles could be due to a lower amount of gA or IoNo incorporated into the membrane compared to addition from the outside, as it depends on the loading and subsequent release from subcompartments (Graft-NPs). Limited amount of ion influx could lead to a more localized actin polymerization directly below the membrane where the local concentration of ions will be highest upon channel insertion. This explanation is also suggested by the fact that addition of ionophores from the outside allows fast and plentiful influx of ions that leads to higher chance of creating extended networks

within lumen, whereas the actin rings below the membrane are also present in the cases of more ion influx. Such mechanistic considerations will need to be further investigated.

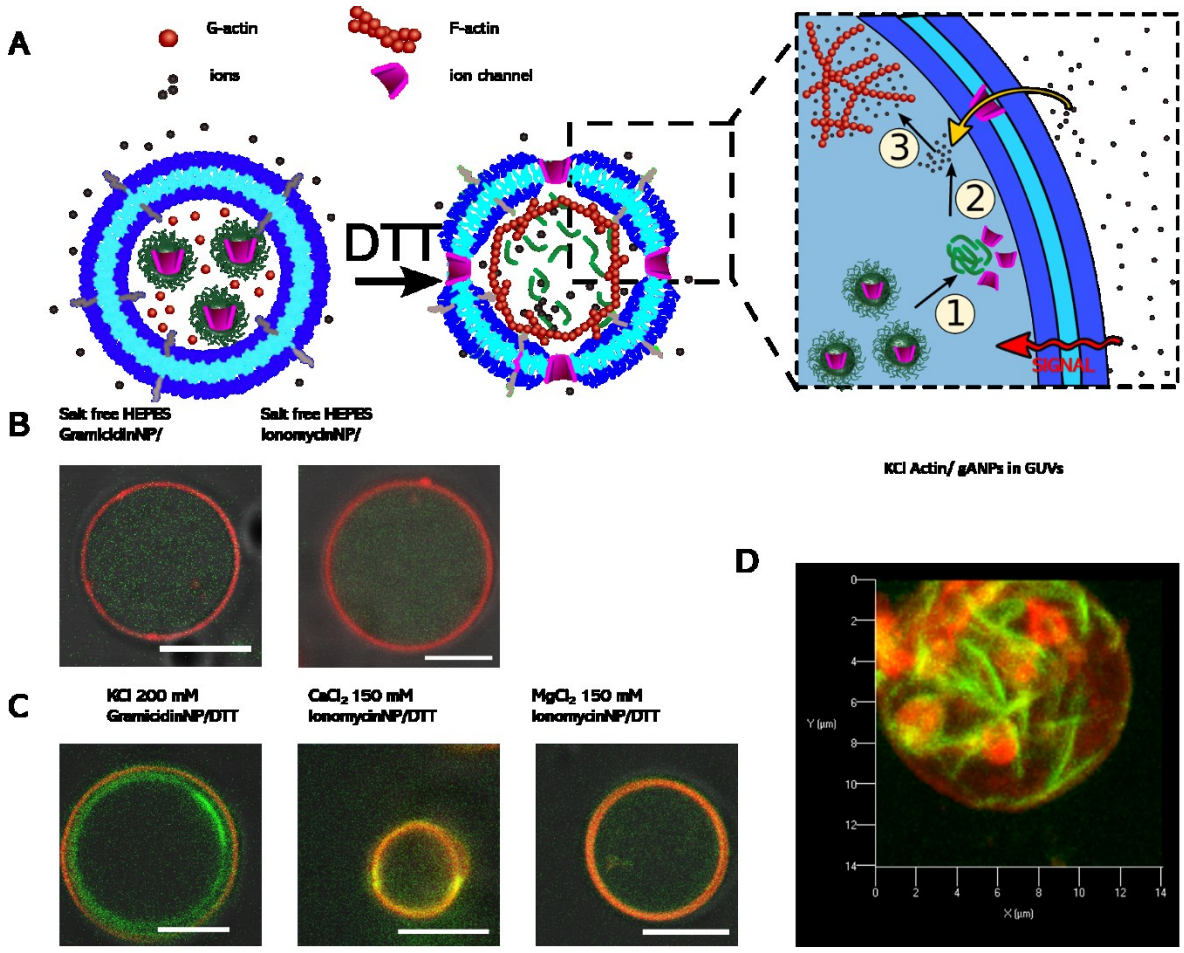

Figure 19. *Stimuli-triggered actin polymerization in synthetic multicompartments. (**A**) Schematic representation of pore mediated import of ions resulting in the formation of actin filaments. Upon DTT addition, the encapsulated pores are released from its NP-Graft and inserts into the GUV membrane boundary. Ions enter from the surrounding solution into the cavity of the GUV, where the actin monomers start to polymerize into filamentous structures. (**B**) CLSM imaging of actin monomer (G-actin, green) and crosslinker filamin co-loaded GUVs (red) remaining in its monomeric form in absence of salts and pores. (**C**) CLSM micrographs of actin filaments (green) in the lumen and inner leaflet of the GUV membrane (red), where actin polymerization is induced in presence of DTT. (**D**) Projections of actin filaments (green) in GUVs (red) via stimuli-responsiveness via internal subcompartments, were imaged with CLSM. The actin samples were incubated for 24 h. Scale bars, 5 µm. Adapted from*[71].

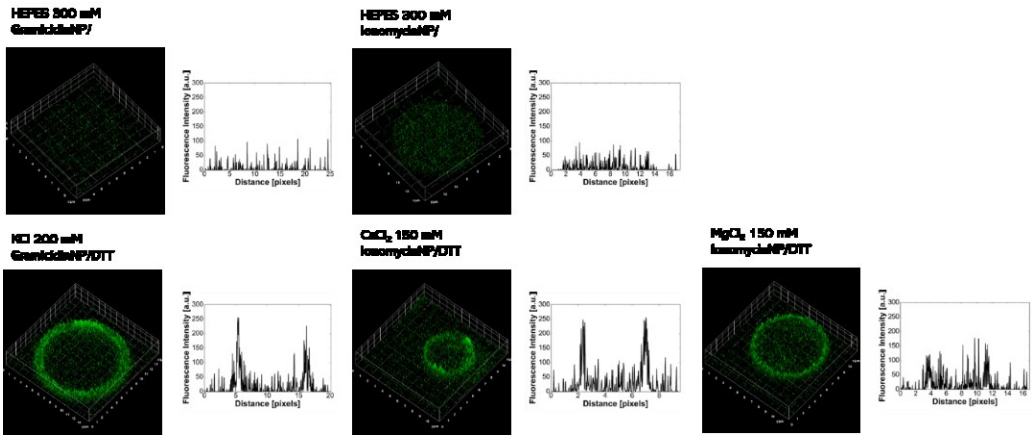

Figure 20. *Surface profile along the surface (left) and plot profile along the diagonal (right) of the stimuli-triggered actin polymerization in multicompartments (fluorescence intensity of the CLSM images of Figure 19). Adapted from*[71]*.*

The formation of an internal protein network was also expected to affect the Brownian motion of encapsulated species, due to molecular crowding. To study the change in viscosity of GUVs due to triggered actin polymerization *in situ* FCS measurements in GUVs loaded with IonoNP and non-responsive fluorescent subcompartments (SRBVes, sulforhodamine B-loaded vesicles) was performed. After selective disassembly of NP-Graft by adding DTT, and formation of filaments after ion influx, we measured FCS within the actin loaded GUV. We observed that the FCS curves shifted towards the right due to slower diffusion of SRBVes resulting in diffusion time changes from 4555 μs to 70277 μs after polymerization. Therefore, we calculated from the diffusion time a change in dynamic viscosity from $8.9*10^{-4}$ Pa*s to $1.4*10^{-2}$ Pa*s after actin polymerization. The actin filaments within the GUV made the lumen more crowded, replicating the molecular crowding of cells (**Figure 21**).

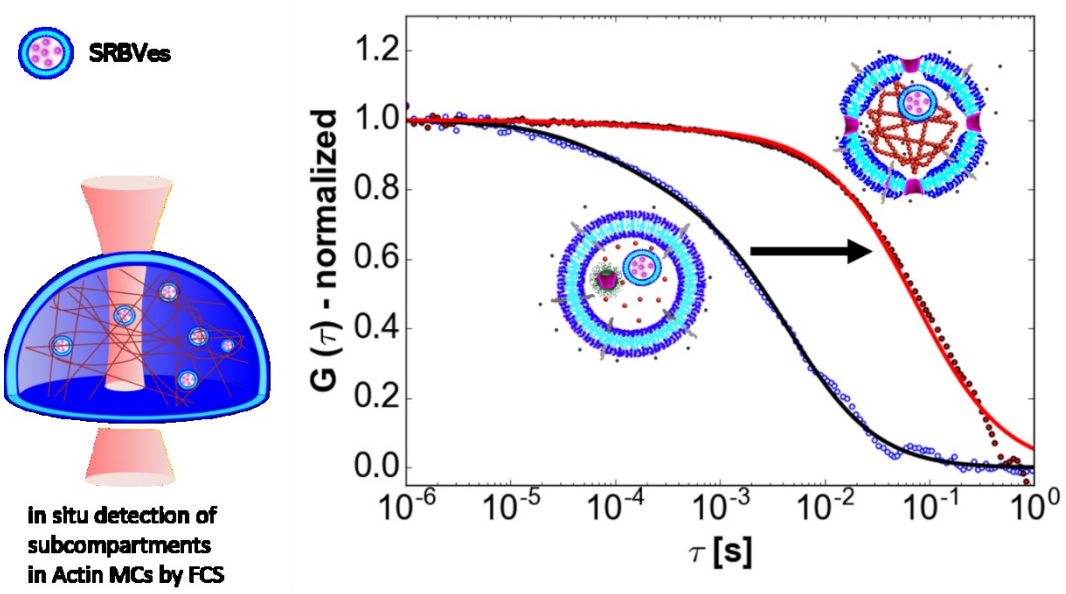

Figure 21. *FCS autocorrelation curve of SRBVes of two-type multicompartments before and after triggered actin filament polymerization. Change in diffusion time can be indicated as viscosity change. (N=3 GUVs before and after addition of DTT). Adapted from*[71].

We then performed a complete morphology analysis. Regarding the shape of the cytoskeleton, we could remark that web-like structures were the main type for actin GUVs (between 71% and 92%). In contrast, formation of cortical actin rings was predominantly observed for actin MCs (between 75% and 80%, N=100 GUVs) (**Figure 22A-B**). The shape of non-spherical actin MCs was also analyzed: the biggest population was represented by elongated vesicles (38%), then vesicles connected through tubular protrusions of their non-ruptured membranes ("beads on a string") and finally round vesicles showing long protrusions (N=60 GUVs) (**Figure 22C**). All these shapes were formed by underlying cortical actin rings. Various parameters such as concentrations of actin, filamin, ions, ionophores, stiffness of the membrane and of the filaments and more, influence the overall shape of the GUVs, which will have to be studied in more detail to depict the mechanism by which these structures are formed and how they dynamically change over time.

3.2.3 Influence of the Membrane on the Diffusion of Polymerization Inhibitors

Actin polymerization is the main target of several natural compounds, which exert their toxic activity by inhibiting the polymerization of actin, which leads to aberrations in cell transport, motility and division.[75] Such natural toxins are candidate cytoskeletal drugs, as their interaction with actin can be a way to inhibit cell proliferation, making them anticancer agents, or biopesticides.[76] These toxins have different potency, meaning that the concentrations needed to achieve an effect can vary due to various

uptake mechanisms and interactions with other cellular targets.[76b] An important factor to consider, when studying cytoskeletal drugs, is whether they rely on passive diffusion or transporters;[77] additionally, secondary targets for the toxins in cells must be accounted for when characterizing their interaction with actin, as the observed cytotoxicity might derive also from other interactions.[76a]

Our system can be used as a cytoskeletal drug screening platform to study the inhibitory action of small molecule actin-polymerization inhibitors. This system developed by narrowing down "cells" into two components: a cell-mimicking membrane, through which molecules can only passively diffuse, and a cytosol-mimicking lumen containing actin, will allow us to study the direct effect of the drugs on mechanical properties of cell-like systems.[78] To test such an application, we induced actin polymerization through DTT-triggered release of ionomycin from NP-Graft and flow of Mg^{2+} in presence and absence of externally added actin polymerization inhibitors. As a proof of concept, we tested four different toxins, all membrane-permeable: latrunculin A (LatA), chaetoglobosin A (ChaetA), cytochalasin B (CytB) and cytochalasin D (CytD). The simultaneous addition of one of four toxins meant that the DTT-triggered actin polymerization had to compete with the compounds, which had in turn to diffuse across the polymer membrane. All screened compounds were added at the same concentration, above their reported EC_{50},[79] so that the only discriminants would be their ability to cross the membrane, and their intrinsic activity. All toxins showed significant ability of reducing what we called *relative F-ratio*, the ratio between GUVs presenting at least one filament and the total population, compared to the untreated MCs. We observed the highest effect with LatA, known to be one of the most potent polymerization inhibitors.[80] We found no significant differences between Chaet A, CytB and CytD. These results suggest that the differences in potency between the compounds could partially be explained by their ability to diffuse through membranes, in addition to their intrinsic activity (**Figure 22D**). ChaetA was a remarkable case, as its addition led to the disassembly of a great number of vesicles (Figure S24), hinting that it interacts with both the membrane and actin, which could be a future research direction to elucidate its toxic action in biological settings. We envision that finding polymerization inhibition in our system is an indicator of potential toxicity of the compound, since the compound could act on many different cells in the body through passive diffusion across the membrane. Interesting drug candidates would be inhibitors of actin polymerization in solution, but present no activity in our system. Such compounds could potentially be delivered to cancer cells specifically using targeted nanocarriers. Our

findings present a possible application of our system, to screen for specific parameters affecting the action of compounds of pharmacological interest.

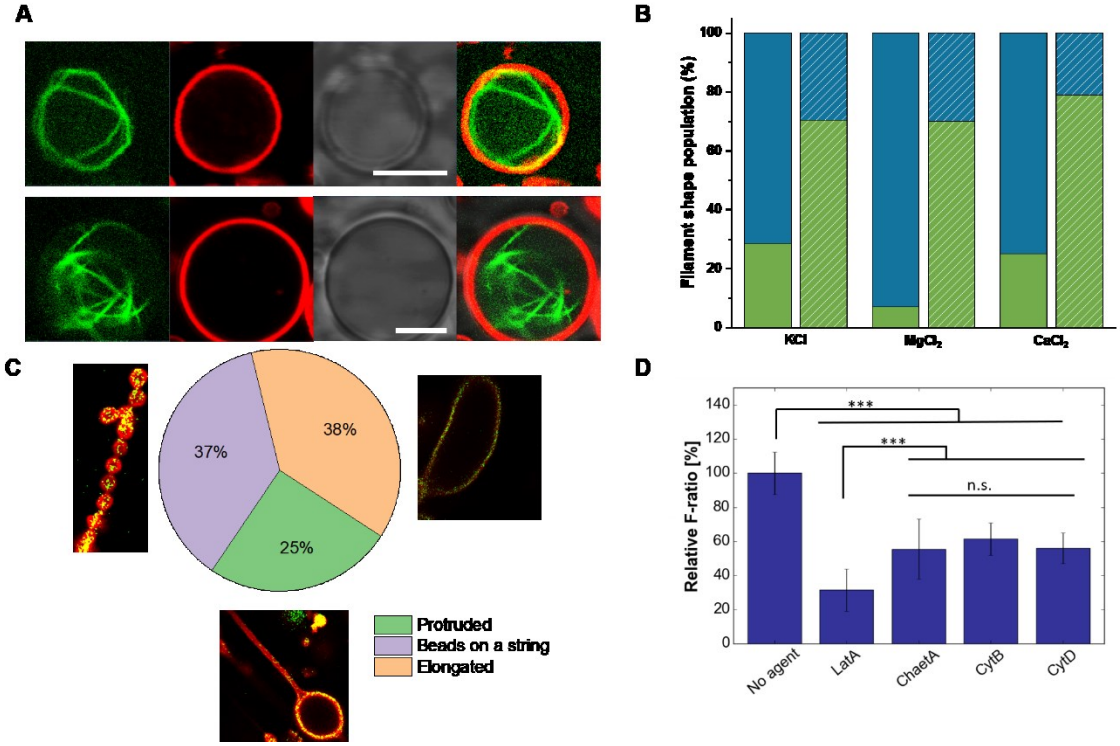

Figure 22 *Analysis of actin filament shapes, GUV shapes and the effect of actin polymerization inhibitors on Actin MCs. (**A**) An actin GUV with a cortical ring cytoskeleton. (**B**) Bar graph showing filament shape frequency for actin GUVs (solid color) and actin MCs (striped color), in presence of different salts. Green: cortical rings, blue: web-like networks. The population of cortical rings increases noticeably in actin MCs (N = 100). (**C**) Shape distribution of non-spherical Actin MCs, showing a prevalence of elongated vesicles with cortical rings, closely followed by bead-like structures and then vesicles with protrusions (N = 60). (**D**) Relative F-ratio of untreated Actin MCs (set as 100%) and MCs treated with different toxins. The F-ratio determines how much a molecule can hinder the polymerization of actin. Error bars given as Mean ± SD (binomial distribution), n between 15 (ChaetA) to 55 (CytD). Values compared through one-way ANOVA, with Tukey's post hoc test. *** p < 0.001; n.s. not significant. Scalebar, 5 µm. Adapted from[71].*

3.3 Conclusions

The complex architecture of living cells including simultaneous action of a myriad of dynamic processes are the inspiration for creating sophisticated cell mimics / protocells, aimed at assembling artificial cells

from of bottom-up. The work of this chapter shows our efforts to develop a synthetic protocell model based on the self-assembly amphiphilic block copolymer, aimed at recreating the responsiveness of living cells. Membrane functionality, sensitivity towards a specific external stimuli and internal response of the multicompartment system was investigated. Driven by an external stimulus, we could kick start enzymatic activity permeability without compromising the polymeric architecture of the GUVs, making the responsive nanoparticles both artificial organelles and intracellular DTT receptors; inspired by signaling pathways in cells, our subcompartments could trigger multistep signaling pathways in our system. Desired molecules (enzymes, reporter compounds) together with corresponding partners (substrates, ionophores) entrapped in responsive nanoparticles were simultaneously co-encapsulated within GUVs to be spatially segregated. Once having crossed the GUV membrane, DTT induced the disintegration of the sensitive nanoparticles and subsequent release of their content. In the case of LipVes, the enzyme was no longer segregated from its substrate DGGR. Building on this mechanism, ion channels (gA) were released and recruited to the membrane of Na^+Ves, allowing the flow of sodium ions to the lumen of the GUV.

To mimic the cellular cytoskeleton, actin polymerization was triggered within the interior of a synthetic protocell, thanks to changes in ion concentration. This was obtained both by directly adding ionophores (ionomycin, gA) to the membrane, or by first entrapping them in NP-Graft and then releasing with DTT. We observed an increase in diffusion time for non-responsive subcompartments after triggering actin polymerization inside multicompartments, which can be attributed to a change in viscosity and gives another indication of successful cytoskeleton formation. In the future, quantitative analysis of the actin loaded GUVs in terms of viscoelasticity and tension can be studied to generate more detailed knowledge of the interplay between actin fibers and the polymer membrane. The combination of the three main cytoskeletal components (actin filaments, microtubules and intermediate filaments) within the GUVs would be another interesting to study with respect to morphology of the synthetic systems.

As a first proof of concept, we showed how we could differentiate the influence of cross-membrane diffusion of different actin polymerization inhibitors. Future research will aim at using less potent reducing agents (e.g. GSH), which will require insertion of additional membrane proteins to permeabilize the polymeric membrane for such molecules.[14c, 81] The lack of control over the size

distribution of multicompartments will be improved with the adoption of a microfluidic-based assembly approach.[82]

Our developed strategy for cell-like materials has the advantages a very simple preparation method, high versatility and a straightforward manner to induce auto-controlled sequences of reactions/changes inside microcompartments and, for the first time, we showed how such a versatile cell mimic could be used as a drug screening platform.

4 Orthogonal interaction with cells [3]

For this topic, we decided to refer to enzyme-loaded polymersomes, usually referred as nanoreactors, as catalytic nanocompartments (CNC), a more general term that highlights one of their defining features, the segregation of the catalytic unit from the bulk. Before our work, cascade reactions reported within nanocompartments mainly involved encapsulation of one type of enzyme and providing the second enzyme in the surrounding medium. [83] However, if one partner of the cascade reaction is free in solution it might be degraded, resulting in a decrease -or even termination- of the overall reaction. Co-encapsulating enzymes within the same nanocompartment solves this issue, but only a low co-encapsulation efficiency was obtained due to the stochastic process of formation of multi-enzyme-loaded polymersomes. [84] A higher encapsulation efficiency of different enzymes can be achieved by linking the two enzymes together prior to encapsulation or the formation of compartments within compartments where small compartments and free enzymes are encapsulated inside micrometer-size compartments.[62, 85] Both binding the enzymes in one complex and the approach of compartments within compartments, which often uses organic solvents and emulsions, have the disadvantage of affecting the catalytic activity of the enzymes thus decreasing the efficiency or blocking the reaction. One approach, which allows for modularity while preserving the protection of the enzymes involved in the cascade reaction is to design catalytic compartments working in tandem. [84]

[3] PARTS OF THIS CHAPTER HAVE BEEN PUBLISHED AND ADAPTED WITH PERMISSION FROM:

Belluati Andrea, Craciun Ioana, Liu Juan, Palivan Cornelia G. Nanoscale enzymatic compartments in tandem support cascade reactions in vitro. Biomacromolecules. 2018.

However, there are only very few examples of tandem of (CNC) [25a, 86] and, up to this point, none had been evaluated in physiologically relevant environment or *in vitro*. In addition, the kinetics of the cascade reactions in separate compartments and the molecular factors affecting them were not investigated to determine whether such catalytic compartments still function in a more complex medium than buffers or to propose a therapeutically relevant solution. We used an amphiphilic block copolymer poly(2-methyloxazoline)-*block*-poly(dimethylsiloxane)-*block*-poly(2-methyloxazoline) ($PMOXA_6PDMS_{44}PMOXA_6$) for the formation of the nanocompartments [87], and their membrane was rendered permeable by insertion of the bacterial porin Outer membrane protein F (OmpF). [88] Thanks to this setup, we could study the concept of a two-step, two-compartment cascade reaction as an orthogonal, non-native cascade to detoxify uric acid.

4.1 Bioactivity of a non-native cascade: UOX-HRP cascade

4.1.1 Introduction

For this work, we selected as enzymes for the cascade reaction uricase (UOX) and horseradish peroxidase (HRP), which uses H_2O_2 resulting from the UOX reaction as the substrate to initiate the second reaction (**Figure 23**). [89] This orthogonal combination of enzymes serves to simultaneously decrease the concentration of uric acid, and of H_2O_2, resulting in a possible dual therapeutic approach. First we were interested to understand the molecular factors supporting the cascade reaction between separate compartments such to optimize their overall function. Next, we investigated their ability to function at increasing distances to mimic intra- and intercellular bio-distances as well as in human serum prior to applying them to decrease uric acid and H_2O_2 from the cellular milieu to explore their therapeutic application.

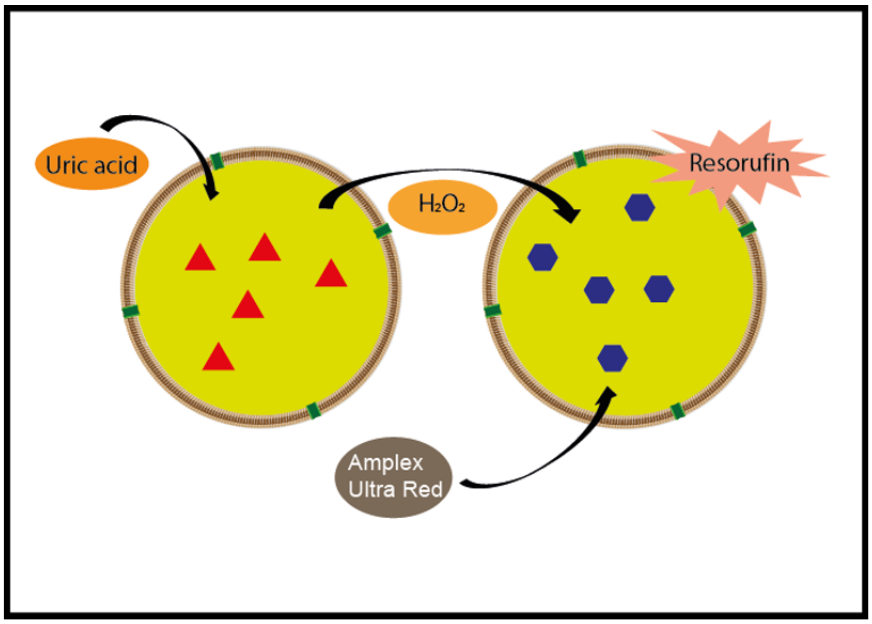

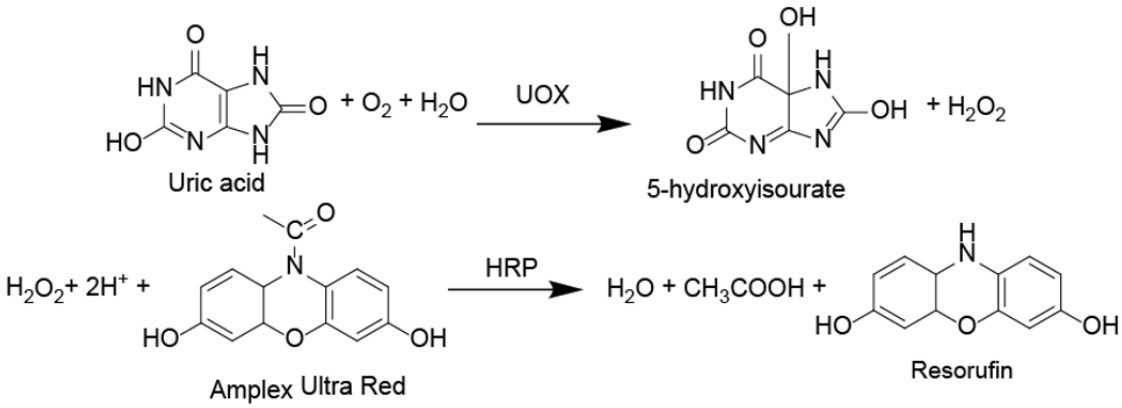

Figure 23 *Schematic representation of catalytic nanocompartments working in tandem, and detailed cascade reaction mediated by a combination of uricase (UOX) and horseradish peroxidase (HRP). The oxidation of uric acid results in formation of 5-hydroxyisourate and hydrogen peroxide. The later serves as substrate for HRP reaction in the presence of co-substrate Amplex Red, AR. The final product, resorufin, can be monitored by fluorescence spectroscopy.*

4.1.2 Physical characterization of CNCs

We encapsulated UOX and HRP inside the supramolecular assemblies formed during the self-assembly process of the copolymer by using film rehydration method due to its mild conditions, which does not affect the biomolecules [35g, 84]. The architecture of the supramolecular assemblies in presence and absence of enzymes was established by a combination of light scattering and transmission electron microscopy. We used static light scattering to obtain the radius of gyration R_g, and dynamic light

scattering for the hydrodynamic radius, R_h because the ratio of these values R_g/R_h, called ρ-factor, is indicative of the different architectures, e.g. 1 for hollow spheres while 0.77 for solid spheres [90]. In the case of empty supramolecular assemblies, R_g and R_h values were 70 nm and 84 nm respectively, and the calculated ρ-factor of 0.96 indicates hollow sphere architecture, thus formation of polymersomes. In the presence of UOX (UOX-CNC), we determined for the supramolecular assemblies R_g of 68 nm and R_h of 73 nm (ρ = 0.95), while in the presence of HRP (HRP-CNC) they had R_g of 74 nm and R_h 85 nm (ρ = 0.87) (**Figure 24**).

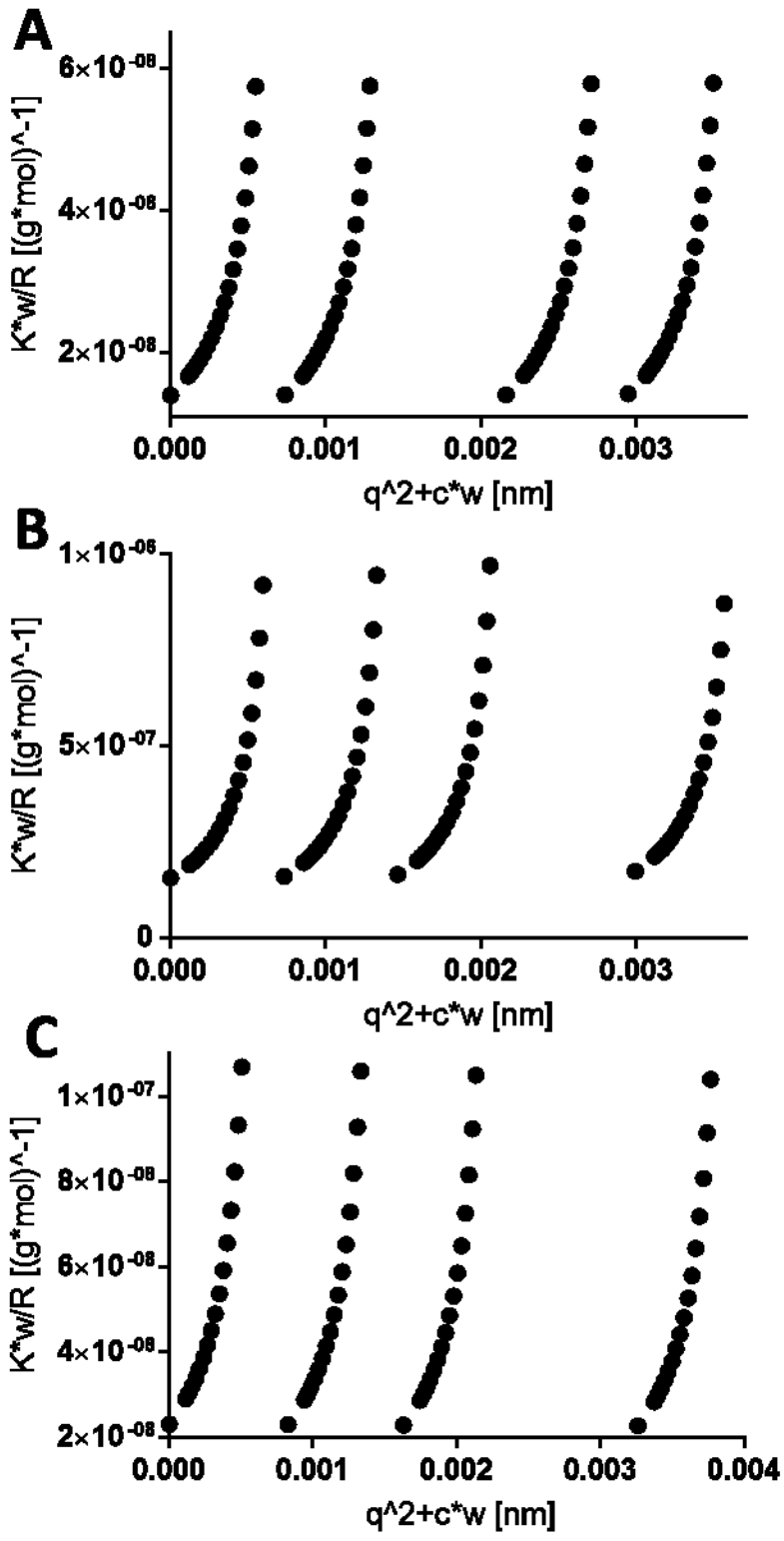

Figure 24 Zimm fits (from SLS) of **A:** empty polymersomes. **B:** UOX-CNC. **C**: HRP-CNC. The Zimm plot, obtained from SLS data, is built from a double extrapolation to 0 concentration and 0 angle from different measured angles and coefficients.

In both cases, the enzymes did not affect the self-assembly process and the resulting polymersome architecture, in agreement with the TEM micrographs, which show now remarkable differences in presence of UOX, HRP or OmpF, with small aggregates that could be seen regardless of the content, due to the sample preparation under vacuum. (**Figure 25**, **Figure 26**, **Figure 27**, **Figure 28 A,C**).

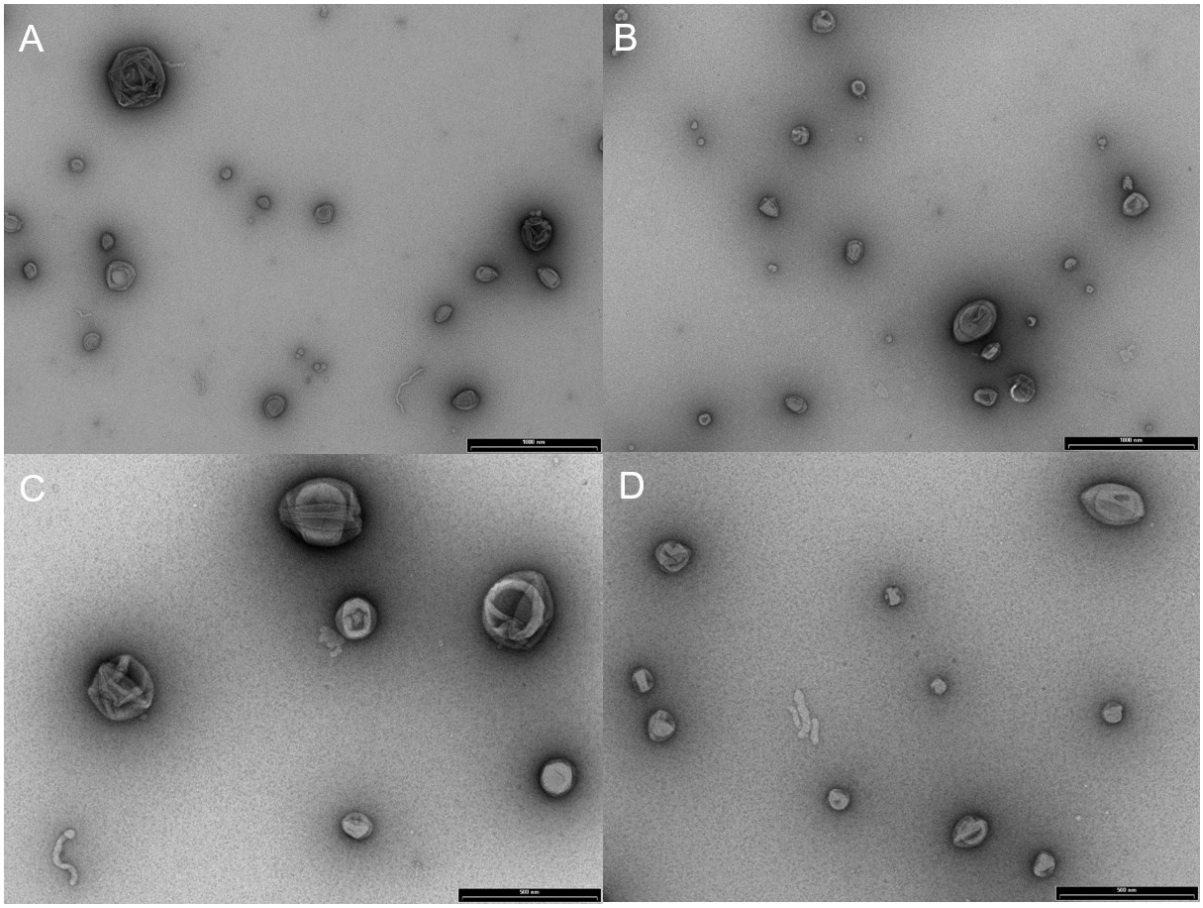

Figure 25 *TEM micrographs of UOX-CNCs. Scale bar 1000 nm (**A, B**) and 500 nm (**C, D**).*

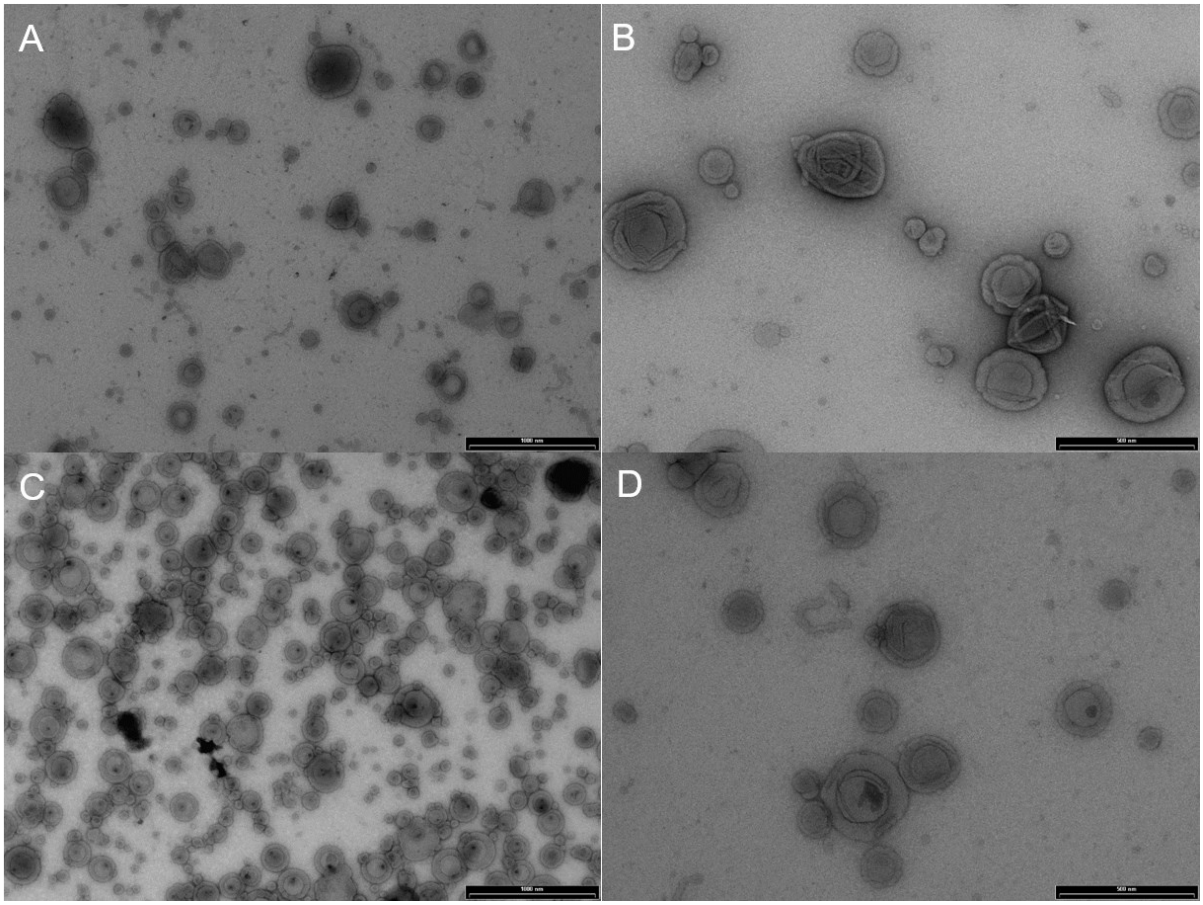

Figure 26 *TEM micrographs of HRP-CNCs. Scale bar 1000 nm* ***(A, C****) and 500 nm (****B, D****).*

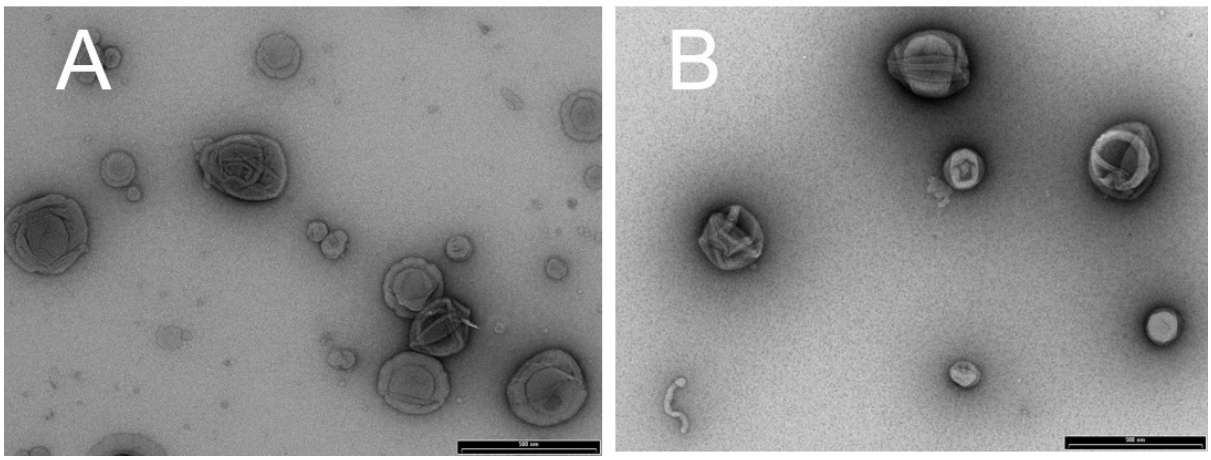

Figure 27 *TEM micrographs of UOX-CNCs OmpF-less (**A**) and HRP-CNCs OmpF-less (**B**). The spherical shape is maintained regardless of the insertion of OmpF in the membrane. Scale bar 500 nm.*

In order to quantify the amount of encapsulated enzymes inside the nanocompartments we used a combination of brightness measurements in fluorescence correlation spectroscopy (FCS), and bicinchonic acid assay (BCA). Fluorescence auto-correlation spectroscopy (FCS) measures the fluorescence fluctuations due to the Brownian motion of fluorescent species in a fL-sized volume, yielding molecular parameters, such as diffusion time and the number of particles that can be used to evaluate interactions/encapsulations of the fluorescent dyes with/into supramolecular assemblies[91]. By labelling the vesicle membrane with BODIPY 630/650, and using a 2-component fit (fixing the diffusion time of free dye as one of the components) we obtained their average diffusion time (τ_D 5000 µs for both CNCs, compared to τ_D = 57 µs of the free dye) and overall number of fluorescent vesicles in solution. The fraction of dye-polymersomes was 99% for UOX-CNC and 94% for HRP-CNC (2.6×10^{11} and 3.9×10^{11} polymersomes × μL^{-1}, respectively), while that of the free dye, of 1 and 4% indicated that the great majority of the dye partitioned into the polymersome membrane. The confocal volume of 1 fL, was obtained by a calibration with free BODIPY (**Figure 28B** and **D**).

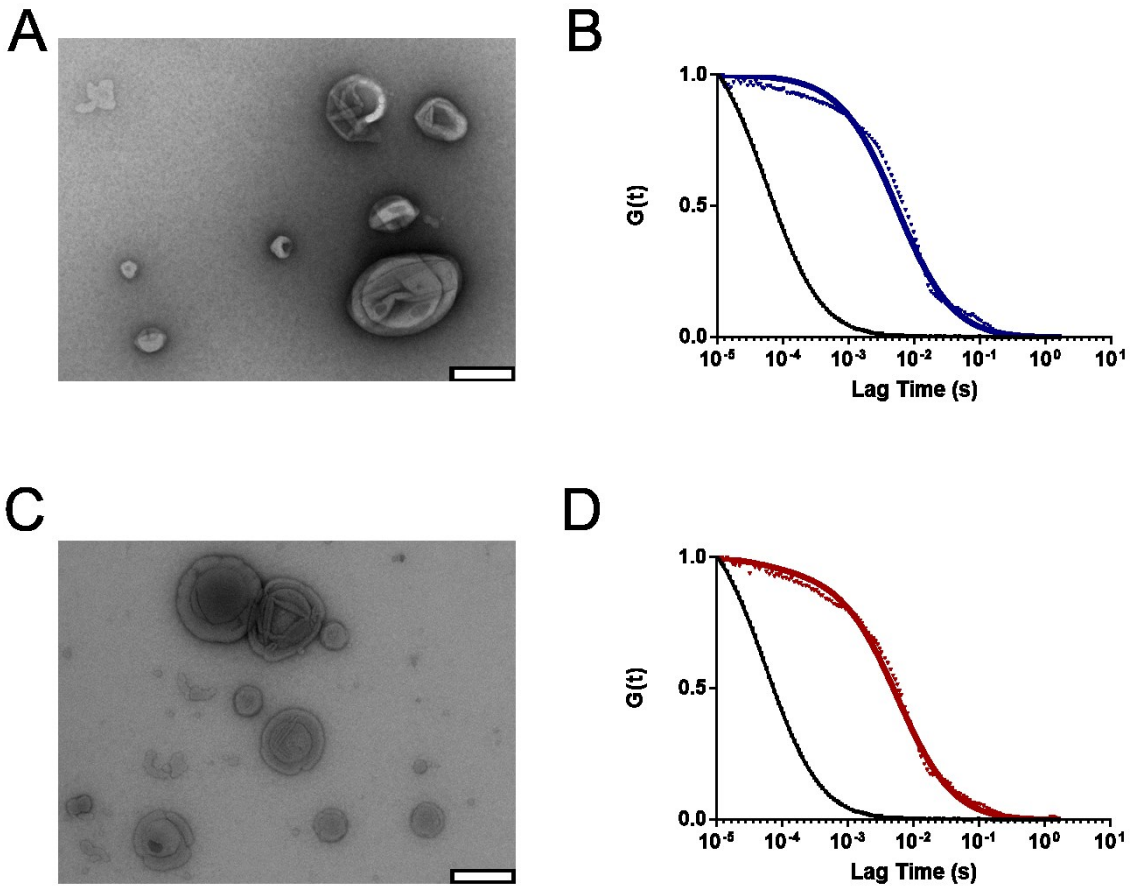

Figure 28 Formation of UOX-CNCs and HRP-CNCs. TEM micrograph of UOX-CNCs (**A**) (scale bar: 200 nm). **B**: normalized FCS autocorrelation curve of the dyed UOX-CNC (dots: normalized raw data; solid line: fitted data, black line: free BODIPY 630/650). TEM micrograph of HRP-CNCs (**C**) (scale bar: 200 nm). **(D)**: normalized FCS autocorrelation curve of the dyed HRP-CNC (dots: normalized raw data; solid line: fitted data, black line: free BODIPY).

A total protein concentration of 30 μgmL^{-1} for UOX and 18.6 μgmL^{-1} for HRP, respectively, was obtained by bicinchonic acid assay (BCA) (**Figure 29**).

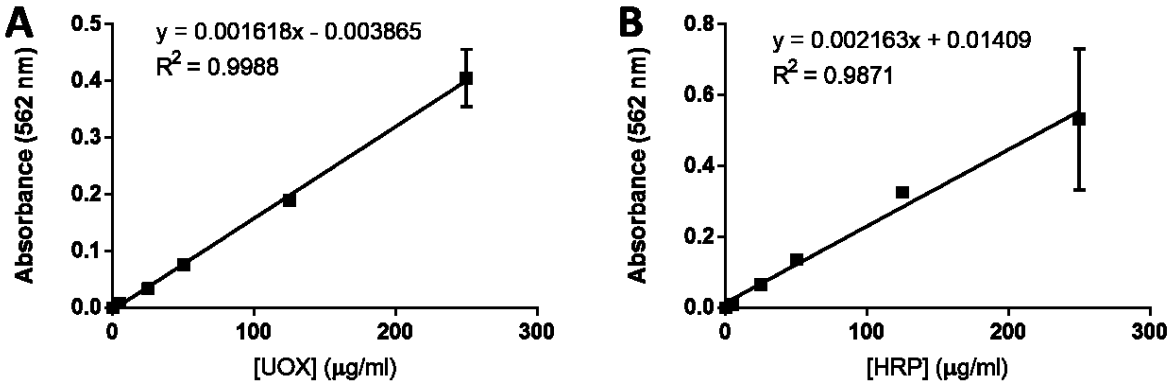

Figure 29. *Calibration curves for BCA assay, using UOX (**A**) and HRP (**B**) standards instead of BSA.*

Dividing the protein concentration by the number of polymersomes obtained by brightness measurements, we determined an average of 11±7 enzymes in UOX-CNCs and 6±2 enzymes in HRP-CNCs. An encapsulation efficiency of 36±12 % for UOX and 22±4% for HRP inside CNCs was obtained, in agreement with the encapsulation efficiency values obtained for other enzymes inside polymersomes. [35g, 84]

4.1.3 Influence of encapsulation on kinetics

Having determined the amounts of encapsulated enzymes, we used the same concentrations in bulk to evaluate the efficiency of the cascade reaction. The cascade reaction takes place when the enzymes are free or encapsulated in separate nanocompartments equipped with OmpF (**Figure 30**A). On the contrary, the reaction cannot proceed when the membrane of the nanocompartments is not equipped with OmpF to allow molecular passage through (**Figure 30**B) or when one of the enzymes or substrates is removed from the cascade (**Figure 30**C).

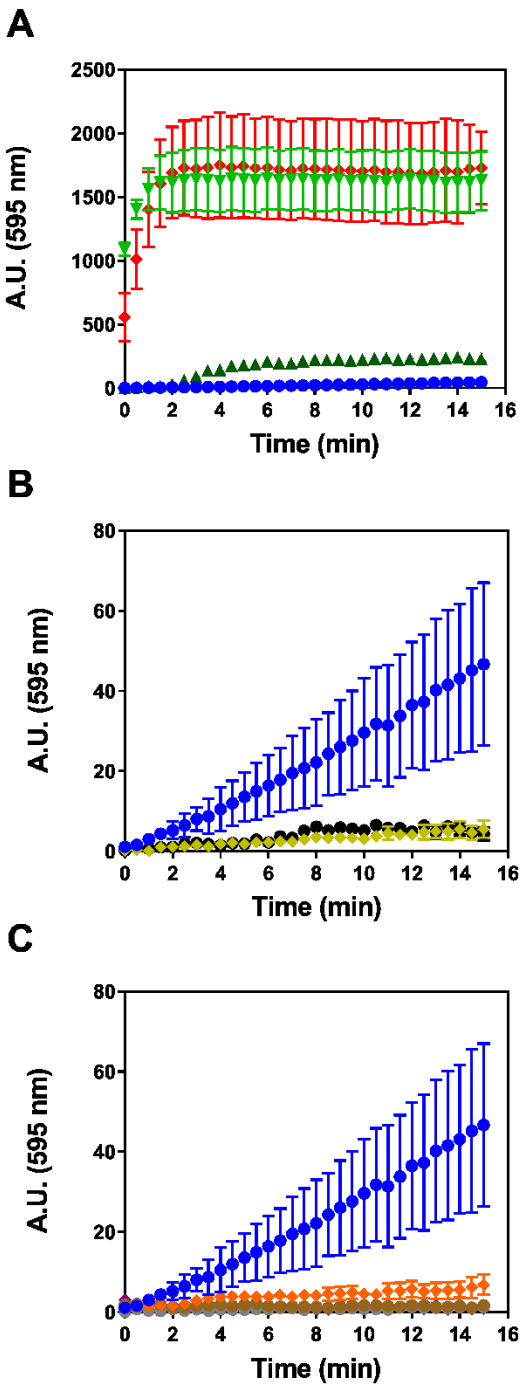

Figure 30 Cascade reaction with different setups. **A**: Enzyme kinetics when both enzymes are free (red), only HRP is free (light green), only UOX is free (dark green) and both UOX and HRP are encapsulated inside polymersomes (blue). **B**: Cascade with permeabilized CNCs (blue), unpermeabilized UOX-loaded polymersomes (olive), unpermeabilized HRP-loaded polymersomes (black). **C**: Cascade reaction with both CNCs and the corresponding substrates (blue), and in the absence of one of the reaction compounds: HRP (orange), UOX (brown), AR (grey), and uric acid (purple). Error bars are given as mean ± SD (n = 3), in some cases bars are smaller than the corresponding dot.

As expected, the cascade reaction between separate nanocompartments is significantly slower than that of the free enzymes. We were interested in establishing the effect of the molecular diffusion through OmpF of substrates and products, the probability that the product of the first reaction penetrates in a second CNC containing the HRP and the distance between different CNCs on each step of the reaction and on its overall efficiency. The conversion of Amplex Ultra Red (AR) to resorufin (AR conversion) was used as a comparison standard, because it represents the last step of the cascade reaction and therefore accounts whether the whole cascade reaction takes place. First, we studied the influence of molecular diffusion through OmpF as a key factor, which might limit the *in situ* enzymatic reaction inside CNCs. Having one of the enzymes free in solution and the second one encapsulated in the CNCs, AR conversion decreased compared with that of free enzymes. When HRP was surrounding UOX-CNCs, a slight decrease in AR conversion to 92% was observed, while when free UOX was free around HRP-CNCs a significant decrease of AR conversion to 13% was obtained (Figure 3). When both enzymes were inside CNCs working in tandem, AR conversion value decreased significantly, to 3% after 15 minutes. As H_2O_2 is known to rapidly diffuse through OmpF and it passes through the same barriers (membrane and inter-vesicle space) regardless of which enzyme is inside the CNCs, its effect is only minor and is due to its probability to interact with HRP. When only UOX is inside CNCs, the slight decrease in AR conversion is due to an inhomogeneous distribution of UOX, as source of H_2O_2, only inside the nanocompartments. When HRP is inside CNCs, the higher decrease of AR conversion is related to the slow diffusion of AR through OmpF pores, which represents the bottleneck for the cascade reaction for CNCs in tandem, as well (**Figure 31**).

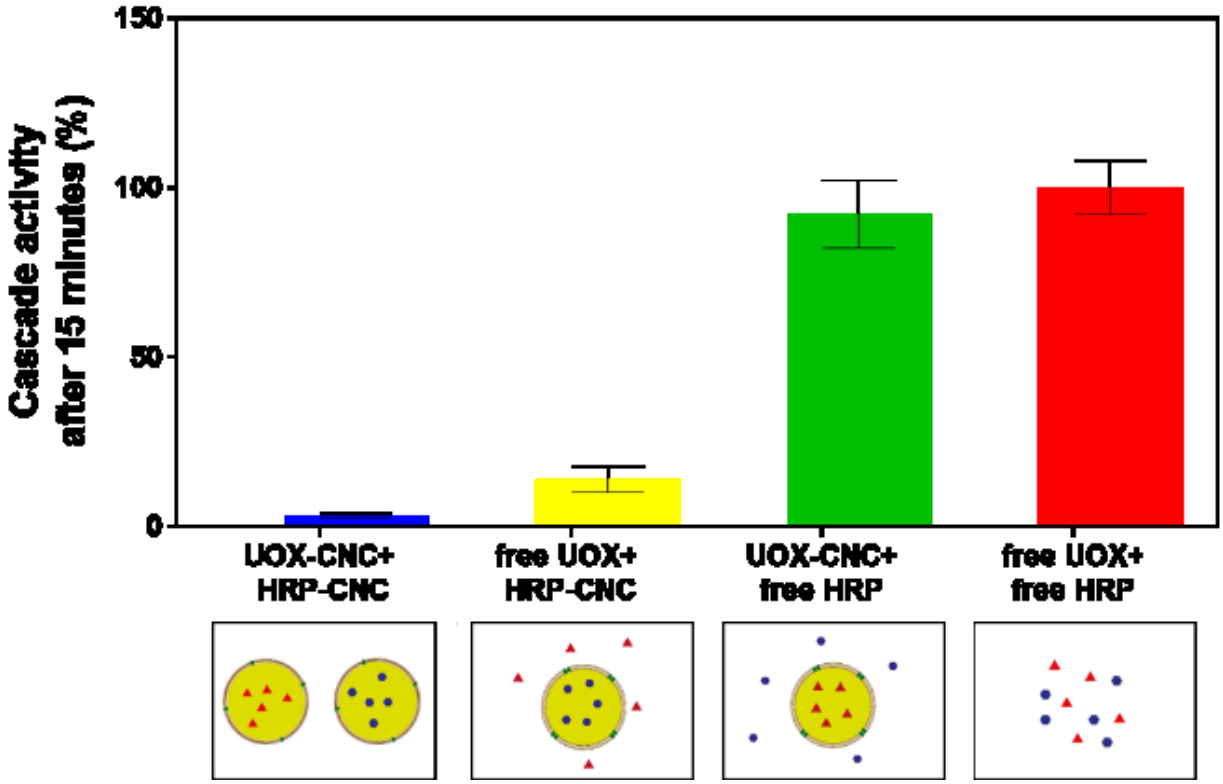

Figure 31 Conversion of AR to resorufin by a cascade enzymatic reaction when: both enzymes are encapsulated (blue), both enzymes are free (red), only UOX is encapsulated (UOX-CNCs) and HRP is free (green), and only HRP is encapsulated (HRP-CNCs) and UOx is free (yellow). Error bars are given as mean ± SD (n = 3).

In the case of CNCs in tandem another factor inducing the decrease of in the overall reaction efficiency is the inhomogeneous enzyme distribution when encapsulated inside polymersomes, which decreases the probability that the substrates of the second reaction reach the HRP-CNCs and support the second step of the cascade reaction. Besides, the necessity of H_2O_2 transfer from UOX- CNCs to HRP-CNCs is proven by introducing free catalase to the reaction mixture, as a competing enzyme that converts H_2O_2 to water and oxygen: when added, catalase strongly hinders the reaction (**Figure 32**).

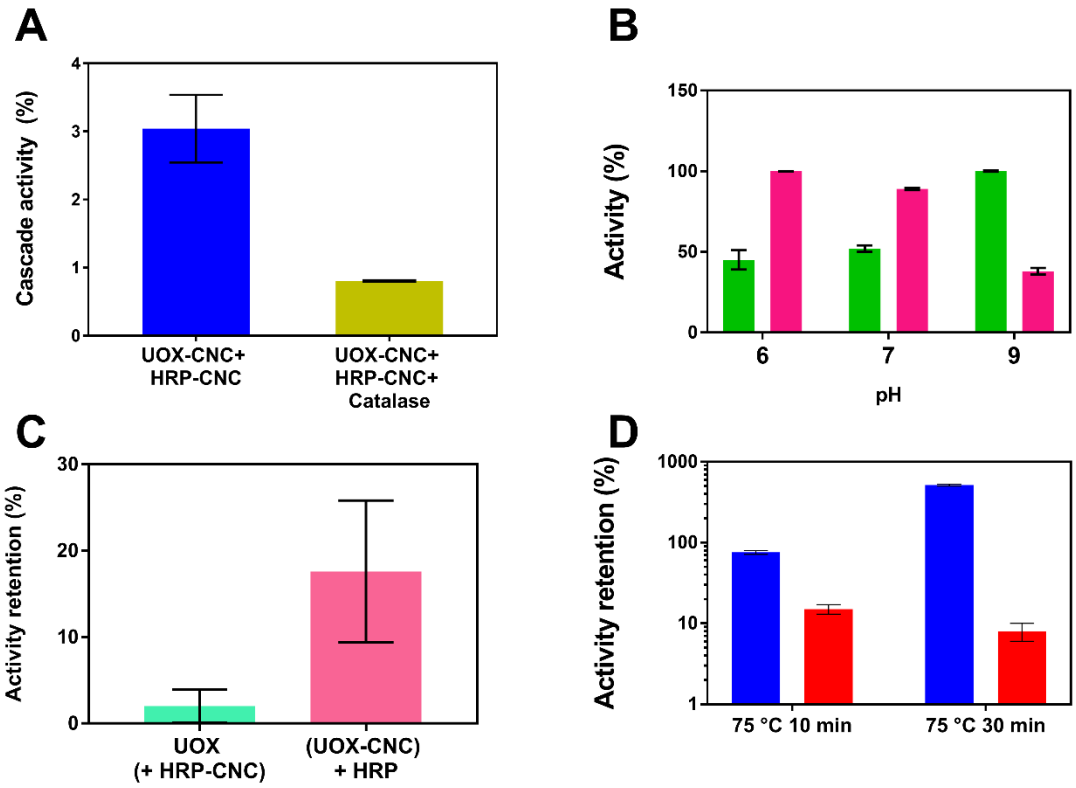

Figure 32 ***A****: interruption of cascade reaction by catalase, removing hydrogen peroxide.* ***B****: relative activity of UOX (green) and HRP (magenta) at their respective pH optima (set as 100%).* ***C****: residual activity from unspecific binding on the vesicles' outer surface: enzymes were added to unpermeabilized vesicles, which were then purified and their activity tested.* ***D****: activity of nanocompartments (blue) and free enzymes (red) after incubation at 75 °C: the nanocompartment activity is apparently much higher than after milder incubations. Error bars are given as mean ± SD (n = 3).*

4.1.4 Kinetic parameters of encapsulated enzymes

It is already known that encapsulation in polymersomes affects the kinetic parameters of enzymes, by increasing their affinity for the substrates or decreasing the velocity, because they are in a different environment than in bulk solution [35g]. To fully characterize the behavior of CNCs in tandem, we compared the kinetic parameters of CNCs when isolated and in cascade by using the Michaelis-Menten model. (**Figure 33**, *Table 3*, *Table 4*).

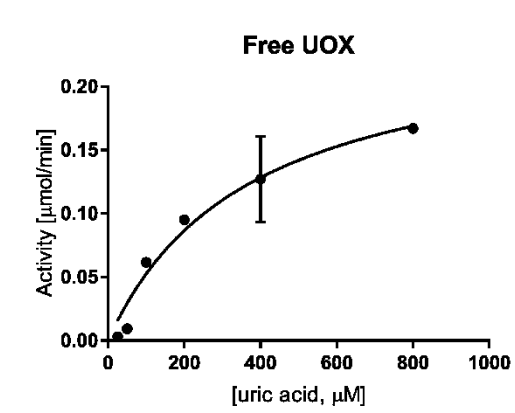
Free UOX
Activity [µmol/min]
0.20
0.15
0.10
0.05
0.00
0
200
400
600
800
1000
[uric acid, µM]

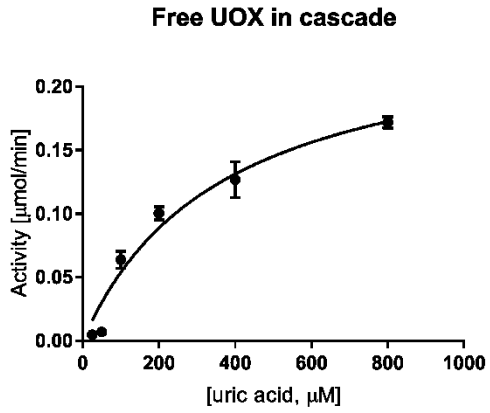
Free UOX in cascade
Activity [µmol/min]
0.20
0.15
0.10
0.05
0.00
0
200
400
600
800
1000
[uric acid, µM]

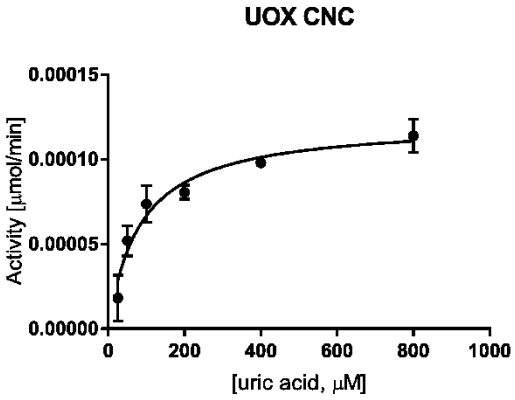
UOX CNC
Activity [µmol/min]
0.00015
0.00010
0.00005
0.00000
0
200
400
600
800
1000
[uric acid, µM]

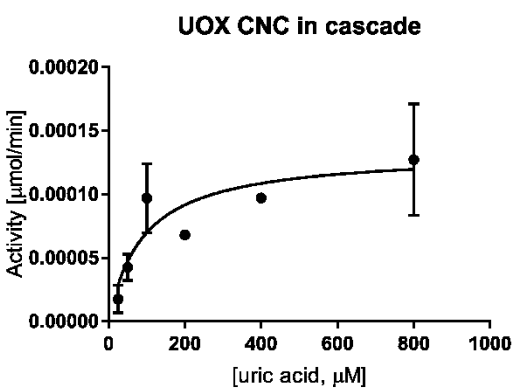
UOX CNC in cascade
Activity [µmol/min]
0.00020
0.00015
0.00010
0.00005
0.00000
0
200
400
600
800
1000
[uric acid, µM]

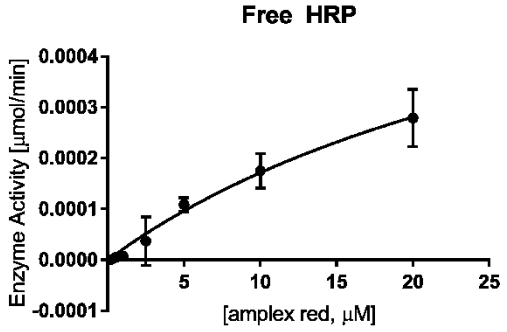
Free HRP
Enzyme Activity [µmol/min]
0.0004
0.0003
0.0002
0.0001
0.0000
-0.0001
5
10
15
20
25
[amplex red, µM]

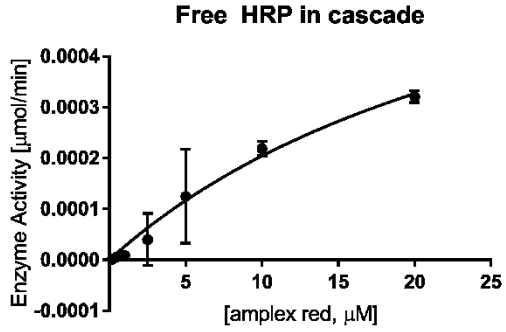
Free HRP in cascade
Enzyme Activity [µmol/min]
0.0004
0.0003
0.0002
0.0001
0.0000
-0.0001
5
10
15
20
25
[amplex red, µM]

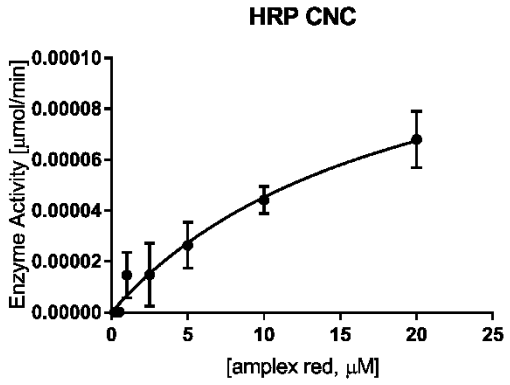
HRP CNC
Enzyme Activity [µmol/min]
0.00010
0.00008
0.00006
0.00004
0.00002
0.00000
0
5
10
15
20
25
[amplex red, µM]

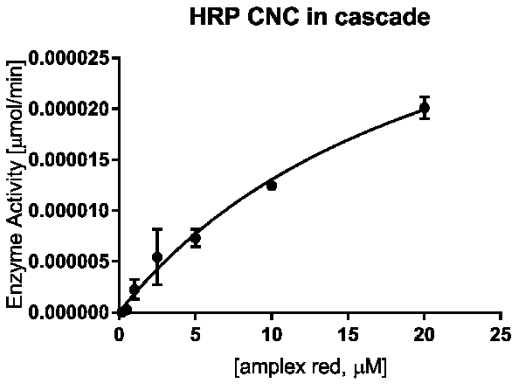
HRP CNC in cascade
Enzyme Activity [µmol/min]
0.000025
0.000020
0.000015
0.000010
0.000005
0.000000
0
5
10
15
20
25
[amplex red, µM]

Figure 33 *Michaelis-Menten kinetics for UOX, UOX + HRP (2x), UOX-CNC, HRP, HRP-CNC and UOX-CNC + HRP CNC. In some cases, error bars are smaller than the dots on the graphs. (n = 3)*

Both steps of the cascade reaction can be modelled in a first approximation by using Michaelis-Menten kinetics because for the first step (UOX-CNCs) uric acid is added in excess, and for the second step both substrates are in excess in the surroundings of HRP-CNCs (AR added in the medium, and H_2O_2 generated by UOX-CNCs with V_{max} of $1.47x10^{-3}$ μM/min, which is one order of magnitude higher than V_{max} of HRP, as presented in Table 1 and 2).

K_M, the Michaelis-Menten constant, defines the affinity of the enzyme for the substrate, and the apparent V_{max} represents the maximal velocity at which the enzyme operates once it is saturated by the substrate (when they are encapsulated inside CNCs). As both K_M and V_{max} are intrinsic enzymes characteristics in specific conditions, it is expected that these parameters are not affected by the enzyme encapsulation (if the substrate/products diffusion is not changing due to possible barriers). However, we observe a completely different situation: both K_M and V_{max} are affected by enzyme encapsulation (Table 1 and 2).

The apparent K_M of both enzymes is lowered once confined into a nanocompartment, 4-times for UOX-CNC and 1.5 times for HRP-CNC. This is not surprising, as the hollow cavity of a polymersome offers a more confined space, increasing the probability of the substrate to access the catalytic center of the enzyme[35g]. In addition, there is a decrease in V_{max} and k_{cat} values. The decrease of both V_{max} and k_{cat} is significant in the case when UOX is encapsulated in CNCs (both for free HRP and for HRP-CNCs) (***Table 3***). On contrary, when HRP is encapsulated (free UOX and UOX-CNCs) the decrease of V_{max} and k_{cat} values is significantly smaller (***Table 4***). We assume the change of k_{cat} values to be associated to a slower influx of the substrates to the enzyme's active site, a slower efflux of the products or a combination thereof when the enzymes are inside CNCs (due to various barriers associated with the polymersomes architecture). Besides, the inhomogeneous spatial distribution of enzymes when one enzyme or both are inside CNCs is affecting the accessibility of each enzyme by its corresponding substrates.

Similarly, k_{cat} /K_M values are decreased when the enzymes are inside the CNCs. While the substrate can easily encounter the enzyme once inside the compartment, the permeation through the membrane that is mediated by OmpF pores effectively hinders the total activity of the cascade. The effect of

diffusion to the enzyme is a well-known parameter affecting and altering enzyme kinetics, as it can become the actual limiting factor in their efficiency. [92]

Table 3 *Apparent kinetic parameters for UOX: Michaelis-Menten constant (K_M), maximal enzyme velocity (V_{max}), turnover rate (k_{cat}) and catalytic efficiency (k_{cat}/K_M).*

	UOX	**UOX in cascade**	**UOX-CNC**	**UOX-CNC in cascade**
K_M (μM)	3.70×10^{2}	3.68×10^{2}	8.32×10^{1}	9.09×10^{1}
V_{max} (μM/min)	2.47×10^{-1}	2.77×10^{-1}	1.22×10^{-4}	1.47×10^{-3}
k_{cat} (1/s)	2.72	2.55	1.34×10^{-3}	2.00×10^{-3}
k_{cat}/K_M (1/(μM s))	7.30×10^{-3}	7.52×10^{-3}	1.60×10^{-5}	2.20×10^{-5}

Table 4 *Apparent kinetic parameters for UOX: Michaelis-Menten constant (K_M), maximal enzyme velocity (V_{max}), turnover rate (k_{cat}) and catalytic efficiency (k_{cat}/K_M).*

	HRP	**HRP in cascade**	**HRP-CNC**	**HRP-CNC in cascade**
K_M (µM)	3.50×10	3.0×10	2.22×10	1.92×10
V_{max} (µM/min)	7.82×10^{-4}	8.19×10^{-4}	4.21×10^{-5}	1.32×10^{-4}
k_{cat} (1/s)	1.14×10^{-2}	1.12×10^{-2}	1.94×10^{-3}	6.19×10^{-3}
k_{cat}/K_M (1/M/s)	4.10×10^{-4}	4×10^{-4}	2.80×10^{-4}	3.22×10^{-4}

We exclude that the decrease in enzyme activity inside the CNCs is due to the confinement of enzymes: encapsulated UOX (molecular radius 4.27 nm [93]) and HRP (molecular radius 2.98 nm [94]) move completely free in a 1000-fold and 12000-fold greater volume, respectively. We calculated the inner volume of polymersomes by assuming a membrane thickness of 10.7 nm (measured for a $PMOXA_6$-$PDMS_{44}$-$PMOXA_6$ compartments of the same block length). [95]

4.1.5 Effect of encapsulation of enzyme stability

In a similar manner as is the case for liposomes, the polymeric membrane of nanocompartments is expected to offers protection of the encapsulated payload from external agents that would degrade it, as for example proteolytic attack [96]. We were interested to establish the protective role of the nanocompartments in the presence of physical factors (high temperatures and different pH values) and degrading agents (Guanidine Hydrochloride (GdnHCl), Proteinase K). We quantified the "activity retention" as the ratio between the production of resorufin under standard conditions (RT, pH 7) and in the presence of degrading conditions.

While below 37°C both encapsulated and free enzymes preserve their activity, for higher temperature, a decrease in activity is observed, but to a significantly higher degree for the free enzymes (Figure 34,

Figure 35 A). The ability of the polymeric membrane to protect the encapsulated payload from the effect of higher temperatures, which denatures the enzymes, is essential for translational applications.

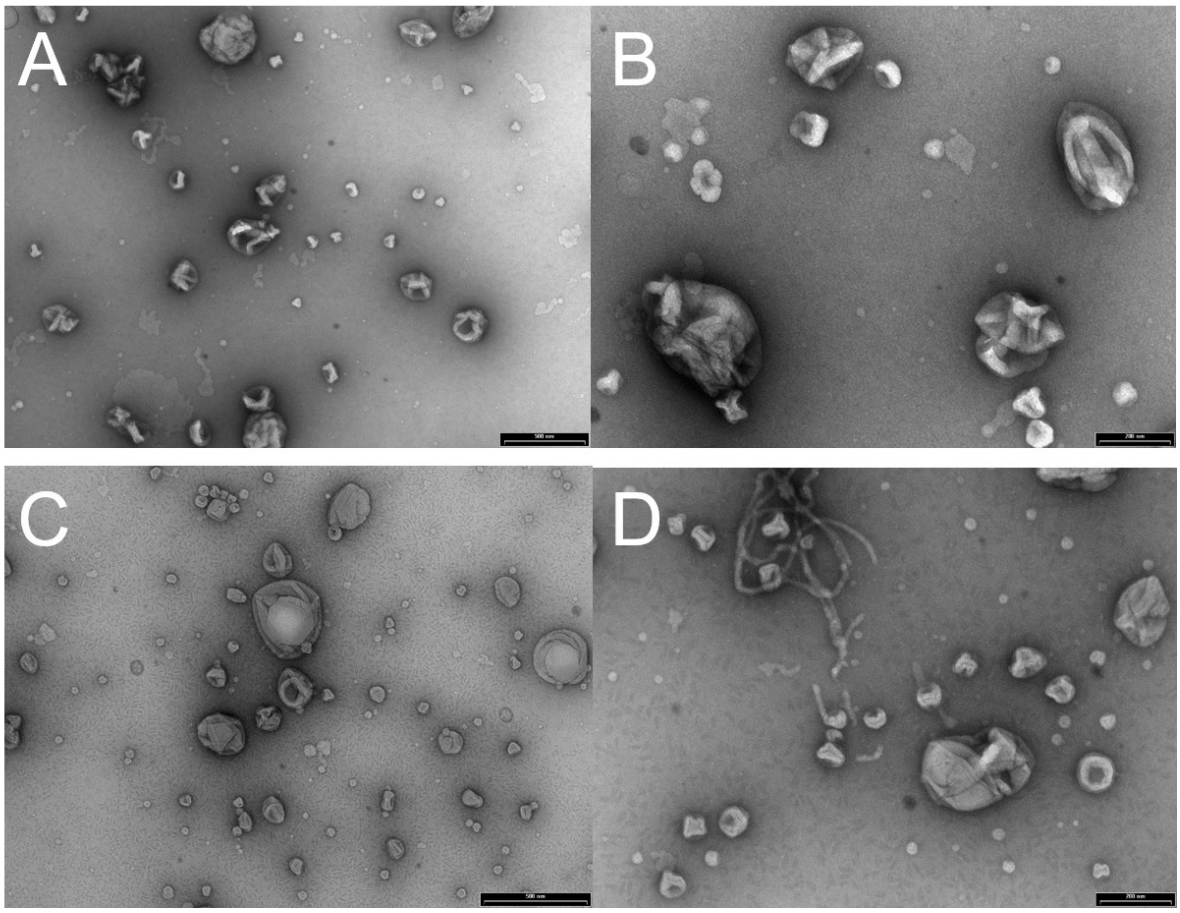

Figure 34 *TEM micrographs of a mixture of UOX-CNCs and HRP-CNCs after 30 minutes of incubation at 60 °C (**A, B**) and 75 °C (**C, D**). Broken vesicles and non-vesicular structures can be seen after the incubation at higher temperature, which could possibly lead to a partial release of the enzymes. Scale bar: 500 nm (**A, C**) and 200 nm (**B, D**).*

The effect of pH was less straight forward, as these two enzymes have different pH optima: basic for UOX and acidic for HRP. [97] While at pH 3 there is no apparent gain in activity from the enzyme encapsulation, at pH 9 the CNCs are significantly more active than the free enzymes acting in tandem. This increase in activity might be due to optimum pH 9 conditions for the first enzyme, UOX, involved in the cascade reaction (**Figure 35**B). However, we chose a neutral pH to evaluate the CNCs in tandem to be closer to physiological conditions, at which both enzymes are still active (**Figure 32**A), and where both the free enzymes and encapsulated ones have similar activity retention values.

To mimic a proteolytic attack, we added Proteinase K both to free enzymes and to CNCs for 2 hours. While a significant decrease in activity retention was observed for the free enzymes (18%±1), in the case of CNCs the decrease was considerably smaller(83%±3), additionally showing that a small fraction of enzyme molecules was adsorbed at the outer interface of the polymersome [98] (**Figure 32**C). The addition of a chemical agent inducing denaturation of enzymes, such as GdnHCl induced a decrease in the enzymes activity, which is significantly more pronounced when the enzymes are free, clearly indicating the protective role of compartmentalization (Figure 35D). The decrease of the activity retention value in the case of CNCs in tandem is due to the probable diffusion of GdnHCl (95 Da) through OmpF, which has a weight cut-off of 650 Da. [99]

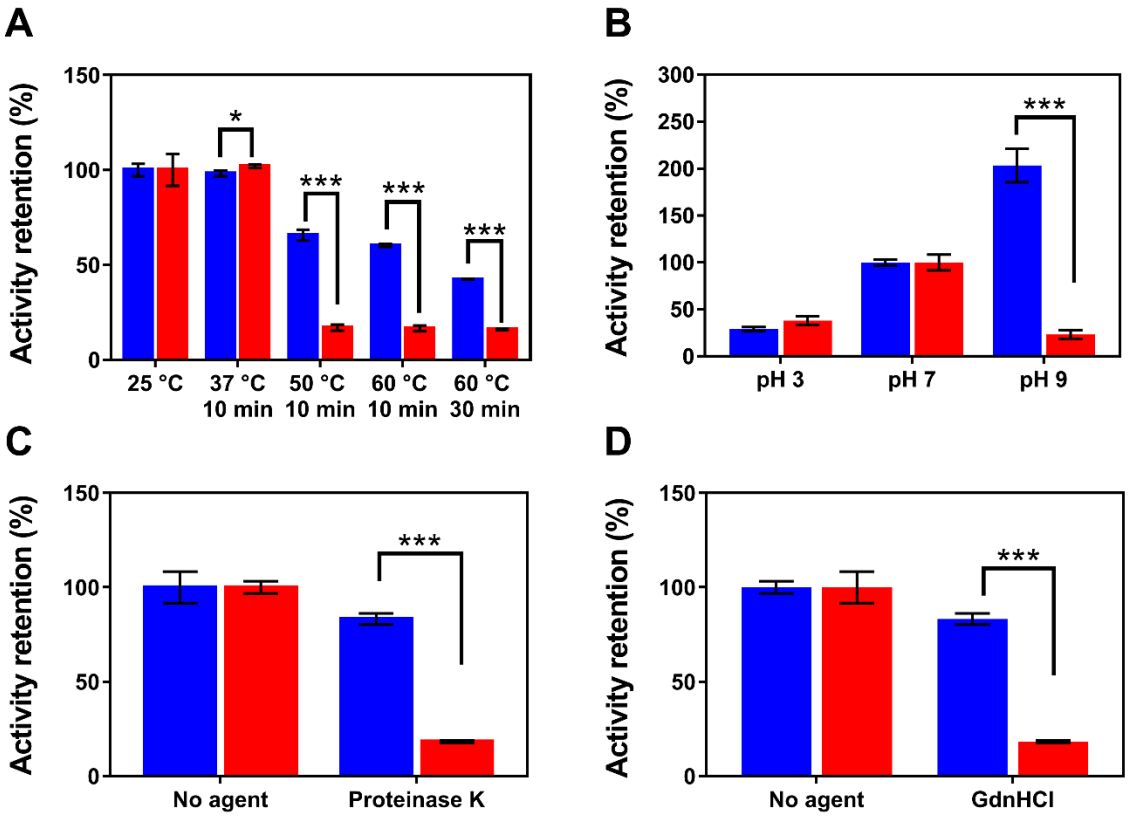

Figure 35 Stability of catalytic nanocompartments and free enzymes (activity normalized *against* CNCs (blue) or enzymes (red) at RT, neutral pH, no agents). **A**: protection from heat. **B**: protection from extreme pH. **C**: protection from denaturing agent GdnHCl. **D**: protection from proteolysis. Error bars are given as mean ± SD (multiple t - test, * $p < 0.05$, ** $p < 0.01$, *** $p < 0.001$, $n = 3$).

It was not possible to determine the amount of enzyme adsorbed or how adsorption affected its activity. Therefore, we considered the overall activity of the CNCs as a whole; however, by adding free enzyme to empty vesicles and then purifying them, it was possible to detect a certain amount of activity due to unspecific binding in the cascade for HRP, estimated to be around 3% of the total (**Table 5**). The auto-oxidation of AR was also taken into account, and subtracted in all blanks.

Table 5 *the activity of HRP (arbitrary fluorescence units) unspecifically adsorbed to the outer polymersome surface is comparable to that obtained from free HRP at 10 ng mL-1, meaning that only around 3% of the signal (used concentration: 300 ng mL-1) derives from external HRP.*

HRP setup	**a.u. (595 nm)**
HRP adsorbed to polymersomes	19.5 ± 0.4
Free HRP 10 ng mL^{-1}	18 ± 1

4.1.6 Influence of distance on reaction efficiency

The passage through barriers and diffusion between compartments represents an essential point in bio-communication because products have, in some cases, to travel to different cellular compartments or take part in inter-cellular communication. Most organelle-to-organelle communications in the cell happen via close association below 50 nm [100] and the average synaptic cleft is around 20 nm [101], whereas it is estimated that a single cell can effectively communicate between 5 and 10 µm in autocrine signaling and up to 250 µm in paracrine signaling. [102] In such cases of communication between organelles or cells, there is no longer a homogeneous distribution of enzymes or receptors but local high concentrations and otherwise empty or low density interstices. We used our CNCs in tandem to mimic communication between bio-assemblies and see the effect of distance on the overall cascade reaction efficiency. We assumed a cubic volume for the compartments, so that the mean inter-compartment distance is calculated, based on the polymersome density obtained by FCS.

The AR conversion values in the case of CNCs in tandem remains almost constant (with some values higher than 100% as values fluctuate around the mean obtained at 0.8 µm, set as reference) until the mean distance between CNCs is 1.29 µm, then the values decrease significantly. This suggests that the

diffusion of molecules through the OmpF pores represents the dominant factor for distances lower than approx. 1.30 µm. Interestingly, the ratio between the mean compartments distance and their diameter is about 10, which has the same order of magnitude as the ratio between a mean cell-cell communication distance and a cell diameter for 1 µm, such as bacteria[103]. For distances between CNCs higher than 1.3 mm, the cascade reaction is rapidly hindered due to a decrease of the probability that H_2O_2 encounters a HRP-CNC (Figure 5). These distances are consistent with distances typical of autocrine signaling. Therefore, our findings based on the simple CNCs in tandem provide the behavior of such confined space reactions in relevant bio-conditions.

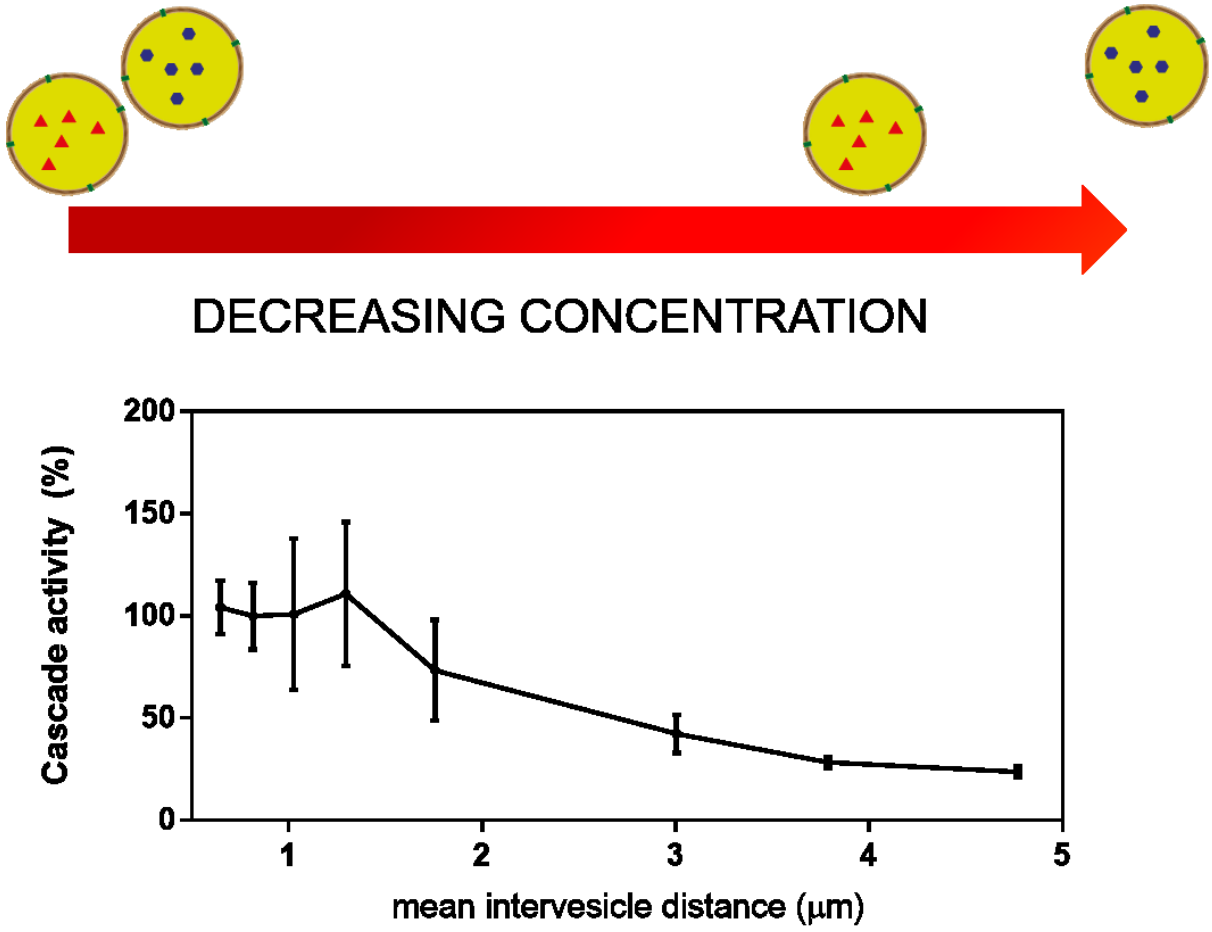

Figure 36 Cascade activity at different mean intervesicle distances. Error bars are given as mean ± SD (n = 3).

4.1.7 The therapeutic potential of CNCs in a cascade

We then evaluated the functionality of the CNCs tandem in biological conditions, both in biofluids and upon incubation with cells, as more apropriate to advance translational applications. First, we used

human blood serum where uric acid was dissolved to reach levels similar to those considered typical for hyperucemia (>6.8 mgdL^{-1} in men). A simple model, defined as

$$\frac{\Delta Abs290_{enzymatic}}{\Delta Abs290_{serum}}$$

Equation 2

for the dilutions of HRP-CNCs gives the relative efficiency of the cascade reaction, which we called Relative Urate Degradation (R.U.D.) (Figure 37A). Interestingly, in such a complex medium, CNCs induce the clearance of uric acid as fast as the free enzyme. In human serum, as a physiological medium CNCs lost most of the disadvantage against free enzymes they had in buffer. Further studies, beyond the scope of the present one, are necessary to understand the bio-molecular factors affecting the efficiency of the overall cascade reaction between CNCs in human serum.

Secondly, we determined the ability of the CNCs to metabolize uric acid and degrade H_2O_2 upon incubation with cells, as an essential step towards medical applications. Prior, we evaluated the cytotoxicity of CNCs when incubated with HEK293T cells overnight in different concentrations of the CNCs (measured in polymer concentration) by MTS assay. CNCs have no cytotoxic effect on the cells, even at the highest polymer concentration (0.19 µgmL^{-1}) (Figure 37B). Next, CNCs were incubated with HEK293T epithelial cells for 24 h in the presence of increasing amounts of uric acid (250 and 350 µM): at physiological concentration and at the lower end of hyperuricemia values. Cell viability decreased to around 60% in the presence of 250 µM uric acid. By addition of either free enzymes or the CNCs, the cell viability was unaffected by the presence of uric acid. An increase in the amount of uric acid to 350 µM reduces the viability of the cells to 2%, while the cascade reaction of the free enzymes and of CNCs in tandem induce a protective effect against uric acid. In addition, due to the combination of enzymes, H_2O_2 as well is degraded thanks to the succesful cascade reaction process (**Figure 37**C and D).

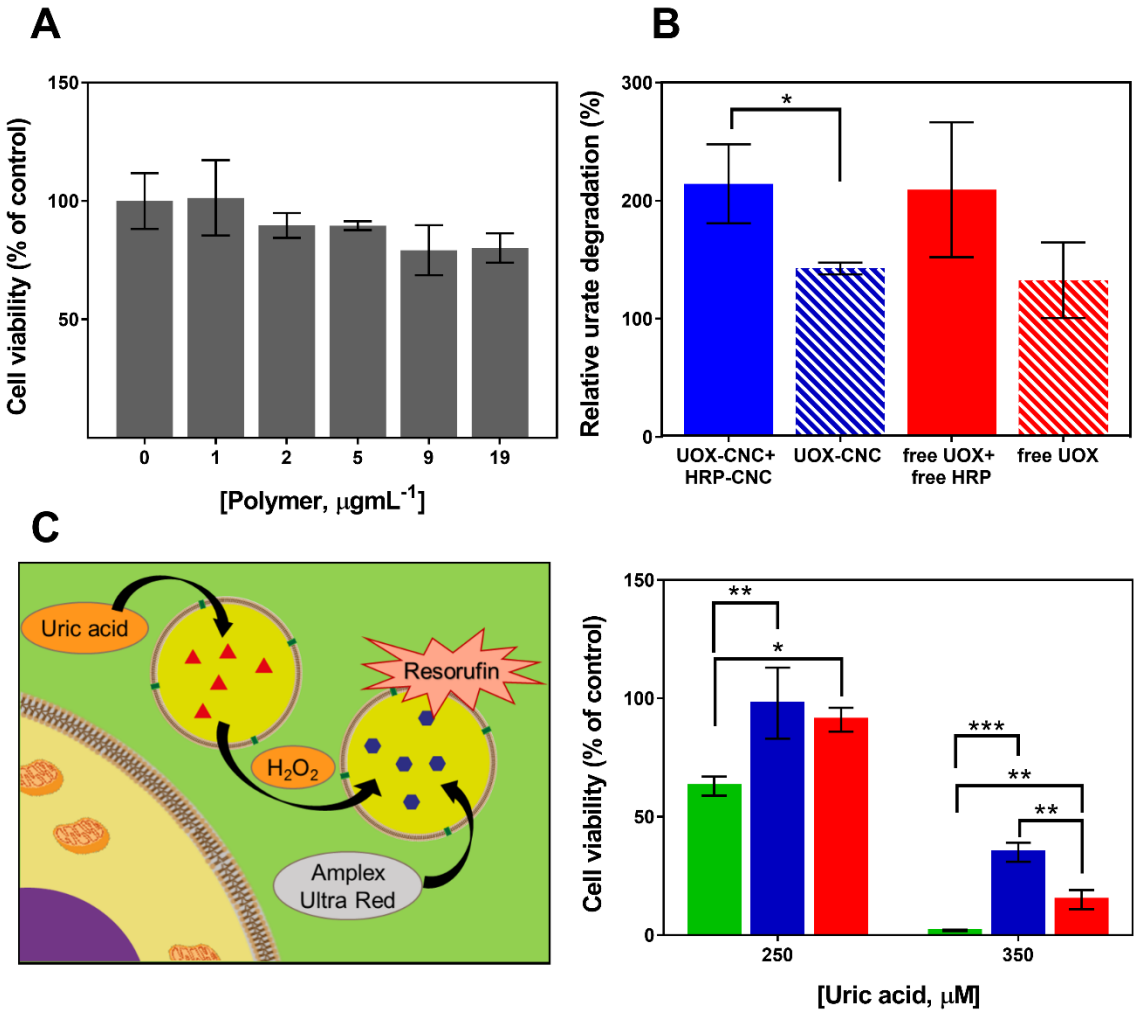

Figure 37 *Activity of CNCs and free enzymes in blood serum and their interaction with cells.* ***A****: clearance of urate with both CNCs (solid blue), UOX-CNC only (striped blue, no HRP-CNC), both free enzymes (solid red) and UOX only (striped red, no HRP-CNC)* ***B****: cell viability of HEK293T cells incubated with CNCs at different concentrations (expressed as polymer concentration).* ***C****: scheme of the CNC-cell interaction and detoxifying activity of the UOX-HRP cascade on cells only (green), cells with free enzymes (blue) and cells with CNCs (red). Error bars are given as mean ± SD (multiple t - test, * p < 0.05, ** p < 0.01, *** p < 0.001, n = 3).*

5 Integration of CNCs into cell metabolism[4]

Current pharmacological research aims to replace whole cellular pathways that are damaged or missing, and disciplines such as tissue engineering and synthetic biology often need metabolome-spanning agents [104]. These extensive modifications are usually achieved via genetic engineering, but when the need for transient modifications of cell behavior arises (e.g. cell differentiation, gene induction) this could be obtained via the *in situ* production of natural messenger molecules with known physiological effects.

A possible tool in enzyme supplementation or even cell engineering that can be used to correct aberrant signaling pathways, is the use of specialized reactive compartments, as the spatiotemporal compartmentalization of reactions allows a more precise kinetic regulation,[2] creating specialized environments and protecting them from the exterior.[37a] This concept has already been applied in nanotechnology where enzymes are entrapped into nano-sized objects such as protein cages, or lipid/polymer based compartments.[105] Polymer compartments with nanometer sizes, called polymersomes are particularly appealing to host ***in situ*** enzymatic reactions, as their membrane is more stable than that of liposomes and can be functionalized with different moieties to support targeting or immobilization on surfaces, while, if appropriately selected, retaining biocompatibility.[13, 38, 84] When loaded with enzymes and rendered permeable for substrates/products, polymersomes serve as efficient catalytic nanocompartments (CNCs) with a broad range of applications depending on the encapsulated enzyme.[38]

[4] PARTS OF THIS CHAPTER HAVE BEEN ADAPTED FROM THE MANUSCRIPT:

Belluati Andrea, Craciun Ioana, Palivan Cornelia G. Bioactive catalytic nanocompartments integrated into cell physiology and their amplification of cGMP signalling cascade. 2020 *Under Revision.*

5.1 The case of iNOS-sGC

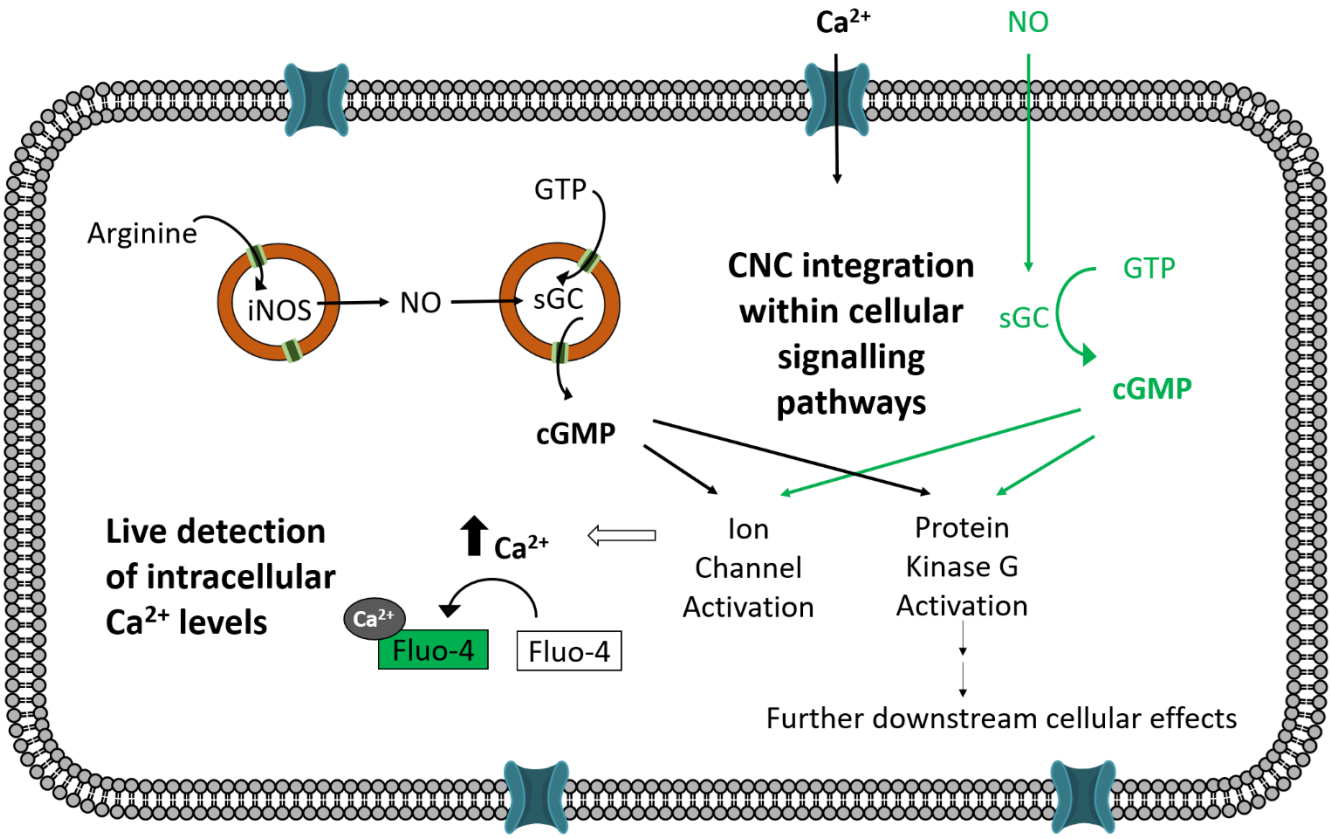

5.1.1 Introduction

An example of an enzymatic with wide-spanning effects is the cascade reaction mediated by nitric oxide synthase (NOS) and guanylyl cyclase (GC). A fine-tuned NOS-GC cascade is essential for cell signaling. The malfunction of one or both of the enzymes has a drastic effect on the homeostasis of living organisms but also influences the growth and differentiation behavior of cells.[106] Nitric oxide synthases (NOS; inducible, endothelial and neuronal) are a family of enzymes that oxidize L-arginine to L-citrulline, producing nitric oxide, which readily diffuses through membranes and plays a role in smooth-muscle relaxation, regulation of apoptosis, ion channel activity, mitochondrial function and immune response.[107] While the -calcium-independent- inducible NOS (iNOS) is usually not linked to receptor-dependent processes, as it is expressed by macrophages to produce locally high concentrations of the radical NO to kill pathogens and other cells, it is still involved in inflammatory vasodilation and other non-toxigenic pathways.[108] Deficiencies in the neuronal and endothelial NOS (nNOS and eNOS,

respectively) are linked to muscular dystrophy and nephropathy[109]; iNOS has recently been suggested to be involved in compensating eNOS malfunctioning, with cardioprotective effects.[110]

Guanylyl cyclases (GC) are widely distributed signal-transduction enzymes that, in response to various cellular stimuli, convert GTP into the second messenger cyclic 3,5-guanosine monophosphate (cGMP) and pyrophosphate (PPi). Binding of NO to the heme moiety of the soluble guanylyl cyclase (sGC) induces the transition from basal to activated sGC. Activated sGC quickly converts guanosine-5'-triphosphate (GTP) to cGMP and pyrophosphate (PPi). cGMP acts as a ubiquitous second messenger in a variety of processes, through intracellular signaling cascades, regulating the activity of a number of downstream proteins, including cGMP-dependent protein kinase G (PKG), cGMP-dependent phosphodiesterases (PDE) and cyclic nucleotide-gated ion channels (CNP). These pathways are involved, for example, in smooth muscle relaxation and vasodilation or immunomodulation [111] in regulating cell growth initiation and differentiation[106b], cholinergic neurotransmission [112] and well as in photo-transduction in the vertebrate retina [113] Aberrant cGMP signaling as a result of mutations in soluble GCs has been associated with a number of diseases, such as retinal dystrophies (Leber's`congenital amaurosis, dominant cone-rod dystrophy, cone dystrophy and central areolar choroidal dystrophy).[111]

A possible tool in enzyme delivery, or even cell engineering, is the use of specialized reactive compartments, as the spatiotemporal compartmentalization of reactions is a fundamental aspect of cellular biology, allowing a more precise kinetic regulation [2], creating specialized environments and protecting them from the exterior.[37a] This concept has already been applied to nanotechnology, entrapping enzymes into nano-sized objects such as protein cages, or lipid/polymer based compartments.[105] Polymersomes are particularly appealing to host *in situ* enzymatic reactions, as their membrane is more stable than that of liposomes and can be functionalized with different moieties to support targeting or immobilization on surfaces, while retaining biocompatibility.[13, 38, 84] When loaded with enzymes, and rendered permeable for substrates/products, polymersomes serve as efficient catalytic nanocompartments based on the enzymatic reactions taking place inside.[38] Beyond single-enzyme catalytic nanocompartments (CNC), cascade reactions represent one step further in increasing the number of biotransformations and inducing multifunctionality within the same system. Such enzymatic cascades can be performed by co-encapsulated enzymes [24, 27, 39], but the co-encapsulation in

nanometric compartments of multiple enzymes is hindered by the low co-encapsulation efficiency.[23b] A way to solve this problem was achieved by encapsulating the enzymes in separated CNCs [41, 114] as demonstrated in Chapter 4.1.

Here we developed a system of two catalytic nanocompartments of biological relevance, and show that it can act on cell signaling pathways, effectively integrating its functionality into native cell metabolism and physiology, instead of operating orthogonally on cells, with no cell communication. To achieve this, we chose an enzymatic cascade mediated by inducible nitric oxide synthase (iNOS) and soluble guanylyl cyclase (sGC) and encapsulated them into polymersomes whose membrane was equipped with a channel porin allowing a molecular flow through. A fine-tuned NOS-GC cascade reaction is essential for cell signaling. The malfunction of one or both of the enzymes has a drastic effect on the homeostasis of living organisms but also influences the growth and differentiation behavior of cells.[106] Nitric oxide synthases (NOS; inducible, endothelial and neuronal) are a family of enzymes that oxidize L-arginine to L-citrulline, producing nitric oxide, which readily diffuses through membranes and plays a role in smooth-muscle relaxation, regulation of apoptosis, ion channel activity, mitochondrial function and immune response.[107] The -calcium-independent- inducible NOS (iNOS), while usually associated to macrophage response, it is still involved in inflammatory vasodilation and other non-toxigenic pathways.[108] Deficiencies in the neuronal and endothelial NOS are linked to muscular dystrophy and nephropathy[109]; iNOS has recently been suggested to be involved in compensating eNOS malfunctioning.[110]

Soluble Guanylyl cyclases (sGC) is a signal transduction enzyme that, in response to various cellular stimuli, converts GTP into the second messenger cyclic 3,5-guanosine monophosphate (cGMP) and pyrophosphate (PPi), after the activation provided by the binding of NO. cGMP acts as a ubiquitous second messenger in a variety of processes, through intracellular signaling cascades, regulating the activity of a number of downstream proteins. These pathways are involved, for example, in smooth muscle relaxation and vasodilation or immunomodulation [111], cell growth initiation and differentiation [106b], cholinergic neurotransmission [112] and in photo-transduction in the vertebrate retina.[113] Aberrant cGMP signaling as a result of mutations in soluble GCs has been associated with a number of diseases, such as retinal dystrophies. [111]

As such cascade is already present in cells, our CNCs could be the first metabolism-enhancing cascade derived from nano-sized compartments. The unique advantage of our binary CNC system derives from their ability of inducing changes in cell homeostasis without the addition of any other compound, only using the arginine and GTP naturally present in the cell or in the culture medium [115] The great importance of this enzymatic cascade prompted us to investigate whether the enzymes were encapsulated into CNCs composed of a PMOXA-PDMS-PMOXA membrane, to be protected from the external environment and be delivered to cells.[23b, 116] We then characterized the assembled iNOS-CNCs and sGC-CNCs both physically (light scattering, electron microscopy, fluorescence microscopy, nanoparticle tracking) and functionally (fluorometric assays). We studied their biological activity on HeLa and smooth muscle C2C12 cells, using the intracellular concentration of calcium as a functionality assay to demonstrate whether the cascade could work in the culture medium in physiological conditions and elicit cellular responses.

5.1.2 Physical characterization of CNCs

Encapsulation of iNOS and sGC into individual CNCs

We encapsulated the two enzymes into biocompatible $PMOXA_6$-$PDMS_{44}$-$PMOXA_6$ polymeric assemblies via film rehydration.[48, 117] This technique consists of vacuum drying the block copolymer to obtain a film, then adding the rehydration buffer containing the molecules of interest. Continuous stirring helps the swelling of the copolymer film leading to self-assembly and formation of structures entrapping the solutes (**Figure 38**).

A

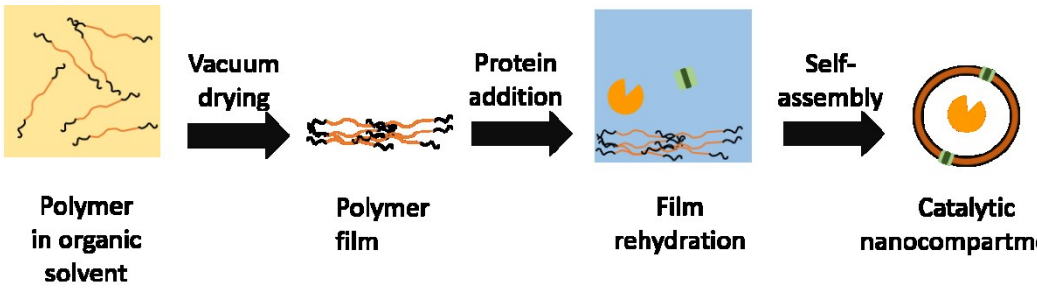

B

	R_g (nm)	R_h (nm)	ρ (R_g/R_h)	Concentration (vesicles ml^{-1})
No protein	102	103 ± 8	0.99	$1.35 \times 10^{12} \pm 7.85 \times 10^{10}$
iNOS (+OmpF)	102	104 ± 9	0.99	$1.72 \times 10^{12} \pm 4.27 \times 10^{10}$
sGC (+OmpF)	104	101 ± 6	1.03	$1.82 \times 10^{12} \pm 8.53 \times 10^{10}$

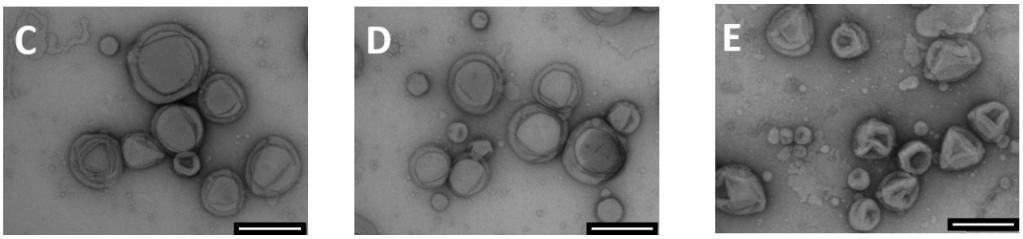

***Figure 38 A**: fabrication workflow of the CNCs. **B**: table of R_g, R_h and vesicle concentration for the CNCs with and without proteins (enzymes and OmpF). **C**: TEM micrograph of empty polymersomes. **D**: TEM micrograph of iNOS-CNC **E**: TEM micrograph of sGC-CNC. Scalebar for TEM micrographs: 200 nm.*

The $PMOXA_6$-$PDMS_{44}$-$PMOXA_6$ block copolymer used in this study self-assembled into supramolecular structures with a radius of gyration R_g = 102 nm and radius of hydration R_h = 103 ± 8; the R_h/R_g ratio (ρ-factor), being close to 1, meant that we obtained hollow vesicles, *i.e.* polymersomes (**Figure 38**B).[118] Upon permeabilization of the membrane with OmpF and encapsulation of iNOS, the radii and spherical morphology of the CNC did not change (iNOS-CNC, R_g =102 nm and R_h = 104 ± 9 nm, ρ-factor 0.99). Also, in the case of sGC-CNC upon permeabilization and enzyme encapsulation no changes in the compartments was observed (sGC-CNC, R_g = 104 nm and R_h = 101 ± 6 nm, ρ-factor 1.03), indicating the polymeric vesicular structures are unaffected by the presence of proteins either in the lumen or within the membrane.

For an efficient tandem CNC reaction it is imperative to have a balance between the amounts of each compartment. Using nanoparticle tracking analysis (NTA) we ensured that there was no significant difference in polymersome concentration between the two CNCs. Empty

polymersomes had a concentration $1.35 \times 10^{12} \pm 7.85 \times 10^{10}$ vesicles mL^{-1}, while iNOS-CNCs had a concentration of $1.72 \times 10^{12} \pm 4.27 \times 10^{10}$ vesicles mL^{-1} and sGC-CNC a concentration of $1.82 \times 10^{12} \pm 8.53 \times 10^{10}$ vesicles mL^{-1} (**Figure 38**B).

Using this method we could also reconfirm the radii, with R_h of 95.5 ± 19 nm for empty polymersomes, 94.95 ± 19 nm for iNOS-CNC and 95.85 ± 17 nm for sGC-CNC(Figure 39). The morphology of iNOS or sGC containing self-assembled nanostructures was observed by TEM, showing spherical shapes with the deflated membrane typical of polymersomes under vacuum (**Figure 38**C-E).

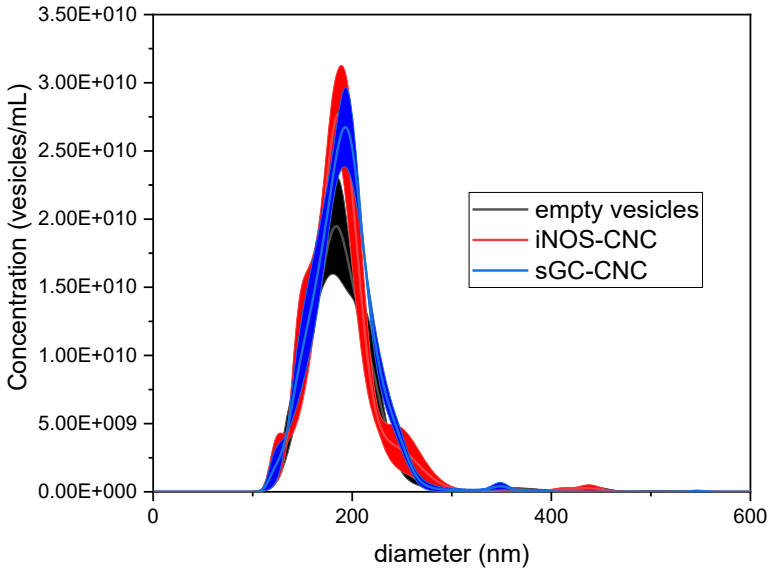

Figure 39 Size vs vesicle concentration (obtained by NTA) for empty vesicles, iNOS-CNC and sGC-CNC, showing the remarkably narrow size dispersivity.

Having determined the concentration of each CNC, next we calculated the encapsulation efficiency as the amount of enzyme encapsulated per compartment. To achieve this, we fluorescently labelled each enzyme. iNOS was labeled with an average of 1 ± 0.3 ATTO488 dye molecules per enzyme while sGC was labeled with an average of 2 ± 0.9 DyLight633 dye molecules per enzymes. Having successfully labeled the enzymes we proceeded to measure fluorescence correlation spectroscopy (FCS) of labelled enzymes and of enzyme-loaded vesicles. This technique allows us to measure differences in diffusion times of fluorescent molecules and

correlate it to the hydrodynamic radius of the molecule/supramolecular structure. The shift to the right of the autocorrelation curves is evidence of an increase of diffusion time (Figure S2A-B), respectively from the free dye to the dye-labelled enzyme and enzyme-loaded vesicle. From the measure diffusion times of enzyme loaded CNC, we confirmed once again the order of magnitude of the hydrodynamic radii: R_h of 94.32 ± 56 nm for iNOS-CNCs and 85.7 ± 33 nm for sGC-CNCs. Similar R_h were also found by fluorescently staining the vesicles' membrane with the hydrophobic BODIPY 630/650 (115 ± 27 nm and 96 ± 37 nm, respectively), confirming again the same size of both CNCs; the small differences are all within the standard deviation.

Finally, brightness measurements, serving to compare the brightness of vesicles and enzymes, allowed us to determined that iNOS CNCs contained 5 ± 4 enzymes per compartment and sGC-CNC contained 3 ± 1 enzymes per compartment. Using a 2-component model, discriminating between enzyme and vesicle signal, we could see that 1% of iNOS was still free in solution after purification, and less than 0.1% of sGC was free in solution following purification, probably due to low unspecific adsorption on the membrane. The encapsulation efficiency, measured by recovering the un-encapsulated enzyme fraction by SEC, was 13% for iNOS and 89% for sGC.

By performing a complete physico-chemical analysis of the polymeric CNC, we confirmed that the CNCs self-assemble into spherical, hollow structures and are not influenced by the presence of OmpF or enzymes in the rehydration buffer, resulting in CNCs with similar polymersome concentrations, vesicle radii and amount of encapsulated enzyme.

5.1.3 CNC activity

The cascade reaction between iNOS and sGC free in solution was first tested using the GTP analog mant-GTP that is transformed by sGC upon NO production into the fluorescent mant-cGMP final cascade product. The reaction proceeded with high activity, which ended in a plateau after 2 minutes (Figure 40), as expected from the high turnover rate of both iNOS and sGC,[119] thus showing that we could follow both reactions by measuring the final product mant-cGMP.

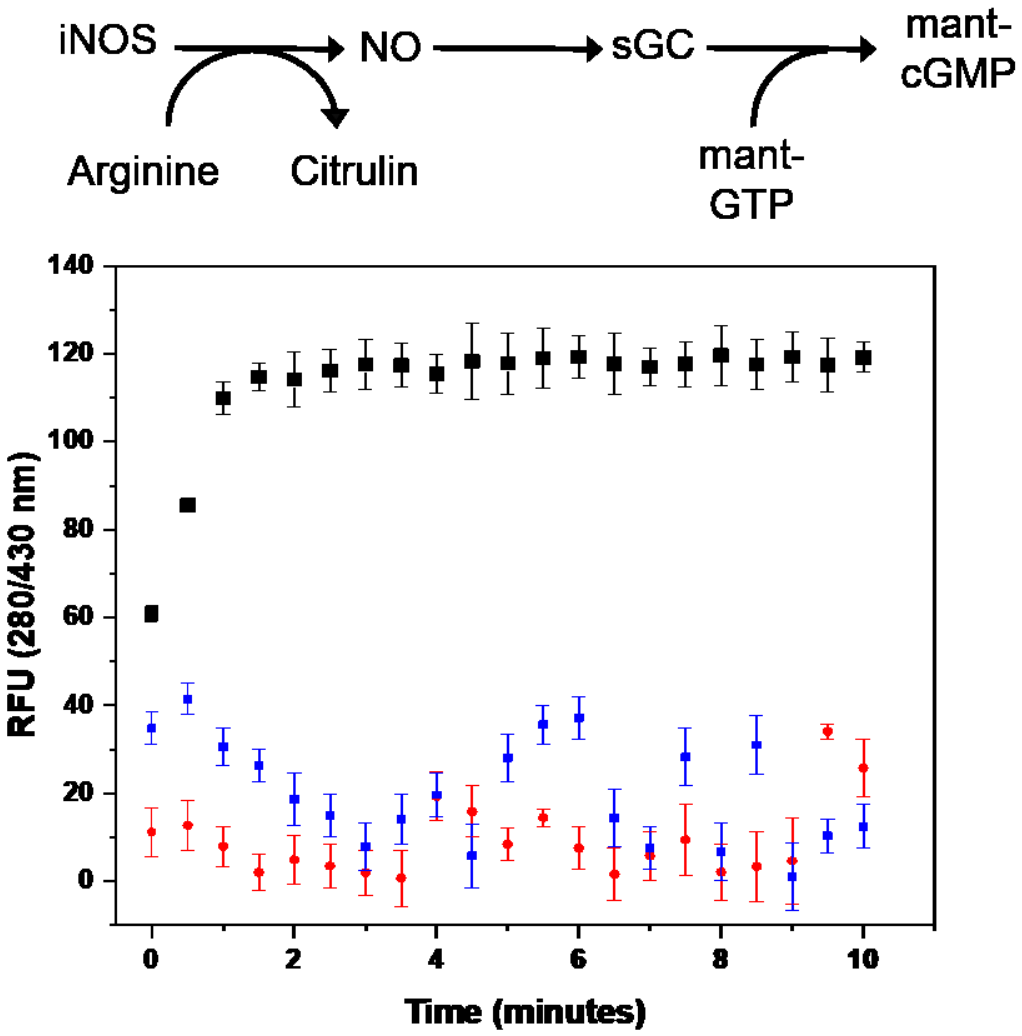

Figure 40 *Reaction scheme and activity of free enzymes in a cascade (black), without NAPDH (blue) and without arginine (red). Values given as mean ± SD, n=3.*

The first enzyme of the cascade, iNOS, was then encapsulated inside polymersomes equipped with OmpF (iNOS-CNC), and its activity compared to iNOS free in solution, by monitoring the fluorogenic reaction between NO and DAF, finding the ratio

$$\frac{Activity_{CNC}}{Activity_{free\ enzyme}}$$

Equation 3

to be 112 ± 47% (Figure 41). A CNC activity equal or higher to that of the free enzyme is not surprising, as it was already shown that encapsulated enzymes could theoretically reach the same or higher activity

than when free in solution thanks to the confinement effect, provided that the diffusion of substrates is not a limiting factor. [116] In this respect, we assume that the diffusion of arginine across OmpF is very fast, as already reported.[120] OmpF-less CNCs show no activity.

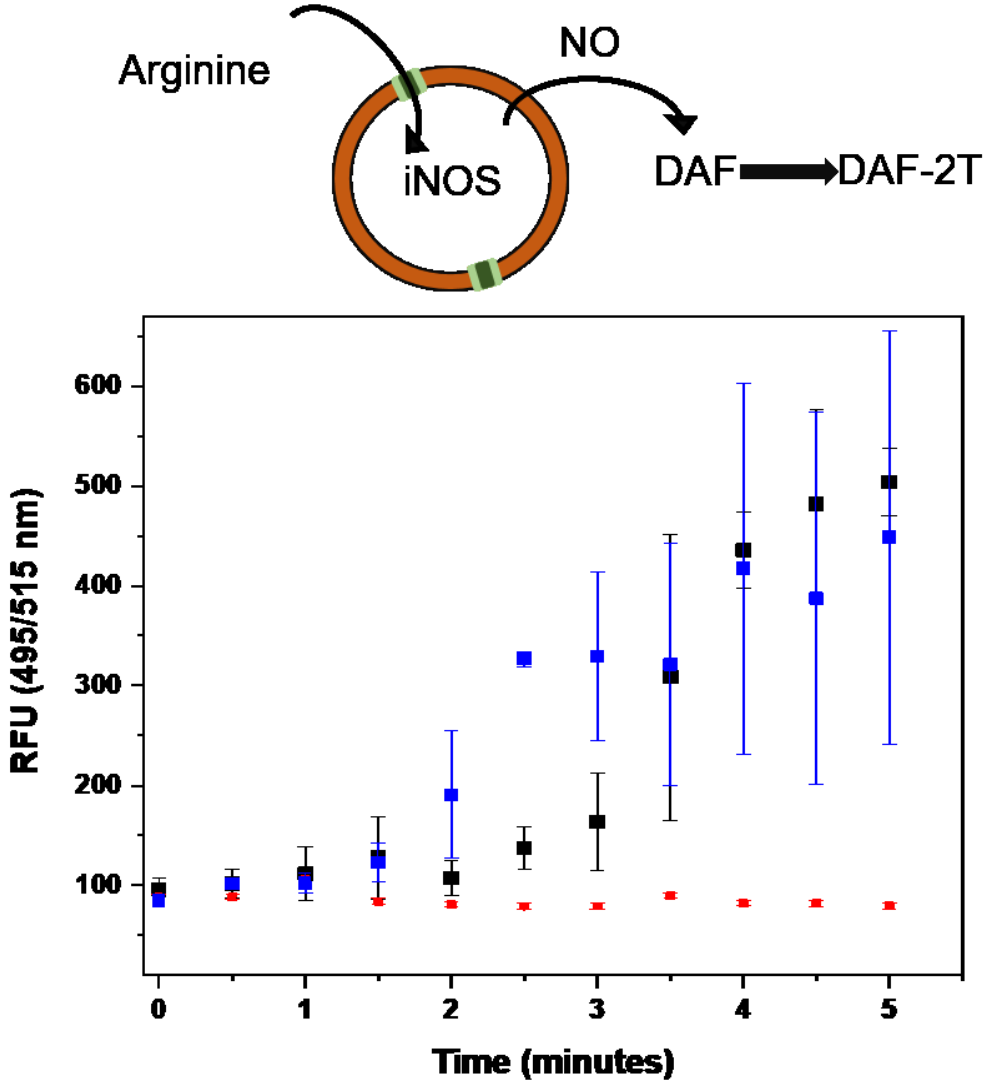

Figure 41 *Reaction scheme and activity of free iNOS (black) iNOS-CNC (blue) and iNOS-CNC without OmpF (red), showing the similar values for both encapsulated and unencapsulated enzymes. Values given as mean ± SD, n=3.*

However, when both iNOS and sGC are encapsulated within their respective CNCs, enzyme activity exhibits a significant decrease. In the timeframe of the unencapsulated cascade (10 minutes), no activity is detected; only after at least 4 hours, we begin to see an appreciable conversion to mant-cGMP, continuing steadily for 12 hours, eventually reaching 49 ± 19 % of the maximal value obtained with the free enzymes. This severe decrease in activity is a limitation due to the diffusion of substrates

across OmpF, which does not affect iNOS-CNC, demonstrated in Figure 4; nor is it dependent on nitric oxide, a small and fast diffusing molecule that is not expected to be hindered by the CNCs' membrane. The main limiting factor must be then ascribed to the diffusion of the substrate of sGC; the devised assay is based on the GTP-derivative mant-GTP (656 Da), whose weight is around the cut-off of OmpF,[121] strengthening the evidence that its bulkiness is the main limiting factor in the overall activity of the CNCs in the cascade (Figure 42). Such behavior reveals a complex scenario, where overall cascade kinetics find a bottleneck in the diffusion of the substrate. To confirm that the limitation was caused by the diffusion across the membrane of the modified GTP, we co-encapsulated mant-GTP together with sGC (inactive, before the presence of NO produced by the iNOS-CNC upstream), this time retained thanks to its extremely slow diffusion across OmpF to the bulk. Doing so yielded a 99 ± 9 % for Equation 3 over the course of 12 hours, but with a completely different kinetic: we observe a fast reaction rate in the first few minutes, which plateaus after 2 hours. At the 4 hours' mark, having consumed the co-encapsulated substrate, the enzyme starts to rely on the external mant-GTP (Figure 5) now diffusing in, as seen in the previous scenario. The diffusion across the CNC membrane is thus confirmed to be the major limiting step for a cascade between CNCs, as already reported for other cascades between CNC.[116]

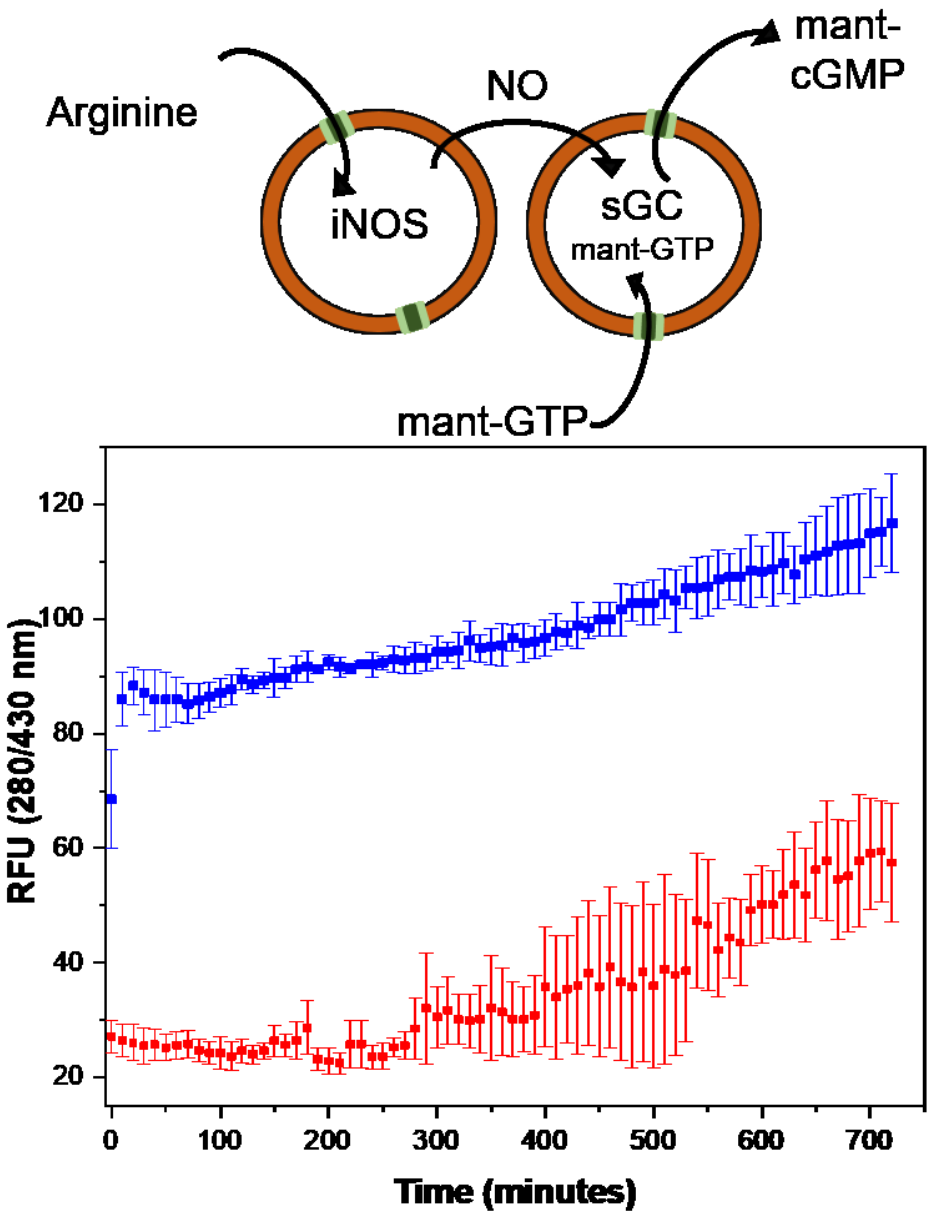

Figure 42 Scheme and activity of the cascade mediated by iNOS-CNC with: sGC-CNC (red) and mant-GTP co-encapsulated with sGC (blue). Values given as mean ± SD, n=3.

We can also exclude that the higher starting signal for co-encapsulated mant-GTP is due to its higher concentration, as no signal was detected with the same system but without the reaction taking place (Figure 43A).

Despite the limitations provided by the interplay between intrinsic CNC features (diffusion across OmpF) and assay-dependent limitations (the substrate's size), we showed that the compartments worked in tandem, and successfully provided the final product cGMP with a slow and constant flow over a long period, akin to the controlled release of drugs. An additional benefit of encapsulation inside CNCs is enzyme resilience: when both free iNOS and sGC were subjected to the same workup and storage conditions as encapsulated enzymes, they lost activity (**Figure 43 A**), while the encapsulated ones were still functional. Enzymes non-specifically adsorbed to the vesicles' outer membrane were also intrinsically unstable and had no catalytic activity (**Figure 43 B**) after workup and storage at 4 °C. The slightly lower signal of **Figure 43 B** would suggest that SEC purification completely removes any free enzyme. Overall, such findings show that any unencapsulated enzyme remaining after the purification would retain no activity by the assay's time.

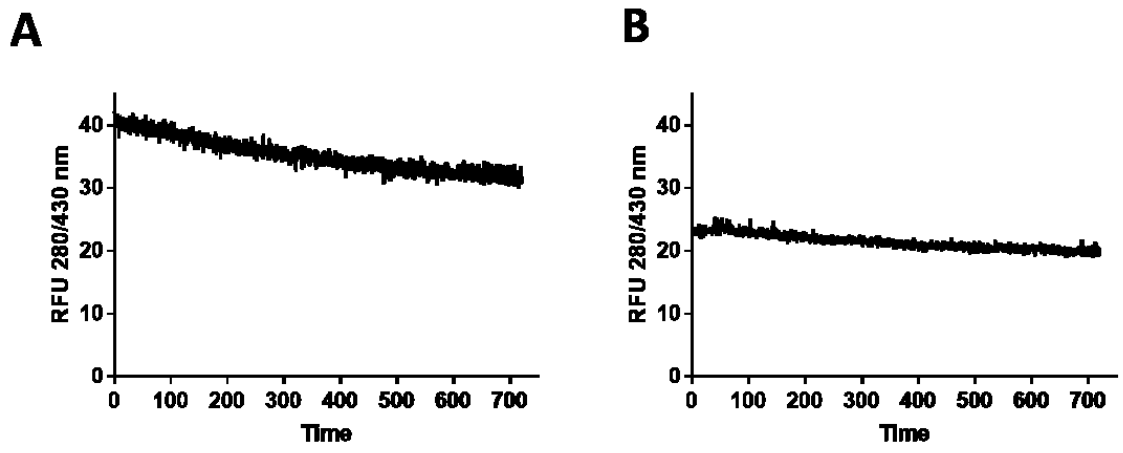

Figure 43 A*: free enzyme activity after being subjected to the same workup of the CNCs, showing their inactivation.* ***B****: activity of free enzymes mixed together with empty vesicles and then purified by SEC. No activity can be observed, meaning that any enzyme unspecifically adsorbed to the outer membrane is inactive.*

5.1.4 Effect on HeLa cells

To this day, CNCs have been used in biological settings as sensors, detoxifying agents, produce or to release/activate prodrugs [38], meaning their effect was parallel to the cell metabolism and had a limited influence on the cell itself, with only one example aimed at complementing defective pathways.[122]

Having shown that a cascade reaction could produce cGMP as a second messenger, we set to study the interaction of our CNCs with live cells, using only the naturally present arginine and GTP substrates and without using mant-GTP, thus overcoming its bulkiness.[115] In nature, the NO/cGMP signaling cascade acts on calcium channels resulting in an increase in free cytoplasmic calcium along with other downstream cellular effects. To determine if our CNCs integrate and function within the cellular metabolism either through extracellular or intracellular signaling, we chose to follow cytoplasmic calcium levels of cells exposed to the CNCs. This was accomplished by monitoring the fluorescence of the calcium-sensitive and cell-permeant Fluo-4-AM dye, added separately from the CNCs, by live cell imaging. Fluo-4-AM is uptaken by the cell and metabolized by esterases so that it is retained for a longer time, and increases its brightness when complexing calcium. PDMS-PMOXA polymersomes, known to be biocompatible [23b, 116], are unspecifically uptaken by cells over the course of hours [23b]; with a cascade that does not require the addition of substrates, but can find them in the culture medium or within the cell, this means that the CNCs exert their activity as soon as they administered. For this reason, we analyzed two scenarios: the short-term effect of CNCs added to cells and the long-term effect after they had been uptaken.

By incubating Atto488- iNOS labeled CNCs and DY633 sGC labeled CNCs together with HeLa cells, we could see that they become internalized starting at 12 hours after administration, thus allowing to discriminate temporarily between extra- and intracellular action. The CNCs appeared to be internalized, thus enabling their intracellular function. (**Figure 44**, **Figure 45**A)

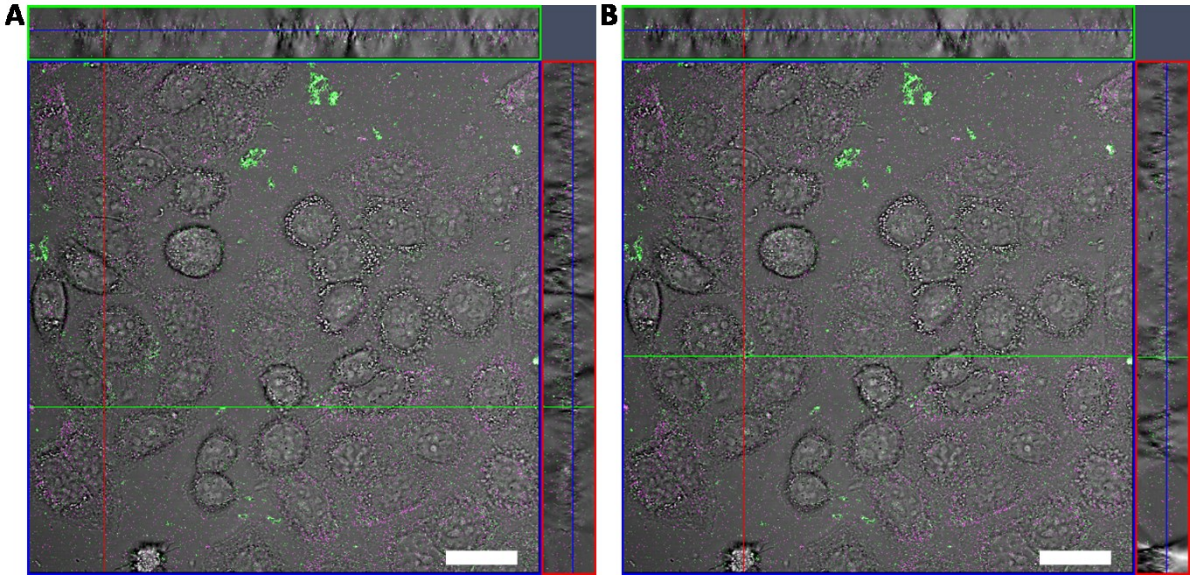

Figure 44 A and B: z-stack orthogonal views, at two different points, of HeLa cells showing the uptaken ATTO-488 iNOS-CNC (green) and DyLight 633 sGC-CNC (purple) within the cells. Scalebar: 10 µm.

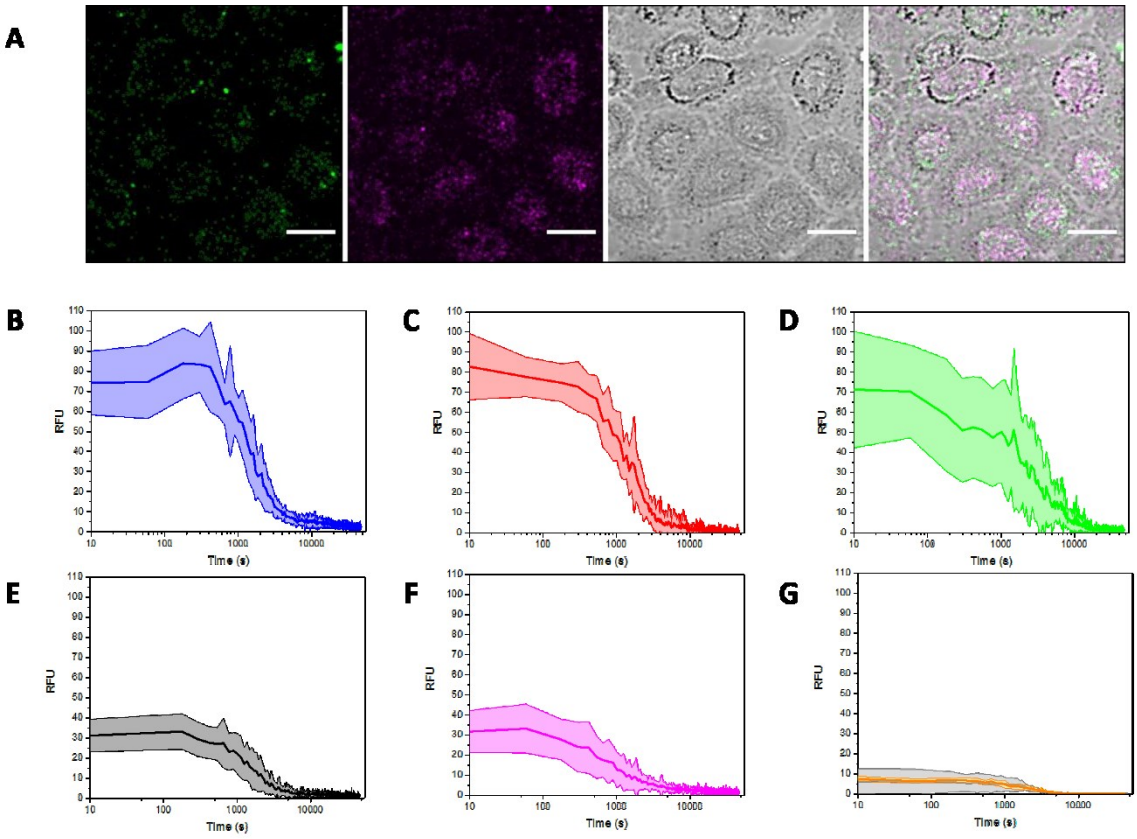

***Figure 45 A**: CLSM micrographs of iNOS-ATTO488-labeled CNCs (green), sGC-DY Light 633-labeled sGC CNCs (purple), HeLa cells (brightfield) and overlay, after 14h of incubation. Scale bar: 10 µm. **B**: intracellular [Ca^{2+}] of HeLa treated iNOS-CNC and sGC-CNC in cell medium. **C**: intracellular [Ca^{2+}] of HeLa treated with NO-donor SNAP and cGMP. **D**: intracellular [Ca^{2+}] of HeLa after the uptake of iNOS- and sGC-CNC. **E**: intracellular [Ca^{2+}] of HeLa treated with iNOS-CNC only. **F**: intracellular [Ca^{2+}] of HeLa treated with sGC-CNC only. **G**: intracellular [Ca^{2+}] of HeLa with no treatment (orange) and intracellular [Ca^{2+}] of HeLa treated with empty polymersomes (grey). Values given as mean ± SD, n=11.*

When the CNCs (1 to 1 CNCs ratios) were added extracellularly to HeLa cell cultures there was a quick increase in fluorescence intensity (<5 minutes) within the cellular cytoplasm indicating that the cascade immediately induced the opening of calcium-specific channels, quickly increasing the intracellular [Ca^{2+}] (**Figure 45**B). This was followed by a slow decrease (2.5 hours) in fluorescence back to resting levels, due to both the decrease in [Ca^{2+}] and eventual excretion of the dye via active transport channels.[123] As a positive control, we added to the cell culture both the NO-donor SNAP and cGMP, *i.e*. directly the molecules derived from the reactions at similar concentrations as would be produced by the CNCs, and

observed a similar increase in [Ca^{2+}] as when the CNCs were added (**Figure 45**C). Since the CNCs, or the reaction products SNAP and cGMP, are added to the cell culture and monitoring of internal [Ca^{2+}] commences within a 5-minute delay, the signaling cascade exerts its effect primarily extracellularly.

To study the intracellular effect of the CNCs on [Ca^{2+}], we incubated the cells in presence of the CNCs for 24 h, followed by rigorous washing of the cells to remove non-uptaken CNCs and loading of the cells with the calcium sensitive Fluo-4-AM dye. Thanks to the slow and constant activity of sGC-CNCs –fueled by iNOS-CNC, even internalized CNCs continued to produce cGMP modulating intracellular [Ca^{2+}] (**Figure 45**D). In fact, they show a very similar fluorescence profile when fresh medium and Fluo-4-AM were subsequently added, after a prior 24h incubation with the CNCs. The similar values obtained for internalized CNCs as for cells measured in presence of externally located CNCs, reveal that they retain their activity for a long time inside the cells, with long-term effects comparable to that of a single exposure.

The addition of only iNOS- or sGC-CNCs showed a much lower activity, suggesting that only one kind of CNC is not enough to increase the calcium-derived fluorescence above a baseline signal (**Figure 45**E and F respectively). A slight increase in fluorescence is indeed observed due to interactions between the iNOS-CNC and native sGC or the sGC-CNC with trace endogenous NO; however, to obtain a complete and effective signaling cascade, both CNCs are required to ensure the quick production of NO and the action on its receptor sGC cause a drastic change in intracellular [Ca^{2+}] levels. Almost no fluorescence was detected for either control untreated cells or cells treated with control empty vesicles (**Figure 45**G).

To compare the rate of change in intracellular [Ca^{2+}] we first normalized the mean fluorescence profiles, thus disregarding the differences in initial [Ca^{2+}], and setting the profile of non-treated cells as the reference over time decrease. It is apparent that SNAP+cGMP treated cells follow a very similar kinetic to that of untreated cells, indicating that intracellular [Ca^{2+}] levels return quickly back to base levels. Uptaken iNOS-CNC+sGC-CNC show an initial rate close to the reference, which then slows down after 3-4h (Figure 46A-B). This second, slower rate of decrease could be due to further downstream intracellular signaling pathways that increase intracellular [Ca^{2+}] with a delay and that cannot be accessed when the CNCs are extracellular. Interestingly, external iNOS-CNC+sGC-CNC and iNOS-CNC treated cells maintain a constant [Ca^{2+}] for 3 hours, then dropping with a similar rate as the reference cells. External sGC-CNC induce a slower rate of Ca^{2+} release than the reference, likely due to the slow

production of cGMP. Such behavior shows clearly that the localization of the CNCs has different effects on the cell physiology, and that they can perform their function at least for 24h after being administered (**Figure 46**).

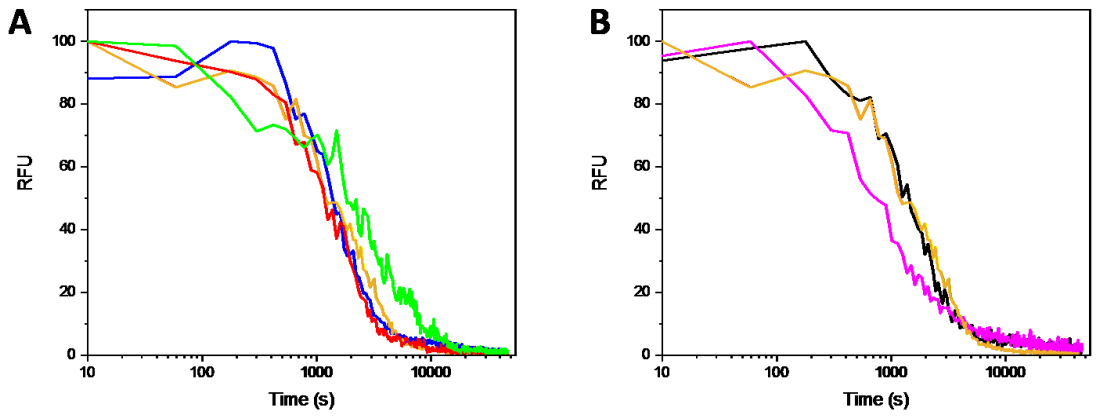

***Figure 46 A**: normalized fluorescence profile of HeLa cells treated with cGMP+SNAP (red), iNOS-CNC + sGC-CNC (blue), uptaken iNOS-CNC + sGC-CNC (green) and untreated (orange). **B**: normalized fluorescence profile of HeLa cells treated with iNOS-CNC (black), sGC-CNC (purple) and untreated (orange).*

The immediate effect observed on cells measured 5 minutes post CNC addition (**Figure 45**) cannot derive from the canonical, well-known effect of cGMP on cGMP-dependent protein kinases (PKG) and cGMP-gated ion channels[124], as those are intracellular pathways. Rather, this must come from the effect of extracellular cGMP on glycine ion channels, inducing activation of calcium ion channels [125], along with the diffusion of NO to cells (which, on the other hand, involves the canonical pathways mentioned before). This is also in line with the fact that HeLa cells usually express a low amount of PKG.[126] On the other hand, the detected intracellular activity should not be due to non-internalized CNCs (as they are removed by washing), but rather to cAMP-activated Ca^{2+} influx, as cyclic nucleotides cGMP and cAMP are known to crosstalk and interact with non-specific targets and, as mentioned, PKG is generally underexpressed in HeLa (**Figure 47**).[124, 127] Overall, these findings suggest that the CNCs not only affect intracellular calcium levels, but also have different protein targets on the cell surface and further downstream proteins within the cytoplasm, resulting in different calcium release rates, depending on the CNC localization.

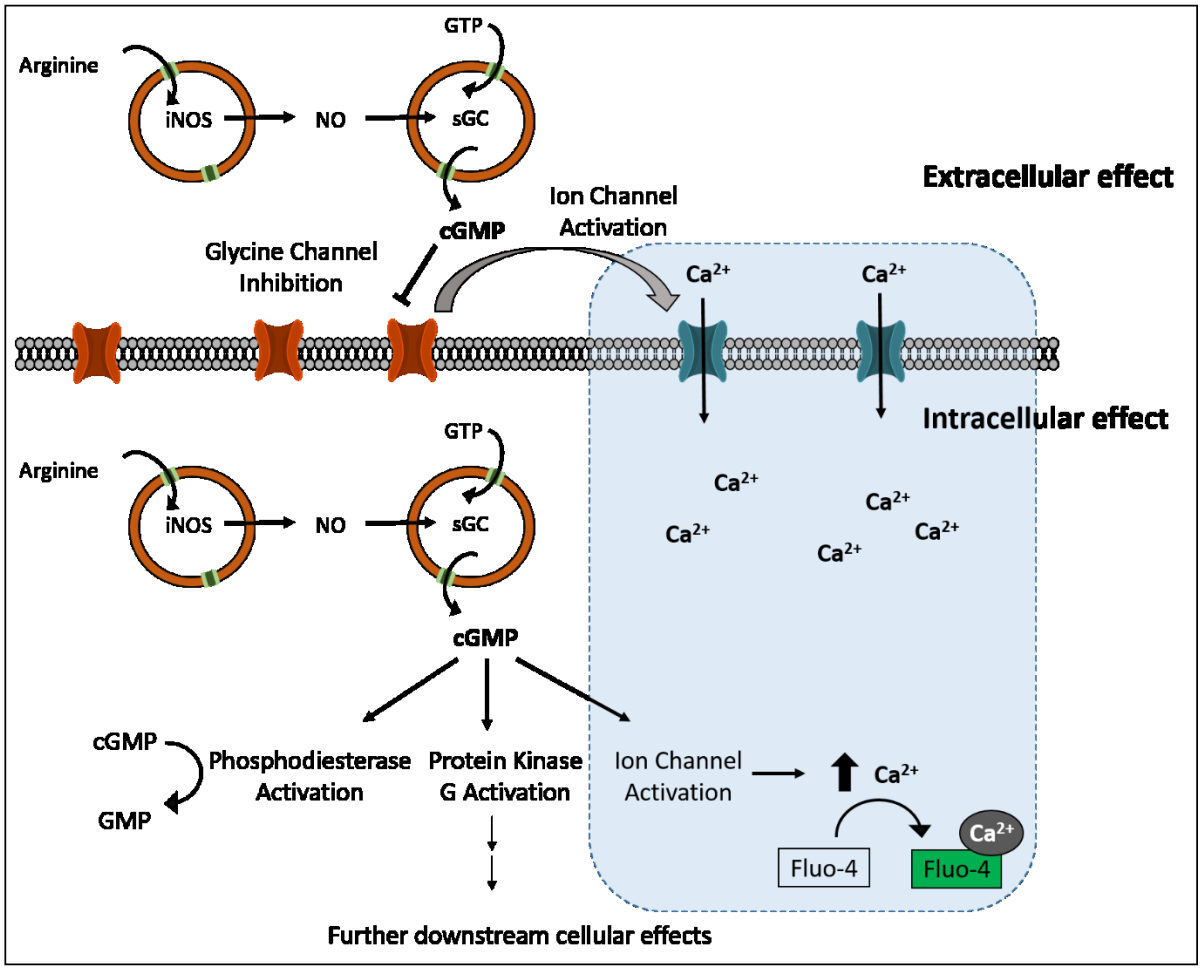

Figure 47 *Mechanism of cell-CNC interaction and possible affected pathways in cells: the CNCs exert their action both extra- and intracellularly, and this can be monitored using the intracellular Ca^{2+} as biomarker.*

5.1.5 Effect on C2C12 cells

Next we analyzed the effect of the CNCs on intracellular [Ca^{2+}] in differentiated C2C12 myocytes, which are more sensitive to calcium levels.[128] In muscle cells, the NO/cGMP signaling cascade results in a complex modulatory effect of [Ca^{2+}], where an increase due to release of stored calcium is first observed followed by a slow depletion.[129] For the positive control, where the NO-donor SNAP and cGMP were used, a high intracellular [Ca^{2+}] concentration was measured (Figure 48A). The CNCs, both freshly added to the medium (Figure 48B) and uptaken CNCs (Figure 48C) showed high initial intracellular [Ca^{2+}] values, marked by higher cellular variability (resulting in greater standard deviation).[130] Furthermore,

the fluorescence signal, resulting from Fluo-4AM complexing intracellular [Ca^{2+}], returned back to baseline levels in a shorter time frame as compared to HeLa cells, indicating a calcium depletion event. Added to the lower resilience of C2C12 cells, with some apoptosis events during imaging, it all hints to the higher susceptibility to calcium levels and derived stress. Such susceptibility plays a role in muscle dystrophy and atrophy (Movie S3).[131] For the negative, no treatment-control, again only a baseline fluorescence was observed (Figure 48D).

Muscle cells are thus more susceptible to the CNC cascade, as cGMP finds more targets, not only in the cell membrane or in the cytoplasm, but also regulates the release of calcium from the sarcoplasmic reticulum.[129a]

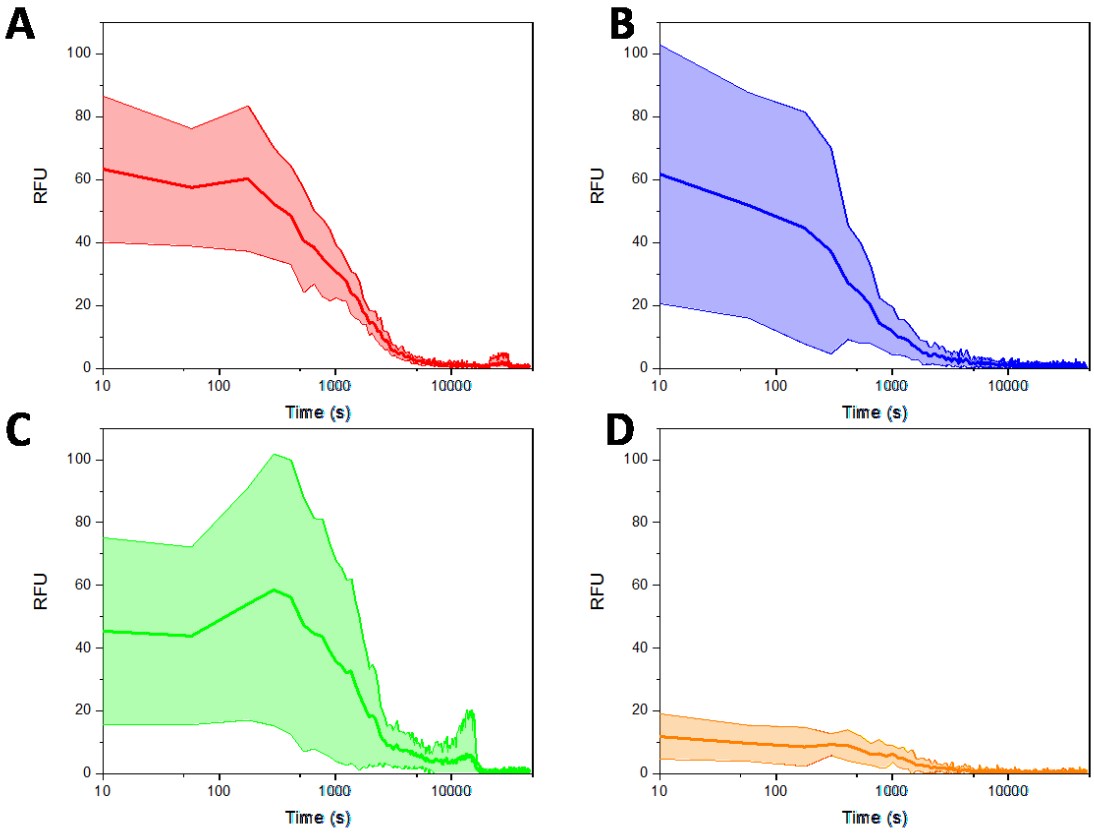

Figure 48 ***A****: intracellular [Ca^{2+}] of C2C12 treated with NO-donor SNAP and cGMP.* ***B****: intracellular [Ca^{2+}] of C2C12 treated iNOS-CNC and sGC-CNC in cell medium.* ***C****: intracellular [Ca^{2+}] of HeLa after the uptake of iNOS- and sGC-CNC.* ***D****: intracellular [Ca^{2+}] of C2C12 with no treatment. Values given as mean ± SD, n=11.*

5.2 Conclusions

Enzymatic cascades between different nanocompartments present both the challenge of communication between compartments and the advantage of increased enzyme stability and modularity. Such potential has only been partially investigated, with very few studies using catalytic nanocompartments as bio-active constructs.

To fill such gap, we designed spatially segregated CNC, supporting cascade reactions in between that mimic sequential reactions between biosystems. First, our enzyme selection (UOX-HRP) allowed us to determine several parameters affecting both cross-membrane and inter-vesicle diffusion and their influence on reaction efficiency. A deep analysis of the factors affecting the overall efficiency indicated the protective role of the compartments, which provide a shield for the encapsulated enzymes, especially important in biological fluids and cell environment. This indicates as limiting factors for the overall reaction the diffusion through the membrane pores inserted into the walls of the compartments and the probability of the product of the first reaction to encounter CNCs containing the second enzyme and reach the encapsulated enzyme molecules for the second step of the cascade. A balance is necessary between the protective role of the nanocompartments and the factors decreasing the efficiency of the cascade reaction for translational applications. The presented study gave many insights on how a two-compartment cascade behaves, compared to ideal conditions. This cascade reaction in separate compartments was been successfully performed in serum and then used to decrease uric acid and H_2O_2 from the cellular milieu as a first step towards medical applications. Additionally, the combination of these enzymes allowed catalytic nanocompartments decrease uric acid and its derived H_2O_2, both involved in various pathologic conditions ranging from gout to oxidative stress. Never had two polymersomes been working in tandem and synergistically with cells to detoxify the cell medium.

In the following study, we presented the first 2-compartment system of this kind ever, where iNOS and sGC operate in unison, as in a native cascade. We encapsulated them and characterized the derived CNCs both physically and functionally. We then studied their *in vitro* activity, as this cascade could use natively present substrates to produce an important bioactive compound, cGMP. The effect of cGMP production was monitored by measuring the intracellular calcium levels over time, showing that the concerted action of both iNOS-CNC and sGC-CNC was needed to elicit the highest response (inducing

calcium influx). These findings demonstrate that CNCs can act on cell physiology, using the substrates already present in the extracellular medium. Additionally, the production of both NO and cGMP paves the way to design more complex nanoassemblies with the potential to induce wide range cell changes, functioning as signaling agents for applications that range from pharmacology to tissue engineering and synthetic biology. Further research will have to elucidate the dose-response behavior to CNCs and confirm the molecular mechanisms of CNC-cell interaction. At first sight, this could look less impressive than an immediate application such as uric acid removal, but it is a very important step in transforming catalytic nanocompartments into real actors of synthetic biology, as they were shown to induce phenotype changes without genetic manipulation, a possible step above traditional synthetic biology techniques.

6 The use of melittin to improve membrane permeability[5]

The systems studied in Chapter 4 both suffered of a decrease in activity due to the difficult diffusion of solutes across OmpF, which was not fully compensated by the advantages of encapsulation. Additionally, it had been shown that the porin could insert in limited numbers (11 per vesicle).[29b] Because of this, we undertook the task of developing a new, agile method for selective permeabilization of PDMS-PMOXA-based membranes, using the natural peptide melittin, known to form pores in biological membranes. We decided to study not only its application, but also to use it as model for the interaction of any membrane-interacting peptide with polymeric membranes, deriving the fundamental molecular factors governing such interaction.

6.1 Introduction

The permeability of porous and stimuli responsive polymer membrane is an intrinsic characteristics of block copolymers that are used for formation of synthetic membranes whereas the selectivity of the membrane is simply based on pore size.[132] In the case of photosensitizer-mediated permeation, the membrane permeability is induced by attachment of a photosensitizer to the polymers that slightly get more hydrophilic under light irradiation.[133] However, all these approaches so far have caused either an irreversible change in the membrane integrity, thus leading to the total release of encapsulated cargo within polymersomes or enable nonspecific exchange between encapsulated cargo within the polymersomes and the environment.

In order to introduce a selective transport of ions/molecules across the synthetic membrane, versatile membrane proteins (e.g. channel proteins and biopores) with specific functionality have been inserted into the synthetic membranes. Membrane protein insertion methods into synthetic membranes (mainly in the form of polymersomes) have similarities to those applied for the lipid membranes (liposomes). Primarily, the reconstitution of membrane proteins into polymersomes have followed two general approaches; (i) spontaneous insertion of protein into polymersomes and

[5] PARTS OF THIS CHAPTER HAVE BEEN PUBLISHED AND ADAPTED WITH PERMISSION FROM:

Belluati, A*.; Mikhalevich, V*.; Yorulmaz Avsar, S.; Daubian, D.; Craciun, I.; Chami, M.; Meier, W. P.; Palivan, C. G., How Do the Properties of Amphiphilic Polymer Membranes Influence the Functional Insertion of Peptide Pores? *Biomacromolecules* 2019.

(ii) addition of protein into detergent stabilized polymersomes and followed by removal detergent by use of biobeads or dialysis.[134] To date, outer membrane protein F (OmpF) [88], aquaporin Z (aqpZ) [135], nucleoside-specific protein (Tsx) [136], ferriochrome-iron receptor (FhuA)[137], glycerol facilitator (GlpF)[138], and alpha hemolysin (αHL)[139] have been reconstituted in the polymersomes whereas αHL [140], aqpZ [141] and the cyclic nucleotide-modulated potassium channel MloK1 have been inserted into planar polymer membrane formed on solid support. Depending on the nature of the proteins that are inserted into the synthetic membranes, they have fine-tuned their permeability to different species. For example, OmpF serves as a molecular sieve, leading to concentration-driven diffusion of the solutes < 600 Da and aqpZ increases the water permeability whereas TsX mediate the specific transport of nucleosides and nucleotides. Despite a successful insertion of different membrane proteins into synthetic membranes with desired permeabilization, the protein-detergent-copolymer interactions make difficult to generalize the membrane protein reconstitution protocols for each membrane forming amphiphilic block copolymers and always need to be taken into account before the desired membrane protein is inserted into the polymer membrane of interest. Moreover, since the membrane proteins possess a particular structure, the cut-off of the permeability obtained from the membrane protein after reconstitution cannot be tuned. Nevertheless, aforementioned drawbacks can be overcome by use of amphipathic (antibiotic) peptides instead of membrane proteins to induce the permeability in the synthetic membranes.

Amphipathic peptides spontaneously insert into natural and synthetic membranes from aqueous solution to form pores (ion channels). [142] Melittin is a model pore forming peptide with 26 amino acids and makes cell membranes permeable by forming pores that cause the rapid loss of ions and small molecules. Melittin exists as a random coil in aqueous solution which undergoes a conformation change from random coil to amphipathic α-helical bent rod, when it comes into contact with the lipid bilayers. [143] Interaction of melittin with the lipid bilayer changes depending on melittin concentration and the composition of the lipid bilayer membranes.[144] As the concentration of melittin increases on the lipid membrane, the melittin undergoes a dynamic reorientation and eventually produces a pore with the diameter of 1.3 nm to 5 nm. Melittin mediated pore formation in the lipid bilayer occurs according to either the barrel-stave or toroidal model.[145] While lipid membranes are used as close mimics of the cell membrane, more recently the field for nanotechnology is shifting towards the use of either hybrid lipid/polymer membranes or completely synthetic ones to overcome the

shortcomings experienced with lipid membranes. To the best of our knowledge, there were no reports on interaction of neither melittin, nor analogue peptides with synthetic membranes and their ability to permeabilize synthetic membranes. Thus, our goal is to investigate the effects of molecular characteristics of amphiphilic block copolymers (e.g. f-ratio, dispersity, and block length) as well as membrane properties (e.g. membrane thickness and membrane curvature) on melittin-synthetic membrane interactions and their roles in membrane permeabilization.

In this present study, we used a library of poly (2-methyl-2-oxazoline)-block-poly (dimethylsiloxane)-block-poly (2-methyl-2-oxazoline) (PMOXAx-PDMSy-PMOXAx) triblock copolymers with different PDMS blocks (y=22, 34, 44, and 56), the dispersity ranging from 1.67 to 2.4 and f-ratios ranging from 0.13 to 0.27 to create the synthetic membranes (polymersomes and supported polymer membranes). Resulting membranes have different membrane thickness. Ellipsometry and cryo-TEM was employed to estimate the membrane thickness of supported polymer membranes and polymersomes, respectively. The interaction of melittin with polymer membranes were investigated by QCM-D and the functionality of inserted melittin in the polymer membrane was assessed via CLSM by recording the changes in fluorescence intensity upon addition of glucose. Additionally, to investigate the effect of membrane curvature on melittin-membrane interactions and membrane permeabilization by melittin, nanometer and micrometer-sized polymer vesicles were prepared by rehydration method. Both DLS and TEM were employed to characterize the nanometer sized polymersomes while micrometer-sized GUVs were monitored by CLSM. The functionality of melittin within the GUVs was assessed by recording the changes in fluorescent intensity of encapsulated dyes whereas its functionality in polymersomes was evaluated by monitoring the catalytic activity. Collectively, our findings support that the insertion of melittin in the synthetic membranes offers a promising approach to permeabilize the stable polymeric membrane, which opens the door for development of new synthetic membrane based-biosensors and enzyme delivery platforms.

6.2 Starting polymer parameters

Four different, already characterized, triblock copolymers were selected for this study, each with different block length, molecular weight, dispersity and f-fraction. In addition, the roughness of their resulting solid-supported planar membranes was measured by AFM, as an indication of the general relative roughness when in tridimensional assemblies (**Table 6**).

Table 6 *Library of amphiphilic triblock copolymers with their respective characteristics: molecular weight (M_n), dispersity (Đ) and f-fraction.*

Code	Block length	M_n (g mol^{-1})	*Đ*	f-fraction	RMS[48] (nm)
$A_3B_{22}A_3$	PMOXA$_3$-PDMS$_{22}$-PMOXA$_3$	2274[87]	1.75[87]	0.22[87]	0.47 ± 0.14
$A_6B_{34}A_6$	PMOXA$_6$-PDMS$_{34}$-PMOXA$_6$	3672[87]	1.67[87]	0.27[87]	0.69 ± 0.04
$A_6B_{44}A_6$	PMOXA$_6$-PDMS$_{44}$-PMOXA$_6$	4412[87]	1.71[87]	0.23[87]	0.45 ± 0.16
$A_5B_{56}A_5$	PMOXA$_5$-PDMS$_{56}$-PMOXA$_5$	6662[146]	2.4[146]	0.13[146]	0.96 ± 0.32

6.3 Parameters influencing melittin insertion

6.3.1 Membrane thickness and insertion technique

In order to elucidate the molecular parameters affecting the functional insertion of melittin, for example the curvature of the membrane, and to estimate the number of pores/membrane we used vesicular assemblies (polymersomes and giant unilamellar vesicles, GUVs). We first selected GUVs, as their size is analogous to the cell size and thus resemble the curved membranes melittin encounters in nature and are known to be impermeable to most hydrophilic molecules.[147] Furthermore, our experimental design allowed us to determine the size of the pores via CLSM, since melittin does not have a defined pore size as compared to other pores, e.g. α-haemolysin or as OmpF [148]. The diameter of the melittin pore can vary depending on how many peptide monomers assemble within the same pore.[149]

First, we confirmed the interaction of fluorescently labelled-melittin with GUVs by CLSM (Figure 49).

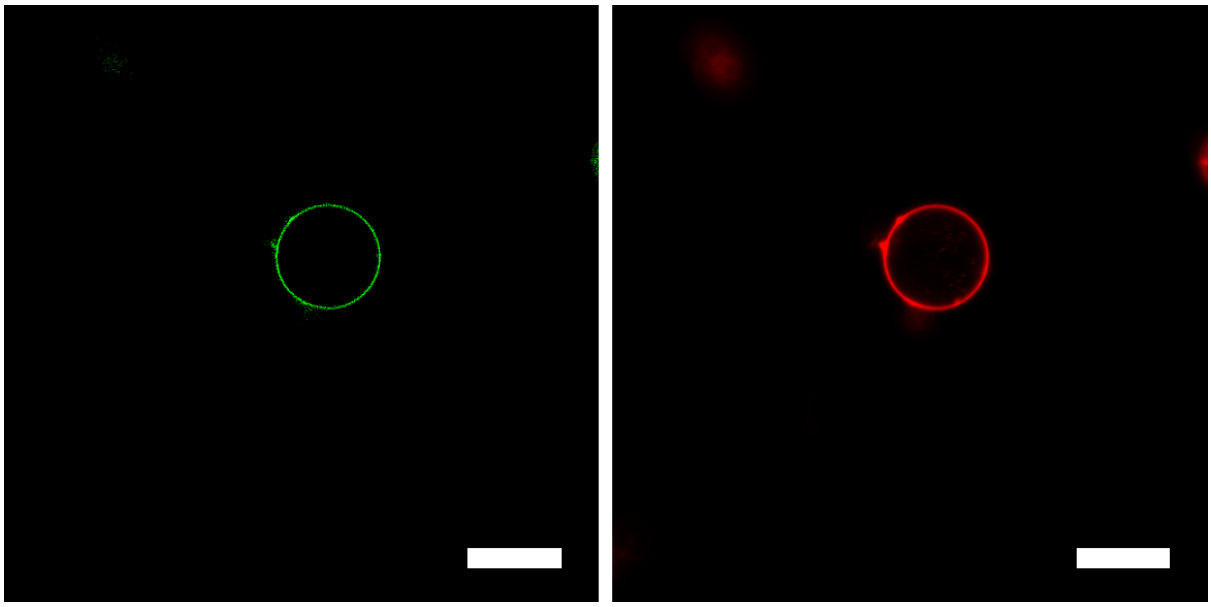

Figure 49 *CLSM micrographs of GUVs FITC-melittin GUV. Green: FITC. Red: BODIPY 630/650. Scalebar: 5 µm.*

In this respect, we formed melittin-GUVs by different procedures: I) co-drying melittin with the polymer followed by self-assembly via rehydration (co-dried), II) addition of melittin to the rehydration buffer used for self-assembly of GUVs (in buffer) and III) addition of melittin to pre-formed vesicles (*ex post*). Fluorophore molecules of increasing molecular weights were added in the surrounding environment of melittin-GUVs and their diffusion into the cavity of the vesicles was determined, to evaluate the difference in the overall percentage of permeabilized vesicles upon functional insertion of melittin, as a function of membrane thickness and the three insertion approaches mentioned above. In addition, an interesting molecular aspect we explored was to establish whether the size of the GUVs play a role in the functional insertion of melittin, knowing that GUVs formed by film rehydration have a size dispersion.

When melittin was co-dried with the block copolymers and then self-assembled by rehydration, the peptide was able to interact with the polymer during the self-assembly process. This resulted in a functional insertion even for the thickest polymer membrane of $A_5B_{56}A_5$ (11.5 nm) with more than 80% permeability for molecules with sizes up to R_h = 0.97 nm (ATTO 488 NHS ester) (Figure 50A). Permeabilization around R_h 1.4 nm (4000 Da) molecules was substantial (70%) for all membranes, but only the thinnest membrane showed an acceptable permeabilization (44%) towards the larger R_h 2.3

nm molecules, meaning that the formation of pores that can accommodate the passage of molecules with R_h above 1 nm begins to be hindered for membrane thicknesses above 6 nm.

Addition of co-dried melittin or to rehydration buffer resulted in a noticeable decrease in the permeabilization of the melittin-GUVs assembly. Molecules with R_h above 0.5 nm were able to diffuse only through $A_3B_{22}A_3$ and $A_6B_{34}A_6$ membranes (6.5 to 9 nm thickness) (Figure 50B), while for $A_5B_{56}A_5$ only 40% of the GUVs had large enough pores to allow passage of R_h 0.5 nm molecules.

When melittin was added ex post (to formed vesicle) to test spontaneous insertion, only the thinnest membranes showed permeabilization, after 1 h incubation, above 70% for molecules with molecular weights of 4000 Da. For membranes with thicknesses above 9 nm, only 10% or less of the GUVs contained functional pores with a radius of up to 0.65 nm that did not increase in size over time (Figure 50C).

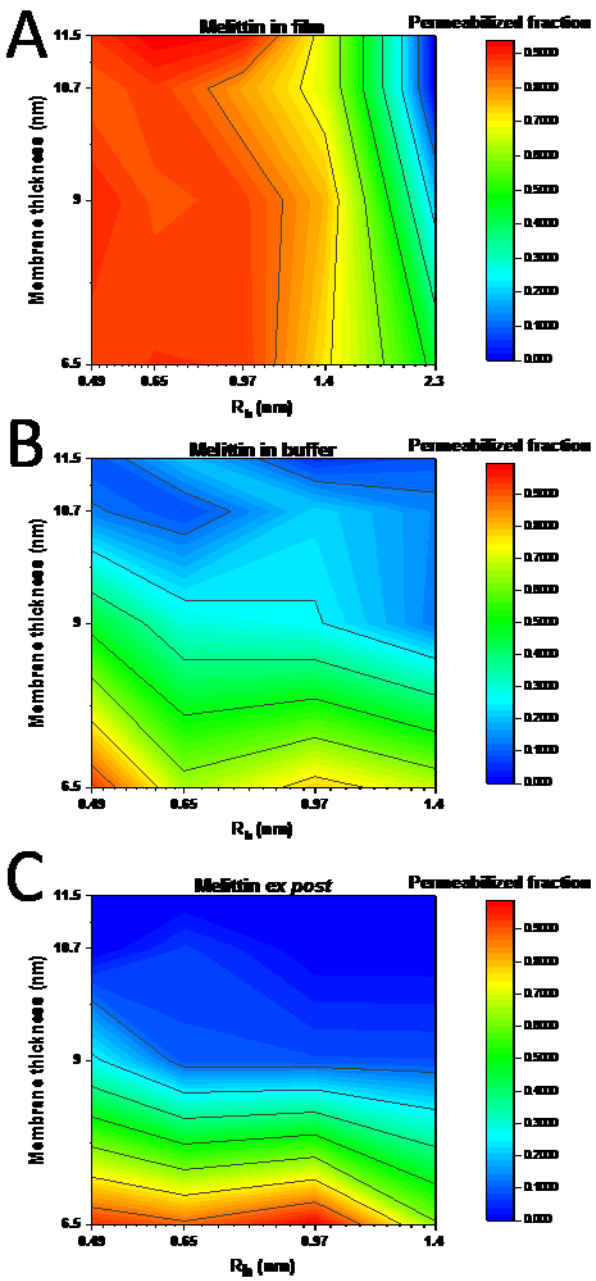

Figure 50 *Contour graphs of relative GUV permeabilization, plotted as hydrodynamic radius R_h vs membrane thickness when melittin is co-dried with the film (**A**), added to the rehydration buffer (**B**) or added to the already-formed vesicles (**C**).*

The ability of melittin to insert and form pores strongly depends on its capability to interact strongly enough with the membrane and eventually change its orientation parallel to the polymer chains, thus allowing the formation of the pore.[150] As PMOXA-*b*-PDMS-*b*-PMOXA membranes are more stable yet thicker than lipid membranes[151], our results indicate that the precise moment of melittin addition is

crucial, because the insertion becomes more strenuous the later melittin comes into contact with the polymer chains, during the self-assembly process. We can thus state that the size of the pore, i.e. its stability, follows a distribution that depends on the membrane thickness and the stage at which melittin was added during their possible interaction.

Several pore sizes have been reported for melittin; in our case, the pore radius varied between 0.49 nm, smaller than the lower limit of about 1.3 nm reported in lipids by dye leakage assay and simulations [152], to a maximum of 2.3 nm, which is in line with the maximum size reported by neutron and X-ray diffraction.[145b, 149b] 1.3 nm is the minimal reported size for a stable melittin pore insertion in lipid membranes; from our results, one possibility could be that, when only molecules smaller than 1.3 nm can diffuse through, melittin only perturbs the membrane, rather than forming stable pores, as it was reported for liposomes with diluted melittin.[149b] Membrane perturbations and transient pores in liposomes, classically, have only been shown to allow the passage of ions, blocking the passage of glucose as well [149b, 153]; however, recent studies on liposomes suggest that melittin and related peptides form transient pores that enable molecules below 1 nm radius to diffuse through the membrane.[154] While the formation of transient pores is the most likely explanation for the passage of molecules with $0.40<R_h<1$ nm, we cannot exclude that stable pores were formed, where melittin either organized into narrower toroidal pores or formed barrel-stave pores, which are by their nature smaller in radius.[145b, 155]

6.3.2 Dependence of melittin insertion on curvature

The permeabilizing ability of melittin has been shown to depend on the curvature of the lipid membranes [144b, 156] with a mechanism favored by positive curvature (*i.e.* outwards). The addition of melittin to pre-formed planar membranes or GUVs (Figure 51A and B) resulted in different permeabilization outcomes, with the planar membranes not favoring functional insertion. We thus postulated that the interaction of melittin with the membrane is not the only phenomenon affecting the insertion and the membrane curvature should be considered too.

We selected sulforhodamine B (SRB, R_h 0.65 nm) as a model molecule representative for the size range of small biomolecules and found that, when measuring the size distribution of the GUVs with melittin added ex post, those permeabilized with SRB had radii 1.5 to 3 times smaller than the empty,

non-permeabilized GUVs, which means that membranes with smaller radius -higher curvature- favor melittin insertion and permeabilization (Figure 51C).

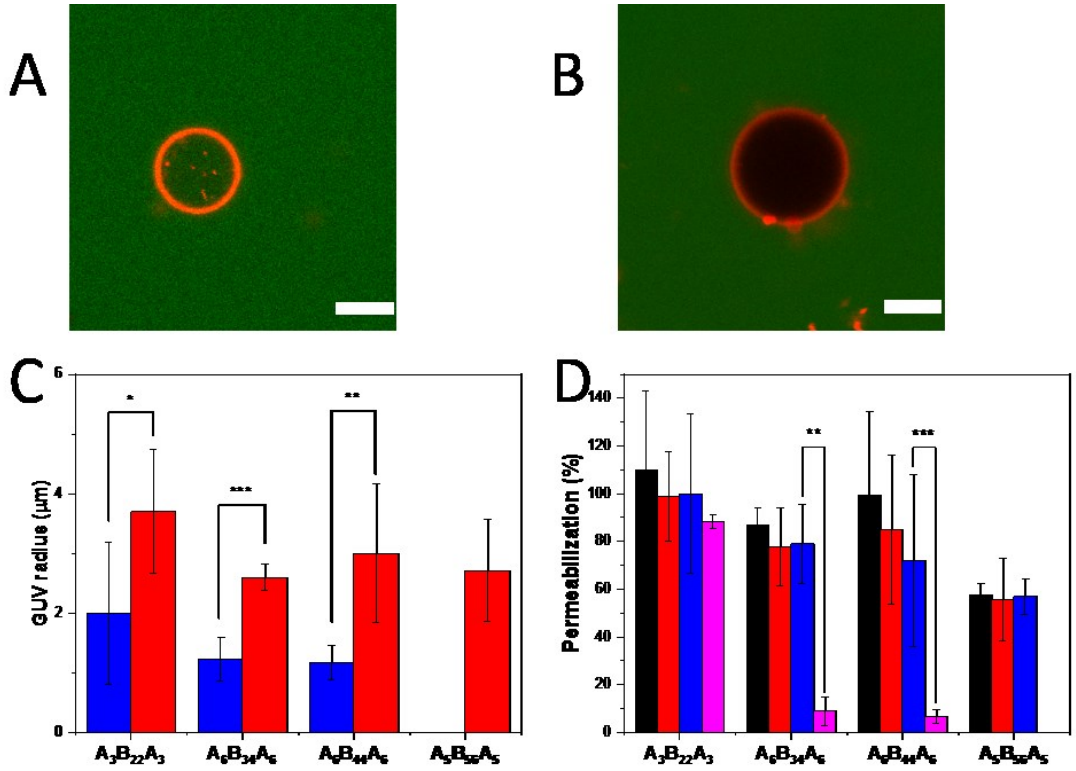

Figure 51 *An $A_3B_{22}A_3$ ATTO488-filled GUV (**A**). An empty $A_3B_{22}A_3$ GUV, with higher radius than the filled one (**B**). Average diameter of permeabilized (blue) and unpermeabilized (red) GUVs (**C**). Percentage of permeabilized vesicles as function of their average radius: ~30 nm (black), ~45 nm (red), ~80 nm (blue), >0.5 µm (GUVs, magenta) (**D**). No permeabilization was observed for $A_5B_{56}A_5$ GUVs. Scale bar: 5 µm. Error bars given as ± SD, n=30 for GUVs (single vesicles), n=3 (replicates) for polymersomes. Significance levels: p<0.5 (*), p<0.01 (**), p<0.001 (***).*

Melittin co-dried or in the rehydration buffer did not result in a significant size difference, suggesting in this case that the functional insertion of melittin is not dependent on curvature, if it occurs while the membrane is not fully formed yet, and that melittin does not influence significantly the self-assembly process (Figure 52).

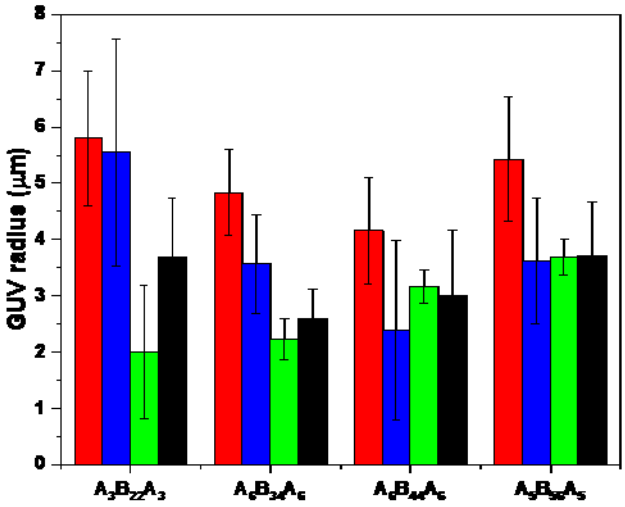

Figure 52 *Radii of GUVs unpermeabilized, melittin in film (red), permeabilized, melittin in film (blue), unpermeabilized, melittin in buffer (green), permeabilized, melittin in buffer (black). As no appreciable difference can be observed, melittin does not change the radius of vesicles. Error bars given as ± SD, n = 3*

To further investigate our hypothesis regarding the membrane curvature dependence, we produced polymersomes. The triblock copolymer $A_3B_{22}A_3$ was able to form hollow-sphere vesicles as well, with a ρ-factor of 1.01, determined by DLS and SLS (Figure 53, Figure 54).

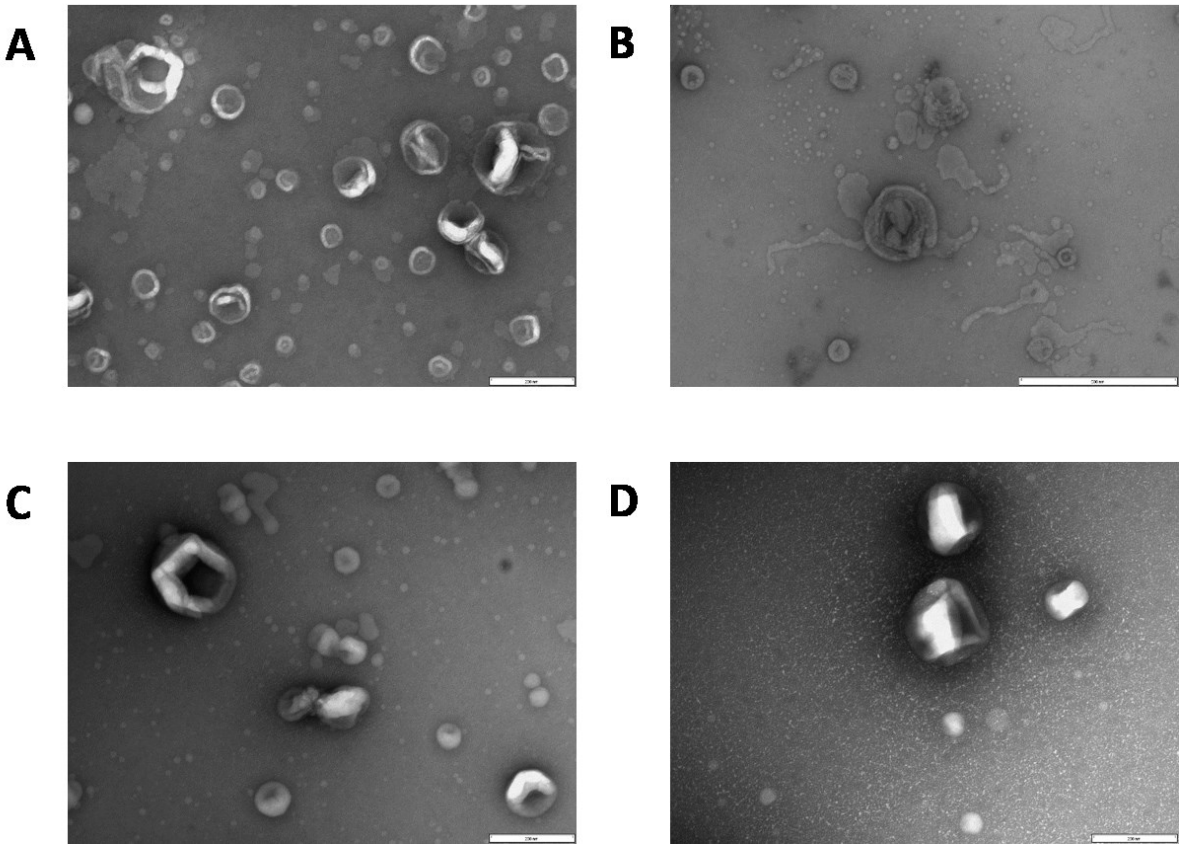

Figure 53 *TEM micrographs of polymersomes.* ***A****:* $A_3B_{22}B_3$. ***B****:* $A_6B_{34}B_6$. ***C****:* $A_6B_{44}B_6$. ***D****:* $A_5B_{56}B_5$. *Scalebar: 200 nm.*

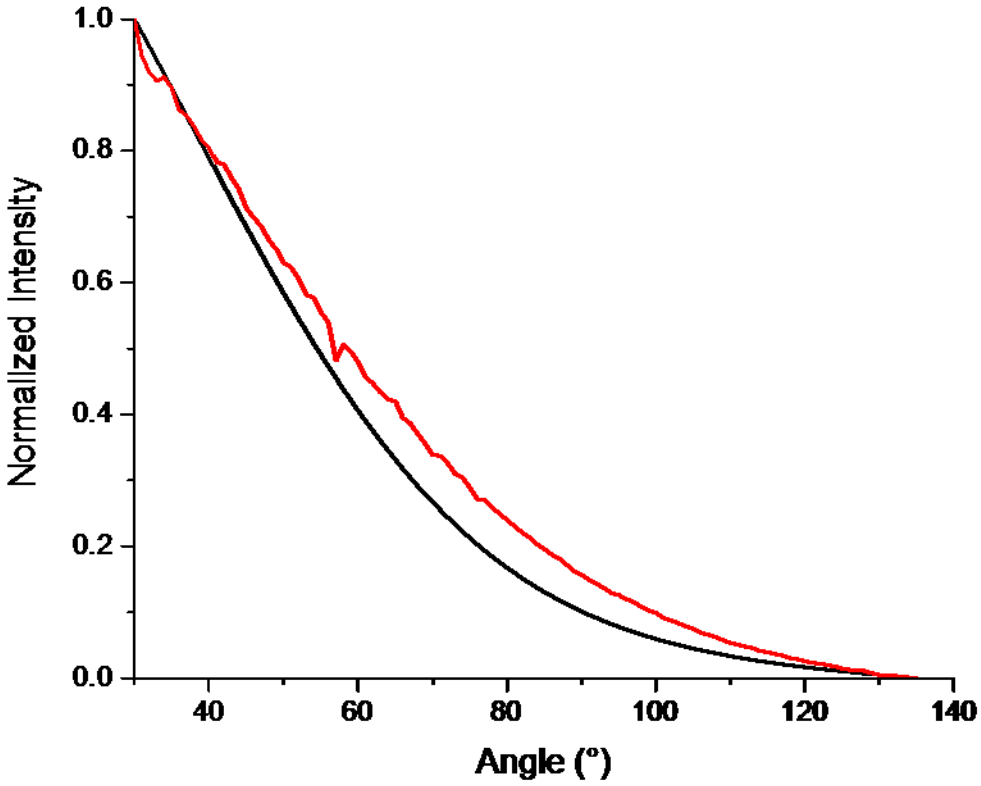

Figure 54 *MIE plot (SLS) for $A_3B_{22}B_3$ (red) and simulated R=125 nm (black), angle dependency.*

The triblock copolymers $A_6B_{34}A_6$, $A_6B_{44}A_6$ and $A_5B_{56}A_5$ were already known to form them, and had already been characterized in size and membrane thickness, the latter further confirmed by cryo-TEM measurements (Figure 55, Table 7).[69, 116, 146]

The vesicles were produced and a ρ-factor ≈ 1 (ratio between R_g and R_h) confirmed that $A_3B_{22}A_3$ could form nanometric vesicles (ρ-factor 1.01), as it was previously shown for the other polymers as well.[69, 116, 146] TEM confirmed that the assemblies were vesicles (Figure S14). The extrusion at different size cut-offs, albeit with high variation, showed a trend in line with the extrusion sizes (Figure 56).

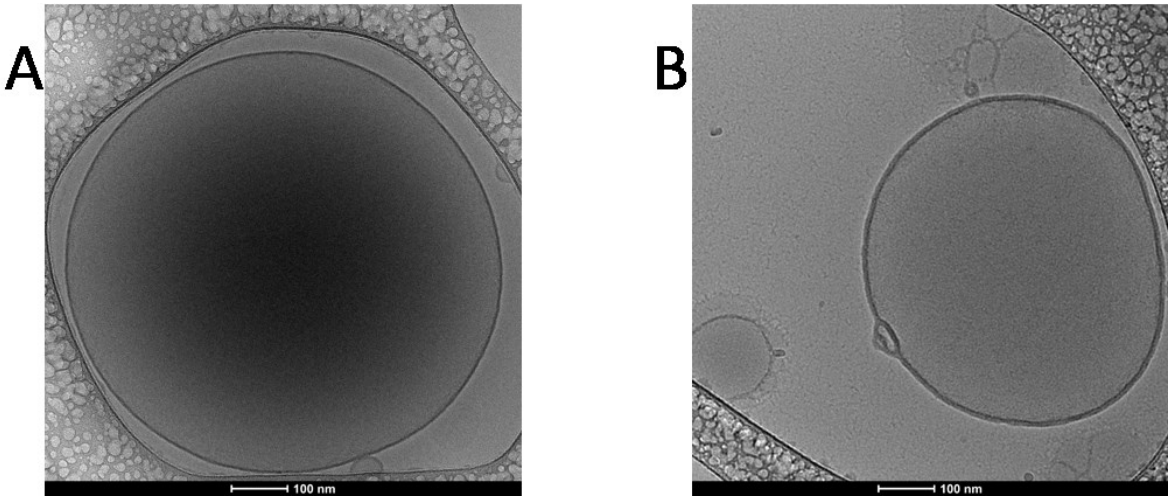

Figure 55 *Cryo-TEM micrographs of GUVs and polymersomes.* ***A****:* $A_3B_{22}A_3$. ***B****:* $A_5B_{56}A_5$.

Table 7 *Vesicular membrane thickness determined by Cryo-TEM.*

Code	**Vesicle membrane thickness (nm)**
$A_3B_{22}A_3$	6.6 ± 0.6
$A_6B_{34}A_6$	9.2 ± 0.5 [95]
$A_6B_{44}A_6$	10.7 ± 0.7 [95]
$A_5B_{56}A_5$	11.5 ± 0.9

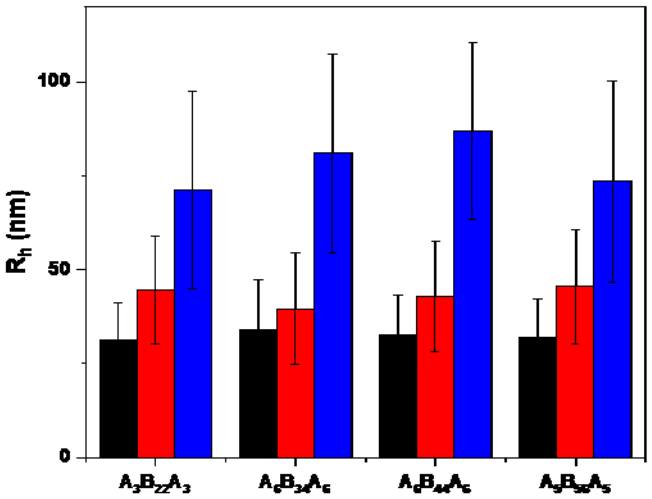

Figure 56 *R_h of polymersomes, after extrusion at 50 nm (black), 100 nm (red), 200 nm (blue).*

We encapsulated SRB within the polymersomes at self-quenching concentration and evaluated its release after addition of melittin to the pre-formed polymersomes, increasing its fluorescence due to dilution (Figure 52), verified that sucrose used to form GUVs does not perturb the membrane stability (Figure 57) and studied the effect of increased membrane curvature by decreasing their radii.

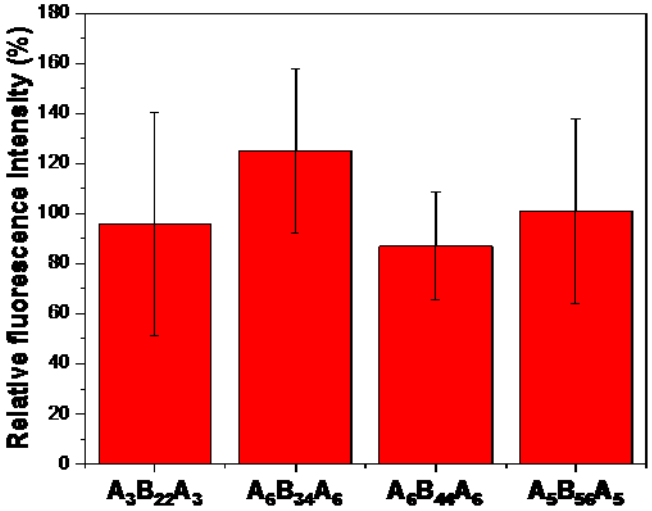

Figure 57 *Relative fluorescence of SRB-filled polymersomes in PBS to polymersomes in sucrose. 100% intensity means no change in fluorescence.*

The permeabilization percentage, for polymersomes with a R_h of 120-130 nm, was between 90% and 100% for $A_3B_{22}A_3$. Interestingly, for $A_6B_{34}A_6$ and $A_6B_{44}A_6$ that showed at most 10% permeabilization in GUVs, in the smaller polymersomes with higher curvature permeabilization increased to 70% and 65% respectively. Moreover, $A_5B_{56}A_5$ which could not be permeabilized when GUVs were formed, in the case of small $A_5B_{56}A_5$ polymersomes 57% permeabilization could be attained. However, further extrusion to smaller average radii (circa 45 and 30 nm) did not significantly increase the permeabilization process (Figure 51D). With a passive, gradient-driven diffusion through the pore, there is no difference between SRB "entering into" (GUV assay) and "being released from" (dye leakage assay in polymersomes), thus allowing us to compare the effect of different curvatures even though the experimental setups are different.

6.4 Quantification of membrane-associated melittin

FITC-melittin was used to quantify the amount of peptide monomers per polymersome by fluorescence correlation spectroscopy, FCS. Melittin was inserted by the approaches presented above: I) co-drying with the polymers and rehydration (co-dried), II) addition to the rehydration buffer (in buffer) and III) addition to pre-formed polymersomes (ex post): the brightness of single vesicles was compared to that of peptides in solution. When melittin was co-dried with the copolymer prior to their rehydration and self-assembly process, the highest number of peptide monomers/polymersome (213 ± 23) was obtained with $A_3B_{22}A_3$ copolymers, while the lowest number (95 ± 2) was determined for $A_6B_{44}A_6$ copolymers. A similar trend was obtained when melittin was added in the rehydration buffer, prior to the self-assembly process, only with slightly lower number of monomers/vesicle (182 ± 27 for $A_3B_{22}A_3$ to 94 ± 19 for $A_5B_{56}A_5$) (Figure 58A). When melittin was added to the pre-formed polymersomes, the number of monomers decreases with the decrease of vesicle size (e.g. from 47 ± 14 to 25 ± 10 for $A_3B_{22}A_3$), which is easily explained by the smaller polymersome surface (Figure 58B). The emerging trend appears to be that, the earlier melittin is added, for example co-dried vs in buffer vs *ex post*, the more it is incorporated into the membrane, as the membrane is less stable and can accommodate more easily the peptide.

However, the surface density of the melittin monomer is not sufficient to explain its interaction with polymer membranes, since it does not consider the molecular features of block copolymers (dispersity

and f-ratio) and surface roughness of resulting polymer membranes. For example, dispersity of the copolymers affects the interaction of melittin with polymer that is with shorter chains whilst the f ratio contributes to the electrostatic interactions between the polymer membrane and melittin. In addition, higher roughness of the membrane means a larger interface for the melittin interaction. Therefore, by considering the molecular characteristics of block copolymers, surface roughness of the resulting polymer membranes as well as melittin surface density, we calculated the volumetric density (ρ_{eff}) of melittin on supported polymer membranes, considering a parallelepiped-shaped box, using the equation:

$$\rho_{eff} = \frac{\sigma \times f \times Đ}{RMS}$$

Equation 4

Where ρ_{eff} is volumetric density of melittin, σ is the surface density of melittin, f is the ratio between the molar mass of the hydrophilic block and total molar mass of the block copolymer, Đ is the dispersity of the block copolymer, defined as the ratio of the weight to number average molar masses, and RMS is the root mean square obtained from AFM measurements.[48]

This resulted in a description of interface interaction between the polymer membrane and peptide, indicating how easy the peptide interacts with a synthetic membrane. If the interaction between melittin and the membrane is based on the membrane characteristics, it also has an influence on the ability of the peptide to stably insert within the polymer membrane. The relationship between ρ_{eff} and membrane thickness (θ) shows an exponential decay, equal to:

$$\rho_{eff} = 6.20 \times e^{0.03(\frac{-\theta}{1.11})}$$

Equation 5

Where Θ is the membrane thickness in nm. Using the membrane thickness measured by Cryo-TEM (Table 3, Figure S11) and we assumed the same membrane roughness as measured with AFM (since the membrane cannot be smooth on a vesicle). We could observe an inversely proportional dependence on thickness for ρ_{eff}, showing that our proposed model holds true for polymersomes (Figure 58C and D). When looking at melittin insertion according to the curvature, we could see that, when the surface density increased (smaller radius, thus higher curvature), the decay was exponential and faster, again confirming the importance of curvature for the insertion (Figure 58D). Additionally,

the interaction and adsorption of melittin is favored for membranes with a higher roughness (higher surface area), whereas melittin insertion is favored for membranes with a lower thickness (ease of penetration).

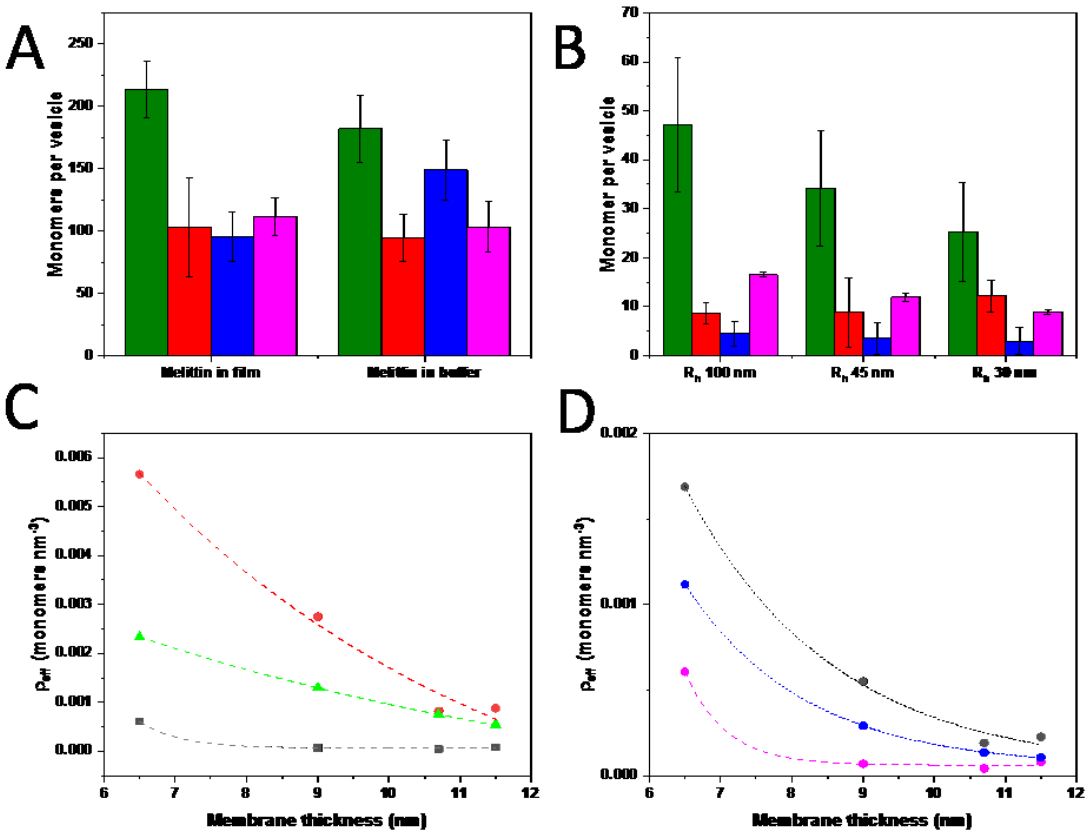

Figure 58 *Number of melittin monomers when melittin is added, either co-dried or in the rehydration buffer, to $A_3B_{22}A_3$ (green), $A_6B_{34}A_6$ (red), $A_6B_{44}A_6$ (blue) and $A_5B_{56}A_5$ (magenta)* ***A****. Number of melittin monomers when melittin is added to pre-formed vesicles (ex post) at different R_h, to: $A_3B_{22}A_3$ (green), $A_6B_{34}A_6$ (red), $A_6B_{44}A_6$ (blue) and $A_5B_{56}A_5$ (magenta)* ***B****. ρ_{eff} dependence of melittin on membranes thickness added in film (red), in buffer (green) and ex post (R_h 100 nm) (grey)* ***C****. ρ_{eff} dependence of melittin on membrane thickness added ex post at R_h 100 nm (magenta), R_h 45 nm (blue) and R_h 30 nm (grey)* ***D****. Error bars given as ± SD, n = 30.*

If we consider the surface density of melittin measured on planar membranes and extrapolate it to the surface density on a model vesicle with a radius 100 nm, we should obtain a melittin density between 1800 times (for $A_3B_{22}A_3$) to 10000 times (for $A_6B_{44}A_4$) higher than what we measured with FCS.[48] We can thus conclude, thanks to the discrepancy between surface density and permeabilization efficiency between planar membranes and polymersomes that the interaction of melittin and its ability to form pores is quantitatively different depending on the curvature.

6.4.1 Pore number estimate

We can only make estimations regarding the melittin pores per vesicle, as we could not take into account their structure: in this case, melittin ranged from 1 to 15 pores per vesicle depending on radius (ex post to preformed vesicles), while melittin co-dried reaches up to 71 pores per vesicle. Extrapolating these calculations for GUVs, $A_3B_{22}A_3$ would reach more than 350 pores per GUV, while the thicker $A_6B_{34}A_6$ and $A_6B_{44}A_6$ have less than 50 per GUV (**Figure 59**).Melittin pores are reported to be composed by 3 to 9 monomers[157]; if we assume a tetrameric pore, with minimal size 1.3 nm, enough for SRB [149c], we can estimate the maximal number of pores per vesicle, knowing the number of monomers per vesicle m_v

$$n_{max} = \frac{m_v}{4}$$

Equation 6

Which we can correct for the permeabilized fraction f, indicating how many of these monomers on a vesicle are actually in the correct conformation

$$n_{corr} = n \times f$$

Equation 7

Knowing the mean R_h allows us to build a linear regression curve to estimate the number of functional pores of a GUV, ranging from 71 ± 7 for melittin added in film to $A_3B_{22}A_3$ to 5 ± 1 for melittin *ex post* 1.5 in $A_6B_{44}A_6$, which is in the same order of magnitude of what reported in the literature with melittin and related peptides [158]. (**Figure 59** A) When melittin is added *ex post*, the number of pores decreases with the decrease of vesicle size (from 15 to 1 pore), since melittin has to spread among more vesicles (**Figure 59** B).

Assuming that polymersomes behave similarly to GUVs with melittin and form pores in the same way, we see a discrepancy between theoretical pores/vesicle (melittin in film or in the rehydration buffer) and permeabilization efficiency found in GUVs, smaller than what expected from such an amount of pores (**Figure 59** C,D).

As previously mentioned, a possible explanation is that interaction with the membrane (measured by FCS) is only one factor in permeabilization, suggesting that there are other physico-chemical properties, namely membrane stiffness and thickness, playing a role; in phospholipids, the main differences arise from the different ratios of lipids.[150, 159]

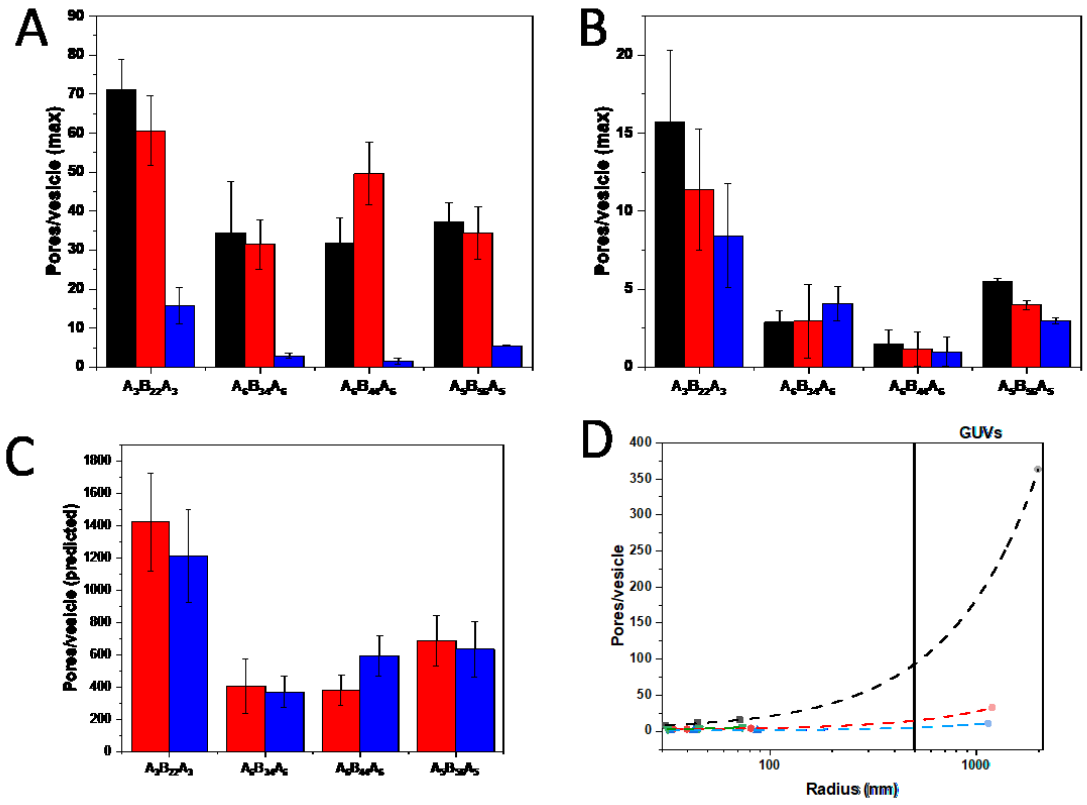

***Figure 59 A**: maximal number of melittin pores per vesicles when melittin is added to the film (black), to the buffer (red), or ex post (blue). **B**: maximal number of melittin pores per vesicles when melittin is added post at R_h 100 nm (black), 45 nm (red) and 30 nm (blue). **C**: predicted number of pores per vesicle on GUVs with melittin added to the film (red) and to the buffer (blue). **D**: regression curve of melittin per vesicle for polymersomes (left) and predicted number of pores for GUVs when melittin is added ex post (x axis in logarithmic scale). Error bars given as ± SD, n = 30.*

6.5 Application to biosensing

A crucial aspect of melittin insertion in curved membranes is the functional insertion of melittin. By encapsulating the enzyme GOX into polymersomes, we obtained vesicles where the enzyme would only be active if glucose could flow through. These GOX catalytic nanocompartments (GOX-CNCs) produce hydrogen peroxide by the *in situ* enzymatic reaction of GOX. H_2O_2 produced inside is released into the surroundings in presence of the melittin pores, and can be determined by using horseradish peroxidase,

HRP, present in the surroundings GOX-CNCs. The released H_2O_2 together with the substrate Amplex Ultra Red take part in the enzymatic reaction catalyzed by HRP resulting in the highly fluorescent product resorufin, which can be easily detected. The limited size of the involved molecules showed that the catalytic efficiency, relative to the same enzyme concentration free in solution, was close to 100% for $A_3B_{22}B_3$ regardless of the insertion approaches, meaning that there were enough pores not to affect catalysis via diffusion; for other polymers, the activity co-dried had a minimum of 75%. The polymersomes with a thicker membrane show a decreased catalytic activity when melittin was added in the rehydration buffer, especially pronounced for $A_5B_{55}B_5$, which only reaches 40% activity. When melittin is added ex post to pre-formed vesicles, both the thicker $A_6B_{44}B_6$ and $A_5B_{55}B_5$ have lower activity, down to 25% for the latter. Again, these results confirm that melittin inserts with different degrees of ease depending on the polymer characteristics, while the insertion strategy influences the insertion amount. In the absence of melittin, we observed trace residual activity, stemming from either the autoxidation of Amplex Ultra Red or polymer-enzyme unspecific binding, which we already identified as playing a small role in this kind of systems (Figure 6).[116]

By adopting this enzymatic reaction, the insertion of melittin can be verified easily in nanometric polymersomes irrespective of the insertion approach. The use of substrates with different sizes would also allow us to discriminate between additional pore widths, thus yielding a general approach to probe the structure and characteristics of inserted pores within membranes. Additionally, this is the first, proof of concept, use of melittin to produce functional catalytic nanocompartments, for either glucose sensing or anticancer ROS therapy.[160]

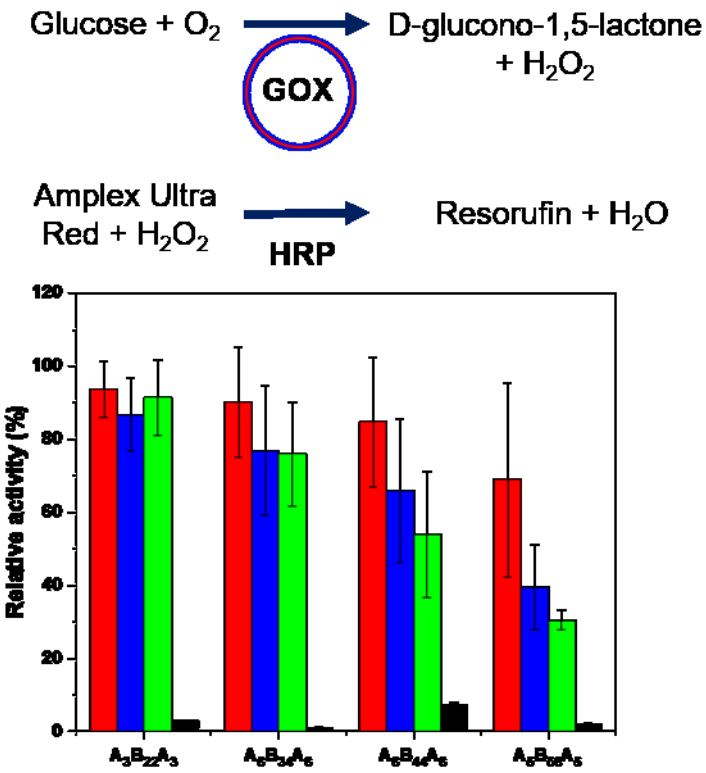

Figure 60 *Reaction scheme and activity of GOX-CNC with melittin co-dried (red), melittin in the rehydration buffer (blue), melittin ex post (green) and without melittin (black). Error bars given as ± SD, n = 30.*

6.6 Conclusions

The use of pore-forming peptides to permeabilize polymeric membranes is an attractive alternative to pore proteins such as OmpF or α-HL, as they can form wide pores. In this regard, melittin was used as a model to elucidate the parameters that affect its insertion into PMOXA-*b*-PDMS-*b*-PMOXA membranes. We studied the "natural" insertion route that happens on cells, *i.e.* insertion into already-formed membranes (ex post), and the insertion when the membrane is not fully formed (co-dried and in the rehydration buffer), showing that in all cases it depends on inherent polymer characteristics (thickness, hydrophilic ratio, dispersity, membrane roughness) and assembly-specific curvature. In fact, we showed how the increase in curvature (from GUVs to polymersomes) increases the insertion efficiency with the same polymer. It was also possible to quantify the melittin surface density and estimate the pore density. This is the first time that such molecular parameters were related to peptide-

polymer assemblies and will be useful for the study and engineering of any peptide insertion into synthetic membranes. Such physical considerations might also be applied to natural membranes. Furthermore, the permeabilization towards glucose was shown to be an evolution of the well-known GOX-HRP biosensing cascade. Our results show that melittin is a good candidate for both triggered and built-in vesicle permeabilization of membranes, provided that the key molecular membrane parameters and curvature are considered and optimized, and could probably be generalized for most interactions between polymer membranes and peptides. Further research will elucidate the influence of relative peptide: polymer ratio, the shape of the pores and the behavior of other membrane-forming peptides.

7 DNA functionalization of CNCs as higher-order organization strategy[6]

Having developed a more straightforward way to permeabilize our polymersomes, another question arose: would fixing the relative positions of the CNCs, and their distance too, improve the cascade efficiency? After all, we had seen in Chapter 4 that intervesicular distance does play a role in such systems. Encapsulating enzymes separately would keep their ratios constant, while linking the resulting vesicles would additionally give a way to always deliver one together with the other, avoiding the issues with co-delivery.

7.1 Introduction to DNA clustering

DNA is a very interesting molecule, where the very tight pairings between complementary bases allow the recognition of specific sequences at very low concentrations. DNA has already been used as a key tether to promote self-organization of super-assemblies with emergent properties, for example to target and cluster enzymes to specific structures. [161] The unique features of DNA enable also the organization of nanostructures into larger superstructures with well-defined orientations, depending

[6] PARTS OF THIS CHAPTER HAVE BEEN ADAPTED FROM A MANUSCRIPT IN PREPARATION

on their intrinsic architecture, DNA origamis.[1,2] Most DNA-based supramolecular structures use DNA-linked rigid nanostructures, *e.g.* gold nanoparticles, which are brought together by the pairing of DNA strands.[162] Recently, soft nanostructures such as liposomes and polymersomes have been subjected to DNA-mediated organization.[13, 163] In the case of liposomes, DNA-mediated assembly led to their precipitation from solution or membrane fusion.[163-164] For polymersomes, the first reported example of clustered vesicles[13] (**Figure 61**) was followed by a report on the cluster's capability of adhering to cell surface and direct activation of cell receptors after a biotransformation,[165] thus making the DNA also a targeting moiety; the cluster size hindered unspecific uptake, making the clusters coat the cell surface. Clustering is also found in cells: for instance, lysosomes are reported to cluster in cells, interacting with endosomes while retaining their integrity, an evidence that distance control is important in cellular biology too.[166]

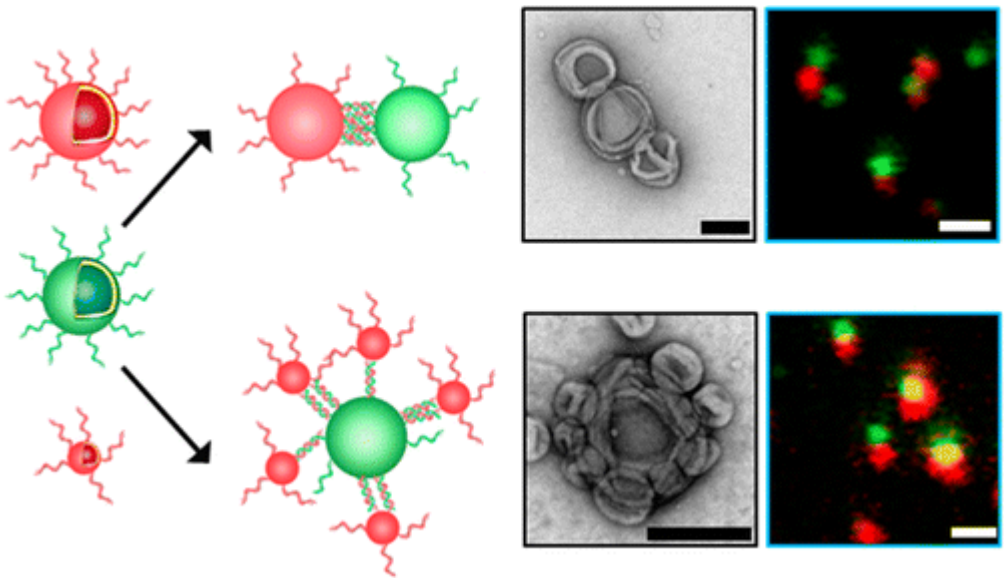

Figure 61. *The first example of polymersome clusters, showing different architectures, based on the relative sizes of the vesicles involved. From left to right: concept figure, TEM micrograph and CLSM images of clusters with differently labeled polymersomes. Adapted with permission from[13].*

7.2 A cascade in clusters: GOX-LPO

7.2.1 Introduction

Having a solid base on how the clusters were formed, we applied that knowledge to produce catalytically active clusters. This time, we used a diblock $PDMS_{26}$-$PMOXA_{12}$ to produce vesicles due to

the better DNA conjugation yield diblocks provide.[13] As a model cascade to apply in clusters, we decided to use glucose oxidase (GOX) and lactoperoxidase (LPO): GOX oxidizes glucose into gluconic acid and H_2O_2, the latter is used by LPO to oxidize a variety of substrates. More generally, the oxidase-peroxidase system is an antibacterial cascade found in many animal secretions (mucus, tears, saliva, milk), as peroxidases can produce bacteriostatic compounds such as hypothiocyanates ($OSCN^-$) from thiocyanates (SCN^-), thanks to the hydrogen peroxide coming from organic substrates (**Figure 62**), and has been suggested for biomedical applications such as oral plaque treatment or as counter to opportunistic infections developed in cystic fibrosis.[167] Moreover, the GOX-LPO cascade has been long studied as both an anticancer and antiviral system.[168] On these grounds, we chose such cascade for its robustness and biological relevance as model to study how distance affects a CNC system, for future nanotechnological applications. Additionally, based on the findings of Chapter 6, we elected to use melittin instead of OmpF, to improve both the fabrication process and the overall catalytic efficiency.

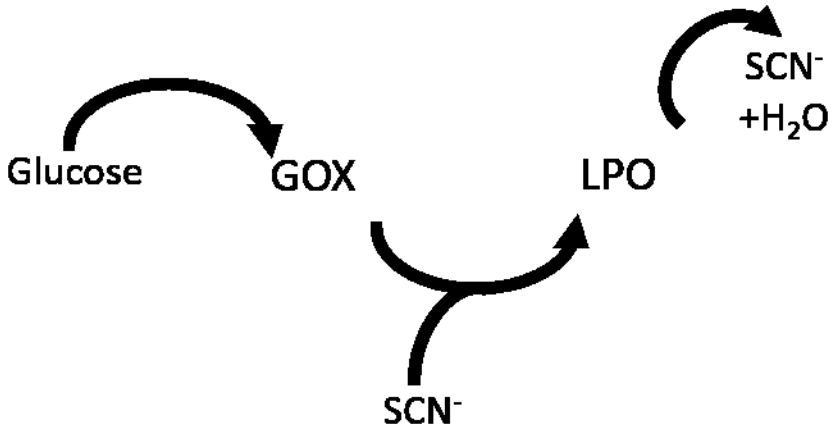

Figure 62. *The concept of the GOX-LPO cascade in biological systems, using the widely-present glucose and thiocyanate to produce cytotoxic hyopthiocyanate.*

7.2.2 Physical characterization

We chose to produce polymersomes made of the block copolymer $PDMS_{26}$-$PMOXA_{12}$, where 50% of the polymer component was the PEGylated, azide-functionalized $PDMS_{26}$-$PMOXA_{12}$-PEG_4-N_3, to provide enough functional groups for the attachment of a dibenzocyclooctine (DBCO)-functionalized DNA, to link DNA to the vesicles via strain-assisted alkyne-azide cycloaddition (SPAAC).[13]

We encapsulated GOX and LPO separately, the same way as previously delineated in Chapter 4, adding melittin to the rehydration buffer, rehydrating the same polymer amount. The ratio between R_h and R_g

showed the production of vesicular structures, with LPO-CNCs with a greater radius, even after extrusion. The vesicle concentration, determined by NTA, consequently showed a slightly higher number of vesicles for GOX-CNC, being smaller. The final enzyme concentration, calculated by recovering the unencapsulated fraction via SEC, showed a roughly similar amount of enzyme encapsulated (**Table 8**). TEM imaging confirmed the usual vesicular shape of CNCs (**Figure 63**).

Table 8 *Physical parameters of the azide-functionalized CNCs*

	GOX-CNC	**LPO-CNC**
R_h	119 ± 8 nm	170 ± 24 nm
R_g	110 nm	150 nm
R_g/R_h	0.9	0.9
Vesicle concentration	$1.66*10^{11} + 8.56^{9}$	$1.17*10^{11} +7.58^{9}$
Enz. concentration	246 µg/mL	220 µg/mL

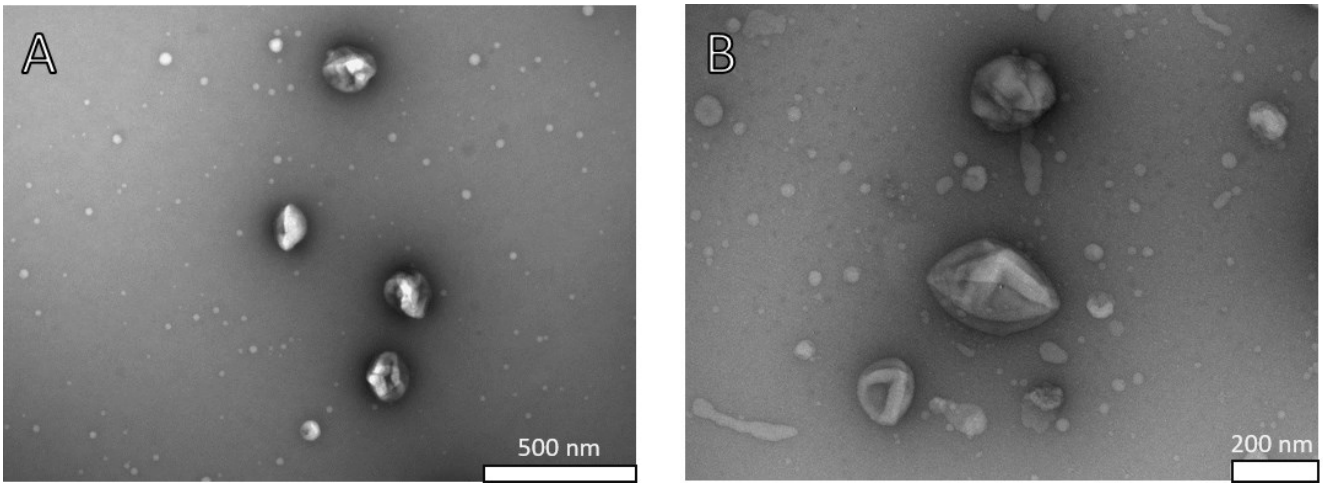

Figure 63 A *TEM micrograph of GOX-CNC.* ***B*** *TEM micrograph of LPO-CNC.*

We labeled both GOX (with ATTO 488) and LPO (with DyLight 633), and then encapsulated them. The FCS curves, as expected, showed that the enzymes could be both labeled and associated to the vesicles (**Figure 64**).

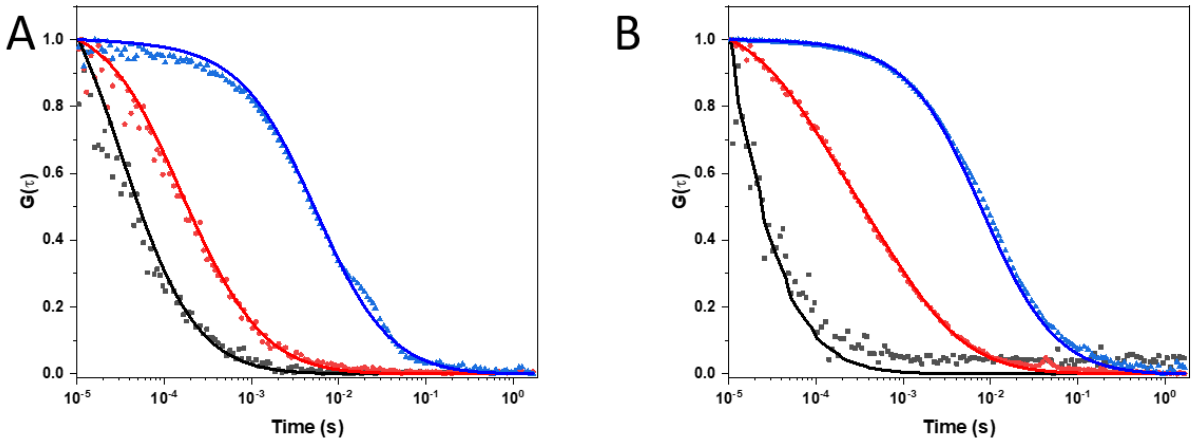

Figure 64 A *FCS autocorrelation curves of free ATTO 488 (black), GOX-ATTO 488 (red) and GOX-ATTO488 –loaded CNCs. Dots: raw data. Line: fitted model.* ***B*** *FCS autocorrelation curves of free DyLight 633 (black), LPO-DyLight 633 (red) and LPO- DyLight 633 –loaded CNCs.*

The intensity of the single species (free enzyme, enzyme, CNC) allowed us to quantify the average number of dyes per enzyme and the enzyme molecules per vesicle, showing a great variability for LPO-CNCs. Additionally, using a two-component autocorrelation fit, we could determine that only 2% of the enzyme in the sample is still free after purification (**Table 9**).

Table 9 *Quantification of several enzyme- and vesicle-related parameters via FCS*

	GOX (ATTO 488)	LPO (DyLight 633)
Dye/enzyme	1 ± 0.24	4 ± 2
Enzyme/vesicle	11 ± 4	52 ± 32
Free enzyme %	2 ± 1	2 ± 1

7.2.3 CNC functionality

Having obtained CNC, we tested their activity. The main question was the insertion of melittin in the polymer membrane, and whether enzymes were unspecifically adsorbed on the outer membrane leaflet. We thus compared melittin-incorporating and melittin-free vesicles, studying the CNCs outside their cascade; both GOX-CNCs and LPO-CNCs showed that melittin was necessary to detect activity, also indirectly showing that no appreciable amounts of enzyme were not encapsulated and still active (**Figure 65**): the colored ABTS derivative could be produced thanks to either CNC, but only when melittin permeabilized the membrane. To test GOX-CNCs, we used their cascade with LPO free in solution, without the constraints of encapsulation.

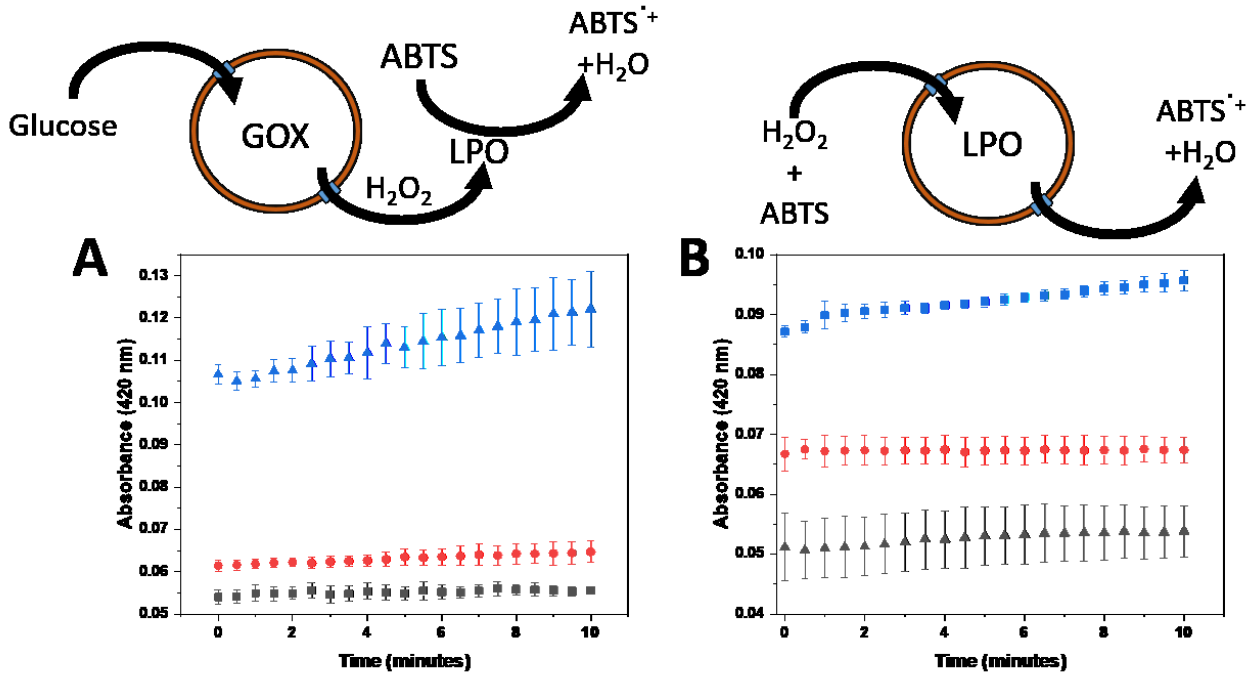

Figure 65 A *Enzymatic activity of GOX-CNC with melittin (blue), without melittin CNCs (black) and substrates alone (red), using LPO as reporter enzyme.* ***B*** *Enzymatic activity of LPO-CNC with melittin (blue), without melittin CNCs (black) and substrates alone (blue). Error bars given as ±SD, n=3.*

7.2.4 Cluster formation

With functional CNCs, we could move on to DNA conjugation. We selected to complementary strands, both presenting 5' non-complementary thymine sequences, as spacers to improve DNA hybridization (**Table 10**).

Table 10 *DNA strands used for this study*

11T-22a	DBCO-5'-TTT TTT TTT TTC CTC GTC CTG CTA ATC CTG TTA-3'
11T-22b	DBCO-5'-TTT TTT TTT TTT AAC AGG ATT AGC AGA GCG AGG-3'

To quantify the amount of DNA strands per vesicle, we hybridized the vesicle-bound DNA with its dye-labeled complementary strand, so that vesicles could be detectable via FCS (**Figure 66**).

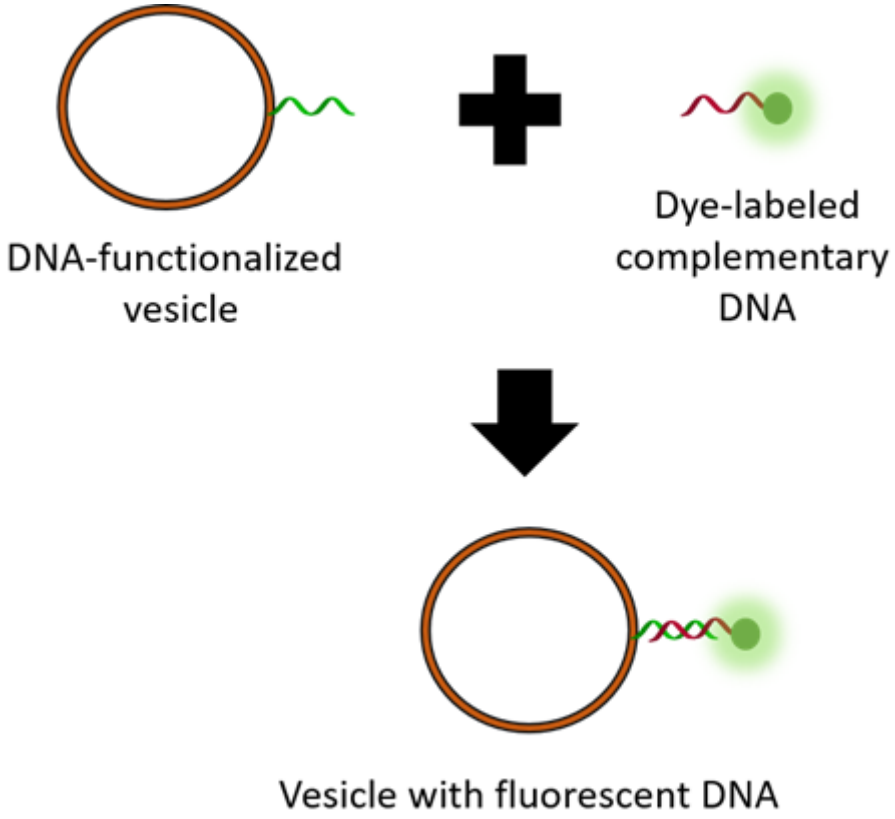

Figure 66 *Labeling technique used to quantify DNA via FCS.*

FCS revealed broad dispersion of the conjugation efficiency, with 11T-22a per vesicle ranging from less than 10 to more than 130 strands per vesicle, and smaller overall amounts for 22b (**Table 11**).

Table 11 *Quantification of the DNA strands via FCS*

	11T-22a (22b-ATTO488)	22b (22a-Cy5)
DNA/vesicle	69 ± 64	34 ± 28

However, the detected amounts were enough to obtain clusters: by mixing 1:1 volume ratios of CNCs, we could observe the clustering thanks to the constant increase of R_h, plateauing around 14 hours of clustering (**Figure 67 A**), plateauing at around 700 nm diameter. TEM confirmed the presence of small clusters (3-4 vesicles) (**Figure 67 B**). The average D_H of a single vesicle pair would be around 580 nm, so it would imply less than 2 vesicles per cluster, but we must remark that DLS assumes a spherical object and is thus not ideal for the ellipsoidal assemblies seen in TEM, being influenced by their rotational diffusion and yielding a Rh that is an weighted average of its radii(**Table 8**);[169]moreover, the soft vesicles deform when close enough, make the whole assembly smaller than the sum of the vesicles.[13] Future research will use fluorescence cross-correlation spectroscopy (FCCS) to have a better insight in the distribution of different GOX/LPO CNCs in the clusters.[23b, 84]

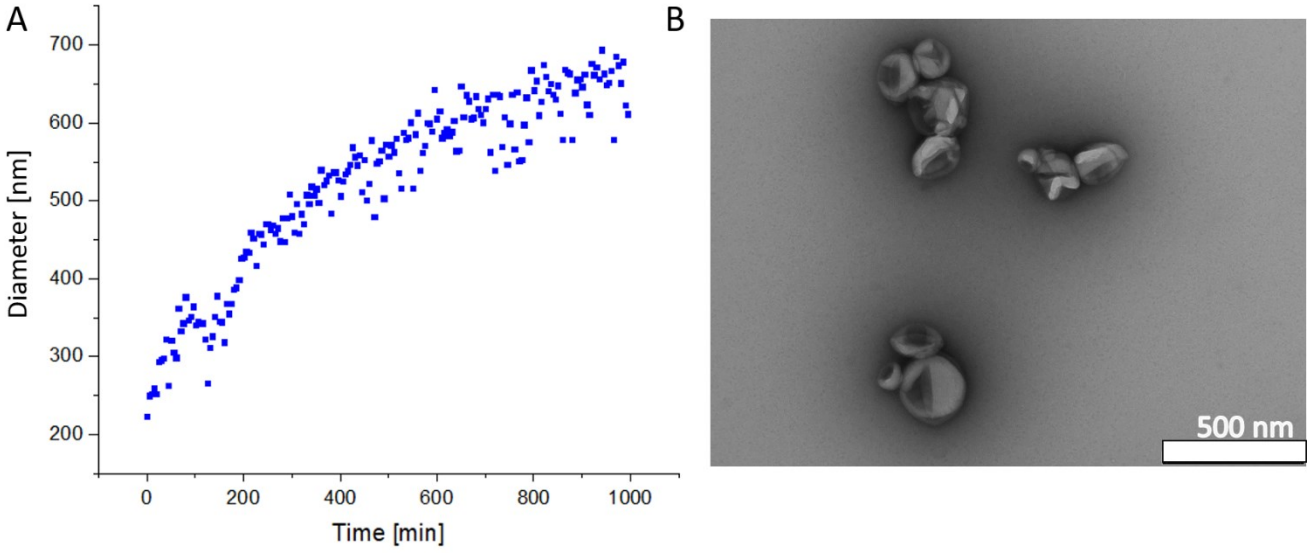

Figure 67 A *DLS profile of the cluster size, over time.* ***B*** *TEM micrograph of CNC clusters.*

7.2.5 CNC activity: effect of distance

Once the clusters were formed, we needed to determine the mean distance between vesicles, both when clustered and unclustered. Adapting a more refined model, developed for hard particles and taking into account their size dispersity, relative CNC concentration and the volume occupied by vesicles.[170]

$$\langle D \rangle = d\left[\xi\left(\frac{\pi}{6\phi}\right)^{\frac{1}{3}} e^{(1.5\ ln^2\sigma)} - e^{(0.5\ ln^2\sigma)}\right]$$

Equation 8

In Equation 8, the mean intervesicle distance ⟨D⟩ depends on the mean size d, the spatial distribution parameter ξ (fixed to 1.1[170]), the volume fraction occupied by vesicles φ and the geometric standard deviation σ. For our system, however, not all vesicles were equal, as the "bridging molecule", H_2O_2, could only go from a GOX- to a LPO-CNC, and we had to consider both their relative concentrations and sizes. The ratios between the d and φ (relative size and frequency) of GOX- and LPO CNCs, *i.e.* the probability of hydrogen peroxide to encounter the right CNC once diffused out of GOX-CNC, yielded the weight that we used to sum the contributions of the CNCs populations, obtaining ⟨D⟩ = 2.3 µm. Had we used the model developed for UOX-CNC and HRP-CNC[23a], we would have calculated a similar value, 2.2 µm.

For clustered vesicles, the distance estimation relies on the average length of the DNA strand. Having both paired and unpaired bases, the average DNA length L –in nm– (and vesicle-to-vesicle surface distance) is based on Equation 9. [171]

$$L\ = n_{BP} \times 0.34 + n_S\ \times 0.676$$

Equation 9

Where n_{BP} is the number of paired bases and n_s the number of unpaired bases. For the used strands, we estimated 14.9 nm, which is in the range of the synaptic cleft[101] and some inter-organelle distances found in cells. [172]

To mimic the conditions of action in the lungs, a possible target organ of such system, we observed the oxidation of the LPO substrate 2,2'-azino-bis(3-ethylbenzothiazoline-6-sulfonic acid) (ABTS) to yield a colored compound, with the glucose concentration found in lungs.[173] The final concentration of enzymes was kept constant, both with and without clusters, thus varying only the distance; the inter-cluster distance, calculated with Equation 8, yielded again ⟨D⟩ = 2.3 μm, at the used enzyme concentrations, so we could consider it as constant.

The comparison with clusters clearly shows an increase in enzymatic activity, not reaching the plateau even after 2.5 hours, whereas unclustered CNCs reach it after 30 minutes, at a much lower level (**Figure 68**).

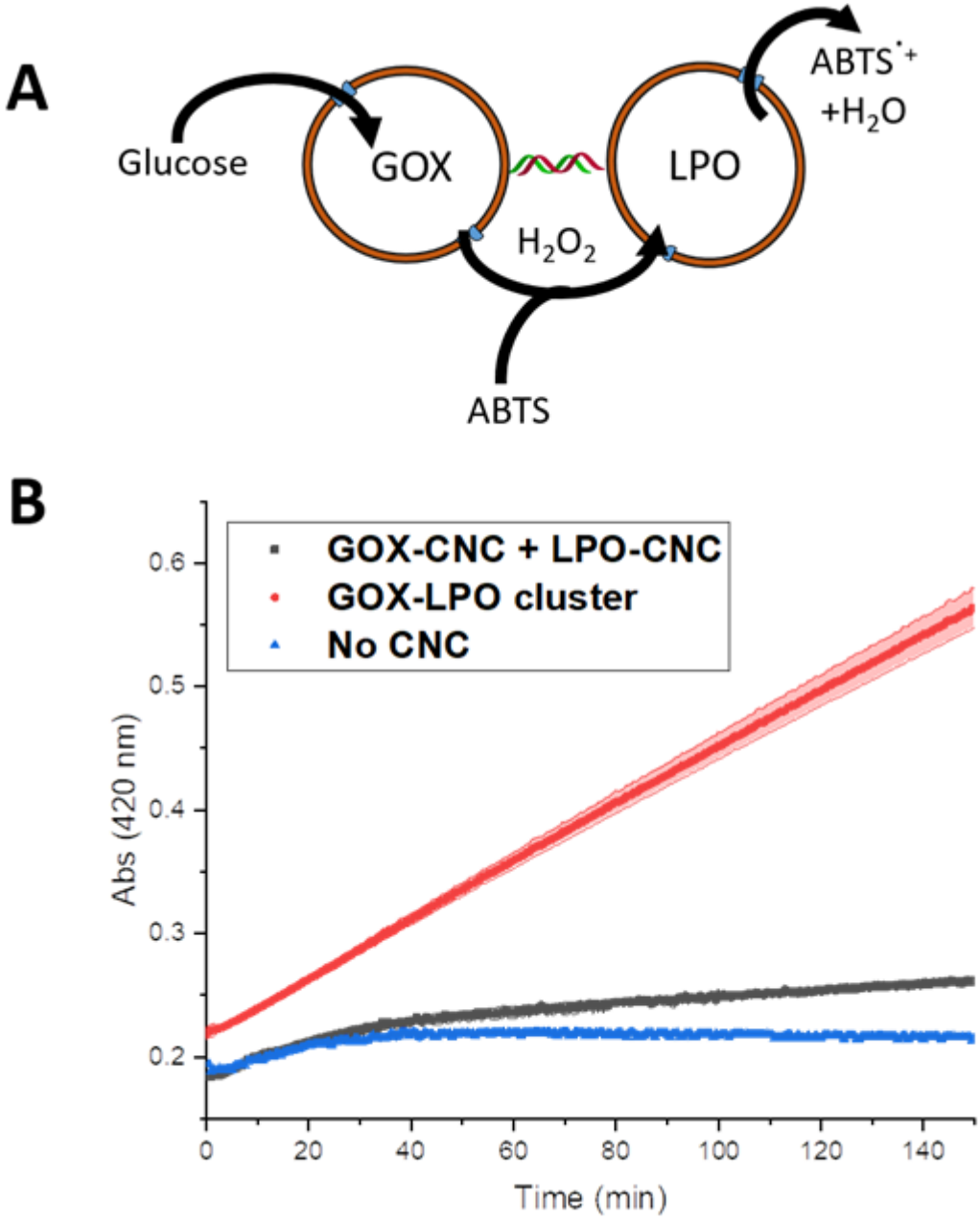

Figure 68 A. *Concept of a clustered GOX-LPO-CNC cascade.* ***B.*** *Enzymatic activity of LPO over 150 minutes of CNC clusters (red), unclustered CNCs (black) and ABTS autoxidation (blue). Error bands given as ±SD, n=3.*

7.2.6 Cell localization

Finally, we studied the localization of CNC clusters on A549 cells. This cell line, being a lung carcinoma, could act as a model both for lung protection from bacterial infections, as a model for cancer targeting and ROS therapy.[174] We clustered the ATTO-488 and DyLight633-labeled CNCs previously used for FCS,

and showed their attachment and colocalization, confirming their potential for targeted biomedical applications **Figure 69**.

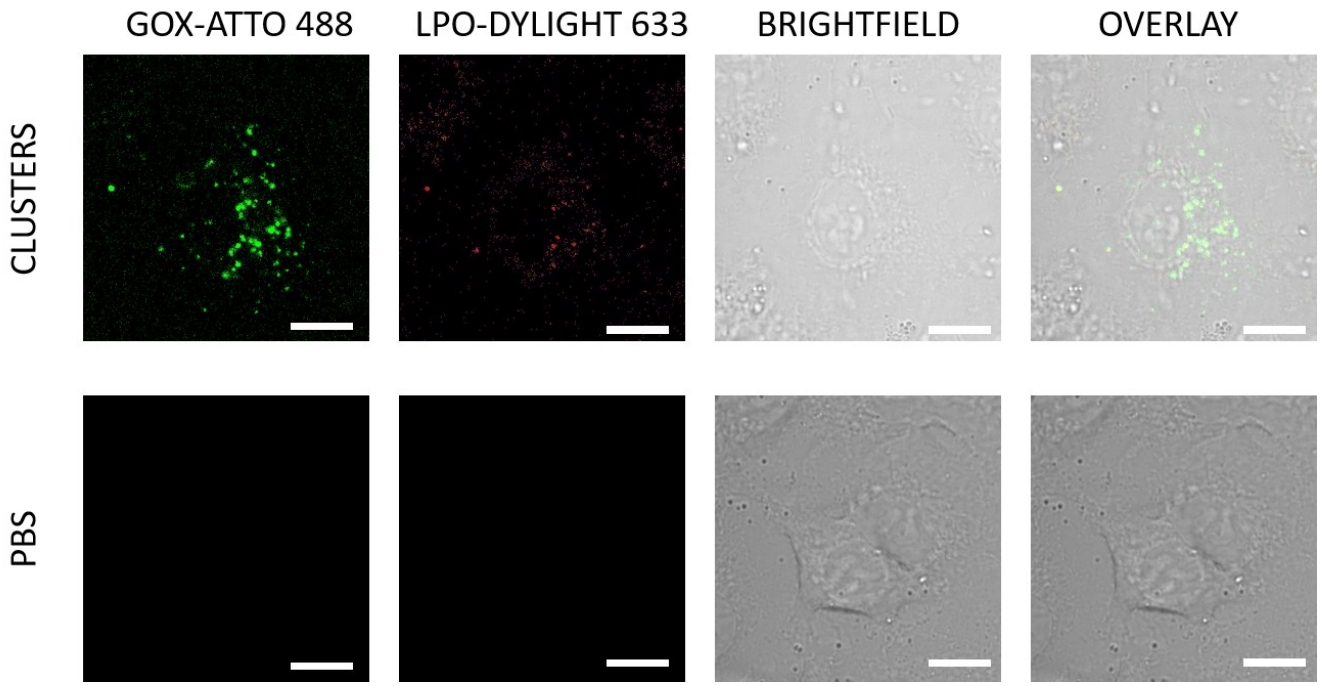

Figure 69 *Localization on A549 cells of clustered GOX-CNC (green) and LPO-CNC (red), the transmission channel and the composite picture, and control performed by adding PBS instead of clusters. Scalebar: 5 µm.*

7.3 Conclusions

The distance between enzymes is an important aspect in the optimization of nanotechnological cascades, aimed at offsetting limiting factors such as membrane diffusion and increase the overall efficiency of the system. We developed a very simple proof of concept, based on two widely used enzymes, to study whether tethering vesicles via DNA could be a good candidate for this task, and showed the extent of such approach. Using DNA also offers the possibility of tuning, base by base, the intervesicle distance, ranging from distances typical of paracrine signaling for unclustered vesicles[102] to those of some inter-organelle interactions [166, 172] or synaptic signaling[101] for clusters, thus offering the possibility of using CNCs as non-living models for compartment communication. The behavior of hybrid polymer-DNA assemblies allowed them to interact with cell surfaces and localize there. The future optimization of enzyme loading and sample concentration will allow to further develop this approach for localized therapeutic or biosensing applications.

8 Overall conclusions and outlook

Whereas artificial life is still just hypothetical concept, mimicking living matter, or some of its aspects, is an attractive way to improve man-made materials, endowing them with specific abilities of cells, namely their compartmentalization, environmental sensitivity, internal plasticity, biotransformation capabilities, selective permeability and controlled distances. We first investigated proper cell-like structures, where we developed internal compartments with the dual function of segregating artificial organelles and receptors, which could then trigger enzymatic activity or ion permeability, thus inducing internal architecture modifications, in the form of cytoskeleton formation, as a first example of how nature-mimicking materials such as PDMS-PMOXA and PMOXA-PCL can acquire complex cell-like behaviors when combined with natural proteins. These *sui generis* chemo-enzymatic cascades were the first example of complex response from polymeric cell mimics.

We then moved to a smaller scale, using sub-micrometer vesicles, to make them act both as downsized cell-mimics and artificial organelles in actual cells, directly acting onto them. Aiming for more constant encapsulation outcomes, we opted to overcome co-encapsulation issues stemming from the film rehydration technique by encapsulating the enzymes separately. In this case we used fully enzymatic cascades, closer to what is found in nature, forming enzyme-loaded polymersomes that we named catalytic nanocompartments, CNCs. With UOX-CNC and HRP-CNC we described in depth the role of the membrane in slowing down the flow of molecules across the membrane, permeabilized by OmpF, and studied the influence of inter-vesicle distance. This compartmentalization, albeit hindering the diffusion of molecules, helped the reaction by creating local high concentrations of enzyme, and protected the proteins from external degrading agents. This allowed them to work in human serum, performing similarly to free enzymes in removing uric acid in hyperuricemia-like conditions. They were also able to help human cells survive better, detoxifying high concentrations of uric acid, which is a metabolic pathway absent in humans, thanks to our orthogonal approach.

The same kind of CNCs, this time harboring iNOS and sGC, were used to produce the second messenger cGMP, both extra- and intracellularly, in both HeLa and C2C12 cells. This led to the quick and sharp increase of cytoplasmic Ca^{2+}, dependent on the several, complex pathways activated by cGMP. For the first time, we truly integrated these CNCs, as artificial organelles, into pre-existing human pathways, an overexpression effect that would otherwise be achieved by genetic or metabolic engineering.

These two systems, however, suffered from the bottleneck represented by OmpF, one of the main factors limiting the transfer rate across the membrane. This brought us to investigate an alternative way to permeabilized PDMS-PMOXA membranes, a way that we found in melittin. The parameters governing the interaction between melittin and our synthetic membranes were studied, extrapolating general rules for membrane-peptide interactions, namely the importance of membrane thickness, curvature and stage of the self-assembly process at which it was added. The pores produced by melittin allowed the production of HRP-CNCs not suffering from the cross-membrane diffusion problems seen with OmpF.

Finally, we tackled the problem of distance, by tethering CNCs together with complementary DNA strands, so that enzymes linked in a cascade would be also physically associated, basically recovering the enzyme proximity lost with the segregation into separate vesicles. The GOX-LPO cascade was shown to be more effective when the CNCs are clustered at distances of a few nm, channeling the molecules in common between the two enzymatic reactions, and proved to be a potential application to the study of inter-organelle and intercellular communication. Additionally, DNA made the clusters coat epithelial cells, suggesting a future use as *in situ* therapeutic agents to act on a specific microenvironment.

Moreover, the use of semi-synthetic materials should be investigated more in depth, having the potential of bridging the well-known biochemical logics and the growing field of pure molecular logics. Our designs showed high versatility and robustness, demonstrating that multicompartment and/or multivesicular, polymer-based assemblies offer an ideal scaffold for the development of complex cell-inspired responsive systems for future applications in biosensing, catalysis and medicine.

9 Experimental

9.1 Chapter 3

9.1.1 Materials

All chemicals were purchased from Sigma Aldrich and were used without further purification, unless stated otherwise.

9.1.2 Synthesis of $PMOXA_5$-b-$PDMS_{58}$-b-$PMOXA_5$

The amphiphilic triblock copolymer poly(2-methyl-2-oxazoline)$_5$-*block*-poly(dimethylsiloxane)$_{58}$-*block*-poly(2-methyl-2-oxazoline)$_5$ ($PMOXA_5$-*b*-$PDMS_{58}$-*b*-$PMOXA_5$) was synthesized according to previously published protocols. [175]

Briefly, the hydroxyl-terminated PDMS (OH-PDMS-OH) was synthesized by acid-catalyzed polycondensation. After purification OH-PDMS-OH was reacted with trifluoromethanesulfonic acid in anhydrous hexane to form bitriflate-activated PDMS macroinitiator. Following filtration of the reaction mixture and evaporation of hexane, anhydrous ethyl acetate was added, in the presence of which the PDMS macroinitiator reacted with distilled 2-methyl-2-oxazoline (MOXA) in a symmetric cationic ring-opening polymerization. After quenching the reaction with TEA/water (1:4 v/v), impurities were removed by ultrafiltration in water/EtOH (1:1 v/v). Finally, the solvent was removed by vacuum distillation and the resulting bihydroxyl-terminated triblock copolymer $PMOXA_5$-*b*-$PDMS_{58}$-*b*-$PMOXA_5$ was dried under vacuum.

9.1.3 Synthesis of $PMOXA_{88}$-g(SS)-PCL_{238}

The synthesis of the reduction sensitive graft copolymer $PMOXA_{88}$-*g*(SS)-PCL_{238} (poly(2-methyl-2-oxazoline)$_{88}$-*graft*(SS)-poly(ε-caprolactone)$_{238}$) was performed according to a previously published method. [66b] In short, the monomer ε-caprolactone and α-benzyl carboxylate-ε-caprolactone were copolymerized using EtOH as an initiator. Pyridyl disulfide functionalized poly (ε-caprolactone) PCL-co-PBCL was synthesized by varying molar ratios of the reaction partners in toluene at 110°C. PCL-co-PBCL was reduced by Pd/C at RT for 42 h under hydrogen to form PCL-co-PCCL. Then 2-pyridylthio cysteamine hydrochloride was added in the presence of N,N'-dicyclohexylcarbodiimid to form PCL-co-PPCL. Thiol-disulfide exchange reaction was performed, where PCL-co-PPCL and PMOXA-SH were dissolved in DMF and a catalytic amount of acetic acid was continuously added to the mixture and stirred at RT under argon for three days. Finally, $PMOXA_{88}$-*g*(SS)-PCL_{238} was purified by precipitation from cold MeOH and a white solid was obtained. [66b]

9.1.4 $PMOXA_6$-b-$PDMS_{65}$-b-$PMOXA_6$

This copolymer was purchased in Polymer Source Inc. The polymer was used either without any further purification steps or we functionalized it with PEG_4-N_3, according to the previously published protocol. [13] Commercially available $PMOXA_6$-$PDMS_{65}$-$PMOXA_6$-OH (200 mg, 0.034 mmol), was dissolved into 5 mL

dry DMF, then succinic anhydride (16 mg, 0.16 mmol), 4-dimethylaminopyridine (15 mg, 0.12 mmol) and TEA (17 mg, 0.16 mmol) were added. The mixture was stirred for 24 h at 60°C. Finally, 180 mg colorless solid product was obtained after the ultrafiltration with a yield of 90%. The resulting $PMOXA_8$-$PDMS_{56}$-$PMOXA_8$-COOH (100 mg, 0.011 mmol) was first dissolved in dry DMF, then 11-azido-3,6,9-trioxaundecan-1- amine (44 mg, 0.20 mmol), N, N'-dicyclohexylcarbodiimide (42 mg, 0.20 mmol) and 4-dimethylaminopyridine (1.2 mg, 0.01 mmol) were added into the above solution. The mixture was stirred for 24 h, at RT. Finally, 86 mg colorless solid product was obtained with a yield of 86%. ^{1}H NMR (500 MHz, Chloroform-d) δ 3.24-3.72 ppm (m, 55H), 2.00-2.32 ppm (m, 32H), 0.40-0.58 ppm (m, 4H), 0.06 (m, 351H). IR: 2961, 2114, 1736, 1635, 1420, 1263, 1007, 787, 682 cm^{-1}.

A thin film of $PMOXA_5$-*b*-$PDMS_{58}$-*b*-$PMOXA_5$ (4 mg mL^{-1} in EtOH) was formed by rotary evaporation of EtOH (100 rpm at 40 °C, 100 mbar for 5 min and 7 mbar for 15min). The film was dried overnight under high vacuum (2 x 10^{-1} mbar). For polymersome formation, the film was gently dislodged using a spatula and subsequently rehydrated in phosphate buffered saline (PBS) (1X, pH = 7.2, BioConcept) and SRB (final concentration 100 µM).

Lipase adsorbed polymersomes (LipVes) were formed by adding lipase (4 mL, 0.2 mg/mL, 100 kU, from porcine pancreas, Sigma-Aldrich) to already formed PBS loaded polymersomes based on $PMOXA_5$-*b*-$PDMS_{58}$-*b*-$PMOXA_5$. For sodium loaded Ves5 (Na^+Ves), the film was rehydrated in PBS (pH 7.2). Remaining non-adsorbed lipase was removed by size exclusion). Samples were stirred overnight at RT and then extruded 15 times through a 100 nm Whatman Nuclepore filter. Size exclusion chromatography (SEC) was equilibrated to remove remaining non-encapsulated (dyes, salts) or non-adsorbed (lipase) cargo against PBS and for Na^+Ves against HEPES (300 mM, pH 7.2). The polymersome fractions were collected and stored at 4°C. [66a, 176]

9.1.5 Solvent Switch Technique

Graft-nanoparticles (NP-Graft, reduction sensitive) were formed using a solvent switch technique. [66b] For DGGR-NP, the lipase substrate 1,2-Di-O-lauryl-rac-glycero-3-(glutaric acid 6-methylresorufin ester, Sigma-Aldrich) (DGGR, 52 µL, 2.5 mM) in 1:1 EtOH:DMSO was added to polymer (1 mg) in DMF (248 µL) under continuous stirring to form DGGR loaded NP-Graft. The resulting turbid mixture was dialyzed against NaCl (150 mM) for at least 48 hours with 5 changes of buffer. After a final dialysis against PBS (pH 7.2), NP-Graft were stored at 4°C. [61]

For the assembly of gramicidin A- or Ionomycin- loaded nanoparticles (gANP, IonoNP), gA (15 µL, 1 mM, *from B. aneurinolyticus*) or ionomycin (15 µL, 1.3 mM, from *S. conglobatus*) in DMSO were added to polymer (1 mg) in DMF (285 µL). Here, the gANP or IonoNPwere dialyzed against HEPES. Non-encapsulated cargo (DGGR, gA or IoNo) was removed from the NP-Graft solution by dialysis as described above. Based on previous results, we know that the reduction sensitive NP-Graft are stable in PBS and also in more complex environments, such as cell culture medium. [66b]

9.1.6 Preparation of Multicompartments

For multicompartment assembly, films of $PMOXA_5$-*b*-$PDMS_{58}$-*b*-$PMOXA_5$ (40 µL, 6 mg mL^{-1}) were rehydrated with sucrose solution (190 µL, 300 mM) and the corresponding nanostructures (10 µL) in PBS unless stated otherwise. For two-type multicompartments we typically used 10 µL of each type nanostructures (in PBS) in 200 µL of 300 mM sucrose solution, unless stated otherwise. In general, film rehydration and storage of giant vesicles compartmentalized with fluorescent nanostructures were carried out at RT in the dark without stirring. To minimize the disruption of giant vesicles that would result in the formation of mostly nano-sized polymersomes, samples were always handled with great care (minimal agitation).

For the assembly of lipase containing multicompartments, we used lipase (40 µL, 100 kU, type VI from porcine pancreas, Sigma-Aldrich) (0.2 mg/mL) in PBS, DGGR loaded NP-Graft (20 µL) in sucrose (300 mM, 180 µL) as rehydration solution. To determine the loading efficiency of DGGR loaded NP-Graft and lipase, we tested 40 single GUVs and obtained the histogram along diagonal of fluorescence.[61] Similarly, for the two-type multicompartment for enzymatic reaction, we added 30 µL of lipase (0.1 mg ml^{-1}) adsorbed polymersomes (LipVes) in PBS and 20 µL of DGGR loaded NP-Graft in 150 µL of sucrose (300 mM) to the thin polymer film. Unadsorbed lipase was recovered via SEC and quantified at 280 nm with Nanodrop 2000 (ThermoFisher Inc.).

For gANP, 30 µL were added to 270 µL Asante Natrium Green 2 (ANG2, TEFlabs) solution (25 µM in 300 mM sucrose) to the polymer film. Similarly, for two-type multicompartment to study ion channel recruitment, we loaded the GUVs with 30 µL gANP-Graft, 30 µL of sodium loaded Ves5 (Na^+Ves) to 140 µL ANG2 in 300 mM sucrose (25 µM) as a rehydration solution.

The non-encapsulated nanostructures and ANG2 were removed from exterior solution by changing the supernatant with HEPES (300 mM, twice daily for 5 days). To determine the loading efficiency of gA

loaded NP-Graft and ANG2, we tested 40 single GUVs and obtained the histogram along diagonal of fluorescence.

9.1.7 Preparation of Actin GUVs

G-Actin loaded giant vesicles (Actin GUVs) were prepared by spontaneous swelling in the absence of stirring also called film rehydration. A mixture of $PMOXA_5$-$PDMS_{65}$-$PMOXA_5$ (60 µL, 10 mg/mL, Polymer Source Inc.) in EtOH and N_3-functionalised $PMOXA_5$-$PDMS_{65}$-$PMOXA_5$ (0.3 µL, 90 mg/mL) was put to a glass vial. A thin polymer film was formed on the bottom of the vial by removing all traces of EtOH in a vacuum chamber (Plasma Cleaner, PDC-002, Harrick Plasma) for one hour. The films were rehydrated in the dark with the actin rehydration solution containing the monomeric protein G-actin (24 µL, 1 mg/mL, Hypermol, rabbit alpha-actin skeletal muscle), ATTO488 labelled G-actin (ATTO488-actin, 2 µL, 1 mg/mL, Hypermol, rabbit alpha-actin skeletal muscle), and the crosslinking agent filamin (4 µL, 1 mg/mL, Hypermol, turkey smooth muscle, ~1:100 actin:filamin ratio, 92% purity) and sucrose (170 µL, 300 mM, containing 0.02 % NaN_3) overnight in the fridge and stored for some days until further characterization.

G-actin, ATTO488- G-actin and filamin in solution (1 mg/mL) was stored for up to 1 week in ice in the fridge and non-solubilized G-actin at -80°C for long term storage.

9.1.8 Preparation of Actin MCs

For G-actin loaded multicompartments (Actin MCs) we prepared the sample similarly as for the formation of Actin GUVs. Instead of adding the pores to the surrounding GUV solution, we rehydrated with the actin components (actin, ATTO488-actin, filamin) and in addition with pore-loaded NP-Graft (IoNo loaded NP-Graft or gA loaded NP-Graft, 20 µL) and sucrose (300 mM). For 2-comp Actin MCs, we loaded 20 µL SRBVes and 20 µL IoNo loaded NP-Graft) and sucrose (300 mM).

9.1.9 Preparation of F-actin

F-actin was prepared in solution by adding monomeric protein G-actin (24 µL, 1 mg/mL, Hypermol, rabbit alpha-actin skeletal muscle) and ATTO488-Actin (2 µL, 1 mg/mL, Hypermol, rabbit alpha-actin skeletal muscle) with salt solutions (100 mM KCl, 70 mM $MgCl_2$, 70 mM $CaCl_2$) or for control with salt-free solution (300 mM HEPES, pH 7.2).

9.1.10 Fluorescence Imaging

Giant vesicles were imaged using an LSM 880 confocal laser scanning microscope (Carl Zeiss, Jena, Germany) with a water immersion objective (C-Apochromat, M=40, NA 1.2). The pinhole for each channel was set to 91 µm and the MBS 488/561/633 filter was used. The transmission PMT (T-PMT) option was used to record bright field images. Imaging settings were kept constant for each experiment. Image processing was carried out with LSM Image Browser (Zeiss) and plot profile from ImageJ.

For imaging of lipase (or LipVes) and DGGR loaded NP-Graft entrapped multicompartments, we added 30 µL of these multicompartments in 232.5 µL PBS with DTT (30 µL, 100 mM) or PBS (262.5 µL) for the controls. Additionally, we added Orlistat (7.5 µL, 2.5 mM) to the 8-well chambers to assure the inactivation of non-encapsulated lipase or LipVes outside of the giant vesicles. The activity in giant vesicles after 2, 24 and 48 hours of incubation in presence of DTT was assayed via CLSM, exciting at 561 nm using beam splitter MBS 488/561 and pinhole of 44 µm.

To study the induced incorporation of gA for the import of sodium ions into the giant vesicles, we added gA loaded NP-Graft and ANG2 entrapped multicompartments (20 µL) in PBS (250 µL) and DTT (30 µL, 100 mM) in PBS or HEPES buffer for the controls to the 8-well. For studying of the export of sodium ions through the gA pores, we added gA loaded NP-Graft (20 µL) and sodium ions entrapped multicompartments, ANG2 (20 µL, 100 µM) in HEPES (300 mM), HEPES (50 µL, 300 mM) and DTT (10 µL, 100 mM) in HEPES (300 mM) or HEPES (300 mM) for the control to the observation chamber. For the two-type multicompartment, Na^+Ves, gA loaded NP-Graft and ANG2 co-loaded into giant vesicles, where these multicompartments (20 µL) were added to DTT (20 µL, 100 mM) and HEPES (160 µL, 300 mM, pH 7.2) or in HEPES (180 µL, 300 mM, pH 7.2) for the controls to the 8-well observation chamber. A 488 nm diode laser, beam splitter MBS 488 and a pinhole of 40 µm was used.

For Actin GUV CLSM imaging we used a 488 nm diode laser for actin filaments and a 633 nm for Bodipy630/650 adsorbed GUV membrane. To induce actin polymerization within the polymeric GUVs, we added Actin GUVs (30 µL) with salt/pore solutions (i) KCl (250 µL, 200 mM) and gA (2 µL, 1 mM), (ii) $MgCl_2$ (250 µL, 150 mM) and IoNo (2 µL, 1.3 mM) and (iii) $CaCl_2$ (250 µL, 150 mM) and IoNo (2 µL, 1.3 mM). As a control we used salt-free HEPES (250 µL, 300 mM, pH 7.2) with or without pores (2 µL). For inducing actin polymerization in multicompartments, we added Actin MCs (20 µL) in corresponding salt solution (250 µL) and DTT (30 µL, 100 mM) and as the control we used HEPES (300 mM, pH 7.2). Here,

no pores were added additionally to the surrounding giant solution. By summing up several confocal fluorescence images along the z-axis in the equatorial plane (x-y plane), we could extract z-stack projections of Actin GUVs/MCs with filaments out-of-plane. For the compartmentalized actin samples, we added Bodipy630/650 (10 µL, 72 µM) to each well of the observation chamber to visualize the GUV membrane.

9.1.11 Fluorescence Correlation Spectroscopy

Fluorescence correlation spectroscopy (FCS) experiments were carried out with an inverted laser scanning confocal microscope (LSM 880 and LSM 510-META/Confocor2, Carl Zeiss) using a water immersion objective (Zeiss C/Apochromat, M=40, NA=1.2). A helium/neon laser (wavelength 633 nm) and an Argon laser (wavelength 488 nm) with appropriate filters (MBS 488/56/633 for 633 nm laser; MBS 488 for 488 nm laser) were used. The fluorescence intensity was recorded on an avalanche photodiode. The pinhole size (19 µm for 633 nm laser and 45 µm for 488 nm laser, 1AU) was adjusted before recording FCS curves of the respective free dye.

For the calibration of the confocal volume, the diffusion constants of the nanostructures and the free dye were used. Free fluorophores were measured for 5 s at RT with 30 measurements recorded, whereas dye loaded nanostructures were measured for 10 s with 10 repeats. Typically, 80% of the FCS curves were suitable and included in the analysis. The experimental autocorrelation curves were fitted according to the following equation for samples with one component diffusion model:

$$G(\tau) = 1 + \frac{1}{N}\left[\frac{1}{1+\frac{\tau}{\tau_D}}\frac{1}{\sqrt{1+R^2\frac{\tau}{\tau_D}}}\right]$$

Equation 10

Where N represents the average number of particles in the observation volume, τ_D is the diffusional correlation time, and R is the structural parameter which was set to 5. In the next equation, the diffusion coefficient D was calculated using the relation between τ_D and the x-y dimension of the confocal volume (ω_{xy}).

$$\tau = \frac{{\omega_{xy}}^2}{4D} \qquad (15)$$

Equation 11

The Einstein-Stokes equation using the diffusion coefficient *D*, the Boltzmann's constant k_B, absolute temperature *T*, viscosity of the surrounding medium η was used to calculate the hydrodynamic radius (R_H) of the nanostructures.

$$D = \frac{k_B T}{6\pi\eta R_H} \qquad (16)$$

Equation 12

Multicompartments were located in microscopy chambers in the bright field imaging mode of the CLSM and a focus in the center of a giant vesicle was marked. Due to higher density (encapsulated sucrose) compared to the outer solution (buffer), the giant vesicles sank to the bottom of the observation chamber. This allowed us to first identify the center of the giant vesicles by bright field imaging and positioning of the confocal volume accordingly, followed by FCS measurement to obtain the corresponding diffusion times. Subsequently, ten times 10 s were recorded at RT for each FCS measurement cycle per multicompartment. After the recordings were normalized and fitted. For the analysis, a customized python script (available on request)[61] was applied to select good fits. Only measurements in the lumen of the giant vesicles, to detect the subcompartments were targeted. Giant vesicles that were moving out of focus during the measurements were also excluded from the analysis. Processing was the same for individual FCS/CLSM measurements. Diffusion time count rate (CR), CPM, numbers of particles, and hydrodynamic diameter from individual FCS measurements were averaged. The data extracted from the FCS data (*N*, CR) were presented as average +/- standard error of mean (SEM) from 40 measurements that were based on at least three independent samples for each type of multicompartment, except the time point at 8 h that was from 5 measurements. Data were statistically analyzed by one-way ANOVA (analysis of variance) using a customized python script (available on

request). Additionally, HSD (honestly significant difference procedure) test for comparing differences between multiple groups was run if significant differences was found ($p<0.05$).

For Actin-MCs, we co-loaded giant polymersomes with SRB loaded polymersome and IoNo loaded NP-Graft. After 24 h incubation of DTT or HEPES for control we measured FCS using a 561 laser (wavelength 561 nm, 1 AU) utilizing a beam splitter of MBS 488/561 to study the viscosity changes.

9.1.12 Transmission Electron Microscopy

Nanostructures (5 µL) were adsorbed on copper grids for 1 min, washed with water, and blotted to remove excess liquid. Specimens were negatively stained with uranyl acetate (2%) for 15 sec, washed and blotted. Transmission Electron Microscopy (TEM) micrographs were recorded on a Philips CM100 with an accelerating voltage of 80 kV.

9.1.13 Pyrene-F-Actin polymerization assays

For pyrene-F-Actin (10%, Hypermol, rabbit alpha-actin skeletal muscle, 99% purity) in 100 mM of the salts buffers (KCl, $MgCl_2$, $CaCl_2$) and as a control in salt-free HEPES (300 mM, pH 7.2) were added to 300 mM sucrose (final volume 200 µL), in a black flat-bottomed 96-well plate (Thermo Fisher Scientific). The measurements were carried out with a SpectraMax M5e microplate reader (Molecular Devices), followed for 90 minutes. Ex/Em 365/407 nm.

9.1.14 Preparation of Actin GUVs for 3D-SIM.

Actin GUVs (15 µL), IoNo (2 µL, 1.3 mM) and $MgCl_2$ or $CaCl_2$ (275 µL, 150 mM) were added each in a well of a sterile obervation chambers (µ-Slide 8 Well Glass Bottom, #1.5H, Ibidi). In addition, Actin GUVs (15 µL), gA (2 µL, 1 mM), and KCl (275 µL, 200 mM) were added to a well. All salt solutions contained NaN_3 (0.02%) and the sample was incubated for 48 h in the fridge for the actin polymerization.

9.1.15 3D-SIM super-resolution Microscopy

Three-dimensional structured illumination microscopy (3D-SIM) was performed on a DeltaVision OMX-Blaze V4 system (GE Healthcare) equipped with 405, 445, 488, 514, 568 and 642 nm solid-state lasers. Images were acquired using a Plan Apo N 60x, 1.42 NA oil immersion objective lens (Olympus) and 4 liquid-cooled sCMOS cameras (pco.edge 5.5, full frame 2560 x 2160; PCO). Exciting light was directed through a movable optical grating to generate a fine-striped interference pattern on the sample plane.

The pattern was shifted laterally through five phases and three angular rotations of 60° for each z section. The 488 nm laser line was used and the optical z-sections were separated by 0.125 µm. Laser power was attenuated to 50% with an exposure of 20 milliseconds.

9.1.16 3D-SIM Image Reconstruction

Raw 3D-SIM images were processed and reconstructed using the DeltaVision OMX SoftWoRx software package (v6.1.3, GE Healthcare). The resulting size of the reconstructed images was of 512 x 512 pixels from an initial set of 256 x 256 raw images. The channels were aligned in the image plane and around the optical axis using predetermined shifts as measured using a target lens and the SoftWoRx alignment tool.

9.1.17 Enzymatic Assays

Enzymatic fluorescence assays were performed using a Spectramax M5 microplate reader (Molecular Devices), in a black flat-bottomed 96- well plate (Thermo Fisher Scientific), final volume in either PBS (200 µL) or sucrose (200 µL, 300 mM). The increase of fluorescence (ex: 529 nm, em: 600 nm) was monitored for 20 minutes at RT and measured in triplicate. With respect to the experiment, lipase was added to a final concentration of 10 µg/mL, DGGR (25 µM), DTT (10 mM), Orlistat (655 µM) and the DGGR loaded NP-Graft (10 µL) suspension were added.

9.1.18 Quantification of actin inhibition

Actin MCs with Iono NP-Graft were prepared as previously described. Together with 10 mM DTT, LatA, ChaetA, CytB and CytD were added to a final concentration of 0.2 mM. GUVs in random locations were imaged with z-stacks, in order to localize any possible filament (between a minimum of 15 to a maximum of 50 GUVs per sample, depending on the sample). The image series were then analyzed, to count the amount of GUVs with polymerized actin still visible after treatment, which was related to the untreated sample (set as 100%). The standard deviation was calculated for a binomial distribution. The values were compared through with one-way ANOVA, significance was determined with *post hoc* Tukey's test.

9.2 Chapter 4

9.2.1 Materials

Dulbecco's Modified Eagle Medium with 4.5 g L^{-1} D-Glucose (DMEM-GlutaMax) was purchased from Gibco life technologies. Fetal calf serum (FCS) was purchased from BioConcept. CellTiter 96® Aqueous One Solution Cell Proliferation Assay (MTS) was purchased from Promega. Soluble guanylyl cyclase was purchased from SantaCruz Biotechnology (USA); DyLight 633 NHS ester and Fetal calf serum (FCS) were purchased from ThermoFisher Scientific (USA); mant-GTP (2'-(or-3')-*O*-(*N*-Methylanthraniloyl) Guanosine 5'-Triphosphate, Trisodium Salt) was purchased from Jena Bioscience (Germany); Nitric Oxide Cofactors (NOC) mix containing flavin adenine dinucleotide (FAD), flavin mononucleotide (FMN), and calmodulin was purchased from Oxford Biomedical Research (USA). FluoroBrite Dulbecco's Modified Eagle Medium (DMEM) live cell imaging medium was from Gibco Life Sciences (USA). All The triblock copolymer $PMOXA_6$-$PDMS_{44}$-$PMOXA_6$ was kindly provided by Prof. Meier and synthetized by Dr. Samuel Lörcher and Dr. Adrian Dinu.[87, 177] All other reagents and enzymes were purchased from Sigma-Aldrich unless otherwise specified.

9.2.2 OmpF expression and extraction

Wild-type OmpF was obtained according to a previously reported protocol,[29a] with a few modifications: bacteria was grown at 30 °C for 6 hours on Terrific Broth (TB) (Difco, USA) and all ultracentrifugations were performed at room temperature (RT).

9.2.3 Preparation of catalytic nanocompartments

All CNCs were prepared at RT using the triblock copolymer $PMOXA_6$-$PDMS_{44}$-$PMOXA_6$ (obtained according to a previously reported procedure[87]) and wild-type OmpF, via the film rehydration technique. Films were rehydrated to a final polymer concentration of 4 mg mL^{-1} with 0.25 mg of UOX or HRP in PBS (pH 7) and 50 µl of previously dialyzed OmpF (60 µg mL^{-1} final concentration) or an equivalent volume of dialyzed octyl glucopyranoside (Anatrace, USA) 3% for the non-permeabilized CNC. Samples were extruded through an Avanti mini-extruder (Avanti Polar Lipids, USA) with a 200 nm pore diameter polycarbonate membrane (11 times). Non-encapsulated enzyme was removed through size exclusion chromatography (SEC) (Sepharose 4B column; 30 cm length).

9.2.4 CNC characterization — Static and Dynamic light scattering

9.2.4.1 Chapter 4.1

Light scattering (LS) experiments were performed at 25 °C, using an ALV/CGS–8F goniometer (Langen/Hessen, Germany) equipped with a frequency-doubled He-Ne laser (LS instruments, λ = 633). Static light scattering (SLS) was performed in 5° steps between 50° and 135° and analyzed with Zimm plot software (LS Instruments). Dynamic light scattering (DLS) was performed at 90° and analyzed through nonlinear decay-time analysis supported by cumulant fit.

9.2.4.2 Chapter 5

SLS and DLS experiments were performed on a setup from LS instruments (Switzerland), equipped with a He-Ne 21 mW laser (λ = 632.8 nm) at scattering angles from 30° to 55° at 25 °C. The radius of gyration (R_g) was obtained from the SLS data with a Guinier plot. The intensity versus angle curve of a diluted sample (to supress multiple scattering) was fit with a linear regression and the slope of the curve *m* was used to calculate R_g according to the equation

$$R_g = 10^9 \times \sqrt{3m}$$

Equation 13

In the case of DLS, second order cumulant analysis of the data between 30° and 155° was performed to obtain the hydrodynamic radius (R_h).

9.2.5 CNC characterization — Transmission electron microscopy (TEM)

CNC suspensions in PBS at 0.25 mg mL^{-1} were deposited on glow-discharged carbon grids (Quantifoil, Germany) stained with 1.5% uranyl acetate solution and deposited on carbon-coated copper grids. A transmission electron microscope (Philips Morgagni 268D) at 293 K was used.

9.2.6 CNC characterization — Fluorescence correlation spectroscopy

9.2.6.1 Chapter 4.1

Vesicles were labeled with BODIPY 630/650 SE (Thermo Fisher Scientific, USA) 100 nM. All measurements were carried out using a CLSM 880 confocal laser microscope (Carl Zeiss, Germany) with a 40x, 1.2 water immersion C-Apochromat objective lens. Measurements were performed at RT using a sample volume of 20 µL on a 22x50 mm glass slide. A HeNe laser at 633 nm was used for excitation of the BODIPY fluorophore, at 1% attenuation and pinhole 62 µm. The fluorescence signal was measured in real time and the autocorrelation function was calculated by the software calculator QuickFit 3.0.[178]

Measurements were recorded over 5 s and each measurement was repeated 30 times. Experimental auto correlation curves were fitted using a two-component model including triplet state, slightly modifying Equation 10:

$$G(\tau) = 1 + \left(1 + \frac{T}{1-T} e^{-\frac{\tau}{\tau_{trip}}}\right) \frac{1}{N} \left(\frac{f_1}{1 + \frac{\tau}{\tau_{D1}} \sqrt{1 + R^2 \frac{\tau}{\tau_{D1}}}} + \frac{f_2}{1 + \frac{\tau}{\tau_{D2}} \sqrt{1 + R^2 \frac{\tau}{\tau_{D2}}}} \right)$$

Equation 14

Where f_1 and f_2 are respectively the fraction of the particles of the corresponding component 1 (dye) or 2 (vesicles), τ_{D1} represents the diffusion time of the dye and τD_2 the diffusion time of the vesicles, T the fraction of fluorophores in triplet state with triplet time τ_{trip}, N is the number of particles and R the structural parameter, fixed at 5, according to the manufacturer's guidelines. The τ_{trip} and τ_D of free dye were determined independently, and subsequently fixed in the fitting procedure for dye-stained vesicles. The confocal volume of 1 fL, was obtained by a calibration with free BODIPY and was necessary to determine the concentration of fluorescent particles (knowing the number of particles detected in the volume).

9.2.6.2 Chapter 5

Stock solutions of iNOS (5 mg mL^{-1}) and GC (5 µg mL^{-1}) were prepared in 0.1M Na_2CO_3 buffer. 5µL of a 1.5 mM Atto-488 NHS ester in DMSO solution was added to 1 ml of the iNOS stock solution and 5µL of 1.5 mM DyLight 633-NHS ester in DMSO was added to 1 ml of sGC solution. Both labelling reactions were mixed overnight at 4 ºC. Free dye was removed by dialysis (Spectrapore dialysis tube, MWCO 12kDA, Spectrum Laboratories Inc) against PBS at 4 ºC for 3 days with frequent buffer exchanges. Upon purification, labelled enzymes were used directly and polymersomes were formed as previously described. Labelled sGC was recovered from an OmpF-free sample and used for quantification. A 488nm argon laser was used to excite ATTO 488 and a 633 nm HeNe laser was used for DyLight633 and BODIPY 630/650. The two lasers were passed through MBS488 and MBS488/561/633 filters and the signals were detected in the range of 500-532 nm and 657-690 nm, respectively. The pinholes were adjusted to maximize the count rate using the respective free dye in PBS and the sample volumes were 20 µL. Fluorescent fluctuations over time were recorded for 20 x 5 s. The raw data was processed and analyzed using Zeiss software. Autocorrelation curves were fitted by a two-component model (except for dye-only samples).

The degree of labelling (DOL) was obtained from the ratio of the counts per molecule (CPM)

$$DOL = \frac{CPM_{labelled\ enzyme}}{CPM_{free\ dye}}$$

Equation 15

and, similarly, the number of enzymes per vesicle was calculated as

$$N_{enzymes} = \frac{CPM_{vesicle}}{CPM_{labelled\ enzyme}}$$

Equation 16

To confirm that the increase in enzyme diffusion times originated only from their encapsulation, BODIPY 630/650 was used to label the vesicles' membranes and compare τ_{D2} (vesicles). A fraction of less than 1% of free dye was detected in this case.

The R_h of the vesicles was calculated, assuming a spherical object, deriving the Stokes-Einstein relation (Equation 12)**.**

9.2.7 Nanoparticle tracking analysis (NTA)

NTA was used as further analysis of particle size and concentration, on a NanoSight NS300 (Malvern Panalytical Ltd., UK), using a flow cell (100 µL min^{-1}), 1:1000 concentration in freshly filtered PBS, yielding particle R_h and concentration (particle mL^{-1}).

9.2.8 Enzyme quantification

9.2.8.1 Chapter 4.1

The non-encapsulated enzyme fraction was recovered via SEC and the enhanced Pierce™ Bicinchonic Acid (BCA) assay was performed according to the supplier's protocol (Thermo Fisher Scientific, USA); instead of the BSA standards, both UOX (35 U mg^{-1}) and HRP (300 U mg^{-1}) calibration curves were prepared for the quantification of the respective samples. The amount of unencapsulated protein was multiplied by the volume recovered from the column and then subtracted from the amount initially added to the rehydration solution, yielding the total amount of enzymes within the vesicles, divided by the volume of the vesicle (first fraction), i.e. the final concentration of the protein. This was performed on samples with no inserted OmpF, assuming that the presence of the porin would not influence the

encapsulation efficiency. The number of enzyme molecules was then divided by the number of vesicles, obtaining the number of enzymes per vesicle.

9.2.8.2 Chapter 5

For iNOS, the unencapsulated protein was recovered and quantified using the bicinchonic acid assay (BCA) kit from ThermoFisher Scientific, and a BSA calibration curve. As the expected final sGC concentration was below the lower sensitivity limit for BCA (5 µg mL^{-1}), unencapsulated DyLight 633-labelled sGC was recovered and its absorbance at both 280 and 627 nm was measured with Nanodrop 200 UV-Vis spectrophotometer (ThermoFisher Scientific).

The DOL was confirmed using the equation:

$$DOL = \frac{A_{max}\ \varepsilon_{prot}}{(A_{280} - A_{max}\ C_{280})\ \varepsilon_{max}}$$

Equation 17

The protein concentration measured at 280 nm was estimated for a 70 kDA protein (BRENDA) with ε=72000 M^{-1} cm^{-1} (eXPAsY).

The total amount of both unencapsulated iNOS and sGC was calculated based on the volume and subtracted from the amount originally added, yielding the total concentration in CNCs and the encapsulation efficiency.

9.2.9 Enzyme activity and kinetics

9.2.9.1 Chapter 4.1

Kinetic parameters were calculated using the Michaelis-Menten model:

$$v = \frac{V_{max}[S]_0}{K_M + [S]_0}$$

$$k_{cat} = \frac{V_{max}}{[E]_0}$$

Equation 18

Where v is the velocity of the enzyme, V_{max} is the maximum velocity at saturating concentration, $[S]_0$ is initial the concentration of the substrate S, K_M is the Michaelis-Menten constant. k_{cat} is the turnover number, the number of chemical conversions per second, $[E]_0$ is the concentration of catalytic sites (both for UOX and HRP it is equivalent with the concentration of enzyme).

In all experiments involving a cascade reaction, UOX was added in excess to HRP, to partially compensate for the former enzyme's lower activity, so that the ratio between production (from UOX, 35 U mg^{-1}) and consumption (from HRP, 350 U mg^{-1}) of hydrogen peroxide would not be the limiting factor. All enzymatic measurements were performed using a Spectramax M5 microplate reader (Molecular Devices, USA), in a in a 96-well, flat bottomed UV-transparent plate (Corning, USA) for uric acid absorbance (290 nm) or in a black plate (Thermo Fisher Scientific) for resorufin fluorescence (excitation 570 nm / emission 595 nm). The final volume in each well was of 200 µL in PBS. UOX concentration was increased ten-fold in cascade reaction experiments, to counter the slower native activity per weight of the enzyme, compared to the downstream enzyme HRP. Both uric acid consumption and resorufin production were quantified by means of calibration curves ($R^2 > 0.9$ for both curves). Each experiment was performed in triplicate and data was collected over 15 minutes (10 for the measurement of kinetic parameters).

9.2.9.1.1 UOX kinetics

UOX or UOX-loaded CNC (final concentration of 3 µg mL^{-1}) were incubated in presence of increasing concentrations of the substrate uric acid (25, 100, 200, 400 and 800 µM) and the initial velocity of the enzymatic reaction was determined. The consumption of uric acid was monitored and the data fitted with Graphpad Prism 7 software, obtaining K_M, V_{max} and k_{cat} values.

9.2.9.1.2 HRP kinetics

HRP or HRP-loaded CNC (final concentration of 3 µg mL^{-1}) were incubated in the presence of 10 µM H_2O_2 and increasing concentrations of Amplex Ultra Red (AR) (Invitrogen) ranging from 0.2 to 20 µM. The initial velocity of the enzymatic reaction was determined by monitoring the formation of resorufin. The data was fitted using Graphpad Prism 7 software, obtaining K_M, V_{max} and k_{cat} values.

9.2.9.1.3 UOX-HRP cascade kinetics

Both reactions were examined when in a cascade: UOX or UOX-loaded CNC (final concentration of 3 µg mL^{-1}) were added to HRP or HRP-loaded CNC (final concentration 300 ng mL^{-1}) and both uric acid and AR were alternatively varied according to the previously listed concentrations.

9.2.9.1.4 Amplex Ultra Red conversion assay in a cascade

The same cascade reaction was tested at different conditions: UOX or UOX-loaded CNC (final concentration of 3 µg mL^{-1}) were added to HRP or HRP-loaded CNC (final concentration 300 ng mL^{-1}), uric acid to a final concentration of 10 µM and AR to a final concentration of 1 µM, unless in controls

where either substrate was missing and was substituted by the same volume of PBS. The reaction profile in presence of catalase (1000 U mg^{-1}, final concentration of 10 µg mL^{-1}) was blanked against the reaction profile of catalase alone in presence of AR, as catalase too has a heme center capable of reacting with the fluorogenic molecule.

9.2.9.2 Chapter 5

Enzymatic assays were performed using a Spectramax M5e microplate reader (Molecular Devices, USA) in a 96-well, flat bottomed black plate (Thermo Fisher Scientific) for fluorescence. The final volume in each well was of 200 µL in PBS. Both free and encapsulated enzymes were added at the same concentration to compare the influence of encapsulation on their activity (50 µg mL^{-1} for iNOS and 0.05 µg mL^{-1} for sGC). For iNOS activity, 10 µM arginine was used as substrate and 4,5-diaminofluorescein (DAF-2) was used to detect the reaction, as it reacts with NO forming a fluorescent triazole (Ex. 495 Em. 515 nm)[179] and additional NADPH (final 25 µM) was added to the reactions, so that it was always in excess. Blanking was always performed.

For sGC activity assays, the same concentrations of arginine and NADPH were used, with 20 µM of mant-GTP added. Upon its conversion to mant-cGMP, it increases its fluorescence (Ex. 280 Em. 430 nm). [180] When mant-GTP was co-encapsulated, the values were blanked with a vesicle only solution. For long-running measurements (12 hours), a quartz cuvette was instead used, volume 2.5 mL, with the same concentrations as above.

9.2.10 Catalytic nanocompartment resilience to degrading agents

Concentrations were 3 µg mL^{-1} for UOX or UOX-CNC and 300 ng mL^{-1} for HRP or HRP-CNC. For the heat resistance assay, aliquots of the polymersome were incubated at 37, 50, 60 and 75 °C for either 10 or 30 minutes. For the chemical and enzymatic resistance assays, aliquots were incubated with 6 M guanidine hydrochloride (GdnHCl) for 1 hour and 0.1 mg ml^{-1} Proteinase K for 2 hours (37 °C), respectively. The production of resorufin was compared to that of the cascade reaction with no additional elements and the ratio was calculated. To verify unspecific binding, the same amount of enzyme (either UOX or HRP) was added to pre-formed empty vesicles and then purified with the same protocol, then mixed with vesicles encapsulating the other enzyme and the cascade kinetics were followed.

9.2.11 Activity of CNCs in serum

Activity in biological fluid was tested in human blood serum (instead of PBS) in which uric acid was dissolved to a final concentration of 500 µM at 37 °C, mimicking hyperuricemia. UOX or UOX-CNCs were added to reach a final concentration of 18 µg ml^{-1}, HRP or HRP-CNC to 900 ng ml^{-1}, AR to 10 µM. The decrease of absorbance at 290 nm was monitored over the course of 6 hours. The degradation of uric acid was defined as

$$Relative\ urate\ degradation = \frac{\frac{\Delta Abs290_{with\ enzyme}}{min}}{\frac{\Delta Abs290_{no\ enzyme}}{min}}$$

Equation 19

9.2.12 Dependence of distance over reaction efficiency

Knowing the amount of CNCs in a given volume as a result of FCS measurements, it was possible to calculate the mean inter-vesicle distance, assuming a cubic space occupied by the compartments, as

$$\frac{1}{\sqrt[3]{\frac{N}{V}}}$$

Equation 20

where N is the number of particles (sum of UOX and HRP vesicles) and V is the reaction volume. UOX-CNCs were kept at constant concentration and HRP-CNCs were added in concentrations 2x, 1x, 0.5x, 0.25, 0.1x, 0.02x, 0.01x and 0.005x, thus increasing the overall distance between vesicles, which was calculated with $N=N_{UOX\text{-}}CNC+N_{HRP\text{-}}CNC$. Again, resorufin production was monitored as described.

9.2.13 Cell culturing

9.2.13.1 Chapter 4.1

HEK293T cells were cultured in a humidified atmosphere with 5% CO_2 at 37 °C in Dulbecco's Modified Eagle Medium with GlutaMAX^{TM}-I (4.5 g L^{-1} D-Glucose, Gibco life technologies)) and supplemented with 10% Fetal calf serum (FCS, BioConcept), 100 U mL^{-1} penicillin and 100 µg mL^{-1} streptomycin (Sigma Aldrich).

9.2.13.2 Chapter 5

HeLa cells (epithelioid cervix carcinoma, human; ATCC, CCL-2) were cultured in DMEM with GlutaMAX^{TM}-I supplemented with 10% fetal calf serum (FCS), 100 units/mL penicillin and 100 µg/mL Streptomycin. C2C12 cells (muscle myoblasts, mouse, ATCC, CRL-1772) were cultured in DMEM with GlutaMAX^{TM}-I supplemented with 20% FCS, 100 units/mL penicillin and 100 µg/mL Streptomycin. Cells were maintained at 37 ^{o}C and 5% CO_2.

9.2.14 Cell viability assay-MTS

For cell viability assessment, a CellTiter 96® Aqueous One Solution Cell Proliferation Assay (MTS, Promega) was used according to manufacturer instructions. Cells were seeded (5 000 cells/well in 100 µL cell culture medium) in a 96-well plate and incubated for 24 h. After 24 h the UOX-HRP-CNCs (concentrations ranging from 1.18 to 18 µg mL^{-1} of total polymer) were diluted in PBS and added to the cells to reach a final volume of 200 µ/well. After 24 h incubation in presence of the CNCs, 20 µL MTS reagent was added to each well. After 4 h absorbance was measured at 490 nm using a Spectramax M5e plate reader. Background absorbance from control wells containing all assay components without cells was subtracted from each well and data normalized to control cells containing all components except CNCs.

9.2.15 Cell viability in presence of uric acid

Cells were seeded at a density of 5 000 cells/well in 100 µL cell culture medium, in a 96-well plate and incubated for 24 h. Next, cells were dosed with 250 or 500 µM of uric acid, final concentration, in the presence or absence of UOX-HRP-CNCs (18 µg mL^{-1} for UOX and 0.9 µg mL^{-1} for HRP, final concentrations in 200 µL final volume) or in the presence of free enzymes (UOX and HRP) at the same concentration. AR (1 µM, final concentration in 200 µL final volume) was added to each well as a co-substrate for the HRP-CNCs. After a 24 h incubation period, 20 µL MTS reagent was added to each well. The absorbance was measured at 490 nm after 4 h. Background absorbance from control wells containing all assay components apart from the cells was subtracted from each well and data normalized to control cells containing all components except CNCs and uric acid.

9.2.16 Live cell imaging of Hela cells

Freshly trypsinized HeLa cells were seeded at a density of 6 x10^4 cells per well in an 8-well glass bottom ibidi plate. After 24 h, the cell supernatant was removed and replaced with 0.1 mM Fluo-4-AM in

FluoroBrite DMEM live cell imaging medium supplemented with 10% FCS and 1% Penicillin/Streptomycin. The cells were incubated for 20 min in presence of the calcium sensitive dye, followed by rinsing 3 times and addition of 300 µL live cell imaging medium. The cells were then dossed with 100 µL of either (a) 1 mg mL^{-1} iNOS-CNCs and 1 mg mL^{-1} sGC-CNC in PBS; (b) 1 mg mL^{-1} iNOS-CNC in PBS alone; (c) 1 mg mL^{-1} sGC-CNC in PBS alone; (d) 2 mg mL^{-1} empty polymersomes as an internal control to ensure the polymer does not cause interference; (e) 0.22 mM NO-donor SNAP and 0.2 mM cGMP in PBS as a positive control; (f) PBS only as a negative control.

After dosing, cells were immediately visualized by confocal laser scanning microscopy (CLSM) on a LSM 880 confocal laser microscope with a 40x, 1.2 water immersion C-Apochromat objective lens, using ATTO 488 laser and light path parameters. Cells were imaged continuously for 12 hours, in an enclosed incubator at 37 °C and 5% CO_2, with 1 frame/minute capture and constant diffraction-based refocusing.

To visualize the CNC uptake and also determine the effect of the CNCs after uptake, the procedure described above was slightly modified. Cells were plated at the same seeding density and cultured for 24 h. After 24 h the supernatant was removed and replaced with 300 µL supplemented DMEM and 100 µL of (a) 1 mg mL^{-1} iNOS-ATTO488-labeled CNCs and 1 mg mL^{-1} sGC-DY Light 633-labeled CNCs in PBS; or (b) 1 mg/mL^{-1} iNOS-CNCs and 1 mg mL^{-1} sGC-CNC in PBS. After a 24 h incubation the supernatant was removed. In the case of the fluorescently labelled CNCs, the cells were directly imaged via CLSM. In the case of the non-labelled CNCs (sample b above), the supernatant was replaced with the 0.1 mM Fluo-4-AM solution. The cells were incubated for 20 min in presence of Fluo-4-AM, followed by rinsing 3 times and addition of 400 µL live cell imaging medium.

9.2.17 Live cell imaging of C2C12 cells

Freshly trypsinized C2C12 cells were seeded at a density of $3x10^3$ cells per well in an 8-well glass bottom Ibidi plate. After 24 h, the cell supernatant was removed and replaced with differentiating medium (DMEM supplemented with 2% horse serum). The cells were differentiated for 5 days. After 5 days the supernatant was removed and replaced with 0.1 mM Fluo-4-AM in live cell imaging medium as described above. The cells were incubated for 20 min in presence of the calcium sensitive dye, followed by rinsing 3 times and addition of 300 µL live cell imaging medium. The cells were then dossed with 100 µL of either (a) 1 mg mL^{-1} iNOS-CNCs and 1 mg mL^{-1} sGC-CNC in PBS; (b) 0.22 mM NO-donor SNAP and

0.2 mM cGMP in PBS as a positive control; (c) PBS only as a negative control. After dosing, cells were immediately visualized by CLSM using the same settings described above for the HeLa live cell imaging.

To determine the effect of CNCs after uptake, the procedure described above was slightly modified. C2C12 cells were plated at the same seeding density and differentiated for 5 days as described above. After 5 days the supernatant was removed and replaced with 300 µL supplemented DMEM and 100 µL solution of 1 mg mL^{-1} iNOS-CNCs and 1 mg mL^{-1} sGC-CNC in PBS. After a 24 h incubation, the supernatant was replaced with the 0.1 mM Fluo-4-AM solution. The cells were incubated for 20 min in presence of Fluo-4-AM, followed by rinsing 3 times and addition of 400 µL live cell imaging medium.

9.2.18 Statistics

9.2.18.1 Chapter 4.1

Multiple t-tests were run using Graphpad Prism 7 software, comparing datasets, without assuming constant SD. Statistical significance ($p<0.05$) was corrected using the Holm-Sidak method. Significance was marked as * $p < 0.05$, ** $p < 0.01$, *** $p < 0.001$, sample size was always n = 3.

9.2.18.2 Chapter 5

Similarly, multiple t-tests were run using Originlab 2019 software, with the same parameters. Sample size was n = 3 for enzymatic assays, n = 11 for cell imaging assays.

9.3 Chapter 6

9.3.1 Materials

BODIPY 630/650 and ATTO 488-NHS ester were purchased from ThermoFisher Scientific (USA). FITC-melittin was purchased from Genscript (USA). All other reported compounds were purchased from Sigma-Aldrich (USA) unless otherwise stated.

9.3.2 Synthesis of amphiphilic copolymers

A small library of amphiphilic $PMOXA_x$-*b*-$PDMS_y$-*b*-$PMOXA_x$ triblock copolymers was synthesized according to a reported synthesis procedure (**Table 6**), and formed polymersomes by film rehydration method.[87, 146]

9.3.3 Preparation of GUVs

Stock solutions at 6 mg mL^{-1} block copolymers in ethanol were prepared. 40 µL of each copolymer stock solution was added to a 1.5 mL glass vial and dried overnight under vacuum. Next day, 300 µL of a 300

mM solution of sucrose containing 0.2% sodium azide was added to the dried polymer film and rehydrated overnight.

Melittin was added to the copolymer GUVs in three ways: I) co-dried with the copolymer to form a mixed copolymer film (co-dried), so that it would have a final 15 μM concentration after rehydration, II) added to the rehydration buffer of the copolymer film to a final concentration of 15 μM (in rehydration buffer) and III) added to pre-formed vesicle suspension, to a final concentration of 15 μM (*ex post*).

9.3.4 Confocal laser scanning microscopy (CLSM) of GUVs

GUVs were visualized in plasma-activated Nunc® Lab-Tek 8-well chambers (Thermo Fisher Scientific, USA), using Zeiss 880 CLSM microscope (Zeiss, Germany) with a water-immersion objective (C-Apochromat 40x/1.2 W Korr FCS M27).5 μL of GUV suspension was added to a final 5 μM solution of BODIPY 630/650 and, respectively i) 200 μM of carboxyfluorescein (CF), ii) 200 μM of sulforhodamine B (SRB), iii) 200 μM of ATTO 488 NHS ester iv) 0.1 mg mL^{-1} fluorescein isothiocyanate (FITC) conjugated to dextran 4000, v) FITC-dextran 10000 Da and vi) FITC-melittin in a total of 200 μL of PBS. .

GUVs (diameter ≥ 1 μm) were imaged, by BODIPY 630/650 staining the membrane to discriminate between hollow vesicles and spherical polymeric aggregates. To image the GUVs, 488 nm argon laser, 561 nm DPSS 5561-10 laser and 633 nm HeNe laser were used. For CF, ATTO 488-NHS ester and FITC, an argon laser (488 nm) was used, with 493-629 nm filters, MBS 488; for SRB a DPSS (561 nm) with 563-629 nm filters, MBS T80/R20; for BODIPY, a diode laser (633 nm) was used, MBS 488/561/633. Pinhole aperture was always 39 μm except for SRB experiments, where it was 41 μm. An n = 30 vesicles per sample was imaged and the fraction of filled vesicles was calculated.

The hydrodynamic radius R_h of CF (MW 376 Da), SRB (MW 558 Da) and ATTO 488-NHS ester (981 Da) was estimated according to the empirical ratio for small molecules, where MW is the molecular weight[181]

$$R_h = 0.00083327 \times MW + 0.18$$

Equation 21

The R_h for FITC-dextrans (4 kDa, 10 kDa) was obtained from Sigma Aldrich specifications.

9.3.5 Preparation of empty polymersomes

For nanometer-sized polymersomes, 4 mg mL^{-1} of copolymer solutions in ethanol were dried and rehydrated with 1 mL PBS for 24 h under constant stirring. Either melittin or FITC-labeled melittin, to a final concentration of 15 µM, was added in three scenarios: i to the polymer solution and co-dried along with the polymer (co-dried), added to the rehydration (in rehydration buffer) and added to the polymersomes suspension (*ex post*). All polymersome solutions were extruded through an Avanti mini-extruder (Avanti Polar Lipids, USA) with 200, 100 or 50 nm polycarbonate membrane (11 times) and purified by size exclusion chromatography (SEC) (Sepharose 2B column; 20 cm length).

9.3.6 Light scattering of polymersomes

The dynamic light scattering (DLS) measurements to determine the hydrodynamic radius (R_h) were performed on a Zetasizer Nano ZSP at 25 °C. 5 µL of polymersomes were added to an 800 µL PBS solution in the cuvette. The measurement angle was 173° and the data was analyzed by number distribution. Multi-angle DLS was performed on a setup from LS instruments (Switzerland), equipped with a He-Ne 21 mW laser (λ = 632.8 nm) at scattering angles from 30° to 150° at 25 °C. Second order cumulant analysis of the data for various angles was performed to obtain the R_h.

Static light scattering (SLS) measurement for $A_3B_{22}A_3$ was performed on a setup from LS instruments (Switzerland), equipped with a He-Ne 21 mW laser (λ = 632.8 nm) at scattering angles from 30° to 150° at 25 °C. The radius of gyration (R_g) was obtained from the SLS data using a MIE fit. The Intensity versus angle curve of a diluted sample (to suppress multiple scattering) was fit using the Mie scattering model (MiePlot, UK) for η=1.35 and 5% polydispersity. R_g was then calculated using the obtained R and the formula for a spherical structure: $R_g^2 = (3/5)R^2$.

$$R_g^2 = \frac{3}{5}R^2$$

Equation 22

9.3.7 Transmission electron microscopy (TEM)

4 µL of polymersomes (1:4 dilution) were absorbed on copper grids with 400 mesh square. The grids were further stained with 2% uranyl acetate and the negatively stained image of nanostructures was performed on a transmission electron microscope (Philips CM100) at an acceleration voltage of 80 kV.

9.3.8 Fluorescence correlation spectroscopy (FCS)

FCS measurements were obtained with a Zeiss 880 laser-scanning microscope in FCS mode. All measurements were performed at room temperature (RT) using a sample volume of 12 µL on a 22x50 mm, 1.5 mm thick glass slide. Free FITC-melittin was measured with a 488 nm argon laser, MBS 488, 1% attenuator, pinhole 34 µm, thirty repetitions for 2 seconds each. At the same conditions, 12 µL of FITC-melittin vesicles (prepared by "co-dried", "in rehydration buffer" and "*ex post*" procedures) were measured.

Experimental autocorrelation curves were fitted using: i) a one-component model including triplet state for the "co-dried" and "in rehydration buffer" preparation methods and ii) a two-component fit for "*ex post"* preparation method. The software ZEN 2.3 was used for analysis of the data, using Equation 10and Equation 14.

The ratio of the resulting average counts per molecules (CPM) yielded the average melittin monomers per vesicle m_v:

$$m_v = \frac{\frac{CPM_{melittin}}{4}}{CPM_{vesicles}}$$

Equation 23

$CPM_{melittin}$ was divided by 4 as in solution melittin assembles into a tetramer. The maximal amount of melittin pores was obtained based on the minimal number of peptides per pore (3).

$$n_{polymersome} = \frac{m_v}{3}$$

Equation 24

For melittin added to the copolymer film and to the rehydration buffer, the maximal number of pores in GUVs was simply extrapolated using:

$$n_{GUV} = \frac{R_{GUV} \times n_{polymersome}}{R_{polymersome}}$$

Equation 25

With R_{GUV} being the average radius measured from CLSM micrographs.

For melittin added to pre-formed polymersomes ("*ex post"*), a linear regression curve was fitted through the average number of polymersomes with different sizes and extrapolated to obtain the

corresponding R_{GUV}, which was then multiplied by the permeabilization efficiency of GUVs to SRB to obtain the curvature-corrected number of pores.

9.3.9 Dye leakage assay

4 mg mL^{-1} of copolymer was dried and then rehydrated with 1 mL of 250 µM solution of SRB. The solution was then extruded with 200, 100 and 50 nm filters and purified by SEC (Sepharose 2B, 20 cm column). Melittin solution in PBS (15 µM final concentration) was added to the polymersome suspension. SRB fluorescence intensity (excitation 565 nm / emission 586 nm) was measured using a Spectramax M5 microplate reader (Molecular Devices, USA), in a flat bottom black 96-well plate (Thermo Fisher Scientific), final volume of the sample 200 µL. The increase in fluorescence intensity was monitored after 20 minutes and related to the fluorescence of the same sample treated with 1% Triton X-100, yielding the maximum fluorescence value that would be achieved if the dye was completely free to diffuse.

9.3.10 Catalytic nanocompartment (CNC) formation and characterization

1 mL of 0.25 mg mL^{-1} GOX in PBS was added to 4 mg of dried copolymer film and upon rehydration overnight under constant stirring the solution was extruded, yielding a dispersion of GOX catalytic nanocompartments in PBS (GOX-CNC). 15 µM of melittin was added in three scenarios: i) co-dried together with the copolymers (co-dried), ii) in the rehydration buffer of the copolymer films (in rehydration buffer) and iii) in the solution of pre-formed polymersomes after their extrusion (*ex post*). All solutions were extruded with 200 nm filters and then purified by SEC as described above.

The non-encapsulated enzyme fraction, separated by SEC, was then recovered and measured at 280 nm with a Nanodrop 2000 UV-Vis spectrophotometer (Thermo Fisher Scientific, USA). The amount of un-encapsulated protein was multiplied by the volume recovered from the column and then subtracted from the amount initially added to the rehydration solution, yielding the total amount of enzyme molecules within the polymersomes, divided by the volume of the polymersome (first fraction), i.e. the final concentration of the protein. The calculation of the number of enzyme/polymersome was performed on samples with no melittin, because the presence of the hydrophobic peptide does not influence the encapsulation efficiency of hydrophilic enzymes. The concentration of GOX enzymes was obtained as 60 µg mL^{-1} in all cases.

All enzymatic tests were performed using the same concentration for the free and encapsulated enzymes (concentrations specified below), respectively with a fluorescence endpoint measurement after 5 minutes.

D-glucose (final concentration, 10 µM) and the fluorogenic Amplex Ultra Red (Thermo Fisher Scientific, USA) (final concentration 2.5 µM) were used to measure the activity of GOX-CNCs (Spectramax M5e, fluorescence excitation 570 nm / emission 595 nm). GOX, either free or encapsulated, and free HRP were used at final concentration of 1.5 µg mL^{-1} and 50 ng mL^{-1}, respectively.

9.3.11 Cryogenic transmission electron microscopy (Cryo-TEM)

A 4 µL aliquot of polymersome solution was adsorbed onto holey carbon-coated grid (Lacey, Tedpella, USA), blotted off with Whatman 1 filter paper and vitrified into liquid ethane at -178 °C using a Leica GP plunger (Leica, Austria). Frozen grids were transferred onto a Talos electron microscope (FEI, USA) using a Gatan 626 cryo-holder. Electron micrographs were recorded at an accelerating voltage of 200 kV and a nominal magnification of 57000 x, using a low-dose system (20 e^{-} $Å^{-2}$) and keeping the sample at low temperature. Micrographs were recorded on a CETA camera. Micrographs were obtained and the membrane thickness was measured as previously described.[95] Briefly, the polymersome micrographs were analyzed with ImageJ, measuring 30 times the length of the darker portion of the membrane. The pixel size on the images corresponds to 2.02 Å.

9.3.12 Statistical analysis of the datasets

Multiple two-sample t-tests were performed using Origin 2016 software, comparing datasets, without assuming constant standard deviation (SD). Statistical significance ($p < 0.05$) was corrected using the Holm-Sidak method. Significance was marked as * $p < 0.05$, ** $p < 0.01$, *** $p < 0.001$, sample size was $n = 30$ for single imaged GUVs and 3 replicates for polymersome experiments.

9.4 Chapter 6

9.4.1 Materials

DyLight 633 NHS ester and ATTO 488-NHS ester were purchased from ThermoFisher Scientific (USA). All other reported compounds were purchased from Sigma-Aldrich (USA) unless otherwise stated.

9.4.2 Synthesis of diblock copolymers

The COOH-terminated diblock $PMOXA_{12}$-*b*-$PDMS_{26}$ was synthesized according to the already reported procedure.[13] Briefly, OH-terminated $PMOXA_{12}$-*b*-$PDMS_{26}$ was dissolved into 5 mL anhydrous

chloroform, then succinic anhydride (6.5 mg, 0.066 mmol), 4-dimethylaminopyridine (1.32 mg, 0.011 mmol) and TEA (8.7 mg, 0.088 mmol) were added. After deoxygenating by three vacuum-argon cycles, the mixture was stirred for another 72 h at RT under the Ar atmosphere. Finally, 180 mg

colorless solid product was obtained after the ultrafiltration, yield 90%. ^{1}H NMR (400 MHz, $CDCl^{3}$): δ 3.20-3.60 ppm (m, 170H), 2.00-2.20 ppm (m, 115H), 1.50 ppm (b, 2H), 1.20 ppm (m, 4H), 0.80 ppm (t,

3H), 0.45 ppm (m, 4H), 0 ppm (m, 456H) (**Figure 70**). To produce $PMOXA_{12}$-*b*-$PDMS_{26}$-PEG-N_3, the polymer (100 mg) was then first dissolved into anhydrous chloroform, then 11-azido-3,6,9-trioxaundecan-1-amine (11.80 mg, 0.055 mmol), N, N'-dicyclohexylcarbodiimide (15.6 mg, 0.078 mmol) and 4-dimethylaminopyridine (1.2 mg, 0.01 mmol) were added into the above solution. After deoxygenating three times, the mixture was further stirred for another 48 h, at RT. Finally, a colorless solid product was obtained after the ultrafiltration.

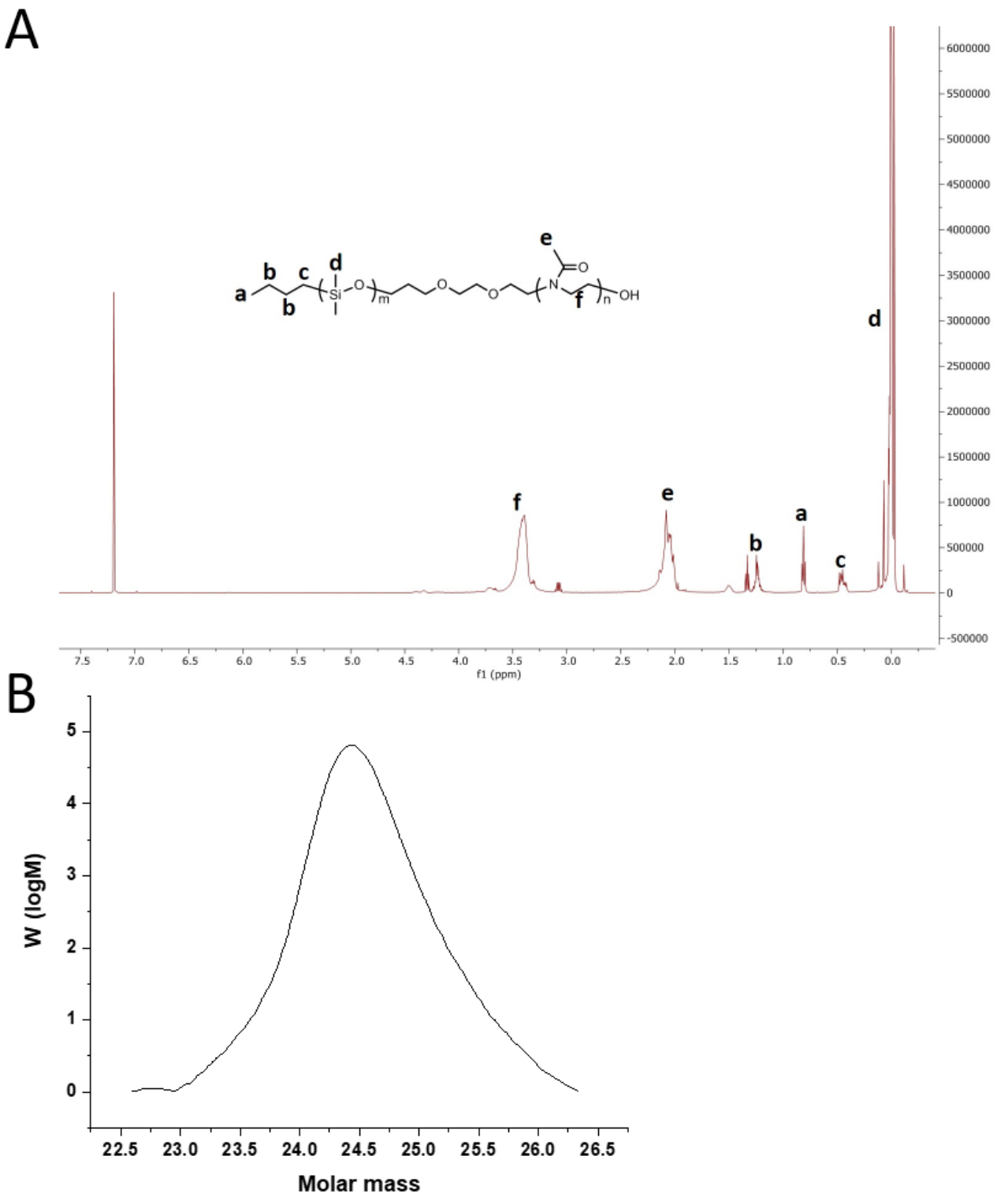

Figure 70 *(A) ^{1}H NMR spectra of PDMS26-PMOXA$_{12}$-COOH and (B) its GPC trace.*

9.4.3 Preparation of CNCs

CNCs were prepared at RT, with 50% (molar ratio) of the polymer . Films were rehydrated to a final polymer concentration of 10 mg mL^{-1} with 1 mg of GOX or LPO in PBS (pH 7) and 25 µl of melittin 1 mM (from bee venom). Samples were extruded through an Avanti mini-extruder (Avanti Polar Lipids, USA) with a 200 nm pore diameter polycarbonate membrane for GOX; LPO-CNCs were first extruded through 400 nm and then 200 nm, 11 times each. Non-encapsulated enzyme was removed through size exclusion chromatography (SEC) (Sepharose 4B column; 30 cm length).

9.4.4 Catalytic nanocompartment characterization — Static and Dynamic light scattering

SLS and DLS experiments were performed on a setup from LS instruments (Switzerland), equipped with a He-Ne 21 mW laser (λ = 632.8 nm) at scattering angles from 30° to 55° at 25 °C. The radius of gyration (R_g) was obtained from the SLS data with a Guinier plot. The intensity versus angle curve of a diluted sample (to supress multiple scattering) was fit with a linear regression and the slope of the curve *m* was used to calculate R_g according to the equation

$$R_g = 10^9 \times \sqrt{3m}$$

Equation 26

In the case of DLS, second order cumulant analysis of the data between 30° and 155° was performed to obtain the R_h.

Clustering was followed on a Zetasizer Nano ZSP (Malvern Instruments, UK) at 20 °C, where 50 µL of each DNA-functionalized CNC were added to 200 µL of PBS, measuring the R_h for 14 hours.

9.4.5 Catalytic nanocompartment characterization — Transmission electron microscopy (TEM)

CNC suspensions in PBS at 0.25 mg mL^{-1} were deposited on glow-discharged carbon grids (Quantifoil, Germany) stained with 1.5% uranyl acetate solution and deposited on carbon-coated copper grids. A transmission electron microscope (Philips Morgagni 268D) at 293 K was used.

9.4.6 Nanoparticle tracking analysis (NTA)

NTA was used as further analysis of particle size and concentration, on a NanoSight NS300 (Malvern Panalytical Ltd., UK), using a flow cell (100 µL min^{-1}), 1:1000 concentration in freshly filtered PBS, yielding particle R_h and concentration (particle mL^{-1}).

9.4.7 Enzyme quantification

Unencapsulated enzyme was recovered from melittin-less samples, and quantified at 280 nm, using a Nanodrop 2000 UV-Vis spectrophotometer.

9.4.8 DNA functionalization and clustering

200 µM Stock solutions of the DBCO-modified DNA strands (Microsynth, Switzerland) were prepared in nuclease-free water. 50 µL of each solution was added to 150 µL of corresponding CNCs, and made to react at 37 °C overnight. The vesicles were thus purified with a 10 cm-Sepharose 2B column, mixed 1:1 (volumetrically) and let to rest at 4°C overnight to allow clustering for further experiments.

9.4.9 Fluorescence correlation spectroscopy

Stock solutions of GOX (2 mg mL^{-1}) and LPO (2 mg mL^{-1}) were prepared in 0.1M Na_2CO_3 buffer. 5µL of a 1.5 mM Atto-488 NHS ester in DMSO solution was added to 1 ml of the GOX stock solution and 5µL of 1.5 mM DyLight 633-NHS ester in DMSO was added to 1 ml of LPO solution. Both labelling reactions were mixed overnight at 4 ºC. Free dye was removed by spin filtration with Amicon Spin Filters 30 MWCO (Merck, Germany). Upon purification, labelled enzymes were used directly and polymersomes were formed as previously described, with no melittin added. A 488nm argon laser was used to excite ATTO 488 and a 633 nm HeNe laser was used for DyLight633. The two lasers were passed through MBS488 and MBS488/561/633 filters and the signals were detected in the range of 500-532 nm and 657-690 nm, respectively. The pinholes were adjusted to maximize the count rate using the respective free dye in PBS and the sample volumes were 15 µL. Fluorescent fluctuations over time were recorded for 20 x 5 s. The raw data was processed and analyzed using Zeiss software. Autocorrelation curves were fitted by a two-component model (Equation 12), except for dye-only samples.

The degree of labelling (DOL) was obtained from the ratio of the counts per molecule (CPM) (Equation 15).

To quantify DNA, 11T-less strands (thus, 22a and 22b) were used, labeled with Cy5 and ATTO488, respectively. An excess amount (10 µL of a 200 µM stock) was added to vesicles with complementary strands, clustered and then purified via SEC. Fits were defined using Equation 12, the amount of DNA per vesicles with Equation 15.

9.4.10 Enzymatic assays

Enzymatic assays were performed using a Spectramax iD3 microplate reader (Molecular Devices, USA) in a 96-well, flat bottomed transparent plate (Corning, USA) for absorbance. The final volume in each well was 200 µL in PBS.

9.4.10.1 GOX-CNC

20 µL of GOX-CNCs (with or without melittin), glucose (final concentration 60 µM), free LPO (final concentration 2 µg mL^{-1}) and ABTS (final concentration 50 µM) were added to each well. The change in absorbance at 420 nm was monitored for 10 minutes.

9.4.10.2 LPO-CNC

For LPO-CNCs, 20 µL of LPO-CNCs (with or without melittin), H_2O_2 (final concentration 10 µM) and ABTS (final concentration 50 µM) were added to each well. The change in absorbance at 420 nm was monitored for 10 minutes.

9.4.10.3 GOX-LPO cascade

Knowing the sample concentration after workup, GOX-CNC (free or clustered) were added at a final concentration of 8 µg mL^{-1} and LPO-CNC (likewise) to 7 µg mL^{-1}, with 60 µM glucose and 50 µM ABTS. To mimic a biological setting, the reaction was followed at 37 °C for 2.5 hours.

9.4.11 Live cell imaging of A549 cells

Freshly trypsinized A549 human carcinoma cells were seeded at a density of 6 $x10^4$ cells per well in an 8-well glass bottom ibidi plate. After 24 h, the cell supernatant was removed and replaced with fluorescently-labeled CNC clusters, or PBS. The cells were incubated for 24h in presence of the calcium sensitive dye, followed by rinsing 3 times and addition of 300 µL live cell imaging medium.

Cells were then visualized by confocal laser scanning microscopy (CLSM) on a LSM 880 confocal laser microscope with a 40x, 1.2 water immersion C-Apochromat objective lens, using ATTO 488 laser and DyLight 633 light path parameters.

9.5 List of abbreviations

Polymers

BCP	2-hydroxy-4-(methacryloyloxy)-benzophenone
P(Asp-AP)	Poly[(5-aminopentyl)-α,β-aspartamide
P(CPTMA-co-PEMA)	Poly(methacryloyloxy)ethyl camptothecin oxalate (CPTMA) and poly(methacryloyloxy)ethyl camptothecin oxalate 2-(piperidin-1-yl)ethyl methacrylate
P(S-co-TMI)	Poly(styrene-co-3-isopropenyl-α,α-dimethylbenzene isocyanate)
PAA	Poly(acrylic acid)
PAH	Polyallylamine
PB	Poly(butadiene)
PDA	Poly(dopamine)
PDEAEM	Poly(2-(diethylamino)ethyl methacrylate)
PDMIBM	Poly(3,4- dimethyl maleic imido butyl methacrylate)
PDMS	Poly(dimethylsiloxane)
PEG/PEO	Poly(ethylene glycol)/Poly(ethylene oxide)
PHPMA	Poly(2-hydroxypropyl methacrylate)
PHPMA-*co*-PPFMA	Poly(hexyl methacrylate)-*co*-poly(pentafluorophenyl methacrylate)
PIAT	Polyisocyanoalanine(2-thiophene-3-yl-ethyl)amide
PLGA	Poly(lactic-glycolic acid)
PLL	Poly(l-lysine)
PMA	Poly(methacrylic acid)
PMAc	Poly(methacrylic acid) co-(cholesteryl methacrylate)
PMOXA	Poly(2-methyloxazoline)
PNMD	Poly(*N*-isopropyl acrylamide)-block-Poly(methacrylic acid-co-3,4- dimethyl maleic imidobutyl methacrylate)
PNVP	Poly(*N*-vinyl pyrrolidone)
Poly(Ser-S-NI)	Polyserine 2-nitroimidazole modified via a thioether moiety
PPG	Poly(propylene glycol)
PS	Polystyrene
RGD	Arginylglycylaspartic acid

Proteins

AO	Ascorbate oxidase
ADH	Alcohol dehydrogenase
AGE	N-acyl-d-glucosamine 2-epimerase
Alc	Alcalase

CalB	Lipase B from *Candida antarctica*
Cat	Catalase
Ccox	Cytochrome C oxidase
CSS	CMP-sialic acid synthetase
cytC	Cytochrome C
GLDH	Glutamate dehydrogenase
GlpF	Glycerol facilitator
GOX	Glucose oxidase
GTR	Glutathione reductase
Hb	Hemoglobin
HRP	Horseradish peroxidase
Lac	Laccase
L-ASNase	L-asparaginase
iNOS	Inducible nitric oxidase synthase
LPO	Lactoperoxidase
Mb	Myoglobin
NAL	N-acetylneuraminate lyase
OmpF	Outer membrane protein F
PA	Penicillin acylase
PAL	Phenylalanine ammonia lyase
PAMO	Phenylacetone Monooxygenase
PGM	Phosphoglucomutase
RDH	Ribitol-dehydrogenase
sGC	Soluble guanylyl cyclase
SOD	Superoxide dismutase
Tr	Trypsin
UOX	Urate oxidase
α-HL	α-haemolysin
β-Gal	B-galactosidase

10 References

1. (a) Göpfrich, K.; Platzman, I.; Spatz, J. P., Mastering Complexity: Towards Bottom-up Construction of Multifunctional Eukaryotic Synthetic Cells. *Trends in Biotechnology* **2018,** *36* (9), 938-951; (b) Jia, H.; Schwille, P., Bottom-up synthetic biology: reconstitution in space and time. *Current Opinion in Biotechnology* **2019,** *60*, 179-187; (c) Brea, R. J.; Hardy, M. D.; Devaraj, N. K., Towards self-assembled hybrid artificial cells: novel bottom-up approaches to functional synthetic membranes. *Chemistry (Weinheim an der Bergstrasse, Germany)* **2015,** *21* (36), 12564-12570.

2. Alberts B, J. A., Lewis J, et al., The Compartmentalization of Cells. In *Molecular Biology of the Cell*, 4th ed.; Garland Science: New York, 2002.

3. (a) Ikegami, T.; Mototake, Y.-i.; Kobori, S.; Oka, M.; Hashimoto, Y., Life as an emergent phenomenon: studies from a large-scale boid simulation and web data. *Philosophical Transactions of the Royal Society A: Mathematical, Physical and Engineering Sciences* **2017,** *375* (2109), 20160351; (b) Lasher, C. D.; Rajagopalan, P.; Murali, T. M., Summarizing cellular responses as biological process networks. *BMC Systems Biology* **2013,** *7* (1), 68; (c) Macklem, P. T., Emergent phenomena and the secrets of life. *Journal of Applied Physiology* **2008,** *104* (6), 1844-1846.
4. Richards, T. A.; Massana, R.; Pagliara, S.; Hall, N., Single cell ecology. *Philosophical Transactions of the Royal Society B: Biological Sciences* **2019,** *374* (1786), 20190076.
5. (a) Aguilera-Gomez, A.; Rabouille, C., Membrane-bound organelles versus membrane-less compartments and their control of anabolic pathways in Drosophila. *Developmental Biology* **2017,** *428* (2), 310-317; (b) Nott, Timothy J.; Petsalaki, E.; Farber, P.; Jervis, D.; Fussner, E.; Plochowietz, A.; Craggs, T. D.; Bazett-Jones, David P.; Pawson, T.; Forman-Kay, Julie D.; Baldwin, Andrew J., Phase Transition of a Disordered Nuage Protein Generates Environmentally Responsive Membraneless Organelles. *Molecular Cell* **2015,** *57* (5), 936-947; (c) Alberti, S., The wisdom of crowds: regulating cell function through condensed states of living matter. *Journal of Cell Science* **2017,** *130* (17), 2789-2796; (d) Spannl, S.; Tereshchenko, M.; Mastromarco, G. J.; Ihn, S. J.; Lee, H. O., Biomolecular condensates in neurodegeneration and cancer. *Traffic* **2019,** *20* (12), 890-911.
6. (a) Gobbo, P.; Tian, L.; Pavan Kumar, B. V. V. S.; Turvey, S.; Cattelan, M.; Patil, A. J.; Carraro, M.; Bonchio, M.; Mann, S., Catalytic processing in ruthenium-based polyoxometalate coacervate protocells. *Nature Communications* **2020,** *11* (1), 41; (b) Mason, A. F.; van Hest, J. C. M., Multifaceted cell mimicry in coacervate-based synthetic cells. *Emerging Topics in Life Sciences* **2019,** *3* (5), 567-571; (c) Martino, C.; deMello, A. J., Droplet-based microfluidics for artificial cell generation: a brief review. *Interface Focus* **2016,** *6* (4), 20160011-20160011; (d) Nuti, N.; Verboket, P. E.; Dittrich, P. S., Multivesicular droplets: a cell model system to study compartmentalised biochemical reactions. *Lab on a Chip* **2017,** *17* (18), 3112-3119; (e) Gao, J.; Wang, C.; Wang, J.; Tan, H., Cascade-Amplified Time-Resolved Fluorescent Assay Driven by an Enzyme-Integrated Catalytic Compartment as an Artificial Multi-Enzyme Complex. *Chemistry – A European Journal* **2019,** *25* (41), 9629-9633.
7. (a) Salehi-Reyhani, A.; Ces, O.; Elani, Y., Artificial cell mimics as simplified models for the study of cell biology. *Exp Biol Med (Maywood)* **2017,** *242* (13), 1309-1317; (b) Booth, M. J.; Cazimoglu, I.; Bayley, H., Controlled deprotection and release of a small molecule from a compartmented synthetic tissue module. *Communications Chemistry* **2019,** *2* (1), 142.
8. (a) Bayoumi, M.; Bayley, H.; Maglia, G.; Sapra, K. T., Multi-compartment encapsulation of communicating droplets and droplet networks in hydrogel as a model for artificial cells. *Scientific Reports* **2017,** *7* (1), 45167; (b) Zhou, X.; Wu, H.; Cui, M.; Lai, S. N.; Zheng, B., Long-lived protein expression in hydrogel particles: towards artificial cells. *Chemical Science* **2018,** *9* (18), 4275-4279; (c) Drobot, B.; Iglesias-Artola, J. M.; Le Vay, K.; Mayr, V.; Kar, M.; Kreysing, M.; Mutschler, H.; Tang, T. Y. D., Compartmentalised RNA catalysis in membrane-free coacervate protocells. *Nature Communications* **2018,** *9* (1), 3643; (d) Bakshi, M. S., Colloidal micelles of block copolymers as nanoreactors, templates for gold nanoparticles, and vehicles for biomedical applications. *Advances in Colloid and Interface Science* **2014,** *213*, 1-20.
9. Arsalan, A.; Younus, H., Enzymes and nanoparticles: Modulation of enzymatic activity via nanoparticles. *International Journal of Biological Macromolecules* **2018,** *118*, 1833-1847.
10. Zhao, C.; Zhu, M.; Fang, Y.; Liu, X.; Wang, L.; Chen, D.; Huang, X., Engineering proteinosomes with renewable predatory behaviour towards living organisms. *Materials Horizons* **2020,** *7* (1), 157-163.
11. Egli, S.; Schlaad, H.; Bruns, N.; Meier, W., Functionalization of Block Copolymer Vesicle Surfaces. *Polymers* **2011**.
12. (a) Alexandridis, P., Amphiphilic copolymers and their applications. *Current Opinion in Colloid & Interface Science* **1996,** *1* (4), 490-501; (b) Johnston, A. P. R.; Cortez, C.; Angelatos, A. S.; Caruso, F., Layer-by-layer engineered capsules and their applications. *Current Opinion in Colloid & Interface Science* **2006,** *11* (4), 203-209; (c) Hosta-Rigau, L.; Chung, S. F.; Postma, A.; Chandrawati, R.; Städler, B.; Caruso, F., Capsosomes with "Free-Floating" Liposomal Subcompartments. *Advanced Materials* **2011,** *23* (35), 4082-4087; (d) Anraku, Y.; Kishimura, A.; Oba, M.; Yamasaki, Y.; Kataoka, K., Spontaneous Formation of Nanosized Unilamellar Polyion

Complex Vesicles with Tunable Size and Properties. *Journal of the American Chemical Society* **2010,** *132* (5), 1631-1636.
13. Liu, J.; Postupalenko, V.; Lörcher, S.; Wu, D.; Chami, M.; Meier, W.; Palivan, C. G., DNA-Mediated Self-Organization of Polymeric Nanocompartments Leads to Interconnected Artificial Organelles. *Nano Letters* **2016,** *16* (11), 7128-7136.
14. (a) Brož, P.; Benito, S. M.; Saw, C.; Burger, P.; Heider, H.; Pfisterer, M.; Marsch, S.; Meier, W.; Hunziker, P., Cell targeting by a generic receptor-targeted polymer nanocontainer platform. *Journal of Controlled Release* **2005,** *102* (2), 475-488; (b) Ren, T.; Erbakan, M.; Shen, Y.; Barbieri, E.; Saboe, P.; Feroz, H.; Yan, H.; McCuskey, S.; Hall, J. F.; Schantz, A. B.; Bazan, G. C.; Butler, P. J.; Grzelakowski, M.; Kumar, M., Membrane Protein Insertion into and Compatibility with Biomimetic Membranes. *Advanced Biosystems* **2017,** *1* (7), 1700053; (c) Garni, M.; Thamboo, S.; Schoenenberger, C.-A.; Palivan, C. G., Biopores/membrane proteins in synthetic polymer membranes. *Biochimica et Biophysica Acta (BBA) - Biomembranes* **2017,** *1859* (4), 619-638.
15. Yorulmaz Avsar, S.; Kyropoulou, M.; Di Leone, S.; Schoenenberger, C.-A.; Meier, W. P.; Palivan, C. G., Biomolecules Turn Self-Assembling Amphiphilic Block Co-polymer Platforms Into Biomimetic Interfaces. *Frontiers in Chemistry* **2019,** *6* (645).
16. Li, F.; Danquah, M.; Mahato, R. I., Synthesis and Characterization of Amphiphilic Lipopolymers for Micellar Drug Delivery. *Biomacromolecules* **2010,** *11* (10), 2610-2620.
17. Israelachvili, J. N., 19 - Thermodynamic Principles of Self-Assembly. In *Intermolecular and Surface Forces (Third Edition)*, Israelachvili, J. N., Ed. Academic Press: San Diego, 2011; pp 503-534.
18. (a) Durand, G.; Abla, M.; Ebel, C.; Breyton, C., New amphiphiles to handle membrane proteins: "ménage à trois" between chemistry, physical chemistry and biochemistry. In *Membrane Proteins Production for Structural Analysis*, Isabelle, M.-V., Ed. Springer: New York, 2014; pp 205-251; (b) Smart, T.; Lomas, H.; Massignani, M.; Flores-Merino, M. V.; Perez, L. R.; Battaglia, G., Block copolymer nanostructures. *Nano Today* **2008,** *3* (3), 38-46.
19. (a) Austen Angell, C.; Sivarajan, S., Glass Transition☆. In *Reference Module in Materials Science and Materials Engineering*, Elsevier: 2017; (b) Loadman, M. J. R., The glass transition temperature of natural rubber. *Journal of thermal analysis* **1985,** *30* (4), 929-941; (c) Ebnesajjad, S., Introduction to Plastics. In *Chemical Resistance of Engineering Thermoplastics*, Baur, E.; Ruhrberg, K.; Woishnis, W., Eds. William Andrew Publishing: 2016; pp xiii-xxv; (d) Dionzou, M.; Morère, A.; Roux, C.; Lonetti, B.; Marty, J. D.; Mingotaud, C.; Joseph, P.; Goudounèche, D.; Payré, B.; Léonetti, M.; Mingotaud, A. F., Comparison of methods for the fabrication and the characterization of polymer self-assemblies: what are the important parameters? *Soft Matter* **2016,** *12* (7), 2166-2176.
20. (a) von Heijne, G., Membrane-protein topology. *Nature Reviews Molecular Cell Biology* **2006,** *7*, 909; (b) Palivan, C. G.; Goers, R.; Najer, A.; Zhang, X. Y.; Car, A.; Meier, W., Bioinspired polymer vesicles and membranes for biological and medical applications. *Chem Soc Rev* **2016,** *45* (2), 377-411.
21. Zhu, Y.; Yang, B.; Chen, S.; Du, J., Polymer vesicles: Mechanism, preparation, application, and responsive behavior. *Progress in Polymer Science* **2017,** *64*, 1-22.
22. (a) Berrocal, J. A.; Teyssandier, J.; Goor, O. J. G. M.; De Feyter, S.; Meijer, E. W., Supramolecular Loop Stitches of Discrete Block Molecules on Graphite: Tunable Hydrophobicity by Naphthalenediimide End-Capped Oligodimethylsiloxane. *Chemistry of Materials* **2018,** *30* (10), 3372-3378; (b) Rikken, R. S.; Engelkamp, H.; Nolte, R. J.; Maan, J. C.; van Hest, J. C.; Wilson, D. A.; Christianen, P. C., Shaping polymersomes into predictable morphologies via out-of-equilibrium self-assembly. *Nat Commun* **2016,** *7*, 12606; (c) Yingying, D.; Bingsheng, W.; Mingliang, J.; Ying, Y.; Guofu, Z.; Lingling, S., A review on self-assembly in microfluidic devices. *Journal of Micromechanics and Microengineering* **2017,** *27* (11), 113002.
23. (a) Belluati, A.; Craciun, I.; Liu, J.; Palivan, C. G., Nanoscale enzymatic compartments in tandem support cascade reactions in vitro. *Biomacromolecules* **2018**; (b) Tanner, P.; Balasubramanian, V.; Palivan, C. G., Aiding Nature's Organelles: Artificial Peroxisomes Play Their Role. *Nano Letters* **2013,** *13* (6), 2875-2883.

24. Klermund, L.; Poschenrieder, S. T.; Castiglione, K., Biocatalysis in Polymersomes: Improving Multienzyme Cascades with Incompatible Reaction Steps by Compartmentalization. *ACS Catalysis* **2017,** *7* (6), 3900-3904.
25. (a) Grafe, D.; Gaitzsch, J.; Appelhans, D.; Voit, B., Cross-linked polymersomes as nanoreactors for controlled and stabilized single and cascade enzymatic reactions. *Nanoscale* **2014,** *6* (18), 10752-61; (b) Li, J.; Li, Y.; Wang, Y.; Ke, W.; Chen, W.; Wang, W.; Ge, Z., Polymer Prodrug-Based Nanoreactors Activated by Tumor Acidity for Orchestrated Oxidation/Chemotherapy. *Nano Lett* **2017,** *17* (11), 6983-6990; (c) Liu, X.; Formanek, P.; Voit, B.; Appelhans, D., Functional Cellular Mimics for the Spatiotemporal Control of Multiple Enzymatic Cascade Reactions. *Angewandte Chemie International Edition* **2017,** *56* (51), 16233-16238.
26. (a) Chen, H.; Tian, J.; He, W.; Guo, Z., H2O2-Activatable and O2-Evolving Nanoparticles for Highly Efficient and Selective Photodynamic Therapy against Hypoxic Tumor Cells. *Journal of the American Chemical Society* **2015,** *137* (4), 1539-1547; (b) Jang, W.-S.; Park, S. C.; Reed, E. H.; Dooley, K. P.; Wheeler, S. F.; Lee, D.; Hammer, D. A., Enzymatically triggered rupture of polymersomes. *Soft Matter* **2016,** *12* (4), 1014-1020; (c) Yu, J.; Qian, C.; Zhang, Y.; Cui, Z.; Zhu, Y.; Shen, Q.; Ligler, F. S.; Buse, J. B.; Gu, Z., Hypoxia and H2O2 Dual-Sensitive Vesicles for Enhanced Glucose-Responsive Insulin Delivery. *Nano Letters* **2017,** *17* (2), 733-739.
27. Hvasanov, D.; Peterson, J. R.; Thordarson, P., Self-assembled light-driven photosynthetic-respiratory electron transport chain hybrid proton pump. *Chemical Science* **2013,** *4* (10), 3833-3838.
28. Lomora, M.; Gunkel-Grabole, G.; Mantri, S.; Palivan, C. G., Bio-catalytic nanocompartments for in situ production of glucose-6-phosphate. *Chem Commun (Camb)* **2017,** *53* (73), 10148-10151.
29. (a) Einfalt, T.; Goers, R.; Dinu, I. A.; Najer, A.; Spulber, M.; Onaca-Fischer, O.; Palivan, C. G., Stimuli-Triggered Activity of Nanoreactors by Biomimetic Engineering Polymer Membranes. *Nano Lett* **2015,** *15* (11), 7596-603; (b) Edlinger, C.; Einfalt, T.; Spulber, M.; Car, A.; Meier, W.; Palivan, C. G., Biomimetic Strategy To Reversibly Trigger Functionality of Catalytic Nanocompartments by the Insertion of pH-Responsive Biovalves. *Nano Letters* **2017,** *17* (9), 5790-5798.
30. (a) Roskoski, R., Michaelis-Menten Kinetics☆. In *Reference Module in Biomedical Sciences*, Elsevier: 2015; (b) Engelking, L. R., Chapter 6 - Enzyme Kinetics. In *Textbook of Veterinary Physiological Chemistry (Third Edition)*, Engelking, L. R., Ed. Academic Press: Boston, 2015; pp 32-38.
31. (a) Atkins, W. M., NON-MICHAELIS-MENTEN KINETICS IN CYTOCHROME P450-CATALYZED REACTIONS. *Annual Review of Pharmacology and Toxicology* **2005,** *45* (1), 291-310; (b) Pinto, M. F.; Martins, P. M., In search of lost time constants and of non-Michaelis–Menten parameters. *Perspectives in Science* **2016,** *9*, 8-16.
32. Berry, H., Monte Carlo Simulations of Enzyme Reactions in Two Dimensions: Fractal Kinetics and Spatial Segregation. *Biophysical Journal* **2002,** *83* (4), 1891-1901.
33. Sueyoshi, D.; Anraku, Y.; Komatsu, T.; Urano, Y.; Kataoka, K., Enzyme-Loaded Polyion Complex Vesicles as in Vivo Nanoreactors Working Sustainably under the Blood Circulation: Characterization and Functional Evaluation. *Biomacromolecules* **2017,** *18* (4), 1189-1196.
34. Barlow, J.; Gozzi, K.; Kelley, C. P.; Geilich, B. M.; Webster, T. J.; Chai, Y.; Sridhar, S.; van de Ven, A. L., High throughput microencapsulation of Bacillus subtilis in semi-permeable biodegradable polymersomes for selenium remediation. *Applied Microbiology and Biotechnology* **2017,** *101* (1), 455-464.
35. (a) Küchler, A.; Yoshimoto, M.; Luginbühl, S.; Mavelli, F.; Walde, P., Enzymatic reactions in confined environments. *Nature Nanotechnology* **2016,** *11* (5), 409-420; (b) Begum, G.; Goodwin, W. B.; deGlee, B. M.; Sandhage, K. H.; Kröger, N., Compartmentalisation of enzymes for cascade reactions through biomimetic layer-by-layer mineralization. *Journal of Materials Chemistry B* **2015,** *3* (26), 5232-5240; (c) Alam-Nazki, A.; Krishnan, J., Spatial Control of Biochemical Modification Cascades and Pathways. *Biophysical Journal* **2015,** *108* (12), 2912-2924; (d) Uhrich, D.; von Langermann, J., Preparation and Characterization of Enzyme Compartments in UV-Cured Polyurethane-Based Materials and Their Application in Enzymatic Reactions. *Frontiers in Microbiology* **2017,** *8* (2111); (e) Quin, M. B.; Wallin, K. K.; Zhang, G.; Schmidt-Dannert, C., Spatial organization of multi-enzyme biocatalytic cascades. *Organic & Biomolecular Chemistry* **2017,** *15* (20), 4260-4271; (f) Schmidt-Dannert, C.; Lopez-Gallego, F., A roadmap for biocatalysis – functional and spatial orchestration of enzyme cascades. *Microbial Biotechnology* **2016,** *9* (5), 601-609; (g) Baumann, P.; Spulber, M.; Fischer, O.; Car,

A.; Meier, W., Investigation of Horseradish Peroxidase Kinetics in an "Organelle-Like" Environment. *Small* **2017,** *13* (17).
36. Milker, S.; Fink, M. J.; Oberleitner, N.; Ressmann, A. K.; Bornscheuer, U. T.; Mihovilovic, M. D.; Rudroff, F., Kinetic Modeling of an Enzymatic Redox Cascade In Vivo Reveals Bottlenecks Caused by Cofactors. *ChemCatChem* **2017,** *9* (17), 3420-3427.
37. (a) Zecchin, A.; Stapor, P. C.; Goveia, J.; Carmeliet, P., Metabolic pathway compartmentalization: an underappreciated opportunity? *Current Opinion in Biotechnology* **2015,** *34*, 73-81; (b) Agapakis, C. M.; Boyle, P. M.; Silver, P. A., Natural strategies for the spatial optimization of metabolism in synthetic biology. *Nature Chemical Biology* **2012,** *8* (6), 527-535; (c) Polka, J. K.; Hays, S. G.; Silver, P. A., Building Spatial Synthetic Biology with Compartments, Scaffolds, and Communities. *Cold Spring Harb Perspect Biol* **2016,** *8* (8), a024018.
38. Belluati, A.; Craciun, I.; Meyer, C. E.; Rigo, S.; Palivan, C. G., Enzymatic reactions in polymeric compartments: nanotechnology meets nature. *Curr Opin Biotechnol* **2019,** *60*, 53-62.
39. Abdelmohsen, L. K. E. A.; Nijemeisland, M.; Pawar, G. M.; Janssen, G.-J. A.; Nolte, R. J. M.; van Hest, J. C. M.; Wilson, D. A., Dynamic Loading and Unloading of Proteins in Polymeric Stomatocytes: Formation of an Enzyme-Loaded Supramolecular Nanomotor. *ACS Nano* **2016,** *10* (2), 2652-2660.
40. van Dongen, S. F. M.; Nallani, M.; Cornelissen, J. J. L. M.; Nolte, R. J. M.; van Hest, J. C. M., A Three-Enzyme Cascade Reaction through Positional Assembly of Enzymes in a Polymersome Nanoreactor. *Chemistry – A European Journal* **2009,** *15* (5), 1107-1114.
41. Blackman, L. D.; Varlas, S.; Arno, M. C.; Fayter, A.; Gibson, M. I.; O'Reilly, R. K., Permeable Protein-Loaded Polymersome Cascade Nanoreactors by Polymerization-Induced Self-Assembly. *ACS Macro Letters* **2017,** *6* (11), 1263-1267.
42. (a) Anraku, Y.; Kishimura, A.; Kamiya, M.; Tanaka, S.; Nomoto, T.; Toh, K.; Matsumoto, Y.; Fukushima, S.; Sueyoshi, D.; Kano, M. R.; Urano, Y.; Nishiyama, N.; Kataoka, K., Systemically Injectable Enzyme-Loaded Polyion Complex Vesicles as In Vivo Nanoreactors Functioning in Tumors. *Angewandte Chemie International Edition* **2015,** *55* (2), 560-565; (b) Hosta-Rigau, L.; York-Duran, M. J.; Kang, T. S.; Städler, B., Extracellular Microreactor for the Depletion of Phenylalanine Toward Phenylketonuria Treatment. *Advanced Functional Materials* **2015,** *25* (25), 3860-3869.
43. Nishimura, T.; Sasaki, Y.; Akiyoshi, K., Biotransporting Self-Assembled Nanofactories Using Polymer Vesicles with Molecular Permeability for Enzyme Prodrug Cancer Therapy. *Advanced Materials* **2017,** *29* (36), 1702406.
44. Dobrunz, D.; Toma, A. C.; Tanner, P.; Pfohl, T.; Palivan, C. G., Polymer Nanoreactors with Dual Functionality: Simultaneous Detoxification of Peroxynitrite and Oxygen Transport. *Langmuir* **2012,** *28* (45), 15889-15899.
45. Langowska, K.; Kowal, J.; Palivan, C. G.; Meier, W., A general strategy for creating self-defending surfaces for controlled drug production for long periods of time. *Journal of Materials Chemistry B* **2014,** *2* (29), 4684-4693.
46. Godoy-Gallardo, M.; Labay, C.; Trikalitis, V. D.; Kempen, P. J.; Larsen, J. B.; Andresen, T. L.; Hosta-Rigau, L., Multicompartment Artificial Organelles Conducting Enzymatic Cascade Reactions inside Cells. *ACS Applied Materials & Interfaces* **2017,** *9* (19), 15907-15921.
47. Einfalt, T.; Witzigmann, D.; Edlinger, C.; Sieber, S.; Goers, R.; Najer, A.; Spulber, M.; Onaca-Fischer, O.; Huwyler, J.; Palivan, C. G., Biomimetic artificial organelles with in vitro and in vivo activity triggered by reduction in microenvironment. *Nature Communications* **2018,** *9* (1), 1127.
48. Belluati, A.; Mikhalevich, V.; Yorulmaz Avsar, S.; Daubian, D.; Craciun, I.; Chami, M.; Meier, W. P.; Palivan, C. G., How Do the Properties of Amphiphilic Polymer Membranes Influence the Functional Insertion of Peptide Pores? *Biomacromolecules* **2019**.
49. Rifaie-Graham, O.; Ulrich, S.; Galensowske, N. F. B.; Balog, S.; Chami, M.; Rentsch, D.; Hemmer, J. R.; Read de Alaniz, J.; Boesel, L. F.; Bruns, N., Wavelength-Selective Light-Responsive DASA-Functionalized Polymersome Nanoreactors. *Journal of the American Chemical Society* **2018,** *140* (25), 8027-8036.

50. Spulber, M.; Baumann, P.; Saxer, S. S.; Pieles, U.; Meier, W.; Bruns, N., Poly(N-vinylpyrrolidone)-Poly(dimethylsiloxane)-Based Polymersome Nanoreactors for Laccase-Catalyzed Biotransformations. *Biomacromolecules* **2014,** *15* (4), 1469-1475.
51. Siti, W.; de Hoog, H.-P. M.; Fischer, O.; Shan, W. Y.; Tomczak, N.; Nallani, M.; Liedberg, B., An intercompartmental enzymatic cascade reaction in channel-equipped polymersome-in-polymersome architectures. *Journal of Materials Chemistry B* **2014,** *2* (18), 2733-2737.
52. Louzao, I.; van Hest, J. C. M., Permeability Effects on the Efficiency of Antioxidant Nanoreactors. *Biomacromolecules* **2013,** *14* (7), 2364-2372.
53. Wang, Z.; van Oers, M. C. M.; Rutjes, F. P. J. T.; van Hest, J. C. M., Polymersome Colloidosomes for Enzyme Catalysis in a Biphasic System. *Angewandte Chemie International Edition* **2012,** *51* (43), 10746-10750.
54. Chen, Q.; Schönherr, H.; Vancso, G. J., Block-Copolymer Vesicles as Nanoreactors for Enzymatic Reactions. *Small* **2009,** *5* (12), 1436-1445.
55. Axthelm, F.; Casse, O.; Koppenol, W. H.; Nauser, T.; Meier, W.; Palivan, C. G., Antioxidant Nanoreactor Based on Superoxide Dismutase Encapsulated in Superoxide-Permeable Vesicles. *The Journal of Physical Chemistry B* **2008,** *112* (28), 8211-8217.
56. Garni, M.; Einfalt, T.; Goers, R.; Palivan, C. G.; Meier, W., Live Follow-Up of Enzymatic Reactions Inside the Cavities of Synthetic Giant Unilamellar Vesicles Equipped with Membrane Proteins Mimicking Cell Architecture. *ACS Synthetic Biology* **2018**.
57. Armada-Moreira, A.; Thingholm, B.; Andreassen, K.; Sebastião, A. M.; Vaz, S. H.; Städler, B., On the Assembly of Microreactors with Parallel Enzymatic Pathways. *Advanced Biosystems* **2018,** *2* (5), 1700244.
58. Zhang, Y.; Baekgaard-Laursen, M.; Städler, B., Small Subcompartmentalized Microreactors as Support for Hepatocytes. *Advanced Healthcare Materials* **2016,** *6* (15).
59. Thingholm, B.; Schattling, P.; Zhang, Y.; Städler, B., Subcompartmentalized Nanoreactors as Artificial Organelle with Intracellular Activity. *Small* **2016,** *12* (13), 1806-1814.
60. Hosta-Rigau, L.; York-Duran, M. J.; Zhang, Y.; Goldie, K. N.; Städler, B., Confined Multiple Enzymatic (Cascade) Reactions within Poly(dopamine)-based Capsosomes. *ACS Applied Materials & Interfaces* **2014,** *6* (15), 12771-12779.
61. Thamboo, S.; Najer, A.; Belluati, A.; von Planta, C.; Wu, D. L.; Craciun, I.; Meier, W.; Palivan, C. C., Mimicking Cellular Signaling Pathways within Synthetic Multicompartment Vesicles with Triggered Enzyme Activity and Induced Ion Channel Recruitment. *Advanced Functional Materials* **2019**.
62. Peters, R. J.; Marguet, M.; Marais, S.; Fraaije, M. W.; van Hest, J. C.; Lecommandoux, S., Cascade reactions in multicompartmentalized polymersomes. *Angew Chem Int Ed Engl* **2014,** *53* (1), 146-50.
63. Gupta, A., Comprehensive biochemistry for dentistry : textbook for dental students. **2019**.
64. (a) Stuart, M. A. C.; Huck, W. T. S.; Genzer, J.; Muller, M.; Ober, C.; Stamm, M.; Sukhorukov, G. B.; Szleifer, I.; Tsukruk, V. V.; Urban, M.; Winnik, F.; Zauscher, S.; Luzinov, I.; Minko, S., Emerging applications of stimuli-responsive polymer materials. *Nat Mater* **2010,** *9* (2), 101-113; (b) Wei, M. L.; Gao, Y. F.; Li, X.; Serpe, M. J., Stimuli-responsive polymers and their applications. *Polym Chem-Uk* **2017,** *8* (1), 127-143; (c) Jahid, M. A.; Hu, J.; Zhuo, H., Stimuli-responsive polymers in coating and laminating for functional textile. 2019; pp 155-173.
65. Patra, J. K.; Das, G.; Fraceto, L. F.; Campos, E. V. R.; Rodriguez-Torres, M. d. P.; Acosta-Torres, L. S.; Diaz-Torres, L. A.; Grillo, R.; Swamy, M. K.; Sharma, S.; Habtemariam, S.; Shin, H.-S., Nano based drug delivery systems: recent developments and future prospects. *Journal of Nanobiotechnology* **2018,** *16* (1), 71.
66. (a) Najer, A.; Wu, D. L.; Bieri, A.; Brand, F.; Palivan, C. G.; Beck, H. P.; Meier, W., Nanomimics of Host Cell Membranes Block Invasion and Expose Invasive Malaria Parasites. *Acs Nano* **2014,** *8* (12), 12560-12571; (b) Najer, A.; Wu, D. L.; Nussbaumer, M. G.; Schwertz, G.; Schwab, A.; Witschel, M. C.; Schafer, A.; Diederich, F.; Rottmann, M.; Palivan, C. G.; Beck, H. P.; Meier, W., An amphiphilic graft copolymer-based nanoparticle platform for reduction-responsive anticancer and antimalarial drug delivery. *Nanoscale* **2016,** *8* (31), 14858-14869.
67. Lounsbury, K., Chapter 6 - Signal Transduction and Second Messengers. In *Pharmacology*, Hacker, M.; Messer, W.; Bachmann, K., Eds. Academic Press: San Diego, 2009; pp 103-112.

68. Panteghini, M.; Bonora, R.; Pagani, F., Measurement of pancreatic lipase activity in serum by a kinetic colorimetric assay using a new chromogenic substrate. *Ann Clin Biochem* **2001,** *38*, 365-370.
69. Lomora, M.; Garni, M.; Itel, F.; Tanner, P.; Spulber, M.; Palivan, C. G., Polymersomes with engineered ion selective permeability as stimuli-responsive nanocompartments with preserved architecture. *Biomaterials* **2015,** *53*, 406-414.
70. Groten, C. J.; Magoski, N. S., PKC Enhances the Capacity for Secretion by Rapidly Recruiting Covert Voltage-Gated Ca2+ Channels to the Membrane. *J Neurosci* **2015,** *35* (6), 2747-2765.
71. Belluati, A.; Thamboo, S.; Najer, A.; Maffeis, V.; von Planta, C.; Craciun, I.; Palivan, C. G.; Meier, W., Multicompartment Polymer Vesicles with Artificial Organelles for Signal-Triggered Cascade Reactions Including Cytoskeleton Formation. *Advanced Functional Materials n/a* (n/a), 2002949.
72. (a) Carvalho, K.; Tsai, F.-C.; Lees, E.; Voituriez, R.; Koenderink, G. H.; Sykes, C., Cell-sized liposomes reveal how actomyosin cortical tension drives shape change. *Proceedings of the National Academy of Sciences* **2013,** *110* (41), 16456; (b) Dhir, S.; Salahub, S.; Mathews, A. S.; Kumaran, S. K.; Montemagno, C. D.; Abraham, S., Light-induced ATP driven self-assembly of actin and heavy-meromyosin in proteo-tubularsomes as a step toward artificial cells. *Chemical Communications* **2018,** *54* (42), 5346-5349; (c) Kang, H.; Bradley, Michael J.; Elam, W. A.; De La Cruz, Enrique M., Regulation of Actin by Ion-Linked Equilibria. *Biophysical Journal* **2013,** *105* (12), 2621-2628; (d) Loiseau, E.; Schneider, J. A. M.; Keber, F. C.; Pelzl, C.; Massiera, G.; Salbreux, G.; Bausch, A. R., Shape remodeling and blebbing of active cytoskeletal vesicles. *Science Advances* **2016,** *2* (4), e1500465; (e) Tsai, F.-C.; Koenderink, G. H., Shape control of lipid bilayer membranes by confined actin bundles. *Soft Matter* **2015,** *11* (45), 8834-8847; (f) Yewdall, N. A.; Mason, A. F.; van Hest, J. C. M., The hallmarks of living systems: towards creating artificial cells. *Interface Focus* **2018,** *8* (5), 20180023.
73. (a) Weiss, M.; Frohnmayer, J. P.; Benk, L. T.; Haller, B.; Janiesch, J. W.; Heitkamp, T.; Borsch, M.; Lira, R. B.; Dimova, R.; Lipowsky, R.; Bodenschatz, E.; Baret, J. C.; Vidakovic-Koch, T.; Sundmacher, K.; Platzman, I.; Spatz, J. P., Sequential bottom-up assembly of mechanically stabilized synthetic cells by microfluidics. *Nat Mater* **2018,** *17* (1), 89-+; (b) Carvalho, K.; Tsai, F. C.; Lees, E.; Voituriez, R.; Koenderink, G. H.; Sykes, C., Cell-sized liposomes reveal how actomyosin cortical tension drives shape change (vol 110, pg 16456, 2013). *P Natl Acad Sci USA* **2013,** *110* (49), 19969-19969; (c) Loiseau, E.; Schneider, J. A. M.; Keber, F. C.; Pelzl, C.; Massiera, G.; Salbreux, G.; Bausch, A. R., Shape remodeling and blebbing of active cytoskeletal vesicles. *Sci Adv* **2016,** *2* (4); (d) Tsai, F. C.; Koenderink, G. H., Shape control of lipid bilayer membranes by confined actin bundles. *Soft Matter* **2015,** *11* (45), 8834-8847.
74. (a) Luo, T. Z.; Srivastava, V.; Ren, Y. X.; Robinson, D. N., Mimicking the mechanical properties of the cell cortex by the self-assembly of an actin cortex in vesicles. *Appl Phys Lett* **2014,** *104* (15); (b) Schafer, E.; Vache, M.; Kliesch, T. T.; Janshoff, A., Mechanical response of adherent giant liposomes to indentation with a conical AFM-tip. *Soft Matter* **2015,** *11* (22), 4487-4495.
75. Young, E. J.; Briggs, S. B.; Miller, C. A., The Actin Cytoskeleton as a Therapeutic Target for the Prevention of Relapse to Methamphetamine Use. *CNS Neurol Disord Drug Targets* **2015,** *14* (6), 731-737.
76. (a) Allingham, J. S.; Klenchin, V. A.; Rayment, I., Actin-targeting natural products: structures, properties and mechanisms of action. *Cellular and Molecular Life Sciences CMLS* **2006,** *63* (18), 2119-2134; (b) Risinger, A. L.; Du, L., Targeting and extending the eukaryotic druggable genome with natural products: cytoskeletal targets of natural products. *Natural Product Reports* **2020**.
77. (a) Cocucci, E.; Kim, J. Y.; Bai, Y.; Pabla, N., Role of Passive Diffusion, Transporters, and Membrane Trafficking-Mediated Processes in Cellular Drug Transport. *Clinical Pharmacology & Therapeutics* **2017,** *101* (1), 121-129; (b) Sarmento, B.; Andrade, F.; Silva, S. B. d.; Rodrigues, F.; das Neves, J.; Ferreira, D., Cell-based in vitro models for predicting drug permeability. *Expert Opinion on Drug Metabolism & Toxicology* **2012,** *8* (5), 607-621.
78. (a) Bryce, N. S.; Hardeman, E. C.; Gunning, P. W.; Lock, J. G., Chemical biology approaches targeting the actin cytoskeleton through phenotypic screening. *Current Opinion in Chemical Biology* **2019,** *51*, 40-47; (b) Krishnan, R.; Park, J.-A.; Seow, C. Y.; Lee, P. V. S.; Stewart, A. G., Cellular Biomechanics in Drug Screening and Evaluation: Mechanopharmacology. *Trends Pharmacol Sci* **2016,** *37* (2), 87-100.

79. (a) Deshmukh, S. K.; Gupta, M. K.; Prakash, V.; Saxena, S., Endophytic Fungi: A Source of Potential Antifungal Compounds. *J Fungi (Basel)* **2018,** *4* (3), 77; (b) Gao, W.; Ye, G.; Duan, X.; Yang, X.; Yang, V. C., Transferrin receptor-targeted pH-sensitive micellar system for diminution of drug resistance and targetable delivery in multidrug-resistant breast cancer. *Int J Nanomedicine* **2017,** *12*, 1047-1064; (c) Hwang, J.; Yi, M.; Zhang, X.; Xu, Y.; Jung, J. H.; Kim, D., Cytochalasin B induces apoptosis through the mitochondrial apoptotic pathway in HeLa human cervical carcinoma cells. *Oncology Reports* **2013,** *30*, 1929-1935; (d) Jog, N. R.; Rane, M. J.; Lominadze, G.; Luerman, G. C.; Ward, R. A.; McLeish, K. R., The actin cytoskeleton regulates exocytosis of all neutrophil granule subsets. *American Journal of Physiology-Cell Physiology* **2007,** *292* (5), C1690-C1700.
80. Foissner, I.; Wasteneys, G. O., Wide-Ranging Effects of Eight Cytochalasins and Latrunculin A and B on Intracellular Motility and Actin Filament Reorganization in Characean Internodal Cells. *Plant and Cell Physiology* **2007,** *48* (4), 585-597.
81. Belluati, A.; Mikhalevich, V.; Yorulmaz Avsar, S.; Daubian, D.; Craciun, I.; Chami, M.; Meier, W. P.; Palivan, C. G., How Do the Properties of Amphiphilic Polymer Membranes Influence the Functional Insertion of Peptide Pores? *Biomacromolecules* **2020,** *21* (2), 701-715.
82. (a) Shum, H. C.; Kim, J.-W.; Weitz, D. A., Microfluidic Fabrication of Monodisperse Biocompatible and Biodegradable Polymersomes with Controlled Permeability. *Journal of the American Chemical Society* **2008,** *130* (29), 9543-9549; (b) Wang, H.; Liu, Y.; Chen, Z.; Sun, L.; Zhao, Y., Anisotropic structural color particles from colloidal phase separation. *Science Advances* **2020,** *6* (2), eaay1438; (c) Yu, Y.; Shang, L.; Guo, J.; Wang, J.; Zhao, Y., Design of capillary microfluidics for spinning cell-laden microfibers. *Nature Protocols* **2018,** *13* (11), 2557-2579.
83. (a) Schoonen, L.; van Hest, J. C., Compartmentalization Approaches in Soft Matter Science: From Nanoreactor Development to Organelle Mimics. *Adv Mater* **2016,** *28* (6), 1109-28; (b) van Oers, M. C.; Rutjes, F. P.; van Hest, J. C., Cascade reactions in nanoreactors. *Curr Opin Biotechnol* **2014,** *28*, 10-6.
84. Tanner, P.; Onaca, O.; Balasubramanian, V.; Meier, W.; Palivan, C. G., Enzymatic cascade reactions inside polymeric nanocontainers: a means to combat oxidative stress. *Chemistry* **2011,** *17* (16), 4552-60.
85. (a) Bolinger, P. Y.; Stamou, D.; Vogel, H., An integrated self-assembled nanofluidic system for controlled biological chemistries. *Angew Chem Int Ed Engl* **2008,** *47* (30), 5544-9; (b) Brasch, M.; Putri, R. M.; de Ruiter, M. V.; Luque, D.; Koay, M. S.; Caston, J. R.; Cornelissen, J. J., Assembling Enzymatic Cascade Pathways inside Virus-Based Nanocages Using Dual-Tasking Nucleic Acid Tags. *J Am Chem Soc* **2017,** *139* (4), 1512-1519; (c) Marguet, M.; Bonduelle, C.; Lecommandoux, S., Multicompartmentalized polymeric systems: towards biomimetic cellular structure and function. *Chem Soc Rev* **2013,** *42* (2), 512-29.
86. (a) Blackman, L. D.; Varlas, S.; Arno, M. C.; Fayter, A.; Gibson, M. I.; O'Reilly, R. K., Permeable Protein-Loaded Polymersome Cascade Nanoreactors by Polymerization-Induced Self-Assembly. *ACS Macro Lett* **2017,** *6* (11), 1263-1267; (b) Kuiper, S. M.; Nallani, M.; Vriezema, D. M.; Cornelissen, J. J.; van Hest, J. C.; Nolte, R. J.; Rowan, A. E., Enzymes containing porous polymersomes as nano reaction vessels for cascade reactions. *Org Biomol Chem* **2008,** *6* (23), 4315-8.
87. Lörcher, S.; Meier, W., Cosolvent fractionation of PMOXA-b-PDMS-b-PMOXA: Bulk separation of triblocks from multiblocks. *European Polymer Journal* **2017,** *88*, 575-585.
88. Nardin, C.; Thoeni, S.; Widmer, J.; Winterhalter, M.; Meier, W., Nanoreactors based on (polymerized) ABA-triblock copolymer vesicles. *Chemical Communications* **2000,** (15), 1433-1434.
89. (a) Azmi, N. E.; Ramli, N. I.; Abdullah, J.; Abdul Hamid, M. A.; Sidek, H.; Abd Rahman, S.; Ariffin, N.; Yusof, N. A., A simple and sensitive fluorescence based biosensor for the determination of uric acid using H2O2-sensitive quantum dots/dual enzymes. *Biosens Bioelectron* **2015,** *67*, 129-33; (b) Dai, M.; Huang, T.; Chao, L.; Xie, Q.; Tan, Y.; Chen, C.; Meng, W., Horseradish peroxidase-catalyzed polymerization of L-DOPA for mono-/bi-enzyme immobilization and amperometric biosensing of H2O2 and uric acid. *Talanta* **2016,** *149*, 117-123; (c) Miland, E.; Miranda Ordieres, A. J.; Tunon Blanco, P.; Smyth, M. R.; Fagain, C. O., Poly(o-aminophenol)-modified bienzyme carbon paste electrode for the detection of uric acid. *Talanta* **1996,** *43* (5), 785-96.
90. Stauch, O.; Schubert, R., Structure of Artificial Cytoskeleton Containing Liposomes in Aqueous Solution Studied by Static and Dynamic Light Scattering. *Biomacromolecules* **2002**.

91. Habel, J.; Ogbonna, A.; Larsen, N.; Cherre, S.; Kynde, S.; Midtgaard, S. R.; Kinoshita, K.; Krabbe, S.; Jensen, G. V.; Hansen, J. S.; Almdal, K.; Helix-Nielsen, C., Selecting analytical tools for characterization of polymersomes in aqueous solution. *RSC Advances* **2015,** *5* (97), 79924-79946.
92. (a) Bar-Even, A.; Noor, E.; Savir, Y.; Liebermeister, W.; Davidi, D.; Tawfik, D. S.; Milo, R., The moderately efficient enzyme: evolutionary and physicochemical trends shaping enzyme parameters. *Biochemistry* **2011,** *50* (21), 4402-10; (b) Garcia-Viloca, M.; Gao, J.; Karplus, M.; Truhlar, D. G., How enzymes work: analysis by modern rate theory and computer simulations. *Science* **2004,** *303* (5655), 186-95.
93. Caliceti, P.; Schiavon, O.; Veronese, F. M., Biopharmaceutical properties of uricase conjugated to neutral and amphiphilic polymers. *Bioconjug Chem* **1999,** *10* (4), 638-46.
94. Rennke, H. G.; Patel, Y.; Venkatachalam, M. A., Glomerular filtration of proteins: clearance of anionic, neutral, and cationic horseradish peroxidase in the rat. *Kidney Int* **1978,** *13* (4), 278-88.
95. Itel, F.; Chami, M.; Najer, A.; Lörcher, S.; Wu, D.; Dinu, I. A.; Meier, W., Molecular Organization and Dynamics in Polymersome Membranes: A Lateral Diffusion Study. *Macromolecules* **2014,** *47* (21), 7588-7596.
96. Cao, X.; Chen, C.; Yu, H.; Wang, P., Horseradish peroxidase-encapsulated chitosan nanoparticles for enzyme-prodrug cancer therapy. *Biotechnology letters* **2015,** *37* (1), 81-8.
97. (a) Critchlow, J. E.; Dunford, H. B., Studies on Horseradish Peroxidase *The Journal of Biological Chemistry* **1972**; (b) Mahler, H. R. a.; Baum, H. M. c.; Hübscher, G., Enzymatic oxidation of urate. *Science* **1956**.
98. Edlinger, C.; Einfalt, T.; Spulber, M.; Car, A.; Meier, W.; Palivan, C. G., Biomimetic Strategy To Reversibly Trigger Functionality of Catalytic Nanocompartments by the Insertion of pH-Responsive Biovalves. *Nano Lett* **2017,** *17* (9), 5790-5798.
99. Saint, N.; Lou, K. L.; Widmer, C.; Luckey, M.; Schirmer, T.; Rosenbusch, J. P., Structural and functional characterization of OmpF porin mutants selected for larger pore size. II. Functional characterization. *J Biol Chem* **1996,** *271* (34), 20676-80.
100. Achleitner, G.; Gaigg, B.; Krasser, A.; Kainersdorfer, E.; Kohlwein, S. D.; Perktold, A.; Zellnig, G.; Daum, G., Association between the endoplasmic reticulum and mitochondria of yeast facilitates interorganelle transport of phospholipids through membrane contact. *Eur J Biochem* **1999,** *264* (2), 545-53.
101. Barberis, A.; Petrini, E. M.; Mozrzymas, J. W., Impact of synaptic neurotransmitter concentration time course on the kinetics and pharmacological modulation of inhibitory synaptic currents. *Front Cell Neurosci* **2011,** *5*, 6.
102. (a) Francis, K.; Palsson, B. O., Effective intercellular communication distances are determined by the relative time constants for cyto/chemokine secretion and diffusion. *Proc Natl Acad Sci U S A* **1997,** *94* (23), 12258-62; (b) Shvartsman, S. Y.; Wiley, H. S.; Deen, W. M.; Lauffenburger, D. A., Spatial range of autocrine signaling: modeling and computational analysis. *Biophys J* **2001,** *81* (4), 1854-67.
103. Chien, A. C.; Hill, N. S.; Levin, P. A., Cell size control in bacteria. *Curr Biol* **2012,** *22* (9), R340-9.
104. (a) Escobar, G.; Barbarossa, L.; Barbiera, G.; Norelli, M.; Genua, M.; Ranghetti, A.; Plati, T.; Camisa, B.; Brombin, C.; Cittaro, D.; Annoni, A.; Bondanza, A.; Ostuni, R.; Gentner, B.; Naldini, L., Interferon gene therapy reprograms the leukemia microenvironment inducing protective immunity to multiple tumor antigens. *Nat Commun* **2018,** *9* (1), 2896; (b) Plona, K.; Kim, T.; Halloran, K.; Wynshaw-Boris, A., Chromosome therapy: Potential strategies for the correction of severe chromosome aberrations. *Am J Med Genet C Semin Med Genet* **2016,** *172* (4), 422-430; (c) Safary, A.; Akbarzadeh Khiavi, M.; Mousavi, R.; Barar, J.; Rafi, M. A., Enzyme replacement therapies: what is the best option? *Bioimpacts* **2018,** *8* (3), 153-157; (d) Williamson, T. T.; Ding, B.; Zhu, X.; Frisina, R. D., Hormone replacement therapy attenuates hearing loss: Mechanisms involving estrogen and the IGF-1 pathway. *Aging Cell* **2019**, e12939.
105. (a) Kuchler, A.; Yoshimoto, M.; Luginbuhl, S.; Mavelli, F.; Walde, P., Enzymatic reactions in confined environments. *Nat Nanotechnol* **2016,** *11* (5), 409-20; (b) Sakr, O. S.; Borchard, G., Encapsulation of Enzymes in Layer-by-Layer (LbL) Structures: Latest Advances and Applications. *Biomacromolecules* **2013,** *14* (7), 2117-2135.
106. (a) Ruiz-Stewart, I.; Tiyyagura, S. R.; Lin, J. E.; Kazerounian, S.; Pitari, G. M.; Schulz, S.; Martin, E.; Murad, F.; Waldman, S. A., Guanylyl cyclase is an ATP sensor coupling nitric oxide signaling to cell metabolism. *P Natl Acad Sci USA* **2004,** *101* (1), 37-42; (b) Jennissen, K.; Haas, B.; Kunz, W. S.; Pfeifer, A., cGMP and cAMP

differentially regulate differentiation and function of brown adipocytes. *BMC Pharmacology* **2011,** *11* (Suppl 1), P37-P37.
107. (a) Ischiropoulos, H., Protein Modifications by Nitric Oxide and Reactive Nitrogen Species. In *Cell Signaling in Vascular Inflammation*, Bhattacharya, J., Ed. Humana Press: 2005; pp 23-26; (b) Albina, J. E.; Reichner, J. S., Role of nitric oxide in mediation of macrophage cytotoxicity and apoptosis. *Cancer Metast Rev* **1998,** *17* (1), 39-53.
108. (a) Chanthaphavong, R. S.; Loughran, P. A.; Lee, T. Y.; Scott, M. J.; Billiar, T. R., A role for cGMP in inducible nitric-oxide synthase (iNOS)-induced tumor necrosis factor (TNF) alpha-converting enzyme (TACE/ADAM17) activation, translocation, and TNF receptor 1 (TNFR1) shedding in hepatocytes. *J Biol Chem* **2012,** *287* (43), 35887-98; (b) Gnipp, S.; Mergia, E.; Puschkarow, M.; Bufe, A.; Koesling, D.; Peters, M., Nitric oxide dependent signaling via cyclic GMP in dendritic cells regulates migration and T-cell polarization. *Scientific Reports* **2018,** *8* (1), 10969; (c) Zamora, R.; Vodovotz, Y.; Billiar, T. R., Inducible nitric oxide synthase and inflammatory diseases. *Molecular medicine (Cambridge, Mass.)* **2000,** *6* (5), 347-373.
109. (a) Tidball, J. G.; Wehling-Henricks, M., Nitric oxide synthase deficiency and the pathophysiology of muscular dystrophy. *The Journal of Physiology* **2014,** *592* (21), 4627-4638; (b) Zhao, H. J.; Wang, S.; Cheng, H.; Zhang, M.-z.; Takahashi, T.; Fogo, A. B.; Breyer, M. D.; Harris, R. C., Endothelial Nitric Oxide Synthase Deficiency Produces Accelerated Nephropathy in Diabetic Mice. *Journal of the American Society of Nephrology* **2006,** *17* (10), 2664.
110. Lind, M.; Hayes, A.; Caprnda, M.; Petrovic, D.; Rodrigo, L.; Kruzliak, P.; Zulli, A., Inducible nitric oxide synthase: Good or bad? *Biomedicine & Pharmacotherapy* **2017,** *93*, 370-375.
111. Lucas, K. A.; Pitari, G. M.; Kazerounian, S.; Ruiz-Stewart, I.; Park, J.; Schulz, S.; Chepenik, K. P.; Waldman, S. A., Guanylyl cyclases and signaling by cyclic GMP. *Pharmacological reviews* **2000,** *52* (3), 375-414.
112. Durham, J. P., Guanylate cyclase: assay and properties of the particulate and supernatant enzymes in mouse parotid. *European journal of biochemistry / FEBS* **1976,** *61* (2), 535-44.
113. Baehr, W.; Karan, S.; Maeda, T.; Luo, D. G.; Li, S.; Bronson, J. D.; Watt, C. B.; Yau, K. W.; Frederick, J. M.; Palczewski, K., The function of guanylate cyclase 1 and guanylate cyclase 2 in rod and cone photoreceptors. *The Journal of biological chemistry* **2007,** *282* (12), 8837-47.
114. Gräfe, D.; Gaitzsch, J.; Appelhans, D.; Voit, B., Cross-linked polymersomes as nanoreactors for controlled and stabilized single and cascade enzymatic reactions. *Nanoscale* **2014,** *6* (18), 10752-10761.
115. (a) MacKenzie, A.; Wadsworth, R. M., Extracellular L-arginine is required for optimal NO synthesis by eNOS and iNOS in the rat mesenteric artery wall. *British journal of pharmacology* **2003,** *139* (8), 1487-1497; (b) Mancinelli, R.; La Rovere, R. M. L.; Fulle, S.; Miscia, S.; Marchisio, M.; Pierdomenico, L.; Lanuti, P.; Procino, G.; Barbieri, C.; Svelto, M.; Fanò-Illic, G.; Pietrangelo, T., Extracellular GTP is a Potent Water-Transport Regulator via Aquaporin 5 Plasma-Membrane Insertion in M1-CCD Epithelial Cortical Collecting Duct Cells. *Cellular Physiology and Biochemistry* **2014,** *33* (3), 731-746; (c) Pietrangelo, T.; Fioretti, B.; Mancinelli, R.; Catacuzzeno, L.; Franciolini, F.; Fanò, G.; Fulle, S., Extracellular guanosine-5'-triphosphate modulates myogenesis via intermediate Ca(2+)-activated K+ currents in C2C12 mouse cells. *The Journal of physiology* **2006,** *572* (Pt 3), 721-733.
116. Belluati, A.; Craciun, I.; Liu, J.; Palivan, C. G., Nanoscale Enzymatic Compartments in Tandem Support Cascade Reactions in Vitro. *Biomacromolecules* **2018,** *19* (10), 4023-4033.
117. Lomora, M.; Itel, F.; Dinu, I. A.; Palivan, C. G., Selective ion-permeable membranes by insertion of biopores into polymersomes. *Physical Chemistry Chemical Physics* **2015,** *17* (24), 15538-15546.
118. Stauch, O.; Schubert, R.; Savin, G.; Burchard, W., Structure of artificial cytoskeleton containing liposomes in aqueous solution studied by static and dynamic light scattering. *Biomacromolecules* **2002,** *3* (3), 565-78.
119. (a) Ferguson, J. W.; Dover, A. R.; Chia, S.; Cruden, N. L.; Hayes, P. C.; Newby, D. E., Inducible nitric oxide synthase activity contributes to the regulation of peripheral vascular tone in patients with cirrhosis and ascites. *Gut* **2006,** *55* (4), 542-6; (b) Zhao, Y.; Brandish, P. E.; Ballou, D. P.; Marletta, M. A., A molecular basis for nitric

oxide sensing by soluble guanylate cyclase. *Proceedings of the National Academy of Sciences* **1999,** *96* (26), 14753.
120. Wang, J.; Bafna, J. A.; Bhamidimarri, S. P.; Winterhalter, M., Small-Molecule Permeation across Membrane Channels: Chemical Modification to Quantify Transport across OmpF. *Angewandte Chemie International Edition* **2019,** *58* (14), 4737-4741.
121. Rostovtseva, T. K.; Nestorovich, E. M.; Bezrukov, S. M., Partitioning of differently sized poly(ethylene glycol)s into OmpF porin. *Biophysical journal* **2002,** *82* (1 Pt 1), 160-169.
122. Lomora, M.; Gunkel-Grabole, G.; Mantri, S.; Palivan, C. G., Bio-catalytic nanocompartments for in situ production of glucose-6-phosphate. *Chemical Communications* **2017,** *53* (73), 10148-10151.
123. Au - Lee, W.-K.; Au - Dittmar, T., Cytosolic Calcium Measurements in Renal Epithelial Cells by Flow Cytometry. *JoVE* **2014,** (92), e51857.
124. Francis, S. H.; Busch, J. L.; Corbin, J. D.; Sibley, D., cGMP-dependent protein kinases and cGMP phosphodiesterases in nitric oxide and cGMP action. *Pharmacological reviews* **2010,** *62* (3), 525-563.
125. (a) Cabrera-Pastor, A.; Taoro-González, L.; Cuñat, A. N.; Canet-López, D.; Balzano, T.; Felipo, V., Extracellular Cyclic GMP Modulates Membrane Expression of The GluA1 and GluA2 Subunits of AMPA Receptor in Cerebellum: Molecular Mechanisms Involved. *Scientific Reports* **2017,** *7* (1), 17656; (b) Hirsch, J. R.; Weber, G.; Kleta, I.; Schlatter, E., cGMP Serves as an Extracellular Regulator of a Ca²⁺-Dependent K⁺ Channel in Immortalized Human Proximal Tubule Cells. *Cellular Physiology and Biochemistry* **2001,** *11* (2), 77-82.
126. Hou, Y.; Lascola, J.; Dulin, N. O.; Ye, R. D.; Browning, D. D., Activation of cGMP-dependent Protein Kinase by Protein Kinase C. *Journal of Biological Chemistry* **2003,** *278* (19), 16706-16712.
127. Abdel-Latif, A. A., Cross Talk Between Cyclic Nucleotides and Polyphosphoinositide Hydrolysis, Protein Kinases, and Contraction in Smooth Muscle. *Experimental Biology and Medicine* **2001,** *226* (3), 153-163.
128. McMahon, D. K.; Anderson, P. A.; Nassar, R.; Bunting, J. B.; Saba, Z.; Oakeley, A. E.; Malouf, N. N., C2C12 cells: biophysical, biochemical, and immunocytochemical properties. *American Journal of Physiology-Cell Physiology* **1994,** *266* (6), C1795-C1802.
129. (a) Kakizawa, S.; Yamazawa, T.; Iino, M., Nitric oxide-induced calcium release: activation of type 1 ryanodine receptor by endogenous nitric oxide. *Channels (Austin)* **2013,** *7* (1), 1-5; (b) Charles, A., Nitric oxide pumps up calcium signalling. *Nature Cell Biology* **1999,** *1* (8), E193-E195.
130. Gross, S. M.; Rotwein, P., Live cell imaging reveals marked variability in myoblast proliferation and fate. *Skeletal Muscle* **2013,** *3* (1), 10.
131. (a) Botta, A.; Malena, A.; Loro, E.; Del Moro, G.; Suman, M.; Pantic, B.; Szabadkai, G.; Vergani, L., Altered Ca2+ homeostasis and endoplasmic reticulum stress in myotonic dystrophy type 1 muscle cells. *Genes (Basel)* **2013,** *4* (2), 275-292; (b) Pauly, M.; Angebault-Prouteau, C.; Dridi, H.; Notarnicola, C.; Scheuermann, V.; Lacampagne, A.; Matecki, S.; Fauconnier, J., ER stress disturbs SR/ER-mitochondria Ca2+ transfer: Implications in Duchenne muscular dystrophy. *Biochimica et Biophysica Acta (BBA) - Molecular Basis of Disease* **2017,** *1863* (9), 2229-2239.
132. (a) Rodríguez-García, R.; Mell, M.; López-Montero, I.; Netzel, J.; Hellweg, T.; Monroy, F., Polymersomes: smart vesicles of tunable rigidity and permeability. *Soft Matter* **2011,** *7* (4), 1532-1542; (b) Meng, F.; Zhong, Z.; Feijen, J., Stimuli-responsive polymersomes for programmed drug delivery. *Biomacromolecules* **2009,** *10* (2), 197-209.
133. Le Meins, J.-F.; Sandre, O.; Lecommandoux, S., Recent trends in the tuning of polymersomes' membrane properties. *The European Physical Journal E* **2011,** *34* (2), 14.
134. (a) Kuang, L.; Fernandes, D. A.; O'Halloran, M.; Zheng, W.; Jiang, Y.; Ladizhansky, V.; Brown, L. S.; Liang, H., "Frozen" block copolymer nanomembranes with light-driven proton pumping performance. *ACS nano* **2013,** *8* (1), 537-545; (b) Graff, A.; Fraysse-Ailhas, C.; Palivan, C. G.; Grzelakowski, M.; Friedrich, T.; Vebert, C.; Gescheidt, G.; Meier, W., Amphiphilic Copolymer Membranes Promote NADH: Ubiquinone Oxidoreductase Activity: Towards an Electron-Transfer Nanodevice. *Macromolecular chemistry and physics* **2010,** *211* (2), 229-238.

135. Kumar, M.; Habel, J. E.; Shen, Y.-x.; Meier, W. P.; Walz, T., High-density reconstitution of functional water channels into vesicular and planar block copolymer membranes. *Journal of the American Chemical Society* **2012,** *134* (45), 18631-18637.
136. Ranquin, A.; Versées, W.; Meier, W.; Steyaert, J.; Van Gelder, P., Therapeutic nanoreactors: combining chemistry and biology in a novel triblock copolymer drug delivery system. *Nano letters* **2005,** *5* (11), 2220-2224.
137. Nallani, M.; Benito, S.; Onaca, O.; Graff, A.; Lindemann, M.; Winterhalter, M.; Meier, W.; Schwaneberg, U., A nanocompartment system (synthosome) designed for biotechnological applications. *Journal of biotechnology* **2006,** *123* (1), 50-59.
138. Zhang, X.; Lomora, M.; Einfalt, T.; Meier, W.; Klein, N.; Schneider, D.; Palivan, C. G., Active surfaces engineered by immobilizing protein-polymer nanoreactors for selectively detecting sugar alcohols. *Biomaterials* **2016,** *89*, 79-88.
139. Nallani, M.; Andreasson-Ochsner, M.; Tan, C.-W. D.; Sinner, E.-K.; Wisantoso, Y.; Geifman-Shochat, S.; Hunziker, W., Proteopolymersomes: in vitro production of a membrane protein in polymersome membranes. *Biointerphases* **2011,** *6* (4), 153-157.
140. Zhang, X.; Fu, W.; Palivan, C. G.; Meier, W., Natural channel protein inserts and functions in a completely artificial, solid-supported bilayer membrane. *Scientific reports* **2013,** *3*, 2196.
141. Duong, P. H.; Chung, T.-S.; Jeyaseelan, K.; Armugam, A.; Chen, Z.; Yang, J.; Hong, M., Planar biomimetic aquaporin-incorporated triblock copolymer membranes on porous alumina supports for nanofiltration. *Journal of membrane science* **2012,** *409*, 34-43.
142. (a) Wong, D.; Jeon, T.-J.; Schmidt, J., Single molecule measurements of channel proteins incorporated into biomimetic polymer membranes. *Nanotechnology* **2006,** *17* (15), 3710; (b) Le Pioufle, B.; Suzuki, H.; Tabata, K. V.; Noji, H.; Takeuchi, S., Lipid bilayer microarray for parallel recording of transmembrane ion currents. *Analytical chemistry* **2008,** *80* (1), 328-332.
143. (a) Terwilliger, T. C.; Eisenberg, D., The structure of melittin. I. Structure determination and partial refinement. *Journal of Biological Chemistry* **1982,** *257* (11), 6010-6015; (b) Terwilliger, T. C.; Eisenberg, D., The structure of melittin. *J. biol. Chem* **1982,** *257* (601), L6015; (c) Haldar, S.; Raghuraman, H.; Chattopadhyay, A., Monitoring Orientation and Dynamics of Membrane-Bound Melittin Utilizing Dansyl Fluorescence. *The Journal of Physical Chemistry B* **2008,** *112* (44), 14075-14082.
144. (a) Popplewell, J.; Swann, M.; Freeman, N.; McDonnell, C.; Ford, R., Quantifying the effects of melittin on liposomes. *Biochimica et Biophysica Acta (BBA)-Biomembranes* **2007,** *1768* (1), 13-20; (b) Allende, D.; Simon, S.; McIntosh, T. J., Melittin-induced bilayer leakage depends on lipid material properties: evidence for toroidal pores. *Biophysical journal* **2005,** *88* (3), 1828-1837; (c) Lee, M.-T.; Sun, T.-L.; Hung, W.-C.; Huang, H. W., Process of inducing pores in membranes by melittin. *Proceedings of the National Academy of Sciences* **2013,** *110* (35), 14243-14248.
145. (a) Matsuzaki, K.; Yoneyama, S.; Miyajima, K., Pore formation and translocation of melittin. *Biophysical journal* **1997,** *73* (2), 831-838; (b) Yang, L.; Harroun, T. A.; Weiss, T. M.; Ding, L.; Huang, H. W., Barrel-stave model or toroidal model? A case study on melittin pores. *Biophysical journal* **2001,** *81* (3), 1475-1485; (c) Sengupta, D.; Leontiadou, H.; Mark, A. E.; Marrink, S.-J., Toroidal pores formed by antimicrobial peptides show significant disorder. *Biochimica et Biophysica Acta (BBA)-Biomembranes* **2008,** *1778* (10), 2308-2317.
146. Najer, A.; Wu, D.; Bieri, A.; Brand, F.; Palivan, C. G.; Beck, H.-P.; Meier, W., Nanomimics of Host Cell Membranes Block Invasion and Expose Invasive Malaria Parasites. *ACS Nano* **2014,** *8* (12), 12560-12571.
147. Thamboo, S.; Najer, A.; Belluati, A.; von Planta, C.; Wu, D.; Craciun, I.; Meier, W.; Palivan, C. G., Mimicking Cellular Signaling Pathways within Synthetic Multicompartment Vesicles with Triggered Enzyme Activity and Induced Ion Channel Recruitment. *Advanced Functional Materials* **2019,** *0* (0), 1904267.
148. (a) Nikaido, H., Molecular basis of bacterial outer membrane permeability revisited. *Microbiol Mol Biol Rev* **2003,** *67* (4), 593-656; (b) Stefureac, R.; Long, Y.-t.; Kraatz, H.-B.; Howard, P.; Lee, J. S., Transport of α-Helical Peptides through α-Hemolysin and Aerolysin Pores. *Biochemistry* **2006,** *45* (30), 9172-9179.
149. (a) Gimenez, D.; Sanchez-Munoz, O. L.; Salgado, J., Direct observation of nanometer-scale pores of melittin in supported lipid monolayers. *Langmuir* **2015,** *31* (10), 3146-58; (b) Lee, M. T.; Sun, T. L.; Hung, W. C.;

Huang, H. W., Process of inducing pores in membranes by melittin. *Proc Natl Acad Sci U S A* **2013,** *110* (35), 14243-8; (c) Leveritt, J. M., 3rd; Pino-Angeles, A.; Lazaridis, T., The structure of a melittin-stabilized pore. *Biophys J* **2015,** *108* (10), 2424-2426; (d) Lipkin, R.; Lazaridis, T., Computational studies of peptide-induced membrane pore formation. *Philos Trans R Soc Lond B Biol Sci* **2017,** *372* (1726); (e) Sengupta, D.; Leontiadou, H.; Mark, A. E.; Marrink, S. J., Toroidal pores formed by antimicrobial peptides show significant disorder. *Biochim Biophys Acta* **2008,** *1778* (10), 2308-17; (f) Sun, D.; Forsman, J.; Woodward, C. E., Multistep Molecular Dynamics Simulations Identify the Highly Cooperative Activity of Melittin in Recognizing and Stabilizing Membrane Pores. *Langmuir* **2015,** *31* (34), 9388-401.
150. van den Bogaart, G.; Guzman, J. V.; Mika, J. T.; Poolman, B., On the mechanism of pore formation by melittin. *J Biol Chem* **2008,** *283* (49), 33854-7.
151. Nardin, C.; Winterhalter, M.; Meier, W., Giant Free-Standing ABA Triblock Copolymer Membranes. *Langmuir* **2000,** *16* (20), 7708-7712.
152. (a) Kokot, G.; Mally, M.; Svetina, S., The dynamics of melittin-induced membrane permeability. *European Biophysics Journal* **2012,** *41* (5), 461-474; (b) Ladokhin, A. S.; Selsted, M. E.; White, S. H., Sizing membrane pores in lipid vesicles by leakage of co-encapsulated markers: pore formation by melittin. *Biophys J* **1997,** *72* (4), 1762-6; (c) Matsuzaki, K.; Yoneyama, S.; Miyajima, K., Pore formation and translocation of melittin. *Biophys J* **1997,** *73* (2), 831-8; (d) Levitt, J. A.; Morton, P. E.; Fruhwirth, G. O.; Santis, G.; Chung, P.-H.; Parsons, M.; Suhling, K., Simultaneous FRAP, FLIM and FAIM for measurements of protein mobility and interaction in living cells. *Biomedical optics express* **2015,** *6* (10), 3842-3854.
153. (a) Tosteson, M. T.; Tosteson, D. C., The sting. Melittin forms channels in lipid bilayers. *Biophysical journal* **1981,** *36* (1), 109-116; (b) Hanke, W.; Methfessel, C.; Wilmsen, H.-U.; Katz, E.; Jung, G.; Boheim, G., Melittin and a chemically modified trichotoxin form alamethicin-type multi-state pores. *Biochimica et Biophysica Acta (BBA) - Biomembranes* **1983,** *727* (1), 108-114.
154. (a) Kristensen, K.; Ehrlich, N.; Henriksen, J. R.; Andresen, T. L., Single-Vesicle Detection and Analysis of Peptide-Induced Membrane Permeabilization. *Langmuir* **2015,** *31* (8), 2472-2483; (b) Kristensen, K.; Henriksen, J. R.; Andresen, T. L., Quantification of leakage from large unilamellar lipid vesicles by fluorescence correlation spectroscopy. *Biochimica et Biophysica Acta (BBA) - Biomembranes* **2014,** *1838* (12), 2994-3002.
155. Terwilliger, T. C.; Eisenberg, D., The structure of melittin. I. Structure determination and partial refinement. *J Biol Chem* **1982,** *257* (11), 6010-5.
156. van den Bogaart, G.; Mika, J. T.; Krasnikov, V.; Poolman, B., The lipid dependence of melittin action investigated by dual-color fluorescence burst analysis. *Biophysical journal* **2007,** *93* (1), 154-163.
157. Fennouri, A.; Mayer, S. F.; Schroeder, T. B. H.; Mayer, M., Single channel planar lipid bilayer recordings of the melittin variant MelP5. *Biochimica et Biophysica Acta (BBA) - Biomembranes* **2017,** *1859* (10), 2051-2057.
158. (a) Benachir, T.; Lafleur, M., Study of vesicle leakage induced by melittin. *Biochimica et Biophysica Acta (BBA) - Biomembranes* **1995,** *1235* (2), 452-460; (b) Arbuzova, A.; Schwarz, G., Pore-forming action of mastoparan peptides on liposomes: a quantitative analysis. *Biochimica et Biophysica Acta (BBA) - Biomembranes* **1999,** *1420* (1), 139-152.
159. (a) Allende, D.; Simon, S. A.; McIntosh, T. J., Melittin-Induced Bilayer Leakage Depends on Lipid Material Properties: Evidence for Toroidal Pores. *Biophysical Journal* **2005,** *88* (3), 1828-1837; (b) Raghuraman, H.; Chattopadhyay, A., Orientation and dynamics of melittin in membranes of varying composition utilizing NBD fluorescence. *Biophysical journal* **2007,** *92* (4), 1271-1283.
160. (a) Yoo, E.-H.; Lee, S.-Y., Glucose biosensors: an overview of use in clinical practice. *Sensors (Basel)* **2010,** *10* (5), 4558-4576; (b) Fu, L.-H.; Qi, C.; Lin, J.; Huang, P., Catalytic chemistry of glucose oxidase in cancer diagnosis and treatment. *Chem Soc Rev* **2018,** *47* (17), 6454-6472; (c) Belluati, A.; Craciun, I.; Meyer, C. E.; Rigo, S.; Palivan, C. G., Enzymatic reactions in polymeric compartments: nanotechnology meets nature. *Current Opinion in Biotechnology* **2019,** *60*, 53-62.
161. (a) Vogele, K.; List, J.; Simmel, F. C.; Pirzer, T., Enhanced Efficiency of an Enzyme Cascade on DNA-Activated Silica Surfaces. *Langmuir* **2018,** *34* (49), 14780-14786; (b) Linko, V.; Eerikäinen, M.; Kostiainen, M. A.,

A modular DNA origami-based enzyme cascade nanoreactor. *Chemical Communications* **2015,** *51* (25), 5351-5354.
162. (a) Liu, N.; Liedl, T., DNA-Assembled Advanced Plasmonic Architectures. *Chemical Reviews* **2018,** *118* (6), 3032-3053; (b) Raeesi, V.; Chou, L. Y. T.; Chan, W. C. W., Tuning the Drug Loading and Release of DNA-Assembled Gold-Nanorod Superstructures. *Advanced Materials* **2016,** *28* (38), 8511-8518; (c) Rosi, N. L.; Giljohann, D. A.; Thaxton, C. S.; Lytton-Jean, A. K. R.; Han, M. S.; Mirkin, C. A., Oligonucleotide-Modified Gold Nanoparticles for Intracellular Gene Regulation. *Science* **2006,** *312* (5776), 1027-1030; (d) Girard, M.; Millan, J. A.; Cruz, M. O. d. l., DNA-Driven Assembly: From Polyhedral Nanoparticles to Proteins. *Annual Review of Materials Research* **2017,** *47* (1), 33-49.
163. Jakobsen, U.; Simonsen, A. C.; Vogel, S., DNA-Controlled Assembly of Soft Nanoparticles. *Journal of the American Chemical Society* **2008,** *130* (32), 10462-10463.
164. (a) Beales, P. A.; Vanderlick, T. K., Specific Binding of Different Vesicle Populations by the Hybridization of Membrane-Anchored DNA. *The Journal of Physical Chemistry A* **2007,** *111* (49), 12372-12380; (b) Dave, N.; Liu, J., Programmable Assembly of DNA-Functionalized Liposomes by DNA. *ACS Nano* **2011,** *5* (2), 1304-1312.
165. Meyer, C. E.; Liu, J.; Craciun, I.; Wu, D.; Wang, H.; Xie, M.; Fussenegger, M.; Palivan, C. G., Segregated Nanocompartments Containing Therapeutic Enzymes and Imaging Compounds within DNA-Zipped Polymersome Clusters for Advanced Nanotheranostic Platform. *Small n/a* (n/a), 1906492.
166. Ba, Q.; Raghavan, G.; Kiselyov, K.; Yang, G., Whole-Cell Scale Dynamic Organization of Lysosomes Revealed by Spatial Statistical Analysis. *Cell Rep* **2018,** *23* (12), 3591-3606.
167. (a) Kelly, P.; Woonton, B. W.; Smithers, G. W., 8 - Improving the sensory quality, shelf-life and functionality of milk. In *Functional and Speciality Beverage Technology*, Paquin, P., Ed. Woodhead Publishing: 2009; pp 170-231; (b) Magacz, M.; Kędziora, K.; Sapa, J.; Krzyściak, W., The Significance of Lactoperoxidase System in Oral Health: Application and Efficacy in Oral Hygiene Products. *Int J Mol Sci* **2019,** *20* (6), 1443; (c) Łukasz Minarowski, A. U. D. S. A. U. A. M. A. U. A. K. A. U. A. S. A. U. M. G. A. U. E., Thiocyanate concentration in saliva of cystic fibrosis patients. *Thiocyanate concentration in saliva of cystic fibrosis patients.* **2008,** *46* (2), 245-246-245-246.
168. (a) Stanislawski, M.; Rousseau, V.; Goavec, M.; Ito, H., Immunotoxins containing glucose oxidase and lactoperoxidase with tumoricidal properties: in vitro killing effectiveness in a mouse plasmacytoma cell model. *Cancer Res* **1989,** *49* (20), 5497-5504; (b) Patel, U.; Gingerich, A.; Widman, L.; Sarr, D.; Tripp, R. A.; Rada, B., Susceptibility of influenza viruses to hypothiocyanite and hypoiodite produced by lactoperoxidase in a cell-free system. *PLoS One* **2018,** *13* (7), e0199167-e0199167.
169. (a) Wyatt, P. J., Measurement of Special Nanoparticle Structures by Light Scattering. *Analytical Chemistry* **2014,** *86* (15), 7171-7183; (b) Khlebtsov, B. N.; Khlebtsov, N. G., On the measurement of gold nanoparticle sizes by the dynamic light scattering method. *Colloid Journal* **2011,** *73* (1), 118-127; (c) Arenas-Guerrero, P.; Delgado, Á. V.; Donovan, K. J.; Scott, K.; Bellini, T.; Mantegazza, F.; Jiménez, M. L., Determination of the size distribution of non-spherical nanoparticles by electric birefringence-based methods. *Scientific Reports* **2018,** *8* (1), 9502.
170. Liu, Z. H.; Li, Y.; Kowk, K. W., Mean interparticle distances between hard particles in one to three dimensions. *Polymer* **2001,** *42* (6), 2701-2706.
171. Chi, Q.; Wang, G.; Jiang, J., The persistence length and length per base of single-stranded DNA obtained from fluorescence correlation spectroscopy measurements using mean field theory. *Physica A: Statistical Mechanics and its Applications* **2013,** *392* (5), 1072-1079.
172. (a) Perktold, A.; Zechmann, B.; Daum, G.; Zellnig, G., Organelle association visualized by three dimensional ultrastructural imaging of the yeast cell. *FEMS Yeast Research* **2007,** *7* (4), 629-638; (b) Hertlein, V.; Flores-Romero, H.; Das, K. K.; Fischer, S.; Heunemann, M.; Calleja-Felipe, M.; Knafo, S.; Hipp, K.; Harter, K.; Fitzgerald, J. C.; García-Sáez, A. J., MERLIN: a novel BRET-based proximity biosensor for studying mitochondria–ER contact sites. *Life Science Alliance* **2020,** *3* (1), e201900600.
173. Baker, E. H.; Baines, D. L., Airway Glucose Homeostasis: A New Target in the Prevention and Treatment of Pulmonary Infection. *CHEST* **2018,** *153* (2), 507-514.

174. Perillo, B.; Di Donato, M.; Pezone, A.; Di Zazzo, E.; Giovannelli, P.; Galasso, G.; Castoria, G.; Migliaccio, A., ROS in cancer therapy: the bright side of the moon. *Experimental & Molecular Medicine* **2020**.
175. Nardin, C.; Hirt, T.; Leukel, J.; Meier, W., Polymerized ABA triblock copolymer vesicles. *Langmuir* **2000,** *16* (3), 1035-1041.
176. Najer, A.; Thamboo, S.; Duskey, J. T.; Palivan, C. G.; Beck, H. P.; Meier, W., Analysis of Molecular Parameters Determining the Antimalarial Activity of Polymer-Based Nanomimics. *Macromol Rapid Comm* **2015,** *36* (21), 1923-1928.
177. Baumann, P.; Spulber, M.; Dinu, I. A.; Palivan, C. G., Cellular Trojan Horse Based Polymer Nanoreactors with Light-Sensitive Activity. *The Journal of Physical Chemistry B* **2014,** *118* (31), 9361-9370.
178. JW. Krieger; Langowski, J. *QuickFit 3.0: A data evaluation application for biophysics*, http://www.dkfz.de/Macromol/quickfit/, 2015.
179. Sutherland, H.; Zolle, O.; Khundkar, R.; Simpson, A. W.; Jarvis, J. C.; Salmons, S., A nonradioactive assay for nitric oxide synthase activity in tissue extracts. *Methods Mol Biol* **2004,** *279*, 105-11.
180. Newton, M.; Niewczas, I.; Clark, J.; Bellamy, T. C., A real-time fluorescent assay of the purified nitric oxide receptor, guanylyl cyclase. *Analytical biochemistry* **2010,** *402* (2), 129-136.
181. Wayne, R., Chapter 3 - Plasmodesmata. In *Plant Cell Biology (Second Edition)*, Wayne, R., Ed. Academic Press: 2019; pp 55-65.

11 Acknowledgements

A proverb states that it takes a village to raise a child. Maybe a whole village is not necessary for a PhD, yet it definitely requires the effort of many people to lead an unexperienced student to this point. After four years, the list is long and I would like to take the time to thank everyone.

Of course, the first acknowledgement goes to my supervisor, Prof. Dr. Cornelia Palivan, who gave me the opportunity to conduct my PhD research in such a fascinating field, for her continuous support during these years and the many valuable lessons learned that go beyond science. My next acknowledgement goes to Prof. Dr. Wolfgang Meier, for his generous material and theoretical support, and for accepting to chair the PhD exam. Additionally, I wish to thank Prof. Dr. Lucio Isa for the useful discussions and for accepting to be my co-examinator.

This thesis would not have its shape without the huge contribution given by Dr. Ioana Craciun, who has been at my side all along this path, helping me in any way she could, and to whom I am indebted, professionally and personally. Likewise, I owe many of my achievements to Dr. Sagana Thamboo, my partner in the projects that generated Chapter 3 and many more that are on their way.

I am grateful to my colleagues and co-authors Dr. Şaziye Yarulmaz Avşar, Dr. Juan Liu and Dr. Viviana Maffeis, Dr. Adrian Najer and Davy Daubian, for all the help provided during my research and the writing of the articles.

However, no project would have ever seen the light without the work of those who synthesized the polymers that I used, and the valuable discussions: Dr. Samuel Lörcher, Dr. Adrian Dinu, Dr. Dalin Wu, Sven Kasper and Riccardo Wehr.

The other collaborators that I wish to thank are Dr. Elena Candida, Claire Meyer and Stefano Di Leone, Dimitri Hürlimann, Cora-Ann Schönenberger, Vittoria Chimisso, Rosario Vanella, Claudio von Planta Laura Álvarez Francés (ETHZ), Guido Panzarasa (ETHZ), Susanna Zamolo (University of Bern) Prof. Dr. Didier Reinhardt (University of Fribourg), Fabienne Schwab (University of Fribourg), Konrad Manfred (University of Göttingen), Julian Blanchard (Albert Einstein College of Medicine) and Prof. Dr. Jürg Schwaller (Unispital Basel).

Many thanks also to Gabriele Persy, for the so many TEM measurements she performed, Dr. Mohamed Chami for his help with cryo-TEM (C-CINA, University of Basel), Alexia Loynton-Ferrand (IMCF, University of Basel) for 3D-SIM imaging and Viktoria Mikhalevich for providing her AFM data and coming up with challenging pastimes. Thanks a lot to all the supporting staff of the department: Maya Greuter, Dr. Michael Devereux, Beatrice Erismann, Markus Hauri, Susanne Foley.

Not to forget, my students, who did much of the heavy lifting at the early stages of projects: Frida Terne, Felix Erb and Samantha Novak.

A big thank you also to the people who never allowed me to risk our friendship with a collaboration: the soon to be doctors Myrto Kyropoulou and Serena Rigo, Shabnam Tarvirdipour, Dr. Pascal Richard and Dr. Evgeniia Konischeva. And, obviously, all the other group members for such a great working atmosphere.

Setting work aside I need to mention my friends here in Basel, who made the stay so much nicer, my friends back in Italy, who made my trips back worthwhile and my friends all over Europe and the world, who broadened my horizons. A special mention to Alessandro Castrogiovanni, who did not want to be left in Italy and came to Basel with me.

Last but not least comes my family: my girlfriend Federica, who was simply my source of strength through these years and my parents, Luisella and Renato, to whom I wish to dedicate this work: I could have never made it without you.